

**INVESTIGATIONS OF ENTRANCE FLOW AND
PARTIAL FLOW BLOCKAGES IN FUEL
SUBASSEMBLIES OF FAST BREEDER REACTOR**

By

GOVINDHA RASU N

(Enrollment No.: ENGG02201004001)

Indira Gandhi Centre for Atomic Research, Kalpakkam

A thesis submitted to the Board of Studies in Engineering Sciences

In partial fulfillment of requirements

For the Degree of

DOCTOR OF PHILOSOPHY

of

HOMI BHABHA NATIONAL INSTITUTE



December, 2013

Homi Bhabha National Institute

Recommendations of the Viva Voce Board

As members of the Viva Voce Board, we certify that we have read the dissertation prepared by **Mr. Govindha Rasu N** entitled “**Investigations of Entrance Flow and Partial Flow Blockages in Fuel Subassemblies of Fast Breeder Reactor**” and recommend that it may be accepted as fulfilling the dissertation requirement for the Degree of Doctor of Philosophy.



Date: 7/11/2014

Chairman: **Dr. S. Venugopal**



Date: 7/11/2014

Guide / Convener: **Dr. K. Velusamy**



Date: 7-11-2014

Co-Guide / Member: **Prof. T. Sundararajan**



Date: 7/11/2014

Member: **Dr. R.S. Keshavamurthy**



Date: 7/11/2014

External Examiner:

Final approval and acceptance of this dissertation is contingent upon the candidate's submission of the final copies of the dissertation to HBNI.

I hereby certify that I have read this dissertation prepared under my direction and recommend that it may be accepted as fulfilling the dissertation requirement.

Date: 7/11/2014



Place: Indira Gandhi Centre for Atomic Research (IGCAR)

Dr. K. Velusamy

Kalpakkam

(Guide)

STATEMENT BY AUTHOR

This dissertation has been submitted in partial fulfillment of requirements for an advanced degree at Homi Bhabha National Institute (HBNI) and is deposited in the library to be made available to borrowers under rules of the HBNI.

Brief quotations from this dissertation are allowable without special permission, provided that accurate acknowledgement of source is made. Requests for permission for extended quotation from or reproduction of this manuscript in whole or in part may be granted by the Competent Authority of HBNI when in his or her judgment the proposed use of the material is in the interests of scholarship. In all other instances, however, permission must be obtained from the author.

Kalpakkam
December 2013


(Govindha Rasu N)

DECLARATION

I, hereby declare that the investigation presented in the thesis has been carried out by me. The work is original and has not been submitted earlier as a whole or in part for a degree / diploma at this or any other Institution / University.

Kalpakkam

December 2013


(Govindha Rasu N)

This work is dedicated to

***‘My Beloved Grand Mother, Father,
Uncle, Aunt and My Wife’***

(For their love, care, and support in the absence of my mother)

ACKNOWLEDGEMENTS

I take this opportunity to express my thanks to the people who have been very helpful to me during the time it took me to complete this thesis.

First and foremost I acknowledge my Guide **Dr. K. Velusamy**, *Head, Mechanics and Hydraulics Division, Reactor Design Group (RDG), IGCAR* for his persistent encouragement, constant motivation, everlasting patience and valuable technical inputs right from the attending the courses till the end of my thesis work. The joy and enthusiasm he has for his research was contagious and motivational for me, even during tough times in the Ph.D

I record my sincere gratitude to my Co-guide **Prof. T. Sundararajan**, *Head, Department of Mechanical Engineering, IIT-Madras* for his guidance, constant support and invaluable technical inputs starting from course work upto thesis submission.

I highly grateful to my Doctoral Committee (DC) members (**Dr. S. Venugopal, and Dr. R.S. Keshavamurthy**), for their valuable inputs, continuous monitoring of my progress and valuable supports throughout the course of my research.

I sincerely thank to **Dr. P. Chellapandi**, *Director, RDG* for his perpetual support and encouragement throughout my research period. I thank **Dr. P.R. Vasudeva Rao**, *Director, IGCAR*, **Dr. R. B. Grover**, *Director, HBNI, Mumbai* and **Dr. B. K. Dutta**, *Deanr, HBNI, Mumbai* for allowing me to continue my research work. I thank **Shri P. Selvaraj**, *Associate Director, RAG* for his kind support and encouragement throughout my research period. I sincerely thank our guardian **Dr. M. Sai Baba**, *Associate Director, RMG* for his care and support from day one.

My special thanks are due to the officers of Thermal Hydraulics Section **S/Shri M.Asokkumar, R.Gajapathy, U.Partha Sarathy, K.Natesan** and **R.Arulbaskar** for sharing their knowledge and support during my thesis work. I sincerely appreciate

Mr.M.Rajendra Kumar, Mr.Juby Abraham, Mr.Ram Kumar Maity and Mr.L.Ravi for their kind help and sharing scientific their technical knowledge.

I acknowledge the support of **Mr. Bhagwana Ram, Mr. Naga Sivayya, Mr. R. Nandha Kumar, Mr. Ashish Shukla, Mr. Sudharshan, Mr. Srinivas and Mr. Uday Kumar** during the thesis work.

I would like to acknowledge **Smt. R.Vijayashree** for providing the advanced computational facility (SAMDO LAB) and arranging software training programmes. I also thank **Shri. A. Sathyamurthy**, Head, Computer division and **Shri. R. Jahadeesan**, for providing High Performance Scientific Computing Facility. I also acknowledge the support of **Mr. A. Sivakumar, DM/D, THS and Mrs. M. Banumathi, Streno Gr-II** during the thesis work.

I also acknowledge **Prof. M.A. Ramasamy** (Retd IISC, Bangalore), **Dr. Ranganayakalu, General System, ADA** and **Dr. L.S.Ismail, General System, ADA** for motivating me to take research in Thermal Hydraulics.

My special thanks are due to my friends, **Mr. Abhijit** and **Mr. Vijaya kumar** from IIT-Madras and **Mr. Guru Brhamam** from IISC-Bangalore for their help in collecting important literature. I also thank my DGFS-PhD batch friends **Mr. Paawan Sharma, Mr. Arun Babu, Mrs. Hemangi Gawand and Mr. Saptarshi Ghosh** for their support and care during my stay at Kalpakkam. For making a joyous and peaceful stay at JRF Enclave, Kalpakkam, I thank all the research scholars and the staff involved.

I thank all my family members for their constant support. Especially my wife (**Mrs. G.Vijaya Lakshmi**) and my son (**G. Praneth**) have sacrificed many occasions. Last but not least, I thank the Almighty for the blessings to complete my thesis.

CONTENTS

Title	Page No
SYNOPSIS	v
LIST OF FIGURES	viii
LIST OF TABLES	xvii
CHAPTER 1 INTRODUCTION	1 - 8
1.0 FOREWORD	2
1.1 FAST BREEDER REACTOR	3
1.2 THERMAL HYDRAULICS OF FUEL SUBASSEMBLY	5
1.3 MOTIVATION FOR THE PRSENT STUDY	7
1.4 OBJECTIVES AND SCOPE OF THE THESIS WORK	7
1.5 ORGANISATION OF THE THESIS	8
CHAPTER 2 LITERATURE REVIEW	9 - 24
2.0 INTRODUCTION	10
2.1 ENTRANCE FLOW IN DUCTS	10
2.2 EXPERIMENTS IN PIN BUNDLE	12
2.3 NUMERICAL STUDIES IN PIN BUNDLE	18
2.4 FLOW BLOCKAGE STUDIES IN FUEL PIN BUNDLE	21
2.5 CLOSURE	24
CHAPTER 3 MATHEMATICAL MODELING	25 - 35
3.0 INTRODUCTION	26
3.1 GOVERNING EQUATIONS	26
3.2 TURBULENCE MODELLING	27
3.2.1 Bare Pin Bundle	27
3.2.2 Wire-wrapped Pin Bundle	28
3.3 MODELLING OF BLOCKAGE WITHIN THE BUNDLE	30
3.4 ENGINEERING PARAMETERS	32
3.5 BOUNDARY CONDITIONS AND CONVERGENCE	34
3.6 GRID SENSITIVITY STUDY AND VALIDATION	35
3.7 CLOSURE	35

CHAPTER 4	FLOW AND THERMAL DEVELOPMENT IN BARE FUEL PIN BUNDLES	36 - 74
4.0	INTRODUCTION	37
4.1	SOLUTION METHODOLOGY	38
4.1.1	Grid Sensitivity Study	38
4.1.2	Validation Studies	42
4.1.3	Selection of Turbulence Model	46
4.1.4	Selection of Discretization Scheme	49
4.1.5	Selection of Turbulent Prandtl Number	52
4.2	RESULTS AND DISCUSSION	55
4.2.1	Effect of Number of Fuel Pins	55
4.2.2	Effect of Gap Between Peripheral Pin and Hexcan	62
4.2.2.1	<i>7-Pin Bundle</i>	62
4.2.2.2	<i>217- Pin Bundle</i>	65
4.2.3	Effect of Pin Diameter	67
4.2.3.1	<i>7-Pin Bundle</i>	67
4.2.3.2	<i>217- Pin Bundle</i>	70
4.2.4	Effect of Reynolds Number	71
4.3	CLOSURE	74
CHAPTER 5	LAMINAR FLOW AND THERMAL DEVELOPMENT IN HELICAL WIRE-WRAPPED PIN BUNDLES	75 - 94
5.0	INTRODUCTION	76
5.1	SOLUTION METHODOLOGY	76
5.1.1	Grid Sensitivity Study	76
5.1.2	Validation of Sodium Flow through Straight and Helical Pipe	80
5.2	RESULTS AND DISCUSSION	84
5.2.1	Effect of Reynolds Number	85
5.2.2	Effect of Pitch to Diameter Ratio	88
5.2.3	Effect of Helical Pitch	90
5.3	CLOSURE	94
CHAPTER 6	TURBULENT FLOW AND THERMAL DEVELOPMENT IN HELICAL WIRE-WRAPPED PIN BUNDLES	95 - 137
6.0	INTRODUCTION	96
6.1	SOLUTION METHODOLOGY	96

6.1.1	Grid Sensitivity Study	96
6.1.2	Selection of Turbulence Model	98
6.1.3	Validation	99
6.2	RESULTS AND DISCUSSION	103
6.2.1	Effect of Reynolds Number	104
6.2.2	Effect of Helical Spacer Wire Pitch	114
6.2.3	Effect of Number of Fuel Pins	125
6.3	CLOSURE	136
CHAPTER 7	THERMAL HYDRAULIC EFFECTS OF POROUS BLOCKAGE IN HELICAL WIRE-WRAPPED BUNDLES	138 - 176
7.0	INTRODUCTION	139
7.1	SOLUTION METHODOLOGY	139
7.1.1	Grid Sensitivity Study	139
7.1.2	Validation Studies	140
7.2	RESULTS AND DISCUSSION	144
7.2.1	Effect of Blockage in Pin Bundle	146
7.2.2	Effect of Blockage Geometry	157
7.2.2.1	<i>Effect of Blockage Shape</i>	157
7.2.2.2	<i>Effect of Blockage Size</i>	161
7.2.3	Effect of Radial Position of Blockage	165
7.2.4	Effect of Blockage Porosity	169
7.2.5	Detection of Blockage by Core Temperature Monitoring System	172
7.2.6	Effect of thermal conductivity	174
7.3	CLOSURE	175
CHAPTER 8	CONCLUSIONS	177 - 181
8.0	INTRODUCTION	178
8.1	FLOW AND THERMAL DEVELOPMENT IN BARE FUEL PIN	178
8.2	LAMINAR FLOW AND THERMAL DEVELOPMENT IN HELICAL WIRE-WRAPPED PIN BUNDLES	179
8.3	TURBULENT FLOW AND THERMAL DEVELOPMENT IN WIRE-WRAPPED PIN BUNDLES	179
8.4	THERMAL HYDRAULIC EFFECTS OF POROUS BLOCKAGE IN WIRE-WRAPPED BUNDLES	180
8.5	PROPOSED FUTURE WORK	180
APPENDIX		182
REFERENCES		183 - 188
NOMENCLATURE		189 - 192

SYNOPSIS

Fast reactors are one of the promising future energy options. Due to their breeding potential they could utilize a maximum quantity of uranium for energy production. Fast breeder reactors (FBR) have a compact core and have a large volumetric energy production rate. To extract large heat flux without significant increase in fuel and clad temperatures liquid sodium metal is used as the coolant due to the possibility of large heat transfer coefficient. Fuel pins in an FBR are housed in a hexagonal sheath and the pins are provided with helical wire-wrap. Also, the diameter of the fuel pin is small (3 – 6 mm) leading to small hydraulic diameter of the sub-channels. The fuel pin bundle, also known as subassembly, has a large number of tight sub-channels. Because of this, the inter-sub-channel communication is weak. This may have significant effect on the entrance flow characteristics in a subassembly. Further, the possibility of blockage formation within the subassembly and the attendant risk of local temperature increase are high. The present thesis attempts to investigate these aspects which are important in the design of a FBR core. For this purpose, three dimensional conservation equations of mass, momentum and energy are solved by using a finite volume based commercial computational fluid dynamics code employing appropriate turbulence models. The computational model is validated against published sodium experimental results in pipes, cylindrical annulus and rod bundles. Earlier research works were focused mainly on understanding the flow and temperature fields in the fully developed region. Large deviations were reported among published correlations for Nusselt number in pin bundles. Also, interplay between blockage effects and developing flow / temperature fields has not been studied in the past. In the present work a detailed and systematic parametric study has been attempted. The parameters varied include the number of fuel pins, ligament gap, pin diameter, Reynolds number, helical wire-wrap pitch, ratio of triangular pitch to diameter of pins, blockage shapes, size, position and porosity.

Before attempting to study entrance flow in wire-wrap bundle the case of bare bundle is studied. During sodium flow through bare pin bundles development characteristics are seen to be strongly influenced by pin diameter, number of pins, ligament gap between the last row of pins and hexcan wall and Reynolds number. Flow development is achieved within an axial length of ~125 hydraulic diameters, for all the pin bundle configurations considered. But temperature development is attained only if the pin diameter is small or the number of pins is less. In the case of large pin diameter with more pins, temperature development is not be

achieved even after a length of ~ 1000 hydraulic diameters. The reason for this behaviour is traced to be the weak communication among sub-channels in tightly packed bundles. It is seen that the pin Nusselt number decreases from centre to periphery in a bundle. Also, if the ligament gap is narrow, the Nusselt number is large and more uniform. Further, flow development length is short if the Reynolds number is large and the converse is true for thermal development length.

Following bare bundle study, investigation related to wire-wrap bundles has been carried out. During laminar flow through a wire-wrapped pin bundle, the friction factor is seen to exhibit a strong dependence on helical pitch where it increases as the pitch shortens. On the contrary, the Nusselt number does not exhibit such a strong dependence on helical pitch. A strong non-zero cross-stream velocity prevails in the fully developed region, contrary to that observed in straight channels. The mean value of non-dimensional cross-stream velocity is found to scale as $\pi D_r/H$, where, D_r is the pin diameter and H is the helical pitch of spacer wire. The friction factor and cross-stream velocity are relatively high in tight pin bundles.

In turbulent flow through helical wire-wrapped fuel pin bundle, the wire-wrap is found to promote a strong cross-stream velocity. It is found that the magnitude of mean cross-stream velocity in the fully developed region is inversely proportional to the helical pitch length and it is nearly independent of the number of pins. Friction factor is seen to fluctuate periodically over a mean value and the fluctuation over each helical pitch corresponds to a specific position of helical wire. The mean value of the friction factor in the entrance region reduces below the mean value in the fully developed region contrary to that seen in ducted flows. Similarly, the Nusselt number passes through multiple minima before attaining fully developed periodic spatial fluctuations and its development is slower than that of friction factor. For a bundle with large number of pins the thermal development length is long. Traditionally, correlations reported for fully developed flow are considered for core design. But, the present study indicates that this approach may not be conservative. Further, the entrance region effects and the oscillations in the fully developed region have to be properly accounted in the core design. Based on the parametric study a correlation for Nusselt number is proposed as a function of helical pitch and other influencing parameters. The hotspot factor in the pin bundle is found to vary from 3 to 4. Further, it is large, either if Reynolds number is low or the number of pins is more.

In the last part of the research, sodium flow through fuel pin bundles with local blockage is investigated. For this, flow and temperature fields within a 19-pin wire-wrapped

fuel bundle with internal blockage have been predicted. Simulations are carried out for a stream-wise length of 7 helical pitches. Clad temperature, cross-stream sodium velocity and cross-stream temperature distributions are investigated in detail. Axial distribution of clad temperature is seen to exhibit strong spatial variations due to the interaction of helical spacer wire and coolant flow through a subassembly with porous blockage. The maximum difference in the circumferential temperature of clad, which is a critical parameter for fuel pin mechanical design, is large in pins that are partially exposed to blockage. Effect of porous blockage is found to be limited to the porous zone and the peak clad temperature is proportional to the volume of the porous zone. Peak temperature in the blockage is strongly influenced by the radial extent of blockage and it is higher if the radial extent is larger. Maximum difference in the circumferential clad temperature is relatively low for a corner blockage compared to that of a central blockage. Sodium boiling is imminent in fuel pin bundle with six blocked sub-channels located at the centre when porosity value reduces below ~45%.

LIST OF FIGURES

Figure No.	Figure Title	Page No.
Fig. 1.1.	Flow sheet of pool type Fast Breeder Reactor	4
Fig. 1.2	Primary circuit assembly of pool type Fast Breeder Reactor	4
Fig. 2.1	(a) Comparison of friction factor in pin bundles with $H/(D_w+D_r) = 24.4$ employing various correlations	13
	(b) Comparison of Nusselt number in pin bundles employing various correlations	13
Fig. 3.3	Boundary conditions used for the CFD simulations	35
Fig. 4.1	CFD model of 217-pin bundle with sub-channels	39
Fig. 4.2	(a) Mesh used for 217-pin bundle study	39
	(b) Three different mesh used for grid sensitivity study (i) 0.387 millions (ii) 0.735 millions (iii) 1.35 millions	40
Fig. 4.3	(a) Variation of Nusselt number during sodium flow in the entrance region of a circular pipe ($Re = 4.3 \times 10^5$)	42
	(b) Variation of friction factor during sodium flow in the entrance region of a circular pipe ($Re = 4.3 \times 10^5$)	42
Fig. 4.4	(a) Mesh and boundary condition used in 1/6th of triangular sub-channel (All the dimensions are in mm)	44
	(b) Variation of global Nusselt number during flow of sodium in a single triangular sub-channel at $Re = 1.18 \times 10^5$	45
	(c) Circumferential variation of local pin Nusselt number during flow of sodium in a single triangular sub-channel at $Re = 1.18 \times 10^5$	45
	(d) Variation of average clad temperature and global bulk temperature in a single triangular sub-channel at $Re = 1.18 \times 10^5$	46

Fig. 4.5	(a) Global Nusselt number in 7-pin bundle configuration during sodium flow at $Re = 2.58 \times 10^5$	47
	(b) Local Nusselt number in 7-pin bundle configuration during sodium flow at $Re = 2.58 \times 10^5$	47
	(c) Friction factor in 7-pin bundle configuration during sodium flow at $Re = 2.58 \times 10^5$	48
	(d) Velocity in 7-pin bundle configuration during sodium flow at $Re = 2.58 \times 10^5$	48
	(e) Average clad temperature in 7-pin bundle configuration during sodium flow at $Re = 2.58 \times 10^5$	49
	(f) Comparison of thermal development in 7-pin bundle as a function of discretization schemes at $Re = 1.10 \times 10^5$	50
	(g) Comparison of friction factor development in 7-pin bundle as a function of discretization schemes at $Re = 1.10 \times 10^5$	51
	(h) Comparison of axial velocity development in 7-pin bundle as a function of discretization schemes at $Re = 1.10 \times 10^5$	51
	(i) Comparison of axial velocity development in 7-pin bundle as a function of discretization schemes at $Re = 1.10 \times 10^5$	52
	(j) Comparison of thermal development data in 7-pin bundle as a function of turbulent Prandtl number at $Re = 0.842 \times 10^5$	53
	(k) Comparison of flow development data in 7-pin bundle as a function of turbulent Prandtl number at $Re = 0.842 \times 10^5$	53
	(l) Comparison axial velocity in 7-pin bundle as a function of turbulent Prandtl number at $Re = 0.842 \times 10^5$	54
	(m) Comparison average clad temperature in 7-pin bundle as a function of turbulent Prandtl number at $Re = 0.842 \times 10^5$	54
Fig. 4.6	Pin bundle configurations considered for the study: (a). 1-pin, (b). 7-pin, (c).19-pin, (d). 61-pin, (e) 217-pin	55
Fig. 4.7	Cross-stream velocity (m/s) in 7-pin bundle with 6.6 mm pin diameter	56
Fig. 4.8	Non-dimensional axial velocity (u_z/u_{z-in}) in 7-pin bundle with 6.6 mm pin diameter	57
Fig. 4.9	Temperature contours (K) in 7-pin bundle with pin diameter 6.6 mm	57

Fig. 4.10	Flow development in pin bundle with different number of pins at $Re = 0.842 \times 10^5$	58
Fig. 4.11	Variation of overall Nusselt number in pin bundle with different number of fuel pins at $Re = 0.842 \times 10^5$	59
Fig. 4.12	(a) Comparison of global and average pin Nusselt numbers in 7-pin bundle configuration at $Re = 0.842 \times 10^5$	60
	(b) Evolution of temperature during flow of sodium in a 217-pin bundle assembly at $Re = 0.842 \times 10^5$	61
Fig. 4.13	Global Nusselt number in 7-pin bundle: Effect of ligament gap	63
Fig. 4.14	(a) Flow development in 7-pin bundle : Effect of ligament gap	63
	(b) Dimensionless velocity distribution in 7-pin bundle for different ligament gaps at fully developed region	64
Fig. 4.15	(a) Global Nusselt number in 217-pin bundle : Effect of ligament gap	65
	(b) Average pin Nusselt number in 217-pin bundle ($L/D_h = 1972$)	66
	(c) Development of friction factor in 217-pin bundle : Effect of ligament gap	66
Fig. 4.16	Global Nusselt number in 7-pin bundle : Effect of pin diameter	68
Fig. 4.17	(a) Flow development in 7-pin bundle : Effect of pin diameter	68
	(b) Dimensionless velocity distribution in 7-pin bundle for different diameters at fully developed region	69
Fig. 4.18	(a) Global Nusselt number in 217-pin bundle : Effect of pin diameter	71
	(b) Flow development in 217-pin bundle : Effect of pin diameter	71
Fig. 4.19	(a) Flow development in 7-pin bundle : Effect of Reynolds number	72
	(b) Nusselt number development in 7-pin bundle : Effect of Reynolds number	73
Fig. 5.1	Cross-stream grid distribution (a) 36 divisions around fuel pin (b) 72 divisions around fuel pin (c) Mesh division on fuel pin surface and helical wire surface	77

Fig. 5.2	Cross-stream grids considered for 7-pin bundle configurations considered in the present study with (a) $P_t/D_r = 1.42$, (b) $P_t/D_r = 1.14$ and (c) Isometric view of grid generated for the 7-pin bundle with $P_t/D_r = 1.25$	79
Fig. 5.3	(a) Grid used for sodium flow through pipes ($Re = 840$)	81
	(b) Development of cross-stream velocity for sodium flow through pipes ($Re = 840$)	81
	(c) Development of axial velocity vectors for sodium flow through pipes ($Re = 840$)	82
	(d) Developing temperature field for sodium flow through pipes ($Re = 840$)	82
	(e) Development of Nusselt number for sodium flow through pipes ($Re = 840$)	82
	(f) CFD model of helical tube	84
	(g) Development of Nusselt number during water flow through helical pipe for $Re = 250$, $\lambda = 0.6$ and $\delta = 0.05$	84
Fig. 5.4	(a) Development of cross-stream velocity in 7-pin bundle for $H = 100$ mm	86
	(b) Development of friction factor in 7-pin bundle for $H = 100$ mm	86
	(c) Development of Nusselt number in 7-pin bundle for $H = 100$ mm	87
Fig. 5.5	(a) Development of cross-stream velocity in 7-pin bundle for $Re = 840$	89
	(b) Development of friction factor in 7-pin bundle for $Re = 840$	89
	(c) Development of Nusselt number in 7-pin bundle for $Re = 840$	90
Fig. 5.6	(a) Development of cross-stream velocity in 7-pin bundle for $Re = 840$	91
	(b) Development of friction factor in 7-pin bundle for $Re = 840$	92
	(c) Development of Nusselt number in 7-pin bundle for $Re = 840$	92
	(d) Expanded view of friction factor in the fully developed region for $Re = 840$	93
Fig. 6.1	Computational grids considered for 37-pin bundle	98

Fig. 6.2	(a) Prediction of friction factor development in 7-pin bundle by various turbulence models ($Re = 0.842 \times 10^5$)	99
	(b) Prediction of Nusselt number development in 7-pin bundle by various turbulence models ($Re = 0.842 \times 10^5$)	99
Fig. 6.3	(a) Computational grid considered for the experimental geometry	100
	(b) Comparison of predicted Nusselt number development with experimental data	100
Fig. 6.4	(a) Comparison of fully developed friction factor with experimental correlation for $H / (D_w + D_r) = 24.4$	102
	(b) Comparison of fully developed friction factor with experimental correlation for $Re = 0.842 \times 10^5$	102
Fig. 6.5	Comparison of fully developed Nusselt number with experimental correlations	103
Fig. 6.6	(a) Cross-stream velocity in the 1 st helical wire pitch ($Re = 1.8 \times 10^5$)	105
	(b) Fig. 6.6b Cross-stream velocity in the 2 nd helical wire pitch ($Re = 1.8 \times 10^5$)	106
Fig. 6.7	(a) Non-dimensional cross-stream velocity in 7-pin bundle for $Re = 1.8 \times 10^5$	108
	(b) Cross-stream temperature field (K) at $Z = 1.203$ m in 7-pin bundle for $Re = 1.8 \times 10^5$	108
Fig. 6.8	Friction factor development for various values of Reynolds number [$H / (D_w + D_r) = 24.4$]	109
Fig. 6.9	Nusselt number development for various values of Reynolds number [$H / (D_w + D_r) = 24.4$]	110
Fig. 6.10	Amplitudes of periodic variation of Nusselt number and friction factor about mean values	112
Fig. 6.11	(a) Evolution of hot spot factor for central pin in 7-pin bundle subassembly with $H / (D_w + D_r) = 24.4$	112
	(b) Evolution of hot spot factor for peripheral pin in 7-pin bundle subassembly with $H / (D_w + D_r) = 24.4$	113
Fig. 6.12	Cross-stream velocity at the end of 7 th pitch for 7-pin bundle with helical pitch (a) 100 mm (b) 150 mm (c) 200 mm (d) 250 mm and (e) 300 mm for $Re = 0.842 \times 10^5$	115

Fig. 6.13	Non-dimensional cross-stream velocity for $Re = 0.842 \times 10^5$	116
Fig. 6.14	Friction factor development with different helical pitch for $Re = 0.842 \times 10^5$	117
Fig. 6.15	Nusselt number development with different helical pitch for $Re = 0.842 \times 10^5$	118
Fig. 6.16	(a) Comparison of fully developed mean friction factor and mean Nusselt number variations with helical pitch for $Re = 0.842 \times 10^5$	119
	(b) Dependence of coefficient 'C' on triangular pitch and helical pitch	119
Fig. 6.17	(a) Circumferential variation of local Nusselt number at the start of 7 th pitch for central clad with $Re = 0.842 \times 10^5$	121
	(b) Non-dimensional temperature at the start of 7 th pitch for peripheral clad (C - central pin and P – peripheral pin)	121
Fig. 6.18	Hotspot factor variation with helical pitch for $Re = 0.842 \times 10^5$	122
Fig. 6.19	Hotspot factor at 7 th pitch for 200 mm helical pitch configuration and $Re = 842 \times 10^5$	122
Fig. 6.20	(a) Average turbulent kinetic energy variation with different helical pitch for $Re = 0.842 \times 10^5$	124
	(b) Average turbulent dissipation rate variation with different helical pitch for $Re = 0.842 \times 10^5$	124
Fig. 6.21	(a) Cross-stream velocity contours in 7, 19 and 37 pin fuel bundles	127
	(b) Cross-stream velocity in various fuel pin bundles	128
Fig. 6.22	(a) Friction factor development fuel pin bundles	129
	(b) Expanded view of friction factor development in fuel pin bundles	130
Fig. 6.23	Global Nusselt number development in fuel pin bundles	131
Fig. 6.24	(a) Circumferential Nusselt number for central pin in 7-pin bundle at the 6 th helical Pitch	131
	(b) Circumferential Nusselt number for central pin in 7-pin bundle at the 7 th helical pitch	132
	(c) Cross-stream velocity in 7-pin bundle at the 6 th and 7 th helical pitch	134

Fig. 6.25	Hotspot factor in the 7,19 and 37-pin fuel bundles	135
Fig. 7.1	Optimized cross-stream mesh used in 19 pin-bundle CFD studies	140
Fig. 7.2	Validation of present calculation with SCARLET-II experiment (Olive and Jolas, 1990)	141
	(a) SCARLET-II test section	
	(b) Comparison of temperature in the blocked region	
	(c) Experimental non-dimensional axial velocity (V_s / V_i) distribution	143
	(d) Present non-dimensional axial velocity (V_s / V_i) at $Z = 780$ mm	143
Fig. 7.3	(a) Schematic of pin bundle with blockage,	145
	(b) 19-pin bundle with cylindrical and conical blockages (B1, B2 & B3) at the centre of subassembly located within 700-900 mm axial position	
	(c) 19-pin bundle with cylindrical central blockage (B4) at the centre of subassembly located within 700-900 mm axial position and	
	(d) 19-pin bundle with cylindrical blockage (B5) at a corner of subassembly located within 700-900 mm axial position	
Fig. 7.4	(a) Comparison of cross-stream velocity (m/s) vectors of <i>B1</i> bundle with normal bundle (<i>B0</i> -Bundle)	147
	(b) Comparison of isotherms (K) of <i>B1</i> bundle with normal bundle	148
	(c) Axial velocity in <i>B1</i> bundle behind the blockage	149
	(d) Isotherms (K) of <i>B1</i> bundle behind the blockage	149
Fig. 7.5	(a) Comparison of peak and average clad temperature in pin bundle with <i>B1</i> blockage against that without blockage (<i>B0</i>)	151
	(b) Comparison of peak and mean clad temperatures in pin-1	151
	(c) Comparison of peak and mean clad temperatures in pin-7	152
	(d) Comparison of peak and mean clad temperatures in pin-19	153
Fig. 7.6	(a) Circumferential clad temperature distribution in pin bundle with <i>B1</i> type blockage: (a) pin-1	155

	(b) Circumferential clad temperature distribution in pin bundle with <i>B1</i> type blockage: pin-19	155
	(c) Circumferential clad temperature distribution in normal pin bundle: pin-1	156
	(d) Circumferential clad temperature distribution in normal pin bundle: pin-19	156
Fig. 7.7	(a) Cross-stream velocity (m/s) vectors for <i>B2</i> type blockage and (b) Isotherms (K) for <i>B2</i> type blockage	158
Fig. 7.8	(a) Comparison of peak and average clad temperature in <i>B1</i> -blockage bundle with <i>B2</i> -blockage	159
	(b) Comparison of peak and mean clad temperatures in pin-1 (<i>B1</i> and <i>B2</i> -blockages)	160
Fig. 7.9	(a) Cross-stream velocity (m/s) vectors for <i>B3</i> type blockage	162
	(b) Isotherms (K) for <i>B3</i> type blockage	162
Fig. 7.10	(a) Cross-stream velocity (m/s) vectors for <i>B4</i> type blockage	163
	(b) Isotherms (K) for <i>B4</i> type blockage	163
Fig. 7.11	(a) Comparison of peak and average clad temperature in <i>B1</i> -blockage bundle against <i>B3</i> and <i>B4</i> blockage	165
	(b) Comparison of peak and mean clad temperature in pin-7 (<i>B1</i> , <i>B3</i> and <i>B4</i> -blockage)	165
Fig. 7.12	(a) Cross-stream velocity (m/s) vectors for <i>B5</i> type blockage	167
	(b) isotherms (K) for <i>B5</i> type blockage	167
Fig. 7.13	(a) Comparison of peak and average clad temperature in <i>B1</i> bundle against <i>B5</i> bundle	168
	(b) Comparison of mean clad temperatures in pin-1, pin-5, pin-13 and pin-14 in <i>B5</i> bundle	168
Fig. 7.14	Cross-stream velocity (m/s) vectors and isotherms (K) for <i>B1</i> type blockage with different porosity values	170
Fig. 7.15	(a) Comparison of peak clad temperature with 40% porosity <i>B1</i> -blockage against 20% and 60%	171
	(b) Bundle peak clad temperature variation with porosity	171

Fig. 7.16 Comparison of predicted clad temperature adopting different expressions for effective thermal conductivity

175

LIST OF TABLES

Table No.	Table Title	Page No.
Table 2.1	Fully developed friction factor correlations for pin bundle with helical spacer wire and their applicable ranges	14
Table 2.2	Fully developed Nusselt number correlations for pin bundle with helical spacer wire and their applicable ranges	15
Table 4.1	Range of parameters studied using bare pin bundles	38
Table 4.2	(a) Temperature values predicted with different mesh for bare pin bundle	40
	(b) velocity and pressure values predicted with different mesh for bare pin bundle	41
Table 4.3	Summary of development lengths for various cases studied	73
Table 5.1	Comparison of global Nusselt number and friction factor for two different radial grids	78
Table 5.2	(a) Comparison of Nusselt number for four different axial grid sizes	78
	(b) Comparison of friction factor for four different axial grid sizes	78
Table 5.3	Range of parameters analyzed	85
Table 5.4	Non-dimensional amplitudes of friction factor and cross-stream velocity in the fully developed region	93
Table 6.1	Comparison of fully developed friction factor and Nusselt number with two different cross-stream grids	97
Table 6.2	Comparison of fully developed friction factor and Nusselt number with different axial grids	97
Table 6.3	Range of parameters studied	104

Table 6.4	Analogy between turbulent heat and momentum transfer in sodium flow	111
Table 6.5	Non-dimensional amplitudes of friction factor in the fully developed region of turbulent flow	136
Table 7.1	Comparison of non-dimensional axial velocity (V_s/ V_i) with water model experiments	144
Table 7.2	Details of blockages considered in the 19-pin bundle configuration	146
Table 7.3	Maximum difference in circumferential clad temperature $[(\Delta T_\theta)_{\max}]$ (K)	157
Table 7.4	Maximum difference in circumferential clad temperature $[(\Delta T_\theta)_{\max}]$ in K for B2-bundle	161
Table 7.5	Maximum in circumferential clad temperature difference $[(\Delta T_\theta)_{\max}]$ in K for a B5-bundle	169
Table 7.6	Maximum difference in circumferential temperature $[(\Delta T_\theta)_{\max}]$ in K in a bundle with B1-blockage and 20% and 60% porosity values	172
Table 7.7	Actual flow and the corresponding outlet temperature from blocked subassemblies	173

CHAPTER-1

INTRODUCTION

1.0 FOREWORD

Energy demand is continuously growing in most of the countries around the globe. Especially the demand is very high in a developing country like India as population growth is high. So, keeping in mind the per capita energy consumption, there is a need to utilize all the energy potential available at hand. Renewable energy sources like the wind and hydro are seasonal in nature. At the same time, the solar energy demands large capital investment. Presently, thermal power plants based on coal are the prime providers of power. For countries like India with limited coal reserves, there is a strong need for development of alternative energy sources. In this situation nuclear energy is one of the viable options, because of the availability of vast thorium resources. But the thorium is fertile in nature. To convert the fertile thorium into fissile uranium the route of Fast Breeder Reactors (FBR) is required. The FBR is very efficient in breeding compared to thermal reactors. Thermodynamic efficiency of FBR is also higher than the thermal reactors. For the effective utilization of limited uranium and vast thorium resources, a three stage nuclear power programme has been planned in India. The first stage of nuclear reactor is pressurized Heavy Water Reactors (PHWR), which use natural uranium as fuel containing only 0.7% of the fissile isotope of uranium (U^{235}). The second stage of nuclear reactors (FBR) can utilize over 70% of the fertile isotope of uranium, viz., U^{238} after converting it into Pu^{239} which is fissile. Towards development of fast breeder technology in India, a 40 MW thermal power Fast Breeder Test Reactor (FBTR) was constructed at Kalpakkam, India in the year 1985 (Srinivasan et al., 2006). Following FBTR, a 500MW electric power Prototype Fast Breeder Reactor (PFBR) was designed and is

presently under construction in India (Chetal et al., 2006). The flow sheet of a typical pool type fast breeder reactor is depicted in Fig. 1.1.

1.1 FAST BREEDER REACTOR

A typical fast breeder reactor consists of three circuits viz., two sodium circuits to transfer the nuclear heat generated in the core to the steam-water system and power plant circuit to produce steam to run the turbine. The two sodium circuits are known as primary and secondary circuits. Among these two circuits the primary circuit is entirely inside the pool of sodium. The expanded view of primary circuit assembly is depicted in Fig. 1.2. All the primary system components are housed inside a main vessel which is surrounded by a safety vessel. Main vessel houses the hot primary sodium pool (820K) and cold primary sodium pool (670K), inner vessel which separates these pools, control plug, primary pumps (2 numbers), Intermediate Heat Exchanger (4 numbers) etc. The nuclear heat produced in the core is transported to the secondary circuit through the Intermediate Heat Exchangers (IHX). Also, the Safety Grade Decay Heat Removal (SGDHR) system is operating between hot primary sodium and atmospheric air to remove the decay heat produced during the reactor shut down condition. There are two secondary circuits with 4 IHX and eight numbers of steam generators. The steam exit from the turbine is cooled by a condenser.

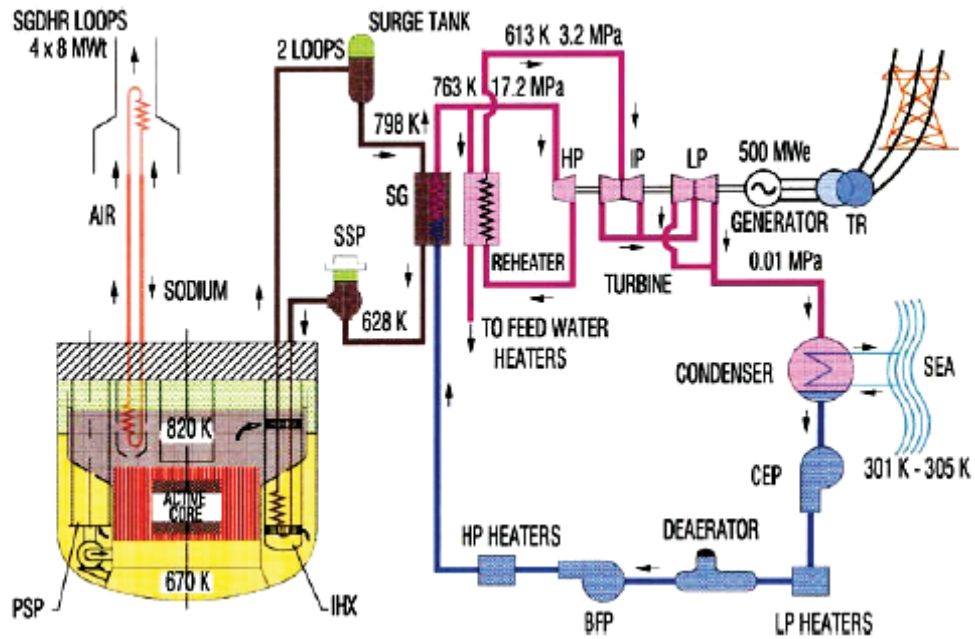


Fig. 1.1. Flow sheet of pool type fast breeder reactor

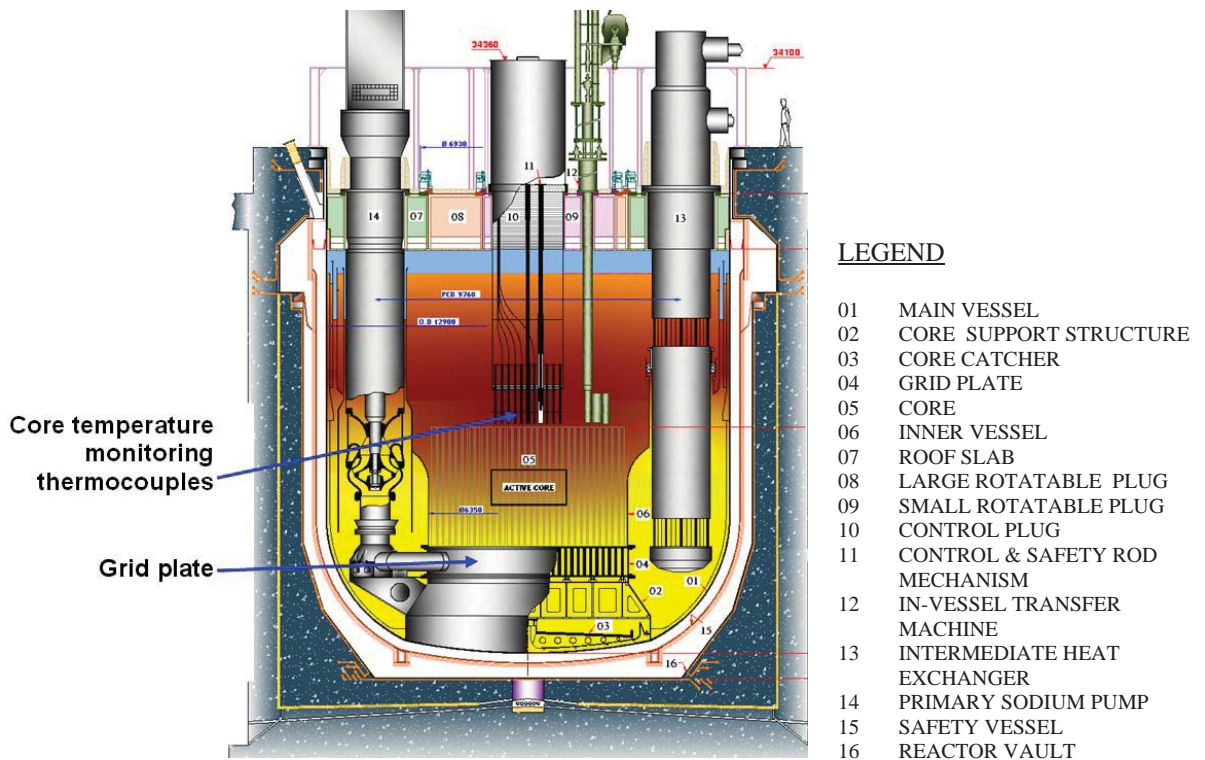


Fig. 1.2 Primary circuit assembly of pool type fast breeder reactor

1.2 THERMAL HYDRAULICS OF FUEL SUBASSEMBLY

FBR fuel pins are arranged in a tightly packed triangular pitch and are housed in a hexagonal sheath forming a subassembly. FBR core is very compact with large power density and hence the heat flux in the fuel pins is $\sim 2 \text{ MW/m}^2$. To extract this large heat flux with small temperature difference between coolant and clad surface, liquid sodium is chosen as the coolant. It has a large heat transfer coefficient due to its large thermal conductivity ($\sim 70 \text{ W/m-K}$) and high boiling point ($\sim 880^\circ\text{C}$) at atmospheric pressure. The main purpose of the spacer wire is to provide lateral support to the pins to guard them against flow induced vibration. The wires also promote mixing of sodium among various sub-channels. Typically the fuel pin diameter is $\sim 6 \text{ mm}$ and spacer wire diameter is $\sim 1.5 \text{ mm}$. The pin length is $\sim 2.5 \text{ m}$. The triangular pitch of the fuel pins $\sim 8 \text{ mm}$ and helical pitch of the spacer wire is $\sim 200 \text{ mm}$. These features lead to complex flow and thermal characteristics. Detailed knowledge of these characteristics is essential to have an efficient and safe core design. Due to the helical wire spacer, there is significant variation in heat transfer coefficient around the circumference of the pin. There are different types of sub-channels in a subassembly. The flow area and hydraulic diameters of these sub-channels are different. Hence, the velocities of sodium through various sub-channels are different leading to non-uniform velocity distribution in the subassembly. Further, the spacer wires cross the sub-channels at periodic intervals that cause periodic flow rate changes in the sub-channels. The complex flow physics within the fuel bundle and its interaction with flow development in the bundle offer interesting challenges in computational modeling of flow and heat transfer in fuel subassemblies.

Experimental determination of detailed flow and heat transfer characteristics of sodium through heat generating fuel pin bundles is very difficult due to the following reasons:

- (i) Sub-channel dimensions are very small (typically 3 mm is the hydraulic diameter),
- (ii) Measuring instruments are required to function at elevated temperatures ($200\text{-}600^\circ\text{C}$),

(iii) Flow visualization is hampered by the opaque nature of sodium and (iv) Water flow cannot correctly simulate sodium heat transfer. Moreover, it is almost impossible to measure detailed temperature distribution of fuel pins in any operating reactor. To overcome these challenges, in the core design of FBRs, Computational Fluid Dynamics is playing a vital role. This is evident from the published work of Tenchine (2010) and Velusamy et al. (2010). However, the computational results have to be suitably assisted by appropriate experiments. The computational results can be partially validated with water tests towards validation of hydraulic models employed in the computer codes. Also, a few global thermal hydraulic parameters can be validated by suitable sodium tests.

Due to the tight packing, the flow communication between the various sub-channels becomes very weak. As a result of this, flow development in sub-channels comprises of two regimes, viz., (i) local flow development within the sub-channels and (ii) global flow redistribution among the sub-channels. While the local flow development in sub-channels is governed by local hydraulic diameter or sub-channel hydraulic diameter, the global flow development is a strong function of the resistance for flow redistribution among the central and peripheral sub-channels. Apart from reactor design, knowledge of flow and temperature characteristics in the entrance region is very essential for proper planning of pin bundle thermal hydraulic experiments.

Because of the miniature gap between fuel pins, there is a finite chance for the formation of local blockage in a coolant sub-channel. This local or partial blockage may be caused by (i) deformation of cladding due to severe swelling, (ii) spacer wire loosening or breaking; (iii) foreign materials left during construction, (iv) fragments from failed fuel and (v) corrosion product deposition in the flow channels. In the case of sub-channels with local blockage, there is risk of local temperature shoot up and sodium boiling with consequent

changes in the reactivity. Since a partial blockage in a subassembly would threaten the safety of the core, the detection of a flow blockage at an early stage is very important.

1.3 MOTIVATION FOR THE PRESENT STUDY

A detailed literature survey indicates that the previous research works were focused to mainly understand the flow and temperature fields in the fully developed region. Reported CFD studies were mostly confined to one helical pitch length. This is due to difficulties in the generation of structured mesh for pin bundle with helical wire-wrap and large computational resource demanded by the use of an unstructured tetrahedral mesh. Simultaneous development of velocity and temperature fields during sodium flow in the entrance region of the pin bundle has not been paid much attention in the past. Also, large deviations were reported among published correlations for Nusselt number in pin bundles. Details of flow features and their influence on circumferential variation of clad temperature are not explicitly brought out in the reported studies. Also, inter-play between blockage effects and developing flow / temperature fields is not studied in the past. These form the motivation for the present research.

1.4 OBJECTIVES AND SCOPE OF THE THESIS WORK

The present research focuses on simultaneous development of flow and temperature in a fast reactor fuel pin bundle where liquid sodium is used as the coolant. The fuel pins are supplied with constant heat flux on the outer surface of the clad. To understand the role of helical spacer wire, bare as well as wire-wrap pin bundles are studied. Dependence of entrance flow on critical parameters, viz., pin pitch, pin diameters, number of pins in the bundle, helical pitch of the wire-wrap and ligament gap between the outermost rows of pins

and hexcan wall are systematically varied as parameters. Both laminar and turbulent flow regimes are investigated. The present research is basically computational in nature. However, detailed validations have been carried out for pin bundle flow against published experimental data for sodium and water. To optimize the number of elements, a structured mesh has been adopted. Three dimensional steady state simulations have been carried out for a large number of axial pitch distances, employing parallel processing computations. The sensitivity of results on grid structure and turbulence models has been investigated in detail.

Following this the effect of a porous blockage inside the bundle on local clad and sodium temperatures has been assessed. The size, shape, position, and porosity of the blockage are varied systematically and conditions which can lead to local sodium boiling are identified. The computational model for porous blockage has been validated against benchmark sodium experiments in pin bundle.

1.5 ORGANISATION OF THE THESIS

Present thesis is divided into four major parts. The first part comprises of three chapters with introduction of the problem in Chapter-1, critical review of literature survey in Chapter-2 and mathematical modeling of flow through pin bundles and partial flow blockage in Chapter-3. The second part comprises of three chapters dealing with entrance flow characteristics of bare pin bundles in Chapter-4 and flow/ temperature development and hot spot factors for sodium flow through pin bundles with wire-wrap during laminar and turbulent flow regimes respectively in Chapters 5 and 6. Third part of the thesis comprises of thermal hydraulic characteristics of flow through porous blockages located in active fuel pin bundles presented in Chapter-7. The final part of the thesis (Chapter-8) is the summary of the major findings of the thesis.

CHAPTER-2

LITERATURE REVIEW

2.0 INTRODUCTION

A large volume of experimental studies have been carried out to understand the thermal hydraulic characteristics of rod bundles (Walter and Reynolds, 1980). Most of the experimental work, during the initial period of FBR development, was focused towards development of sub-channel analysis codes like COBRA (Rowe, 1973), and SUPER ENERGY (Cheng and Todreas, 1986a, b). In the past, researchers carried out experiments with different number of pins of various axial lengths. But no effort was devoted to investigate these parameters on the proposed heat transfer correlations. For liquid sodium flow, the heat transfer coefficient is generally high leading to small temperature difference between sodium and clad surface. Hence as a consequence of these factors, reported correlations for liquid metal heat transfers deviate largely among themselves, especially in the low Peclet number region. Entrance lengths for flow and temperature development in fuel subassemblies are not discussed in the open literature. Towards establishing the current level of understanding in local flow and temperature fields in a heat generating pin bundle, a literature survey has been carried out. Some of the significant literature related to these fields is discussed elaborately in this chapter.

2.1 ENTRANCE FLOW IN DUCTS

Flow and temperature developments in channels and tubes have attracted the attention of heat transfer researchers due to the large heat transfer coefficient and friction factor in the entrance region. A detailed survey of literature in this area can be found in Shah and London (1978). Flow in the entrance region of elliptical ducts and eccentric annular ducts were studied by

Feldman et al. (1982) and Velusamy and Garg (1993). Entrance flows in semi circular ducts were studied by Manglik and Bergles (1988, 1996). All these studies dealing with straight channels indicate that both the friction factor and heat transfer coefficient decrease monotonically along the flow direction in the developing region to stabilize to a constant value in the fully developed region. But, Lin et al. (1997) found that both the friction factor and Nusselt number are oscillatory in the entrance region of helical pipes. Acharya et al. (1993) studied the flow through coiled tubes and found that the Nusselt number in the entrance region falls well below the fully developed value. But, in the developed region, the heat transfer coefficient and friction factor are constant. The complex interaction between growth of boundary layer along the duct wall and the development of secondary flows due to coiled geometry of tubes, leads to this non-monotonic variation.

In the case of nuclear fuel pin bundles, helically wound spacer wires are used to promote mixing of coolant as well as to protect the fuel bundle against flow induced vibration. Provision of spacer wires generates secondary flows in the entrance region of pin bundles. Further, growth of boundary layers around a large number of fuel pins and their interaction with developing secondary flows need to be understood. To the best knowledge of the present author, developing flow in the entrance region of fuel pins with helically wound spacer wire has not been reported in open literature.

Experimental studies using different types of coolant, viz., (i) air (ii) water and (iii) liquid metals have been reported in open literature. However the experiments with liquid metal coolant are limited compared to experiments with air and water. Hydrodynamic and thermal entry lengths are defined as the lengths upto which the velocity and thermal profiles keep changing. For laminar pipe flow, the hydraulic and thermal entry lengths are $\approx 0.05 \times D \times Re$ and $0.05 \times D \times Re \times Pr$ (Cengel, 2007) respectively, where D is the hydraulic diameter . But for turbulent flow, entry lengths are shorter and the hydrodynamic and thermal

lengths are nearly identical ($\approx 10 \times D$). Friction factor (f) is defined as, the dimensionless number used in studying fluid friction in pipes and channels, equal to the diameter times the drop in pressure in the fluid due to friction as it passes through the pipe, divided by the product of the pipe length and the kinetic energy of the fluid per unit volume. In heat transfer at a surface within a fluid, the Nusselt number (Nu) is defined as the ratio of convective to the conductive heat transfer normal to the surface. In heat transfer experiments, the heat is supplied to the coolant in two ways. Heat is supplied to the wall either at constant temperature or as constant heat flux. The fully developed Nusselt number is identical in both methods of heat supply for turbulent flow conditions. But, for laminar flow through pipe the fully developed Nusselt numbers are different. It is 4.36 for pipe flow with constant heat flux boundary condition and 3.66 with constant temperature boundary condition (Cengel, 2007). Rensen (1981) carried out sodium experiment with hollow pipe and reported the results for thermal entrance region as well as fully developed region. He has concluded that the Reynolds number has an appreciable influence on the heat transfer to liquid sodium in the thermal entrance region and thermal entrance length for turbulent flow of liquid sodium is much greater than that for laminar flow. Also, the Prandtl number has only a little influence on the variation of local Nusselt number of liquid metal.

2.2 EXPERIMENTS IN PIN BUNDLE

Many experiments for flow through pin bundle have been reported in the literature with water as coolant to predict the pressure drop. Fully developed friction factor (f) for flow through pin bundle evaluated using different correlations is presented in Fig. 2.1a for a specific value of $H/(D_w + D_r) = 24.4$. Here H is the helical pitch length of space, D_w is wire diameter and D_r is pin diameter. It can be seen from the figure that the correlation reported by Cheng and Todreas (1986b) under predicts the friction factor compared to other correlations. The reason

for this difference may be due to the different number of pins used in the experimental pin bundle. The information available in literature like geometrical parameters, number of pins in the bundle and the range of Reynolds number along with the respective correlations are presented in Table 2.1. It is to be noted that the definitions of Re , Pe , f and Nu identical for all the results depicted in Fig. 2 and Table 2.1 and 2.2.

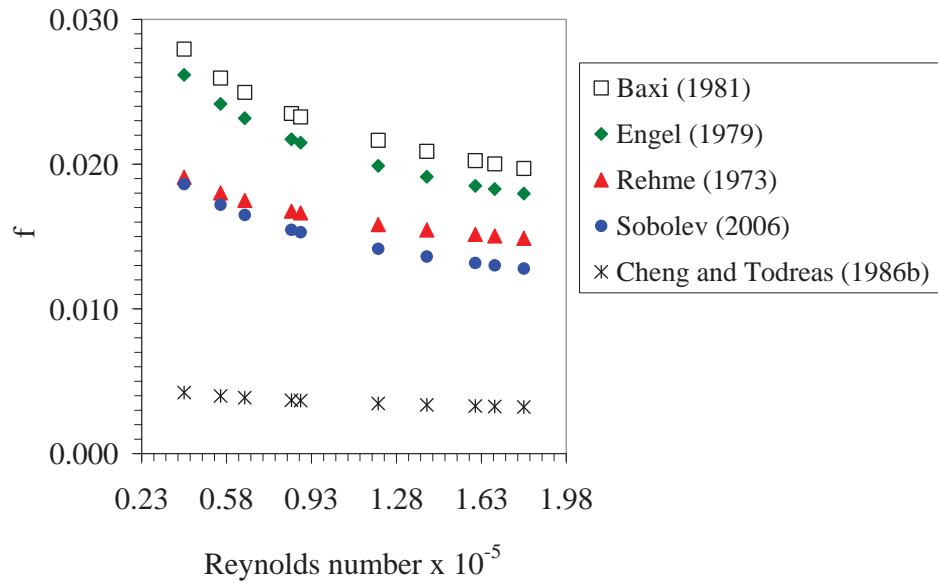


Fig. 2.1a Comparison of friction factor in pin bundles with $H/(D_w + D_r) = 24.4$ employing various correlations

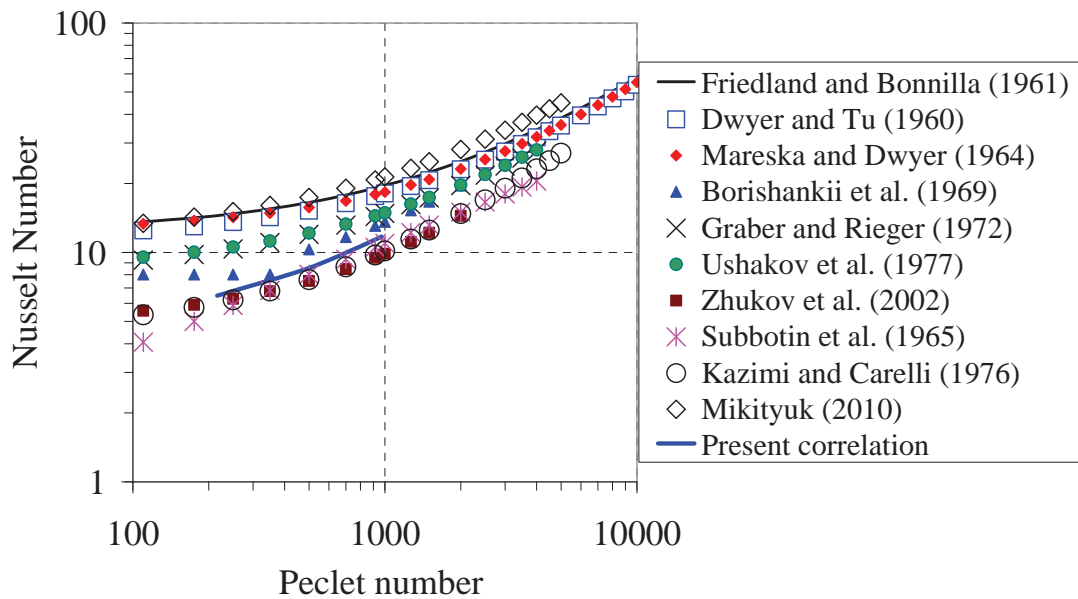


Fig. 2.1b Comparison of Nusselt number in pin bundles employing various correlations

Table 2.1 Fully developed friction factor correlations for pin bundle with helical spacer wire and their applicable ranges

Sl. No.	Reference	Re	X = P_t/D_r	Pins used	Friction factor correlation
1	Rehme (1973)	$200 - 2.5 \times 10^5$	1.125 - 1.417	7 - 37	$f = \left(\frac{64}{\text{Re}} F^{0.5} + \frac{0.0816}{\text{Re}^{0.133}} F^{0.9335} \right) \frac{N \pi D_t}{P_w}$ $\text{where, } F = (X)^{0.5} + \left[\frac{7.6}{W} (X)^2 \right]^{2.16}$
2	Engel et al. (1979)	> 5000	1.079 - 1.082	61	$f = \frac{0.55}{\text{Re}^{0.25}}$
3	Cheng and Todreas (1986b)	$400 - 1 \times 10^5$	1.067 - 1.35	7 - 217	$f = \frac{C_f}{\text{Re}^{0.18}} \text{ where}$ $C_f = \left[0.8063 - 0.9022 \log(W) + 0.3526 \times (\log(W))^2 \right] (X)^{9.7} (W)^{1.78-2(X)}$
4	Baxi and Dalle-Donne (1981)	≥ 5000	-	-	$f = \frac{0.316}{\text{Re}^{0.25}} \left[\frac{1.034}{(X)^{0.124}} + \frac{29.6(X)^{6.94} \text{Re}^{0.086}}{W^{2.239}} \right]^{0.885}$
5	Sobolev (2006)	-	-	-	$f = \left[1 + 600 \left(\frac{D_r}{H} \right)^2 (X-1) \right] \times \left[\frac{0.210}{\text{Re}^{0.25}} (1 + (X-1)^{0.32}) \right]$

Table 2.2 Fully developed Nusselt number correlations for pin bundle with helical spacer wire and their applicable ranges

Sl. No.	Reference	Pe	$X = P/D_r$	coolant used	Number (diameter) of pins	Lattice	Nusselt number correlation
1	Dwyer and Tu (1960)	70 - 10000	1.375 - 2.2	Hg	-	triangle	$Nu = 0.93 + 10.81(X) - 2.01(X)^2$: $+ 0.0252(X)^{0.273}(\psi Pe)^{0.8}$
2	Friedland and Bonnilla (1961)	0 - 100000	1.3 - 10	-	-	"	$Nu = 7.0 + 3.8(X)^{1.52} + 0.027(X)^{0.27}(\psi Pe)^{0.8}$
3	Mareska and Dwyer (1964)	70 - 10000	1.3 - 3	Hg	13 (13 mm)	"	$Nu = 6.66 + 3.126(X) + 1.184(X)^2 + 0.0155(\psi Pe)^{0.86}$
4	Subbotin et al. (1965)	80 - 4000	1.1 - 1.5	Hg		Triangle / square	$Nu = 0.58 \left(\frac{2\sqrt{3}(X)^2}{\pi} - 1 \right)^{0.55} Pe^{0.45}$
5	Borishankii et al. (1969)	60 - 2200	1.1 - 1.15	Na & Hg	7 (22 mm)	triangle	$Nu = 24.15 \log(-8.12 + 12.76(X) - 3.65(X)^2) + 0.0174(1 - e^{-6(X-1)})B$ where $B = \begin{cases} 0 & \text{for } Pe < 200 \\ (Pe - 200)^{0.9} & \text{for } Pe \geq 200 \end{cases}$
6	Graber and Rieger (1972)	110 - 4300	1.2-1.25	NaK	31 (12 mm)	"	$Nu = 0.25 + 6.2(X) + (0.032(X) - 0.007)Pe^{0.8-0.024(X)}$

7	Ushakov et al. (1977)	> 4000	1.3 - 2.0	-	-	"	$Nu = 7.55(X) - \frac{20}{(X)^{13}} + \frac{0.041}{(X)^2} Pe^{0.56+0.19(X)}$
8	Zhukov et al. (2002)	60 - 2000	1.25 - 1.46	<i>NaK</i>	22 (12 mm)	square	$Nu = 7.55(X) - 14(X)^{-5} + 0.007 Pe^{0.64+0.246(X)}$
9	Kazimi and Carelli (1976)	10 - 5000	1.1 - 1.4	<i>Na, Hg</i> & <i>NaK</i>	-	-	$Nu = 4 + \left[0.33(X)^{3.8} \left(\frac{Pe}{100} \right)^{0.86} \right] + [0.16(X)^5]$
10	Mikityuk (2010)	30 - 5000	1.1 - 1.95	-	-	triangle	$Nu = 0.047(1 - e^{-3.8(X^{-1})})(Pe^{0.77} + 250)$

Generally, water experiments are conducted to find the pressure drop in the pin bundles. As discussed in Chapter-1, water experiments cannot simulate liquid metal heat transfer. To predict the liquid metal heat transfer in pin bundles, many experiments were performed and different correlations were proposed. The Nusselt number computed from various correlations are compared in Fig. 2.1b. All the experimental correlations were reported before 1976 except that of Zhukov et al. (2002). The geometrical parameters and the coolant used in the experiments are different in the experiments. Information on the geometrical parameters of pin bundle, range of Peclet numbers and coolant used for experiments along with correlations reported, are given in the Table 2.2.

Cheng and Todreas (1986b) proposed correlations for bundle friction factors, sub-channel friction factors and mixing parameters for flow through bare and wire-wrapped pin bundles. These correlations can predict the bundle average friction factor data within at least $\pm 14\%$ for turbulent flow and within $\pm 30\%$ for laminar flow and all flow split data within $\pm 5\%$. Chun and Seo (2001) studied existing friction factor correlations to identify the best performing correlations for the sub-channel pressure drop in wire-wrapped fuel assembly. They found that the correlation proposed by Novendstern (1972) agrees fairly well with experimental data in the turbulent region and the correlation proposed by Rehme (1972) consistently under predicts the friction factor for all the flow regions. The correlation proposed by Engel et al. (1979) over predicts the friction factor for all the flow regions. Bubelis and Schikorr (2008) also studied the existing wire-wrapped bundle correlations for friction factor and recommended that the friction factor correlation of Rehme (1973) should be used in the thermal hydraulic evaluations in the estimation of the pressure drops in wire-wrapped fuel pin bundles for all types of coolants in reactor. Mikityuk (2009) reviewed various heat transfer correlations reported for pin bundles. He

proposed a new correlation as a best fit for the data analyzed. Further, the correlations proposed by Ushakov et al. (1977) and by Graber and Rieger (1972) were found to be close to the one proposed by him.

2.3 NUMERICAL STUDIES IN PIN BUNDLE

After the year 1975, the number of experimental studies reduced. Because of the difficulties involved in the experimental studies and the advent of fast computing capabilities, CFD simulations became popular and they started replacing experimental studies. Important literature in the domain of numerical simulation is discussed in this section.

Gajapathy et al. (2007) carried out CFD investigation of helical wire-wrapped 7-pin fuel bundle with axial length of one helical pitch adopting the tetrahedral grids. They reported that due to the wire-wrap, the difference in bulk sodium temperature between the peripheral and central sub-channels is reduced by a factor of four when compared to that in bare pin bundle. They also reported that the helical wire induces a secondary swirl in the pin bundle which promotes cross-stream mixing of the coolant to make its temperature more uniform. Fischer et al. (2007) reported large eddy simulation study of wire-wrapped pin bundle adopting periodic boundary condition. They found that the transverse velocities are the principal drivers of inter channel mixing. Also, the periodic computations do not address the important effects of wall and corner channels. Three-dimensional fluid flow and heat transfer studies for 7-pin and 19-pin wire-wrapped bundle have been reported by Raza et al. (2008). It is reported that in both the assemblies, the local axial velocity in the edge sub-channel is higher than the average axial velocity. The maximum temperatures in the central fuel pin and edge fuel pins are higher in the 19-pin assembly. They emphasized that the computational results especially for the thermal field

needs further validation. Shang (2009) carried out CFD investigation of vertical pin bundles and found that temperature at the pin surface is highly non-uniform. Also reported that the upward flow reduces the wall temperature difference and the hexagonal geometry has the lowest wall temperature when compared with other geometries. Large P_t/D_r ratio leads to low wall temperature and small wall temperature difference, but the heat transfer coefficient becomes less. A P_t/D_r value of 1.25 is recommended. Chauhan et al. (2013) studied flow through a 19 pin PHWR bundle. The focus of the study is the effect of sagging of the bundle on heat transfer characteristics. The effect of sagging accounted by, adopting an eccentricity parameter is defined as the radial distance between the central lines of central pin and that of pressure tube. They found that, the overall bundle pressure drop decreases with increase in eccentricity of the bundle and also found that the Nusselt number in the narrow gap region reduces for higher eccentricity.

Gajapathy et al. (2009) numerically studied 7, 19 and 37-pin fuel bundle with helical wire-wrap for one axial pitch length. They reported that the axial velocity is maximum in the peripheral zone, where spacer wires are located between the pins and the hexcan. Chandra et al. (2009) carried out CFD simulations of flow through tube and to pin bundle. They found that a larger domain length is needed to obtain a fully developed temperature profile than that for the velocity profile. They also indicated that grid width corresponding to $y^+ = 50 - 60$ nearest to the wall and $y^+ = 160 - 200$ in bulk region with a maximum grid aspect ratio of about 200 can be employed for pin bundle investigations. Natesan et al. (2010) reported three-dimensional CFD study of wire-wrapped 19-pin bundles. For this simulation an axial length of one helical pitch was modeled. They reported that the friction factor increases with reduction in the wire-wrap pitch while the heat transfer coefficient remains almost unaltered. They also found that the Nusselt number deviates by ~20% from that of the experimental correlation. Peniguel et al.

(2010) investigated the thermal-hydraulics of wire-wrapped fuel bundle and reported that the mesh generation is a challenging task in CFD simulation. They found that the global flow patterns are strong functions of the number of pins. They also mentioned that the experimental correlations for Nusselt number are quite scattered, making it difficult for the assessment of the CFD results. Bieder et al. (2008) reported CFD investigations of 61 pin bundle. They found that the flow through the bundle is hydraulically developed in ~ 1.5 wire-wrap pitches. This justifies the approximation of a periodic zone of the length of one pitch for a hydraulic analysis of the bundle. However, this approximation is not correct for thermal considerations since the temperature field in the assembly is developing axially along the complete axial length.

Sreenivasulu and Prasad (2011) computationally analyzed local flow and heat transfer characteristics for water in a seven pin bundle with helically wrapped wires. Hot spot zone were reported close to the cusp contact between the pin and the wire. They also found that compared to the bare bundle the tangential velocity, turbulence, pressure drop and Nusselt numbers are large for the wire-wrapped bundle. Chandra and Roelofs (2011) carried out a sub-channel analysis and found that the flow anisotropy increases with decreasing pitch to diameter ratio in a pin-bundle and flow oscillations persist in the pin bundle. They suggested that additional investigations are essential to study flow oscillations in the pin-bundles. Roelofs et al. (2012) discussed about low resolution CFD approaches to predict medium scale flow features within the fuel subassemblies. Rolfoa et al. (2012) carried out three-dimensional simulations of flow and heat transfer in fuel assemblies. They found that the number of fuel pins does not influence the main flow features. With the larger bundles (61 and 271 pins), the global swirl stays limited to the edge region, with an increasingly large homogeneous core.

Reported CFD studies were mostly confined to only one helical pitch length. This is due to limitations in the generation of structured mesh for pin bundle with helical wire-wrap and large computational resource demanded by using unstructured tetrahedral mesh. Simultaneous development of velocity and temperature fields during sodium flow in the entrance region of the pin bundle has not been paid much attention.

2.4 FLOW BLOCKAGE STUDIES IN FUEL PIN BUNDLE

As discussed in Chapter-1 the chances for formation of partial blockage within small sub-channels are high. The consequences of blockages are very severe due to large heat source inside the fuel subassembly. Literature dealing with partial blockages is discussed in this section.

Fontana et al. (1973) carried out blockage experiments using 19-pin bundle cooled by sodium. They found that a long (>0.5 inch) heat-generating blockage of a single sub-channel is tolerable, but a blockage of two adjacent channels is not. Also, a 0.25 inch size ring blockage of stainless steel is barely tolerable. A ring blockage of heat-generating material of 0.20 inch radius must be less than 0.125 in. long to be acceptable. Analysis of simple representations of flow in a recirculation zone indicates that the internal fluid temperatures will depend strongly on blockage size and recirculation velocities. To evaluate the maximum possible size and location of blockages, experiment was carried out by Olive and Jolas (1990). Experiments on central and peripheral blockages were performed using sodium. Two types of porous blockages were tested in the SCARLET experiments: a six sub-channel central blockage (SACARLET-II) and a 12 sub-channel edge blockage (SACARLET-III). It was found that the temperatures are very sensitive to the flow field inside the blockage. Also, for a six sub-channel central blockage, the height must not exceed 30 mm to maintain the sodium temperature below 900°C. Han (1979)

experimentally determined heat transfer coefficients for 31-pin sodium-cooled bundle with a 6-central sub-channel blockage. The heat transfer coefficient was generally higher in the unblocked free flow region than in the wake region. A leak at the blockage improved the heat transfer coefficient in the wake region.

Zhimin (2000) carried out experiments in a 19-pin bundle with 24 sub-channels blocked, using sodium as coolant. He found that the maximum temperature position depends on the value of blockage area. Also no cladding damage and sodium coolant boiling occurred in the experiment. Uotani and Haga (1984) carried out sodium boiling experiments in wire-wrapped 37-pin bundle with partially blocked subassemblies. Both central (24 sub-channel) and edge (39 sub-channel) blockages were studied using 5 mm thick blockage plate. They found incipient boiling super heat in both the cases. The reported value of wall super heat is $< 30^{\circ}\text{C}$ and it decreases with increasing coolant velocity. Holtz and Fauske (1971) also carried out boiling experiments and found that the incipient boiling superheat is significantly low in flowing liquid metal systems.

Since a partial blockage in an assembly would threaten the safety of the core, the detection of a flow blockage at an early stage is very important for a liquid metal reactor. A partial flow blockage in an assembly of a liquid metal reactor could result in a cooling deficiency of the core. Local blockages may be active or passive. The active blockages (fragments of failed fuel) can be detected by delayed neutron detection (DND) signal. But, for passive blockages (foreign particles transported with coolant), detection is difficult (Roychowdhury et al. 2002). A numerical study was carried out by Chang et al. (2011). It is reported that the blockage position effect is not significant to the maximum temperature as long as it is located in the neighboring nodes of the highest heat flux position. Seong et al. (2006) developed an algorithm for the

detection of partial blockage and analyzed the temperature fluctuation in the upper plenum due to partial blockage in an assembly. They also investigated design requirements for the flow blockage detection. It was concluded that a fast-response thermocouple might be a good measuring sensor and the location of the thermocouples should be within 25 cm from the exit of the assemblies. The range of the thermocouple should cover more than 1000 K, and the resolution should be less than 2 K. Three-dimensional computational thermal hydraulic studies have been carried out by Maity et al. (2011). They reported that the dilutions in the thermocouple reading of peripheral fuel subassemblies and blanket subassemblies are larger than that in central subassemblies. However, the maximum dilution in fuel subassembly is <3K and that in blanket subassemblies <47 K. Flow reductions around 7% in a fuel subassembly and 12% in a blanket subassembly are detectable by core monitoring thermocouples.

Ravichandar et al. (2007) carried out a theoretical study, to define allowable flow reduction in fuel subassembly. The allowable flow reduction from the point of view of clad mid-wall and sodium boiling under hotspot conditions is found to be 26.5% and 45.6% respectively. From fuel melting point of view, about 29.5% flow reduction is acceptable. Roychowdhury et al. (2000) found that the monitoring sodium outlet temperature of subassemblies may not be sufficient for detecting the local blockage and the local melting is not likely to lead to any significant core melting. George and Dobson (1990) studied the effects of internal blockages within a wire-wrapped subassembly using a CFD code. They found that small internal blockages may cause large temperature rise within a subassembly without altering overall flow rate, and hence insignificant change in mixed mean sodium exit temperature. The problems of internal blockages were found to be worse in the breeder subassemblies than in the driver subassemblies. Also a blockage of 4 sub-channels with a depth of the order of one wire-wrap pitch could result

in sodium boiling. Arai and Hirata (1978) analyzed the flow in the wake region behind the blockage in an LMFBR subassembly. It was found that the turbulent wake is independent of inlet coolant velocity and the velocity of the circulating flow in the wake is proportional to inlet velocity.

2.5 CLOSURE

Detailed literature survey reveals that earlier research works were focused on mainly understanding the flow and temperature fields in the fully developed region. Details of flow features and their influence on circumferential variation of clad temperature are not explicitly brought in the reported studies. Also, inter-play between blockage effects and developing flow / temperature fields is not studied in the past. The lacunae mentioned above form the motivation for the present investigations.

CHAPTER-3

MATHEMATICAL MODELING

3.0 INTRODUCTION

The present study is focused towards numerical analysis of entrance region flow and flow blockage in pin bundles. Mathematical modeling is the heart of any numerical analysis. So, the equations which govern the fluid flow through pin bundles and partial blockage are presented in this chapter. In addition, details about the turbulence models and definition of engineering parameters used in the thesis are also discussed.

3.1 GOVERNING EQUATIONS

The conservation equations that govern steady incompressible sodium flow and heat transfer processes in the pin bundle are: (Todreas and Kazimi, 1993)

Continuity:

$$\frac{\partial}{\partial x_j}(\rho u_j) = 0 \quad (3.1)$$

Momentum balance:

$$\frac{\partial}{\partial x_j}(\rho u_j u_i - \tau_{ij}) = -\frac{\partial p}{\partial x_i} - S_{porous} \quad (3.2)$$

In Eq. (3.2), $\tau_{ij} = 2\mu s_{ij} - \frac{2}{3}\mu \frac{\partial u_k}{\partial x_k} \delta_{ij} - \overline{\rho u_i u_j}$ and $s_{ij} = \frac{1}{2} \left(\frac{\partial u_i}{\partial x_j} + \frac{\partial u_j}{\partial x_i} \right)$

where, $\overline{\rho u_i u_j}$ is the Reynolds stress (turbulent contributions), μ denotes the laminar viscosity and s_{ij} is rate of strain tensor. S_{porous} is an additional source term in momentum equations, to account for pressure drop due to flow blockage. Details of pressure drop are given section 3.3.

Energy balance:

$$\frac{\partial}{\partial x_j} \left(\rho u_j c_p T - K \frac{\partial T}{\partial x_j} - \rho c_p \overline{u_j T'} \right) = 0 \quad (3.3)$$

where, $\rho c_p \overline{u_j T'}$ is the turbulent heat flux

3.2 TURBULENCE MODELLING

3.2.1 Bare Pin Bundle

In bare pin bundle analysis, the effect of turbulence is accounted by considering (i) standard high Reynolds number k - ε model, (ii) k - ω model, (iii) Reynolds Stress model and (iv) Spalart-Allmaras model (FLUENT, 2007). Based on the investigations for a sample 7-pin bundle, it is established that the prediction of standard high Reynolds number k - ε model is not significantly different from the predictions by other models. More discussion on the effect of turbulence model is provided in the section 4.1.3. Hence, the standard high Reynolds number k - ε model is adopted for bare pin bundle study presented in Chapter-4.

The transport equations for the k - ε model are:

Turbulent kinetic energy (k):

$$\frac{\partial}{\partial x_j} \left[\rho u_j k - \left(\mu + \frac{\mu_t}{\sigma_k} \right) \frac{\partial k}{\partial x_j} \right] = -\rho \varepsilon - \frac{2}{3} \left(\mu_t \frac{\partial u_i}{\partial x_i} + \rho k \right) \frac{\partial u_i}{\partial x_i} \quad (3.4)$$

Turbulent dissipation rate (ε):

$$\frac{\partial}{\partial x_j} \left[\rho u_j \varepsilon - \left(\mu + \frac{\mu_t}{\sigma_\varepsilon} \right) \frac{\partial \varepsilon}{\partial x_j} \right] = C_{\varepsilon 1} \frac{\varepsilon}{k} \left[-\frac{2}{3} \left(\mu_t \frac{\partial u_i}{\partial x_i} + \rho k \right) \frac{\partial u_i}{\partial x_i} \right] - C_{\varepsilon 2} \rho \frac{\varepsilon^2}{k} \quad (3.5)$$

Generally a low intensity of turbulence is chosen for the underdeveloped flows compared to fully developed flows. The intensity of turbulence (I) for a fully developed is calculated using,

$$I = 0.16 / \text{Re}^{1/8} \quad (3.6a)$$

In the present case with $Re = 87500$, the value of intensity is $\sim 3.8\%$. So, the half of this value (2%) is considered at the inlet. This defines the value of turbulent kinetic energy at the inlet as,

$$k = \frac{3}{2} (w_{in} I)^2 \quad (3.6b)$$

Where, the mean velocity at the inlet w_{in} is calculated using the free flow area. The value of turbulence dissipation rate at the inlet is evaluated from the following Eq. (3.7) as

$$\varepsilon = C_{\mu}^{3/4} \frac{k^{3/2}}{(0.07D_h)} \quad (3.7)$$

Where C_{μ} is a turbulence model constant equal to 0.09 (FLUENT, 2007).

Standard wall function with turbulent Prandtl number of 0.85 has been adopted based on the experience of Natesan et al. (2010). Also in the present study, dependence of thermal development on turbulent Prandtl number is determined (see, section 4.1.5). The value of y^+ close to pin surfaces is maintained in the range of 30-100. The above set of governing equations is solved by the finite volume based CFD code FLUENT (2007). The pressure-velocity coupling in the incompressible flow formulations is resolved using the SIMPLE algorithm (Patankar, 1980). First order and higher order upwind schemes have been adopted for combining convective and diffusive fluxes in all the transport equations. Based on parametric studies, it is seen that first order upwind scheme is adequate. Detailed discussion on the effect of discretization scheme is provided in Section 4.1.4.

3.2.2 Wire-wrapped Pin Bundle

To account for the effect of turbulence, the RNG $k-\varepsilon$ model (FLUENT, 2007) is adopted for wire-wrapped bundle simulations presented in chapter-6. The unique features of *RNG $k-\varepsilon$* model are: (i) it has an additional term in the turbulent dissipation rate (ε) equation that significantly improves the accuracy of simulation for rapidly strained flows, (ii) the effect of

swirl on turbulence is included, which enhances the prediction capability for swirling flows, (iii) it provides an analytical formula for the computation of position-dependent turbulent Prandtl numbers, and (iv) it provides an analytically-derived formula for the determination of effective viscosity that accounts for low-Reynolds number effects.

The transport equations of the *RNG k-ε* model are:

Turbulent kinetic energy (*k*):

$$\frac{\partial}{\partial t}(\rho k) + \frac{\partial}{\partial x_i}(\rho k u_i) = \frac{\partial}{\partial x_j} \left(\alpha_k \mu_{eff} \frac{\partial k}{\partial x_j} \right) + G_k \quad (3.8)$$

Turbulent dissipation rate (*ε*):

$$\frac{\partial}{\partial t}(\rho \varepsilon) + \frac{\partial}{\partial x_i}(\rho \varepsilon u_i) = \frac{\partial}{\partial x_j} \left(\alpha_\varepsilon \mu_{eff} \frac{\partial \varepsilon}{\partial x_j} \right) + C_{1\varepsilon} \frac{\varepsilon G_k}{k} - C_{2\varepsilon} \rho \frac{\varepsilon^2}{k} - R_\varepsilon \quad (3.9)$$

where, $G_k = -\overline{\rho u_i u_j} \frac{\partial u_j}{\partial x_i}$, represents the generation of turbulent kinetic energy due to mean

velocity gradients. The quantities α_k and α_ε are the inverse effective Prandtl numbers for ‘*k*’

and ‘*ε*’ respectively. The expression for R_ε is given by, $R_\varepsilon = \frac{C_\mu \rho \eta^3 (1 - \eta / \eta_o) \varepsilon^2}{(1 + \beta \eta^3) k}$,

where, $\eta = S k / \varepsilon$, $\eta_o = 4.38$, $\beta = 0.012$, $C_{1\varepsilon} = 1.42$, $C_{2\varepsilon} = 1.68$ and ‘*S*’ is a scalar measure of the deformation tensor. The turbulent viscosity is computed from the differential equation

$$d \left(\frac{\rho^2 k}{\sqrt{\varepsilon \mu}} \right) = 1.72 \frac{\hat{v}}{\sqrt{\hat{v}^3 - 1 + C_v}} d\hat{v} \quad (3.10)$$

where, $\hat{v} = \mu_{eff} / \mu$, and $C_v = 100$.

Equation (3.10) is integrated to obtain an accurate description of effective turbulent transport, allowing the model to handle low-Reynolds number and near-wall flows in a better

manner. In the high-Reynolds number limit, Eq. (3.10) gives $\mu_t = \rho C_\mu \frac{k^2}{\varepsilon}$, where, $C_\mu =$

0.0845. Turbulence, in general, is affected by swirl in the mean flow. The *RNG* $k-\varepsilon$ model provides an option to account for the effects of swirl by modifying the turbulent viscosity appropriately. The modification takes the following functional form:

$$\mu_t = \mu_{t0} f\left(\alpha_s, \Omega, \frac{k}{\varepsilon}\right) \quad (3.11)$$

where, μ_{t0} is the value of turbulent viscosity calculated without the swirl modification using Eq. (3.10), Ω is a characteristic swirl number and α_s is a swirl constant that assumes different values depending on whether the flow is swirl-dominated or only mildly swirling. In the present computation α_s is taken to be 0.07.

The inverse effective Prandtl numbers, α_k and α_ε , are computed as follows.

$$\left| \frac{\alpha - 1.3929}{\alpha_o - 1.3929} \right|^{0.632} \left| \frac{\alpha + 2.3929}{\alpha_o + 2.3929} \right|^{0.3629} = \frac{\mu_{mol}}{\mu_{eff}} \quad (3.12)$$

where, $\alpha_o = 1.0$, $\mu_{mol} / \mu_{eff} \ll 1$, $\alpha_k = \alpha_\varepsilon \approx 1.393$

The intensity of turbulence used in the CFD calculation is 2%. Generally the low intensity of turbulence is chosen for the underdeveloped flow compared to fully developed flow regime. The formula for the intensity of turbulence (I) in the fully developed regime is, $I = 0.16 * (\text{Re}_{D_h})^{(-1/8)}$. In the present case for the maximum $\text{Re} = 97900$, it is 4%. So, the half of the value is considered at the inlet and this defines the value of turbulent kinetic energy and turbulence dissipation rate (ε) at the inlet, given by Eqs. (3.6) and (3.7)

3.3 MODELING OF BLOCKAGE WITHIN THE BUNDLE

The governing equations for continuity, momentum balance and energy balance are the same as Eqs. 3.1-3.7, except that an additional source term (S_{porous}) is added in the momentum equations, to account for pressure drop due to fluid blockage. The turbulence model is turned

off within the blockage. Pressure drop within the porous blockage is modelled using the correlation suggested by Ergun (1952) as given in Eq. (3.15).

$$\frac{|\Delta P|}{\Delta z} = 150 \frac{(1-\varphi)^2}{\varphi^3} \frac{\mu u_s}{d_p^2} + 1.75 \frac{(1-\varphi)}{\varphi^3} \frac{\rho u_s^2}{d_p} \quad (3.13)$$

Where, u_s is the superficial velocity of fluid, d_p is the mean particle diameter and φ is the porosity of the medium.

The porous blockage model facilitates the solution of the energy transport equation in the porous regions with suitable modification to the diffusion term. In the porous region, the effective thermal conductivity (K_{eff}) of the medium is the volume average of the fluid thermal conductivity (K_f) and the solid thermal conductivity (K_s). This can be calculated in the following ways (Nield and Bejan, 2013). If the heat conduction in the solid and fluid phases occurs in parallel, effective thermal conductivity is weighted by arithmetic mean of conductivities K_f and K_s , as given in Eq. 3.18.

$$K_{eff} = \varphi K_f + (1-\varphi) K_s \quad (3.14)$$

If the conductivities are widely different (conduction in series) the harmonic mean will be more appropriate.

$$\frac{1}{K_{eff}} = \frac{\varphi}{K_f} + \frac{(1-\varphi)}{K_s} \quad (3.15)$$

For rough and ready estimate the effective thermal conductivity is calculated by the geometric mean,

$$K_{eff} = K_f^\varphi + K_s^{(1-\varphi)} \quad (3.16)$$

The hybrid differencing scheme (HDS) has been adopted for evaluating the convective and diffusive fluxes in all the transport equations. The HDS scheme is marginally

more accurate than the upwind differencing scheme (UDS), due to the reason that the second order central differencing scheme (CDS) will be used in regions of low Peclet number.

It shall be highlighted that flow over a solid block is expected to exhibit unsteady behavior. However, presence of helical wire-wrap combined with porous nature of the blockage may stabilize the flow. The associated transient flow structures are expected to be complex, demanding critical attention and hence an exclusive investigation. This is included as an important area for future research. However, the present steady state simulation with porous body model for the blockage is expected to provide reasonably accurate time-averaged results for the current practical problem.

3.4 ENGINEERING PARAMETERS

The following parameters are used for the data reduction in this study. The non-dimensional cross-section averaged cross-stream velocity is calculated using

$$V_{cs}^* = \frac{1}{A} \int_A \frac{(u_x^2 + u_y^2)^{1/2}}{u_{z-in}} dA \quad (3.17)$$

The friction factor (f) is computed from pressure drop and is defined as

$$f = \frac{-(dp/dz)D_h}{\rho w_{in}^2 / 2} \quad (3.18)$$

To understand heat transfer in various pin bundle configurations, four different definitions of Nusselt number are adopted. The local pin Nusselt number based on global bulk sodium temperature, T_{G-Na} (which is cross section averaged sodium temperature weighted by local velocity) and local clad temperature ($T_{C\theta}$) is defined as,

$$Nu_{\theta} = \frac{q''(D_h / K)}{[T_{C\theta} - T_{G-Na}]} \quad (3.19)$$

$$\text{Where, } T_{G-Na} = \frac{\int u_z T dA}{\int_A u_z dA} \quad (3.20)$$

The average pin Nusselt number, (Nu_C) at any axial position based on average clad temperature of single pin and the global bulk sodium temperature is defined as,

$$Nu_C = \frac{q'' (D_h / K)}{\left[\frac{1}{2\pi} \int_0^{2\pi} T_{C\theta} d\theta - T_{G-Na} \right]} \quad (3.21)$$

The average pin Nusselt number at any axial position, based on average clad temperature of single pin and average sodium temperature of sub-channels surrounding the particular pin weighted by local velocity (T_{SC-Na}) is defined as,

$$Nu_{C-SC} = \frac{q'' (D_h / K)}{\left[\frac{1}{2\pi} \int_0^{2\pi} T_{C\theta} d\theta - T_{SC-Na} \right]} \quad (3.22)$$

$$\text{Where, } T_{SC-Na} = \frac{\sum_{i=1}^6 \int_A u_{zi} T_i dA}{\sum_{i=1}^6 \int_A u_{zi} dA} \quad (3.23)$$

The global Nusselt number, (Nu_G) at any axial position based on average clad surface temperature of all the pins and the global bulk sodium temperature is defined as,

$$Nu_G = \frac{q'' (D_h / K)}{\left[\frac{1}{2\pi N} \sum_{i=1}^N \left(\int_0^{2\pi} T_{C\theta} d\theta \right)_i - T_{G-Na} \right]} \quad (3.24)$$

In the above equations, q'' is the average heat flux over the pin, D_h is the hydraulic diameter of the pin bundle and 'K' is the thermal conductivity of sodium.

The hotspot factor (F_c) at any axial position can be calculated using the expression

$$F_c = \frac{T_h - T_{G-Na}}{\bar{T}_c - T_{G-Na}} \quad (3.25)$$

where, T_h is the highest clad temperature at a particular axial section and \bar{T}_c is the average clad temperature in the same axial section.

The average clad temperature (T_{C-avg}) is calculated using

$$T_{C-avg} = \frac{1}{2\pi N} \sum_{i=1}^N \left(\int_0^{2\pi} T_{C\theta} d\theta \right)_i \quad (3.26)$$

$$T_{C-avg} = \frac{1}{2\pi N} \sum_{i=1}^N \left(\int_0^{2\pi} T_{C\theta} d\theta \right)_i \quad (3.27)$$

3.5 BOUNDARY CONDITIONS AND CONVERGENCE

The result of any numerical analysis is significantly influenced by the boundary conditions applied. Thus, it is a most essential component for any numerical analysis. In the present problem, at inlet to the pin bundle a known velocity condition and at outlet of the pin bundle a known pressure condition are specified as depicted in Fig. 3.1. Adiabatic and no-slip conditions at hexcan outer walls are specified. It may be highlighted that in the present case, the heat source is from the fuel pin and not from the wire. Secondly, the wire is in line contact with the fuel pin. Further, the heat flux on the wire-wrap is unknown. For a realistic computation, the heat conduction within the fuel pin, clad as well as spacer wire and convection in sodium have to be solved in conjugation. However, in the present studies the wire is assumed to be adiabatic, while the clad is supplied with a constant flux. For declaring convergence, the tolerance on the residual values for all the governing equations is set as 10^{-6} .

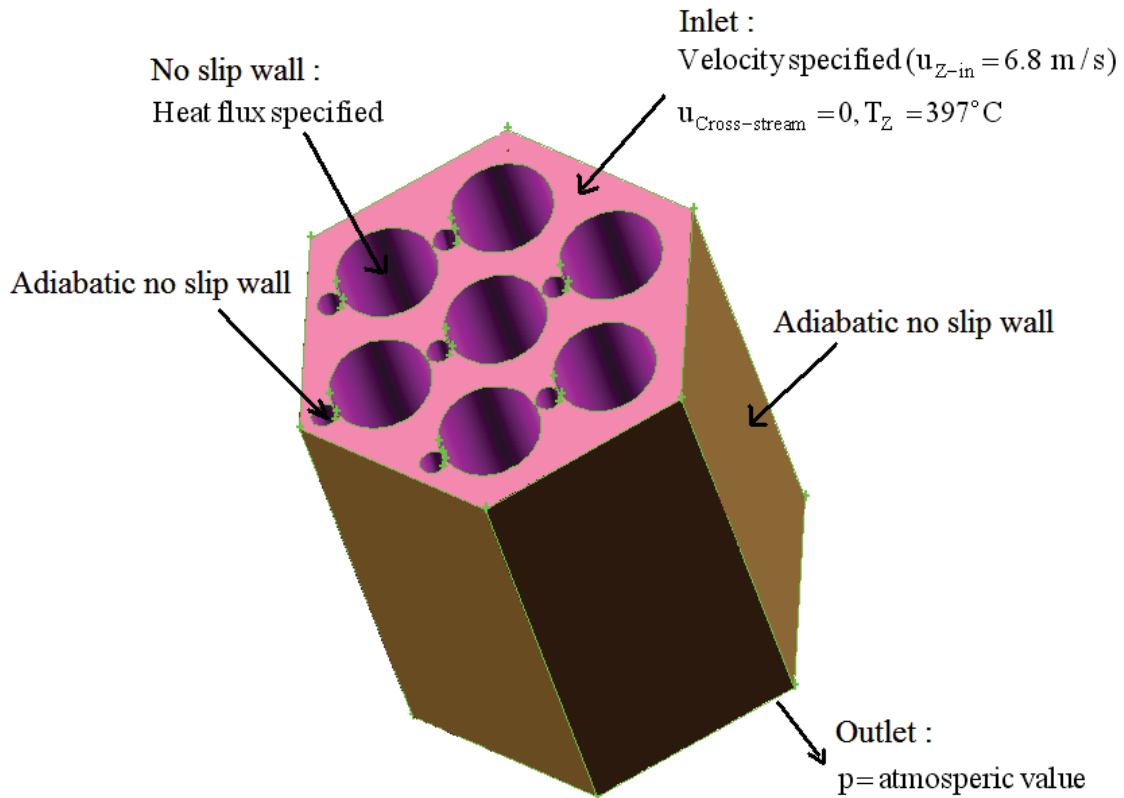


Fig. 3.3 Boundary conditions used for the CFD simulations

3.6 GRID SENSITIVITY STUDY AND VALIDATION

Grid sensitivity and validation studies are important for CFD based research. Hence, elaborate grid sensitivity and validation studies have been performed. The present results are compared with published benchmark experimental / computational results where available. These studies are discussed in Chapters 4-7, as appropriate.

3.7 CLOSURE

The governing equations for analyzing fluid flow, heat transfer and turbulence in the pin bundle and for the porous body model corresponding to internal partial porous blockages, the boundary conditions adopted and the overall computational methodology are elaborated in the present chapter. The results predicted from the CFD simulations are discussed in the subsequent chapters.

CHAPTER-4

FLOW AND THERMAL DEVELOPMENTS IN BARE FUEL PIN BUNDLES

4.0 INTRODUCTION

Fast reactor fuel pin bundle is a tight triangular lattice structure with pitch to diameter ratio close to unity. Also a large number of fuel pins are housed inside a hexagonal tube known as hexcan or sheath. The bundle of pins forms a large number of sub-channels. Due to this tight packing, the flow communication between the various sub-channels becomes very weak. As a result of this, flow development in sub-channels comprises of two regimes, viz., (i) local flow development within the sub-channels and (ii) global flow re-distribution among the sub-channels. While the local flow development in sub-channels is governed by local hydraulic diameter or sub-channel hydraulic diameter, the global flow development is a strong function of the resistance for flow redistribution among the central and peripheral sub-channels. The weaker the communication, the larger is the global development length. The global development regime could be a function of pin diameter, pitch, the clearance between the hexagonal sheath and the outer most pins, Reynolds number etc. Knowledge of flow and temperature characteristics in the entrance region is essential for the thermal hydraulic design of fast reactor core. This knowledge is also essential for setting-up experimental facility for determination of friction factor and Nusselt number.

Because of possible non-uniform flow development in the central and peripheral sub-channels, the local heat transfer coefficients can also vary vastly among the central and peripheral pins. Also the local heat transfer coefficients can be significantly different from the global heat transfer coefficients. Further, measured heat transfer coefficients depend strongly upon (i) the tube bundle length considered in the experiments, (ii) the care exercised in measuring the circumferential temperature variation in pins, (iii) definition of bulk temperature of sodium etc, in addition to geometric parameters. The flow re-distribution

among the central and peripheral sub-channels could be influenced by the gap between the hexagonal sheath and the outermost rows of pins. Hence, in the present three dimensional CFD studies, detailed simulations on bare pin bundles have been carried out towards addressing some of the basic phenomena concerning flow in entrance region. The ranges of various parameters considered in the study are presented in Table-4.1.

Table 4.1 Range of parameters studied using bare pin bundles

N	Ligament gap (mm)	Pin diameter (mm)	Re
1-217	1.43 -5.7	3.3 – 6.6	$0.4 \times 10^5 - 1.4 \times 10^5$

4.1 SOLUTION METHODOLOGY

4.1.1 Grid Sensitivity Study

Towards identifying a suitable grid pattern, a 30° symmetric sector of 217-pin fuel bundle, shown in Fig. 4.1, is considered for the 3-D simulations. A typical structured grid generated for the same is depicted in Fig. 4.2a. Inlet velocity of sodium is prescribed as 6.8 m/s and inlet temperature of sodium is 693 K with pin surface heat flux of 1600 kW/m². The pin diameter is 6.6 mm, pitch is 8.28 mm and the hydraulic diameter is 5.02 mm with the Reynolds number specified as 1.06×10^5 .

At the inlet to the bundle, uniform axial velocity and a uniform inlet temperature of 397°C are considered. The lateral velocity components are taken to be zero. Turbulence intensity of 2% is considered. The value of ϵ is computed from Eq. (3.7). Constant heat flux and no slip wall boundary condition are applied to the fuel pins. Adiabatic and no slip wall boundary conditions are applied to the hexcan wall. Both sides of the 30° sector are imposed with the symmetry boundary condition.

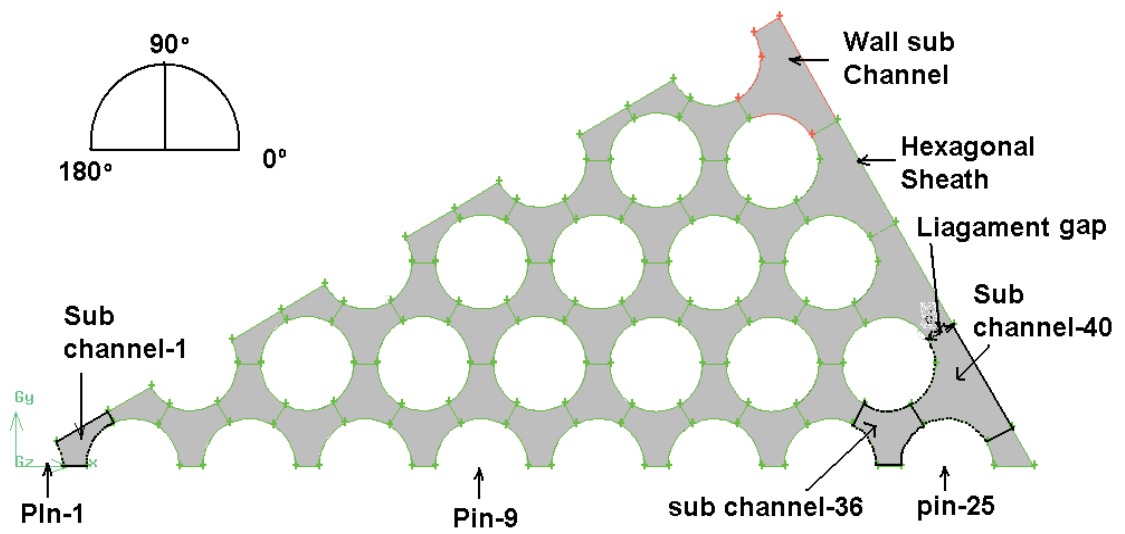


Fig. 4.1 CFD model of 217-pin bundle with sub-channels

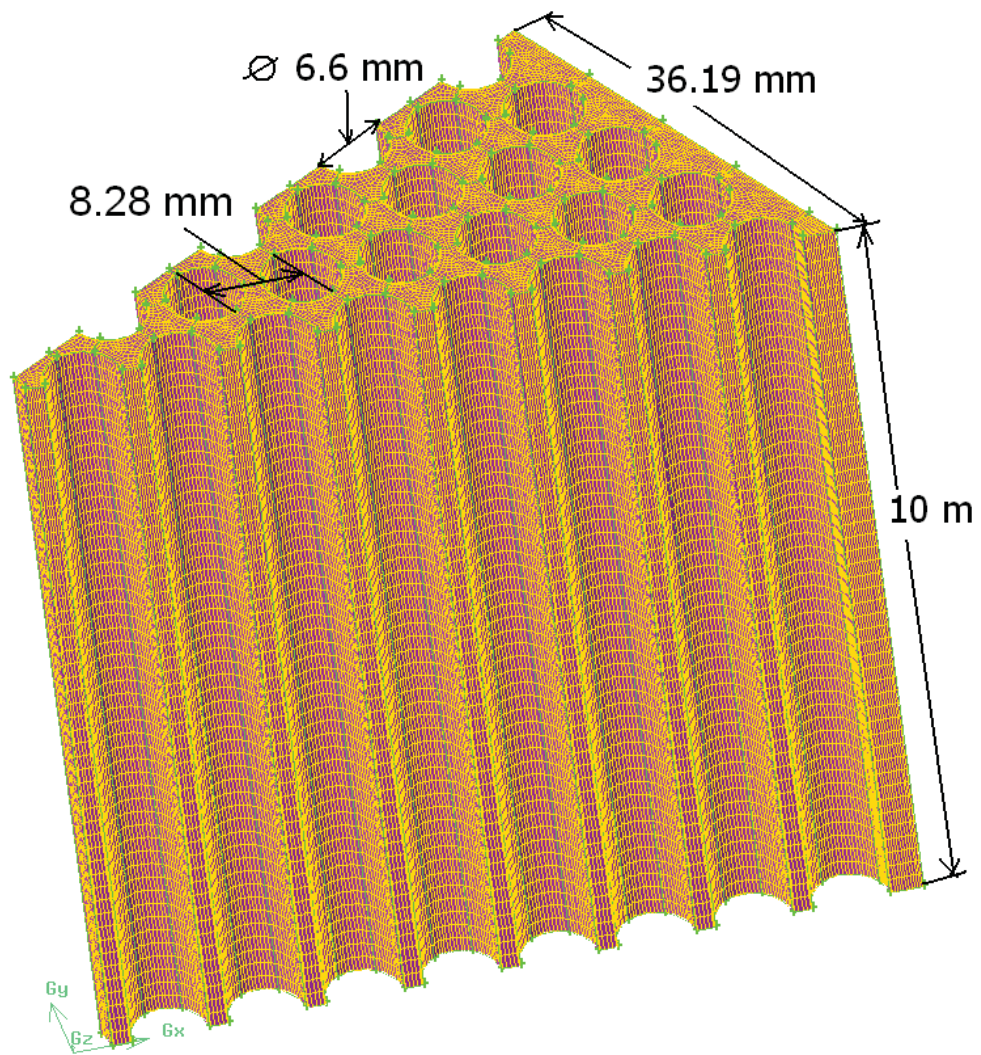


Fig. 4.2a Mesh used for 217-pin bundle study

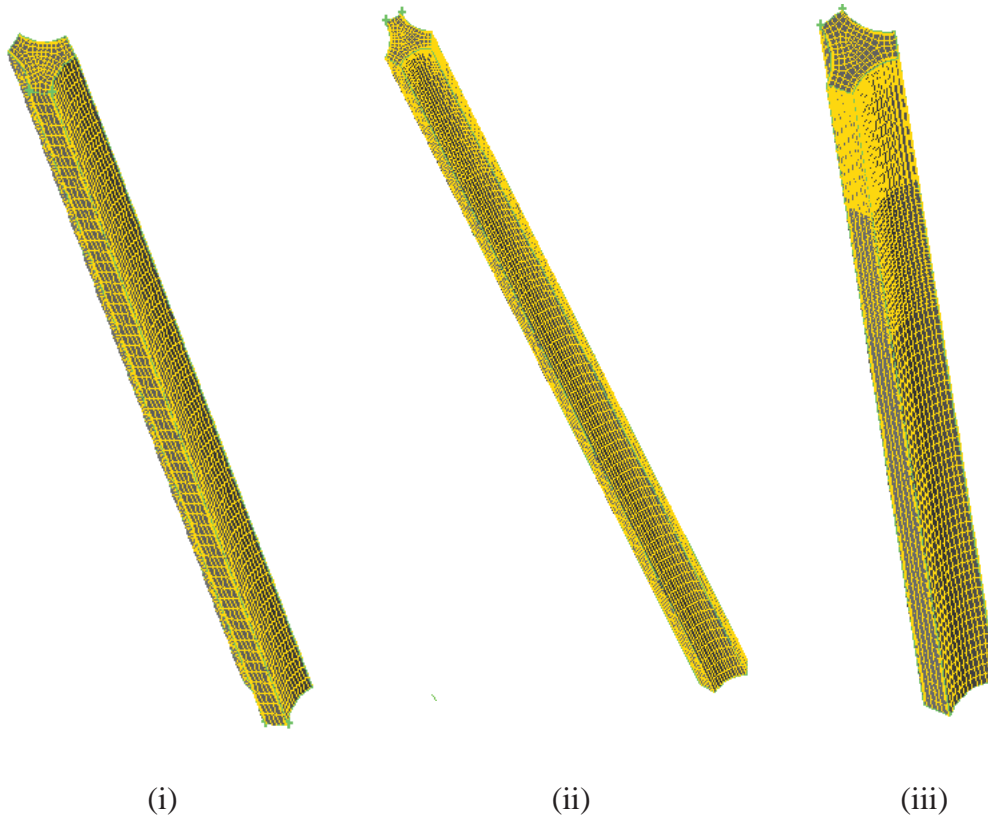


Fig. 4.2b Three different mesh used for grid sensitivity study (i) 0.387 millions (ii) 0.735 millions (iii) 1.35 millions

Table 4.2a Temperature values predicted with different mesh for bare pin bundle

Number of Finite volumes (millions)	L/D_h	\bar{T}_c of central pin (K)	Percentage change in $(\bar{T}_c - T_{in})$ with finer mesh data as reference value	T_{SC-Na} for central pin (K)	Percentage change in $(T_{SC-Na} - T_{in})$ with finer mesh data as reference value
0.387		771.78	-	765.03	-
0.735	79.7	771.96	-0.24	764.96	0.11
1.35		771.82	0.18	764.81	0.21
0.387		788.37	-	781.67	-
0.735	97.6	788.35	0.02	781.33	0.38
1.35		788.18	0.18	781.15	0.20

Table 4.2b velocity and pressure values predicted with different mesh for bare pin bundle

Number of Finite volumes (millions)	L/D_h	Static pressure (Pa)	Percentage change in pressure with finer mesh data as reference value	Velocity magnitude (m/s)	Percentage change in velocity with finer mesh data as reference value
0.387		7548.2	-	6.93	-
0.735	79.7	7350.5	2.62	6.83	1.49
1.35		7347.0	2.67	6.84	1.30
0.387		825.3	-	6.93	-
0.735	97.6	817.2	0.99	6.79	2.09
1.35		817.0	1.01	6.79	2.02

Three different grids have been considered to establish the grid independence of predicted results. Three different grids are shown in Fig. 4.2b for a single sub-channel. The clad temperature of central pin (pin-1 in Fig. 4.1) and sub-channel sodium temperature surrounding the central pin at two different locations along the flow direction, viz., $L/D_h = 79.7$ and 97.6 are presented in Table-4.2a, for various grid patterns. The comparison shows that the variation in the predicted results using 0.387, 0.735 and 1.350 million grids is small ($< 0.38\%$). Apart from sub-channel clad temperature, both velocity and pressure sensitivity on grid refinement is presented in Table-4.2b. The comparison shows that the variation of both bundle average pressure and bundle average velocity in the predicted results using 0.387, 0.735 and 1.350 million grids is within 3%. Therefore, the grid with 0.387 million cells is chosen for further studies. Critical care has been exercised while generating mesh in the cross-stream direction. It is ensured that the y^+ value for all the surfaces is limited within 30-100. Typically the first mesh was about 70 microns away from the wall. These simulations needed a minimum RAM of 4 GB. For convergence, a CPU time of about 48 hours was required in an eight core parallel machine.

4.1.2 Validation Studies

To validate the CFD model, a circular tube of diameter, $D = 0.2$ m and length, $L = 100 \times D$ is considered. The Reynolds number for liquid sodium flow based on diameter and inlet velocity of 1.375 m/s is 4.3×10^5 . Distribution of mesh to respect y^+ values near the walls and to achieve acceptable mesh aspect ratio are paid critical attention during mesh generation. The y^+ values near the wall are maintained in the range from 30 to 41.

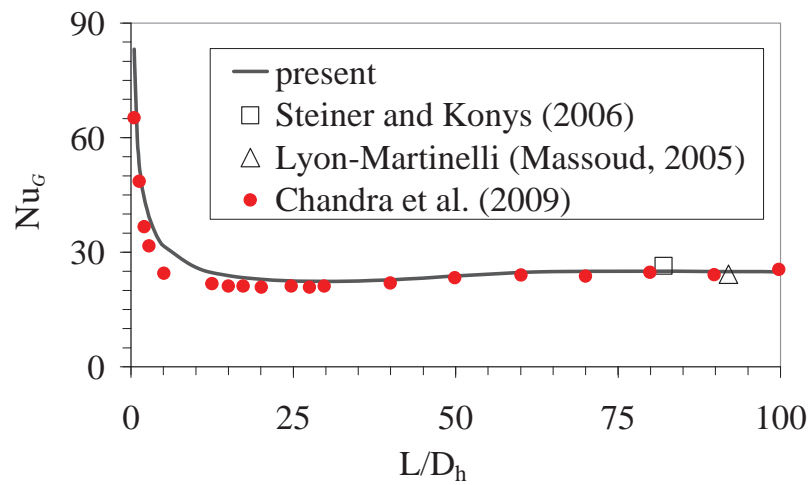


Fig. 4.3a Variation of Nusselt number during sodium flow in the entrance region of a circular pipe ($Re = 4.3 \times 10^5$)

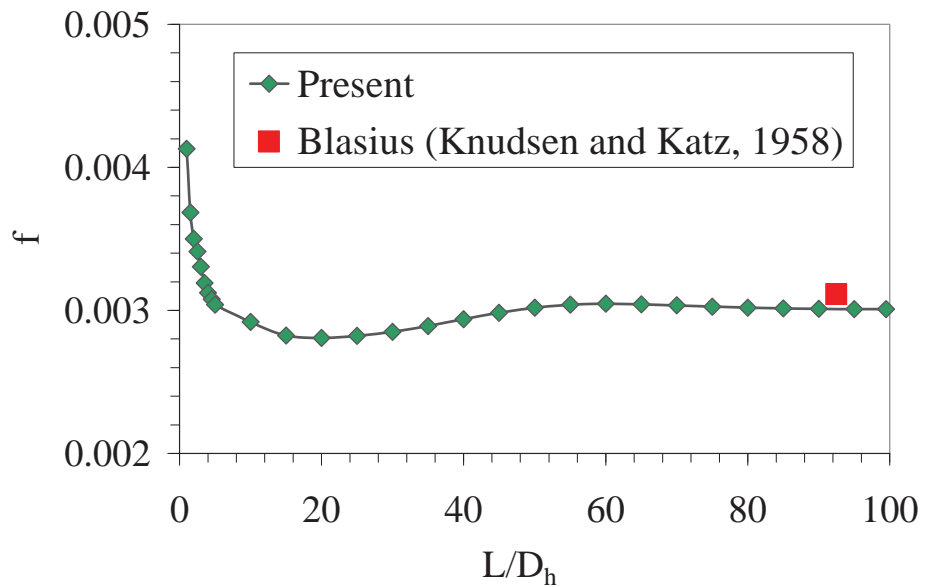


Fig. 4.3b Variation of friction factor during sodium flow in the entrance region of a circular pipe ($Re = 4.3 \times 10^5$)

The predicted wall Nu number along the flow direction is plotted in Fig. 4.3a. Also shown in the same figure are the experimental values of fully developed Nu number for sodium flow through pipes. Nusselt number is evaluated from Lyon-Martinelli correlation ($Nu = 4.8 + 0.025 Pe^{0.8}$) and Steiner and Konys correlation ($Nu = 7 + 0.025 Pe^{0.8}$). It is seen that the present simulation compares very well with the experimental data (-5.5 % against Steiner and Konys (2006) and +3% against Lyon-Martinelli (Massoud, 2005)). Also shown in the same figure are the numerical results of Chandra et al. (2009). The present results agree well with that of Chandra et al. (2009) in the entire entrance region. The predicted friction factor for the circular tube along the flow direction is plotted in Fig. 4.3b. The fully developed value of friction factor compares almost exactly with the prediction by Blasius formula for smooth pipes (Knudsen and Katz, 1958). An interesting feature observed in the entrance region of the pipe is that both Nusselt number and friction factor reduce below their fully developed limits in the region of $10 \leq L/D_h \leq 50$.

Before attempting to predict the flow features in multiple sub-channels, it is imperative to have some base-line data. Simultaneous development of flow and temperature in a single sub-channel (Fig. 4.4a) bounded by 3-pins is the ideal case for this purpose. For this study, 1/6th portion of a triangular sub-channel having dimensions as marked in Fig. 4.4a is considered. The fuel pin is supplied with constant heat flux of 1600 kW/m² for the domain length of 0.7 m. Inlet temperature is taken as 420°C. At the inlet to the sub-channel a uniform axial velocity is assumed. The lateral velocity components are taken to be zero. Turbulence intensity of 2% is considered. Constant heat flux and no slip wall condition are applied to the fuel pin. Other three lateral sides are imposed with the symmetry boundary condition.

Predicted axial variations of Nu_G during flow of sodium in the entrance region are plotted in Fig. 4.4b at $Re = 1.18 \times 10^5$. For the present purpose, the thermal development length is defined as the distance from entrance where the Nu attains a value within 1% of the fully

developed value. The hydraulic diameter for the single sub-channel is found to be 4.85 mm. As per the present definition, the thermal development length is found to be $12.5 \times D_h$. It appears that all the reported experimental results are for fully developed region. Due to the unavailability of published experimental data for the entrance region, fully developed value is compared in the downstream end. The present data compares well with the published data [Friedland and Bonnilla (1961) and Mareska and Dwyer (1964)] in the fully developed regime. Figure 4.4b will be used as base-line data for assessing flow development in multiple sub-channels. The predicted local Nusselt number (Nu_θ) variation along the circumference of the pin at four axial locations, viz., $L/D_h = 5, 10, 20$ and 50 are depicted in Fig. 4.4c.

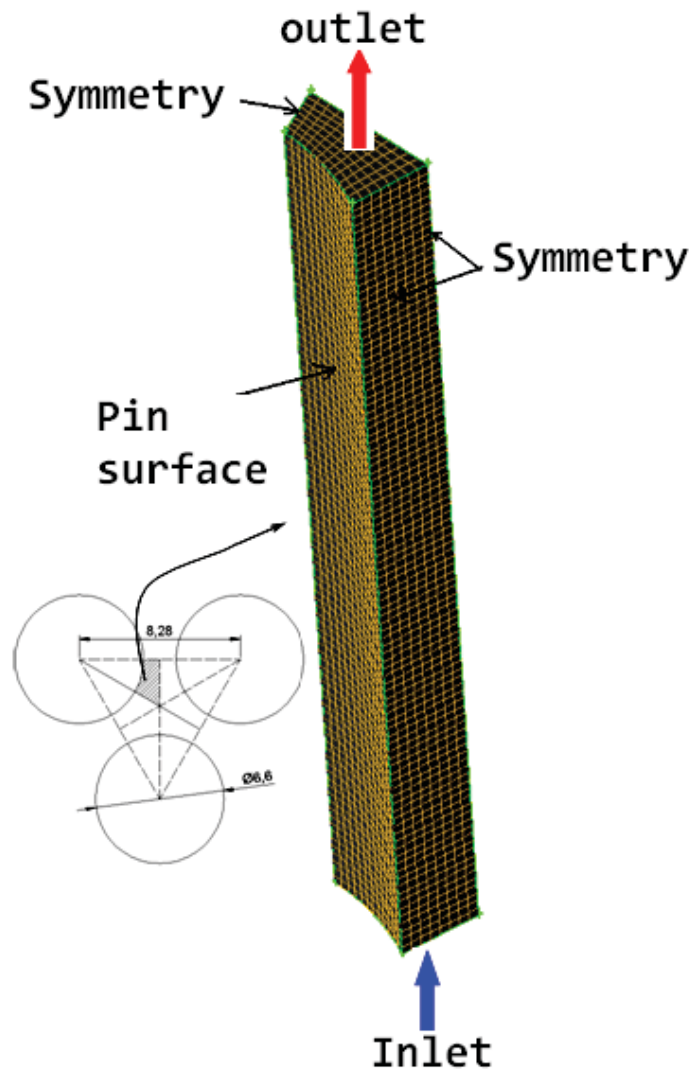


Fig. 4.4a Mesh and boundary conditions used in 1/6th of triangular sub-channel (All the dimensions are in mm)

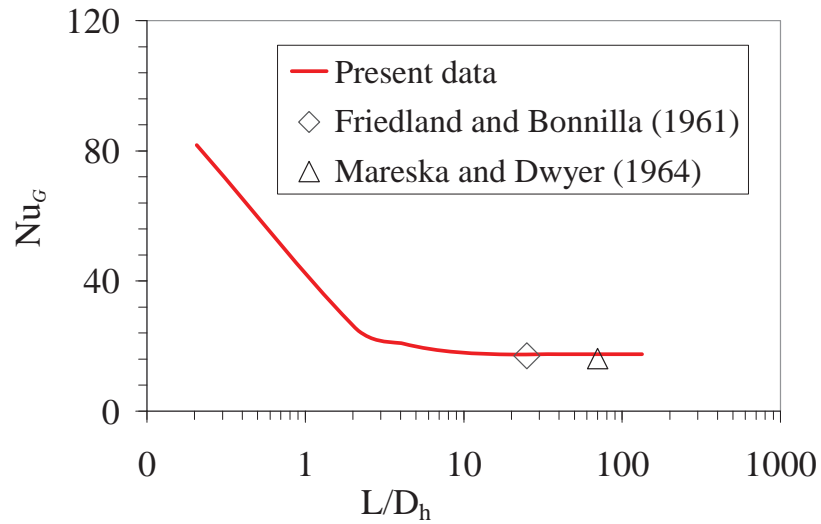


Fig. 4.4b Variation of global Nusselt number during flow of sodium in a single triangular sub-channel at $Re = 1.18 \times 10^5$

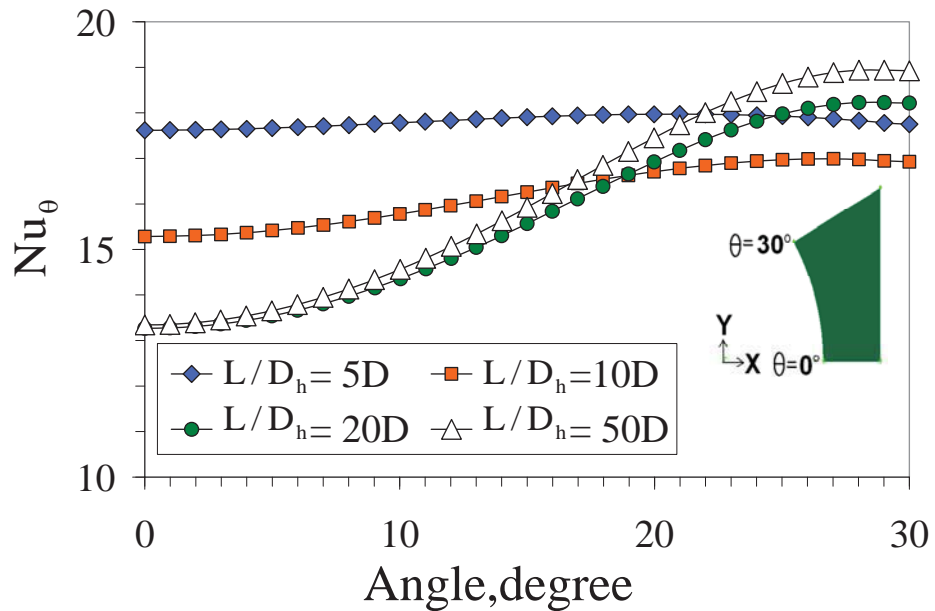


Fig. 4.4c Circumferential variation of local pin Nusselt number during flow of sodium in a single triangular sub-channel at $Re = 1.18 \times 10^5$

It is seen that in the region very close to the entrance, there is insignificant variation in the Nusselt number value along the circumference as the velocity is fairly uniform at the entrance. However, as the flow develops in the downstream, flow redistribution takes place leading to significant velocity non-uniformity. The velocity in the narrow section (around $\theta = 0^\circ$) decreases and that in the wider section (around $\theta = 30^\circ$) increases. As a consequence of this effect, the local Nusselt number decreases around $\theta = 0^\circ$, and it increases around $\theta =$

30°. The ratio of maximum to minimum values of local Nusselt number is about two. This leads to high clad temperatures (hot spots) in the narrow region which needs to be suitably accounted in the safety analysis and clad life prediction calculations.

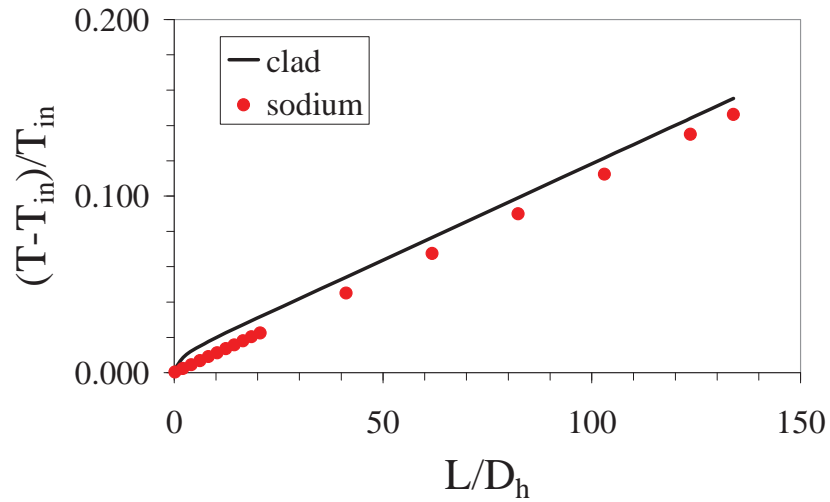


Fig. 4.4d Variation of average clad temperature and global bulk temperature in a single triangular sub-channel at $Re = 1.18 \times 10^5$

The predicted axial variation in mean temperature of sodium in the sub-channel and the circumferentially averaged fuel pin clad temperature are depicted in Fig. 4.5d. It is clear that the temperature difference is low in the entrance region, indicating large heat transfer coefficient values for the iso-flux boundary condition employed. The two curves become linear and parallel to each other in the fully developed region, as expected.

4.1.3 Selection of Turbulence Model

Turbulence models play a major role in numerical prediction. So it is essential to evaluate the capability of available models for the present simulation. For this study, the 7-pin bundle configuration with 3.3 mm pin diameter is considered. The Reynolds number of sodium flow is 2.58×10^5 . The global Nusselt number predicted by various turbulence models is plotted in Fig. 4.5a.

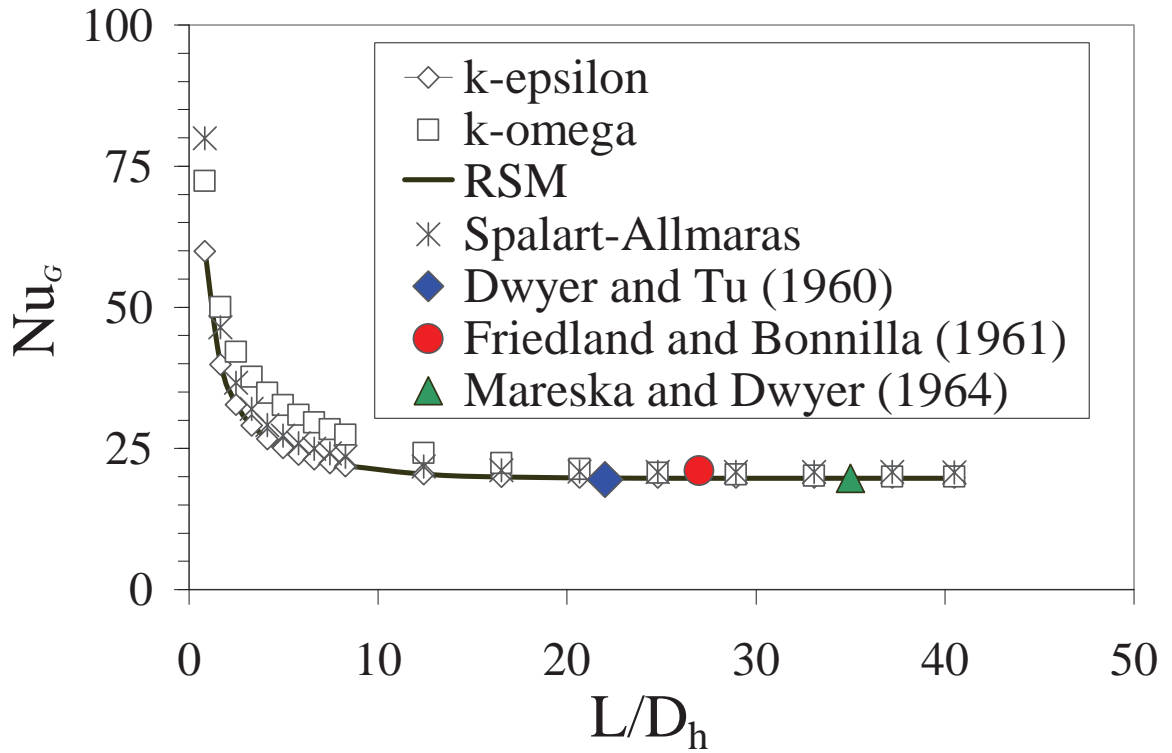


Fig. 4.5a Global Nusselt number in 7-pin bundle configuration during sodium flow at $Re = 2.58 \times 10^5$

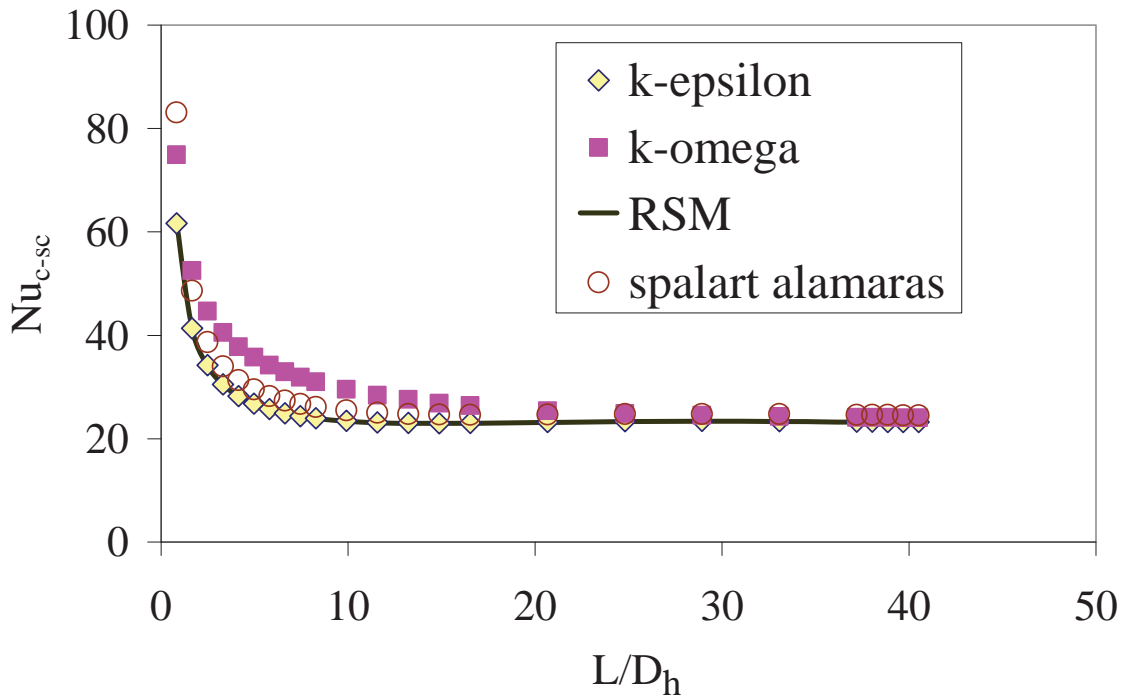


Fig. 4.5b Local Nusselt number in 7-pin bundle configuration during sodium flow at $Re = 2.58 \times 10^5$

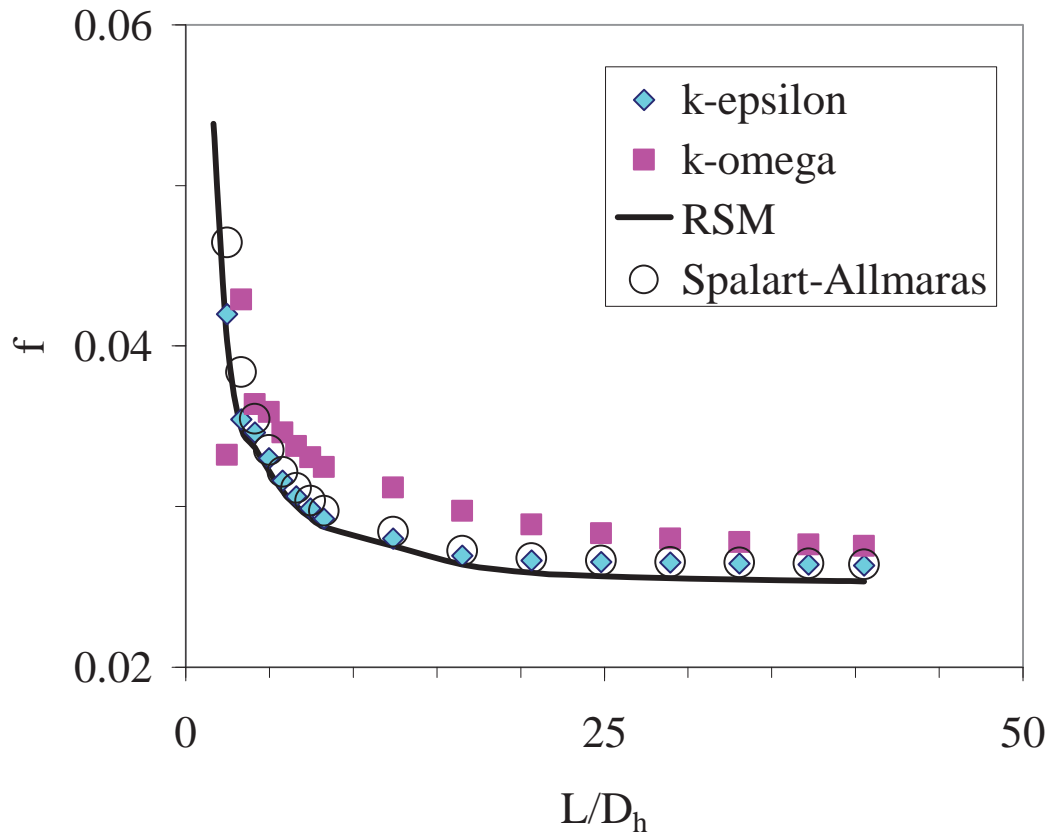


Fig. 4.5c Friction factor in 7-pin bundle configuration during sodium flow at $Re = 2.58 \times 10^5$

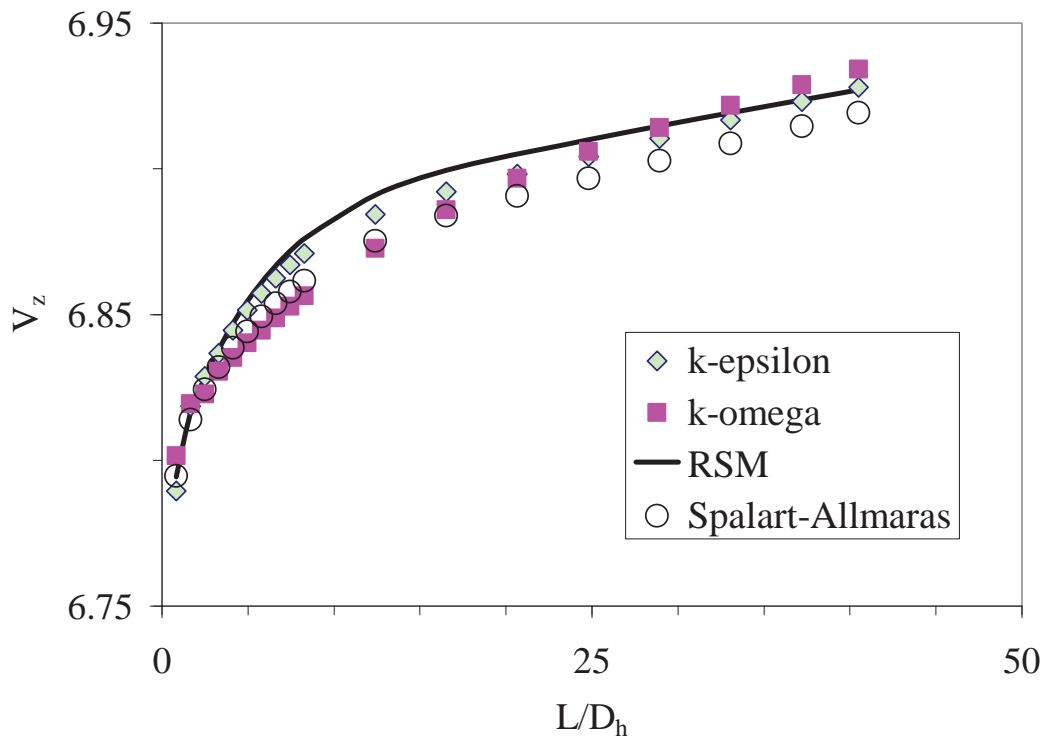


Fig. 4.5d Velocity in 7-pin bundle configuration during sodium flow at $Re = 2.58 \times 10^5$

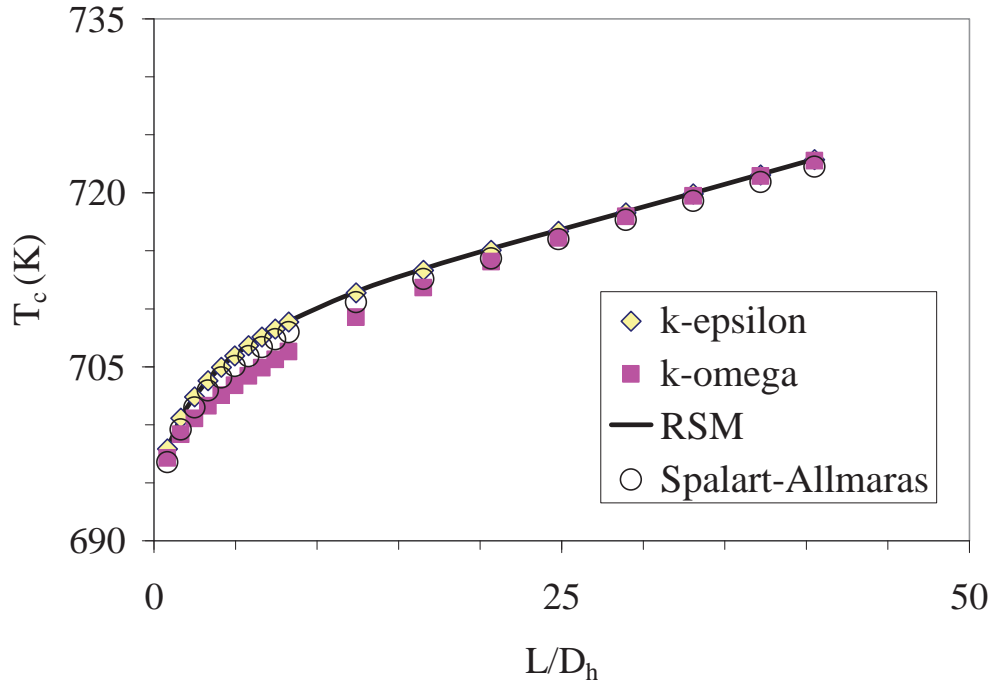


Fig. 4.5e Average clad temperature in 7-pin bundle configuration during sodium flow at $Re = 2.58 \times 10^5$

Among the different turbulence models the results of $k-\epsilon$ and RSM models closely match with each other all along the flow length. Moreover, the fully developed Nusselt numbers predicted by all the models are nearly equal. Also shown in Fig. 4.5a, are the experimental data reported by Dwyer and Tu (1960), Friedland and Bonnillia (1961) as well as Mareska and Dwyer (1964). All the three experimental data sets match with numerical prediction with negligible deviation. In addition to the global Nusselt number local Nusselt number (for central sub-channel), friction factor, axial velocity and clad temperature depicted in Fig. 4b, Fig. 4c, Fig. 4d and Fig. 4e respectively, with different turbulence models. All the results confirm that the prediction of $k-\epsilon$ and RSM models are closer. Therefore, the standard high Reynolds number $k-\epsilon$ model is used for all the subsequent studies.

4.1.4 Selection of Discretization Scheme

It is known that the CFD results depend on the discretization scheme adapted. Towards deciding the scheme, flow development in a 7-pin bare bundle configuration has been

analyzed for $Re = 1.10 \times 10^5$ employing four different schemes, viz., (i) first order upwind, (ii) second order upwind, (iii) power law and (iv) third order MUSCL schemes (Monotone Upstream-Centered Schemes for Conservation Laws) (FLUENT, 2007). The predicted global Nusselt number, Nu_G defined by Eq. (3.25) is plotted in Fig. 4.5f. In addition to the global Nusselt number, friction factor, axial velocity and clad temperature are depicted in Fig. 4g, Fig. 4h and Fig. 4i respectively for different discretization schemes. It can be seen that all the schemes predict nearly identical throughout the developing region, suggesting first order upwind scheme is quite adequate for the present investigations. Similar conclusion was reported by Sreenivasulu and Prasad (2011) for bare pin bundle.

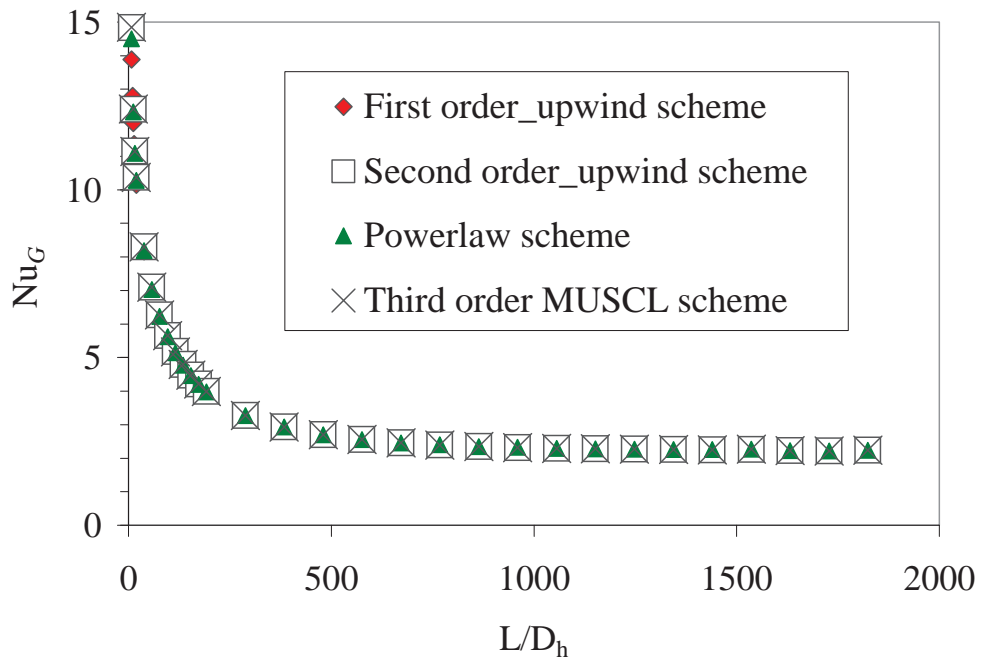


Fig. 4.5f Comparison of thermal development in 7-pin bundle as a function of discretization schemes at $Re = 1.10 \times 10^5$

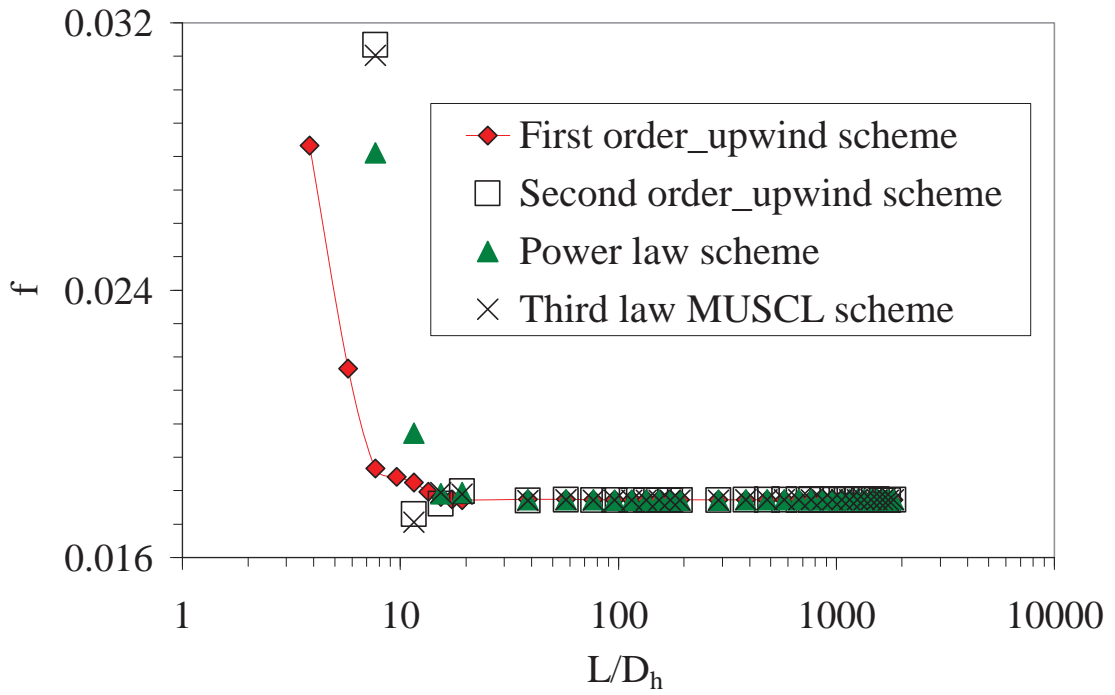


Fig. 4.5g Comparison of friction factor development in 7-pin bundle as a function of discretization schemes at $Re = 1.10 \times 10^5$

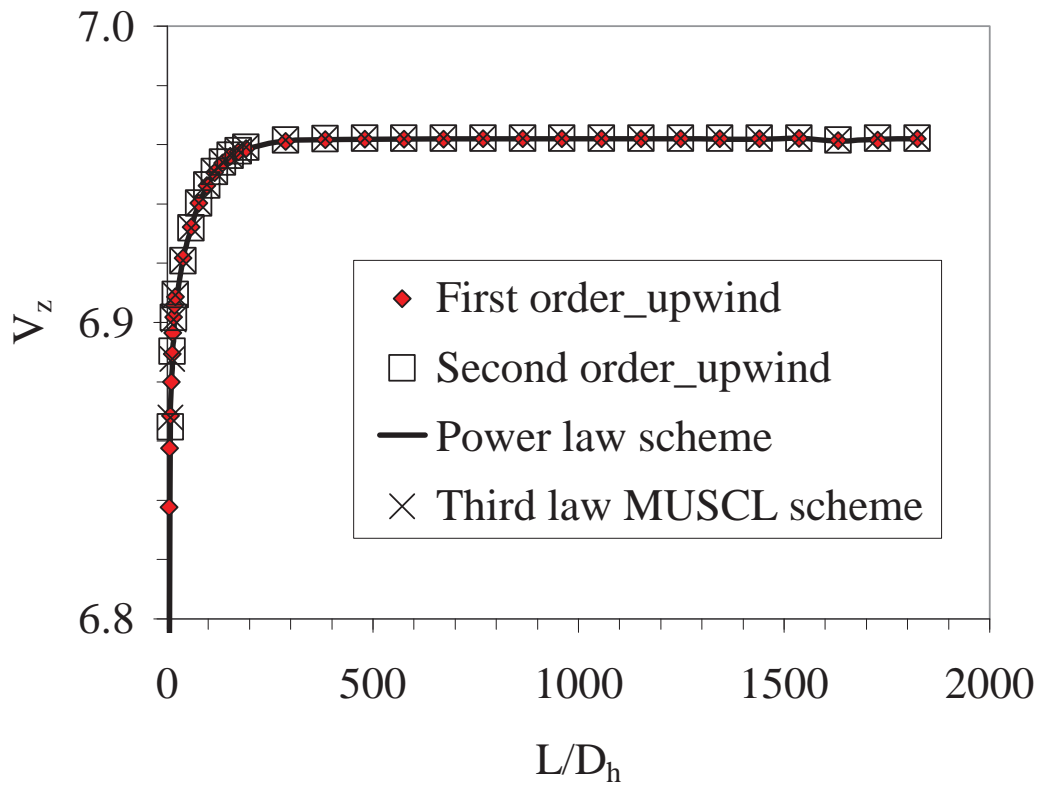


Fig. 4.5h Comparison of axial velocity development in 7-pin bundle as a function of discretization schemes at $Re = 1.10 \times 10^5$

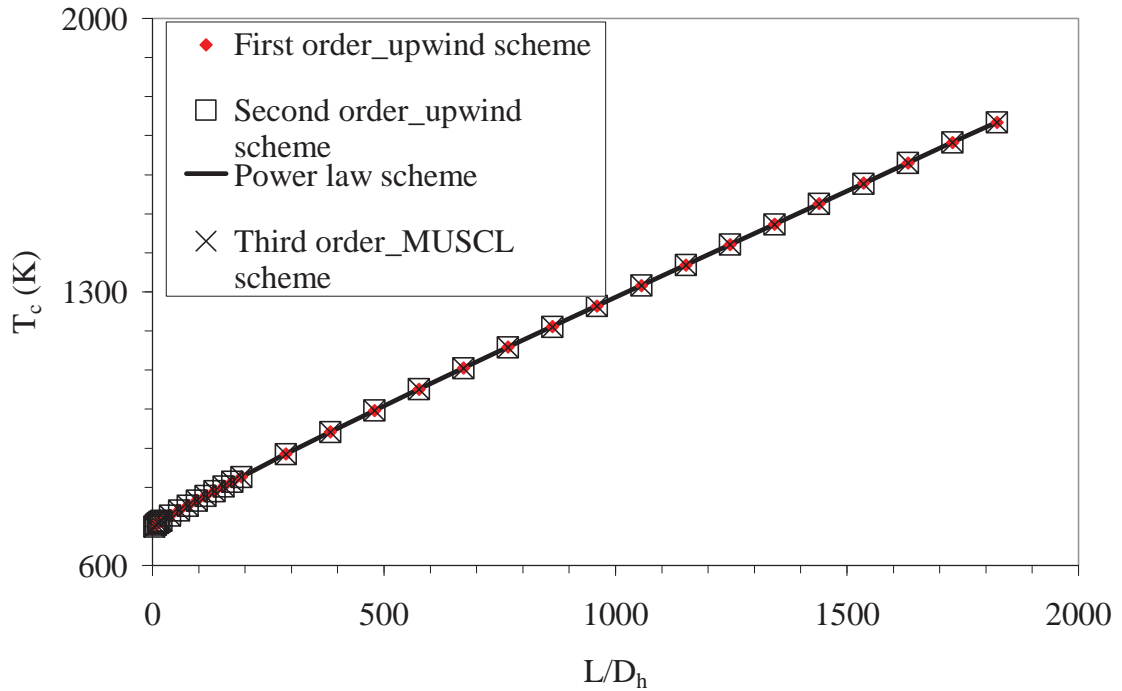


Fig. 4.5i Comparison of axial velocity development in 7-pin bundle as a function of discretization schemes at $Re = 1.10 \times 10^5$

4.1.5 Selection of Turbulent Prandtl Number

Studies by Kawamura et al. (1998) indicate that the turbulent Prandtl number (Pr_t) for liquid metal is different from that of conventional fluids close to the walls. Its value reduces from about three, close to the wall, to unity far away from the wall. In the present study, however, this value is taken to be constant throughout the fluid domain. In order to understand the dependence of thermal development on turbulent Prandtl number, the 7-pin bundle depicted in Fig. 4.6b is considered. For the present study three values, $Pr_t = 1, 2$ and 3 are considered. The values of pin diameter, hydraulic diameter, velocity and Reynolds number are 6.6 mm, 5.21 mm, 5.159 m/s and 0.842×10^5 respectively. The predicted Nusselt number development is depicted in Fig. 4.5j.

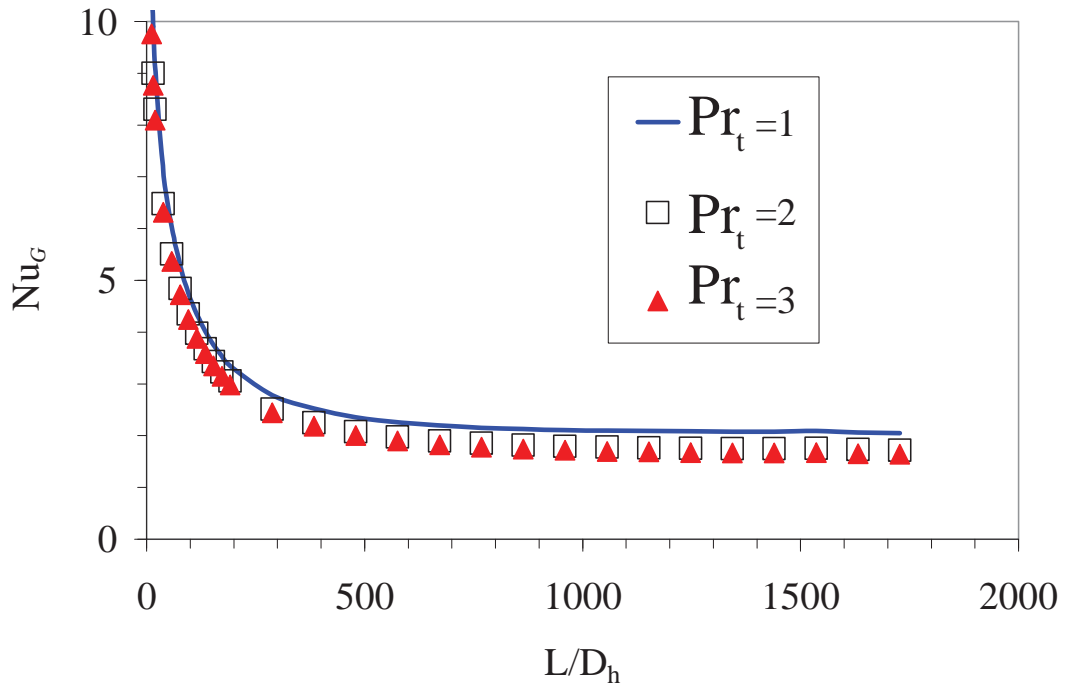


Fig. 4.5j Comparison of thermal development data in 7-pin bundle as a function of turbulent Prandtl number at $Re = 0.842 \times 10^5$

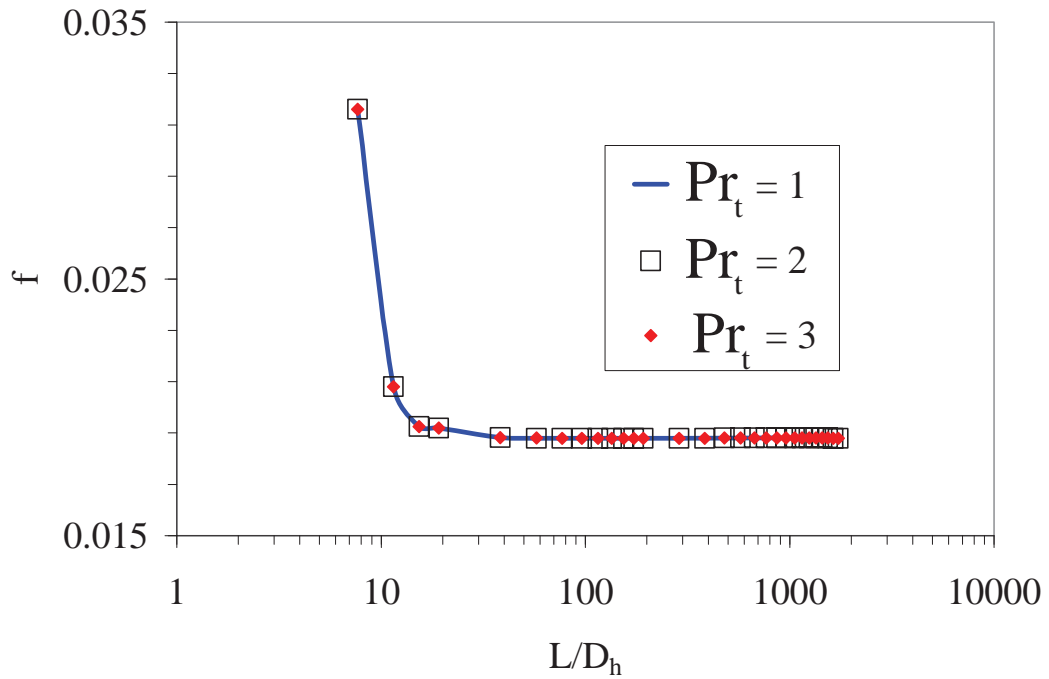


Fig. 4.5k Comparison of flow development data in 7-pin bundle as a function of turbulent Prandtl number at $Re = 0.842 \times 10^5$

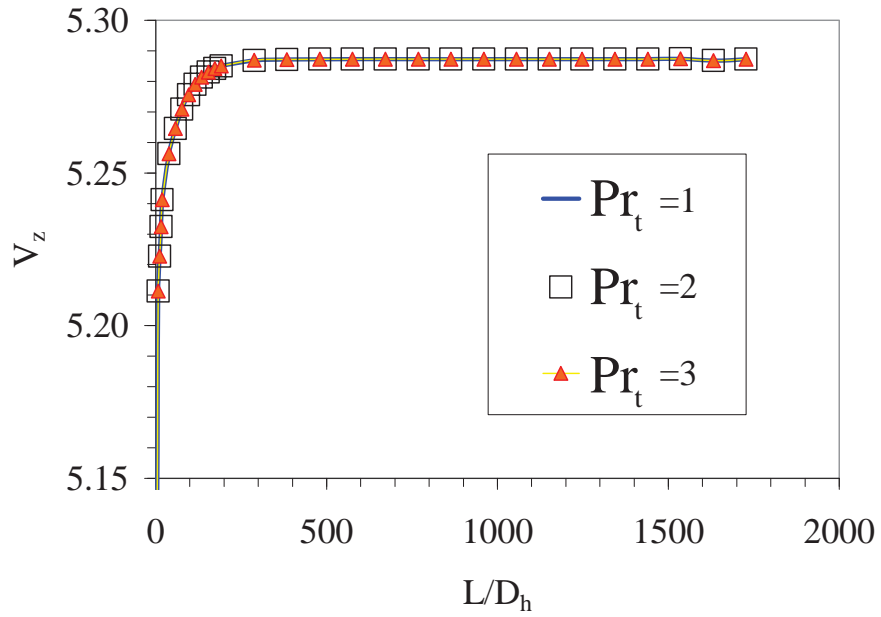


Fig. 4.5l Comparison axial velocity in 7-pin bundle as a function of turbulent Prandtl number at $Re = 0.842 \times 10^5$

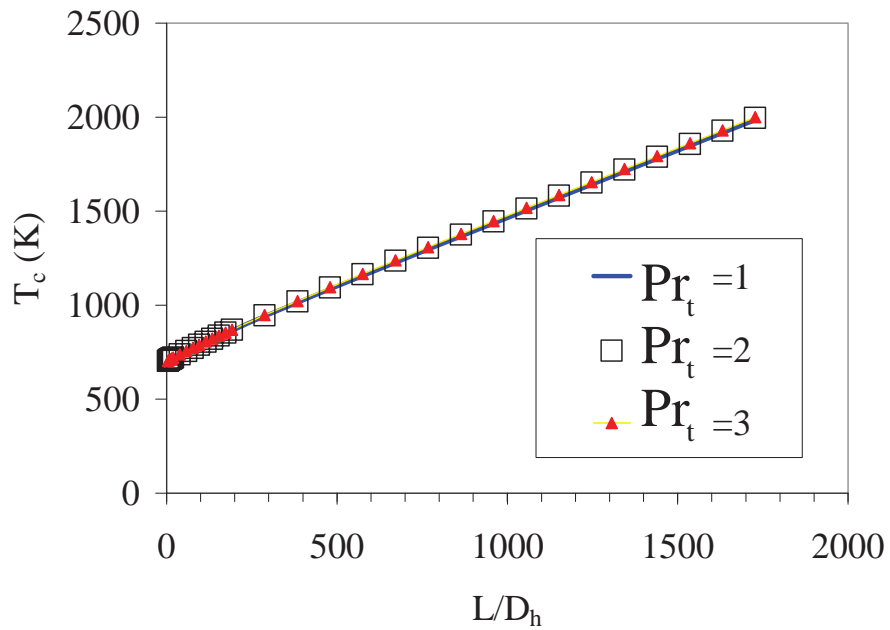


Fig. 4.5m Comparison average clad temperature in 7-pin bundle as a function of turbulent Prandtl number at $Re = 0.842 \times 10^5$

In addition to the global Nusselt number, friction factor, axial velocity and clad temperature are depicted in Fig. 4k, Fig. 4l and Fig. 4m respectively for different discretization schemes. The entrance region characteristics are nearly identical with all these parameters. As a consequence of this, the thermal development length is short for low

turbulent Prandtl numbers. As already indicated in Sectoin-3, a Pr_t value of 0.85 is used in the present studies.

4.2 RESULTS AND DISCUSSION

4.2.1 Effect of Number of Fuel Pins

As already indicated, experiments have been carried out by previous researchers with different number of heat generating pins in the range of 7 to 31 having different pin diameters and pitch to diameter ratios. Hence, in the present study it is decided to vary the number of pins in the bundle from 1 to 217. The different pin bundle configurations studied are depicted in Figs. 4.6a-4.6e. The grids are identical in all the computations.

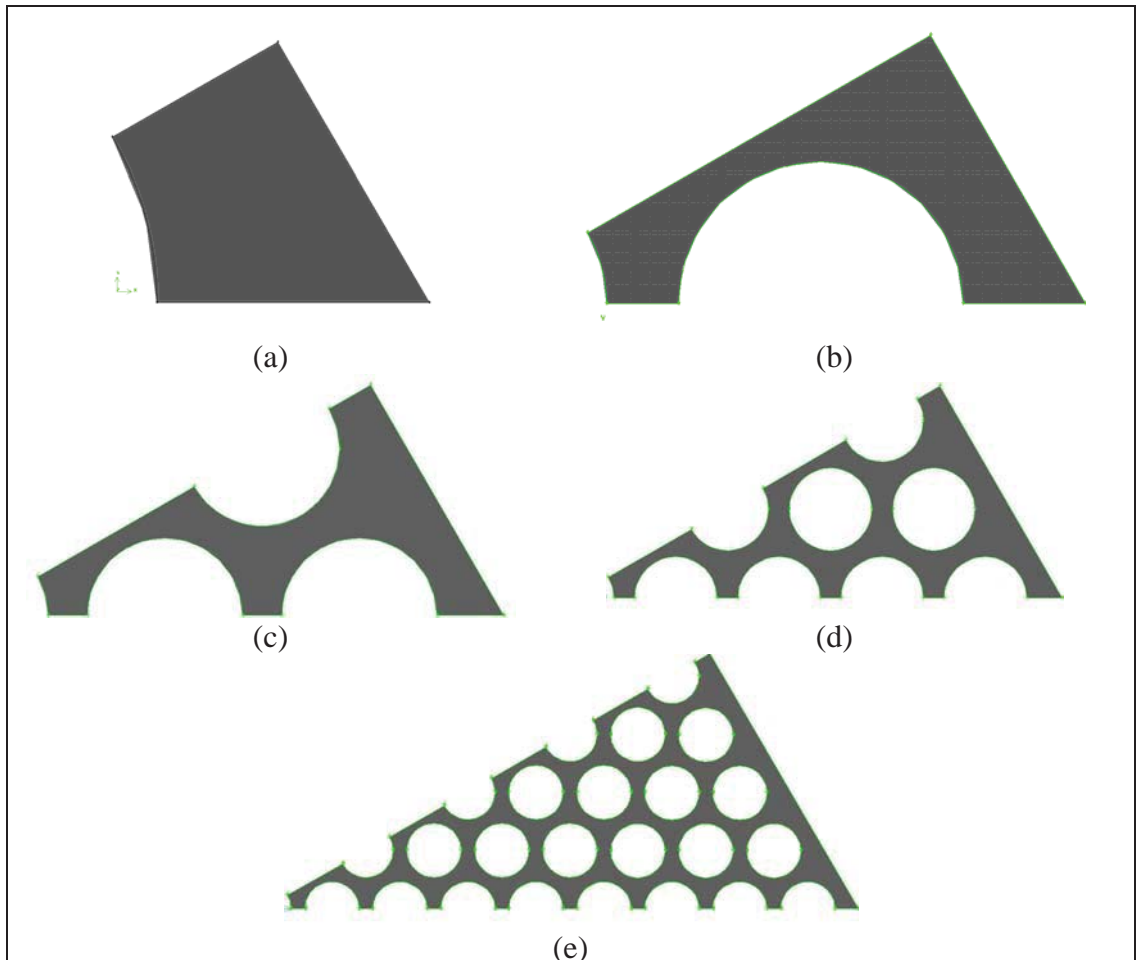


Fig. 4.6 Pin bundle configurations considered for the study: (a). 1-pin, (b). 7-pin, (c).19-pin, (d). 61-pin, (e) 217-pin

The hydraulic diameter, (D_h) values for the configurations with 1, 7, 19, 61 and 217-pin bundles are 4.18, 5.21, 5.21, 5.12 and 5.02 mm respectively. These values are very close to one another. The Reynolds number (0.842×10^5), the minimum gap between the outermost pin and hexcan wall (2.1 mm) are kept constant for all these cases. The corresponding inlet velocities are respectively 6.425, 5.159, 5.16, 5.249 and 5.353 m/s for 1, 7, 19, 61 and 217-pin bundles. For identical domain length, the non-dimensional length (L/D_h or Z/D_h) is more if the hydraulic diameter is less. In these cases, the y^+ value is found to be within 30-100.

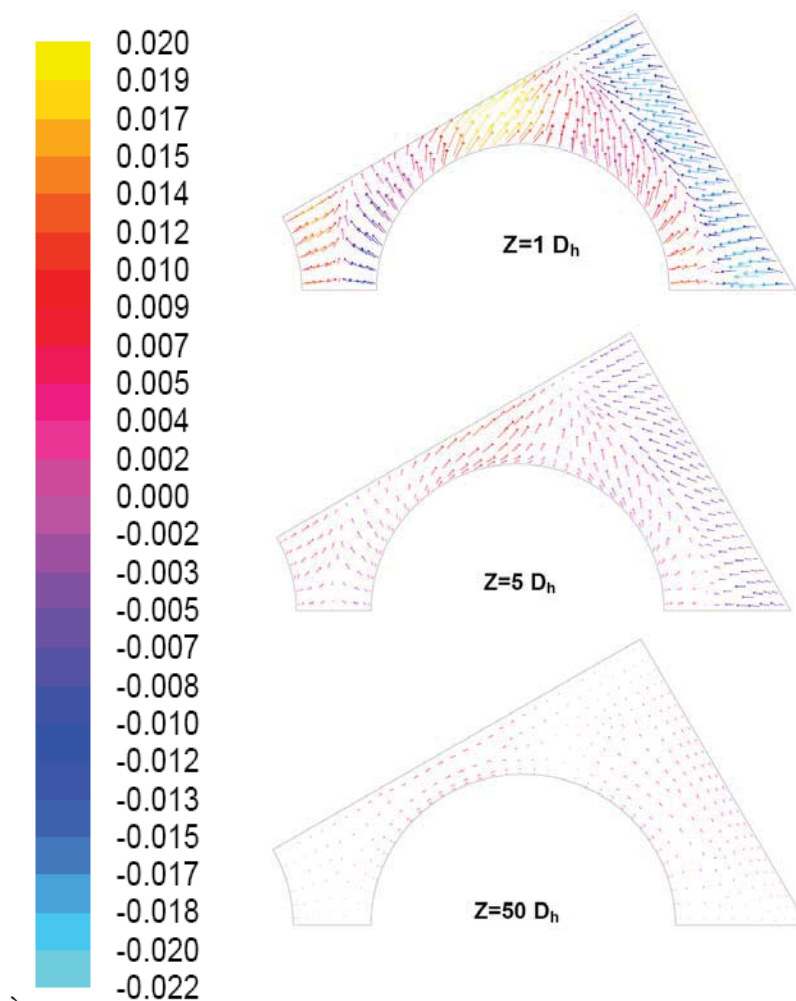


Fig. 4.7 Cross-stream velocity (m/s) in 7-pin bundle with 6.6 mm pin diameter

Development of cross-stream velocity at various axial locations, viz., $Z = D_h$, $5 \times D_h$, and $50 \times D_h$ are depicted in Fig. 4.7, for the 7-pin bare bundle configuration. It is seen that the

flow is diverted away from the boundary layers that grow along the fuel pins and hexcan wall, towards the peripheral sub-channels. This will result in the by-passing of coolant flow towards the peripheral region, away from the central portion of the subassembly, especially in the region close to the entrance. However, the strength of the secondary flow decreases along the flow direction and the cross-stream velocity decreases to nearly zero at $Z \approx 50 \times D_h$.

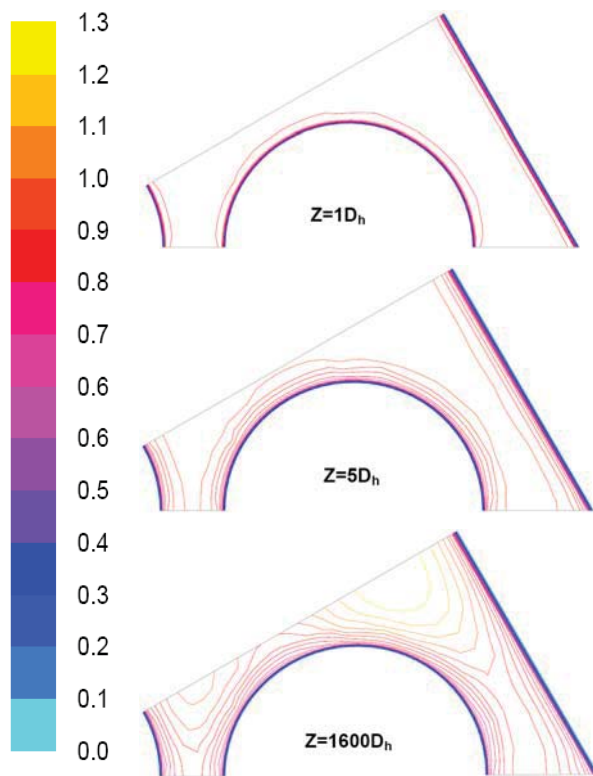


Fig. 4.8 Non-dimensional axial velocity (u_z/u_{z-in}) in 7-pin bundle with 6.6 mm pin diameter

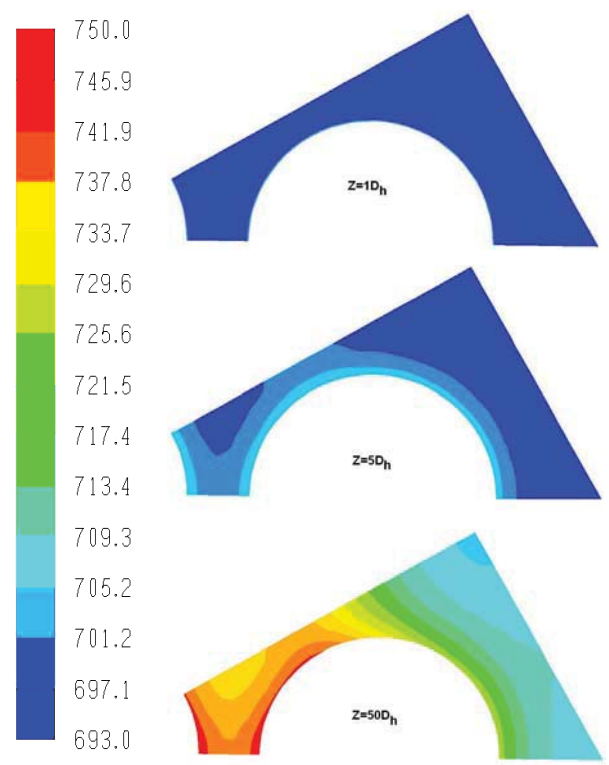


Fig. 4.9 Temperature contours (K) in 7-pin bundle with pin diameter 6.6 mm

The distribution of axial velocity at three different cross sections is depicted in Fig. 4.8. It is evident that the velocity is more uniform close to the entrance and non-uniformity sets in as the flow develops. Development of temperature along the flow direction is depicted in Fig. 4.9 for the same case. It is seen that the temperature gradient adjacent to the fuel pins decreases along the flow direction. Further, the temperature gradient is less in the narrow gap region between two pins and cold spots in sodium are observed at the corners, as expected.

Evolution of friction factor determined from Eq. (3.18) is depicted in Fig. 4.10 for all the pin bundle configurations. It is evident that the flow is hydrodynamically almost fully developed at $L = 30 \times D_h$ for bare bundle configurations. We know that the flow development length for turbulent flow in a duct is given by $L / D_h = 1.359 \times Re^{1/4}$ (Cengel, 2007). For the present Reynolds number of 0.842×10^5 , the value of hydrodynamic entrance length is $23.14 \times D_h$ and it compares very well with this estimate. The friction factor is large at the entrance due to smaller thickness of the boundary layer. As the boundary layer grows along the flow direction, the velocity gradient and the friction factor decrease as expected. It is clear that the fully developed friction factor value increases with number of pins.

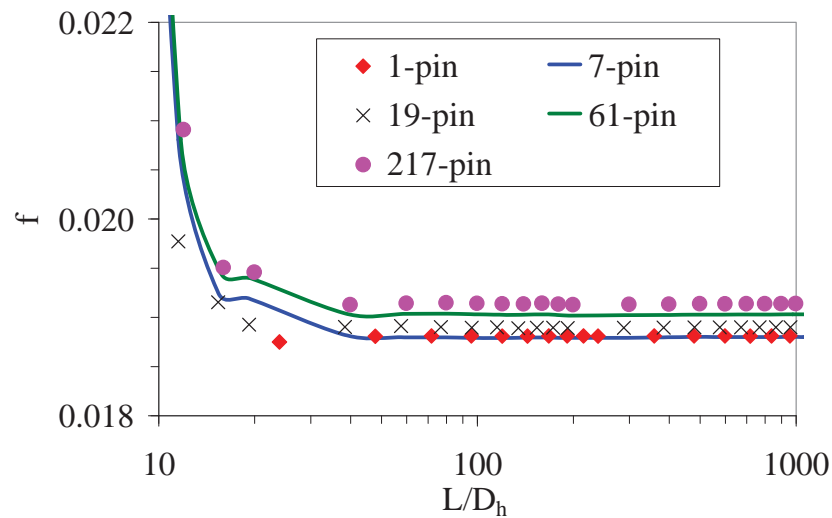


Fig. 4.10 Flow development in pin bundle with different number of pins at $Re = 0.842 \times 10^5$

The constant heat flux boundary condition is implemented on the outer surface of the pins adopting the law-of-the-wall for temperature derived using the analogy between heat and momentum transfers (Launder and Spalding, 1974). The predicted axial variation of global Nusselt number defined by Eq. (3.24) is depicted in Fig. 4.11. It is seen that the Nusselt number decreases gradually from the entrance and it attains the fully developed value at $L/D_h = 50$ for single pin bundle. The fully developed Nu_G value is 8.8 and this is only 50% of the

single sub-channel data. This is because the flow maldistribution between sub-channels is high in the later case. This occurs due to the presence of adiabatic outer hexcan wall which is not present in the single sub-channel case. Development of global Nusselt number for 7-pin bare bundle indicates that thermal development is completed only at around $800 \times D_h$. For the 61 and 217-pin bare bundles, thermal development could not be achieved even at $2000 \times D_h$. In flow through pin bundles, when the number of pins increases the Nusselt number in the outer row is reduces and even goes to negative value. This is because a major flow is diverted towards the outer sub-channels. This is the reason for the lower global Nusselt number when the number of pins is high. It appears that the Nu number for the case of 217-pins will become lower than that of 61-pins on full development. This is evident from the slope of these two curves at $L/D_h = 2000$. The Nusselt number for large bundles can be even lower than the fully developed laminar Nu number for circular pipes, viz. 4.3.

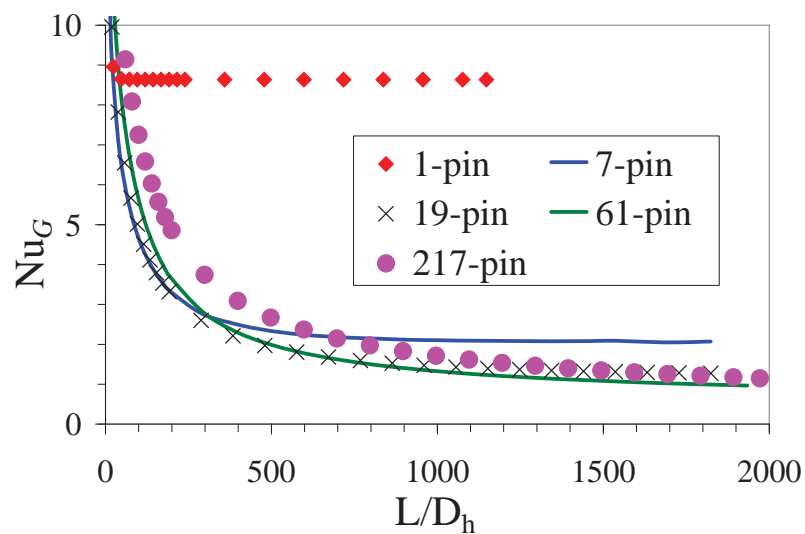


Fig. 4.11 Variation of overall Nusselt number in pin bundle with different number of fuel pins at $Re = 0.842 \times 10^5$

Evolution of average pin Nusselt number (Nu_c) for individual pins defined by Eq. (3.23) is depicted in Fig. 4.12a for the 7-pin bare bundle case. It is seen that Nu_c for the central pin is higher than that of the peripheral pin by a factor of ~ 1.6 . Further, it is seen that

the development is faster for the peripheral pin than that for the central pins. Compared to the fully developed Nusselt number for single sub-channel (17.46), the global Nusselt number for 7-pin bundle configuration is much lower (~ 2). This indicates that the global Nusselt number determined from experimental studies on bundle configuration with small number of pins can give vastly different results from that measured in bundle configuration with large number of pins. The vastly different global Nusselt number for 7-pin and single pin bundles can be attributed to flow by-pass in the peripheral sub-channels.

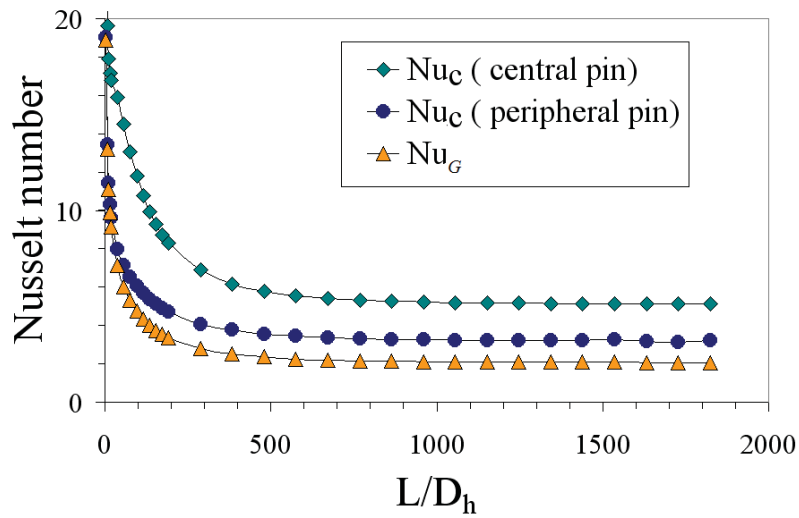


Fig. 4.12a Comparison of global and average pin Nusselt numbers in 7-pin bundle configuration at $Re = 0.842 \times 10^5$

It is of interest to understand the temperature development in pin bundles having large number of pins. Towards this, a 217-pin bundle configuration has been considered for the investigations. The development of flow weighted global sodium temperature is depicted in Fig. 4.12b. Also shown in the same figure is the development of flow weighted sub-channel sodium temperature around the central pin and that around the peripheral pin (pin number 25 in Fig. 4.1). It is seen that there is significant difference between the global, central and peripheral sub-channel sodium temperatures. In fact the peripheral clad temperature (also shown in Fig. 4.12b) is lower than the global sodium temperature. Hence, it is difficult to

define the average pin Nusselt number (Nu_c) for the peripheral pins based on global fluid temperature. This indicates that the peripheral sub-channel and central sub-channel are nearly isolated. Sodium temperatures in these channels are dictated by the corresponding sodium flow rates and heat fluxes. Any heat exchange between them is only by molecular conduction and turbulent exchange. The slopes of these sodium temperature profiles are vastly different and there is no sign of them becoming parallel even after $1000 \times D_h$. However, one would expect that the slope of the central pin sodium temperature profile to reduce and that of the peripheral pin sodium to increase, when the temperature difference between these two pins grows to a large value.

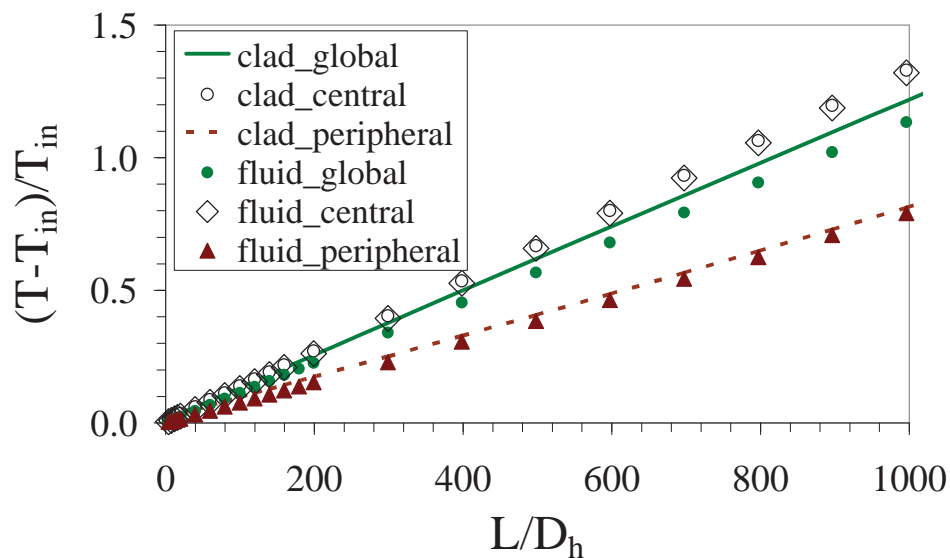


Fig. 4.12b Evolution of temperature during flow of sodium in a 217-pin bundle assembly at $Re = 0.842 \times 10^5$

It is evident from the above discussion that temperature development will be delayed if the number of pins is more. This is expected since the flow redistribution and subsequent inter-channel conduction / turbulent exchange requires longer length if the number of sub-channels is more. Thus, the development length is a strong function of the number of rows, the hexcan dimension as well as the resistance for the sub-channel flows.

4.2.2 Effect of Gap between Peripheral Pin and Hexcan

It was seen in the earlier section that sodium is transported towards the peripheral sub-channels as the flow develops. This phenomenon, known as ‘flow by-pass’, is a strong function of the gap between the peripheral pins and the hexcan. This gap is referred as the ligament gap. Thus, the ligament gap is surmised to influence flow and temperature field developments in the fuel pin bundles. Towards understanding the effect of ligament gap, detailed parametric studies were undertaken. Three ligament gaps namely 1.43 mm (half ligament), 2.85 mm (nominal ligament), and 5.7 mm (double ligament) have been considered for the 7-pin and 217-pin bundle configurations.

4.2.2.1 7-Pin Bundle

In the case of 7-pin bundle, the value of D_h is seen to be a very strong function of ligament gap and these values are 3.59, 5.21 and 8.63 mm respectively for half ligament, nominal ligament and double ligament. The corresponding Re values are 0.76×10^5 , 1.10×10^5 , and 1.84×10^5 respectively. It may be reiterated that in all these simulations sodium entry velocity to the pin bundle configuration is 6.8 m/s. Development of global Nusselt number for the three ligament cases is depicted in Fig. 4.13. It is evident from Fig. 4.13 that the Nu_G value is more if ligament gap is less. This is due to the fact that flow by-pass (through the peripheral pins and hexcan) is constrained by reducing the ligament. It is also clear that the ratio of Nusselt number between half ligament and double ligament is ≈ 3.5 . This is much different from the hydraulic diameter ratio, viz., $8.63/3.59 = 2.4$. Thus, it can be concluded that the heat transfer coefficient is higher in the half ligament case, because the flow by-pass is reduced. It can be seen from Fig. 4.13 that the percentage reduction in Nusselt number reduces when ligament gap increases, suggesting that the fully developed Nusselt number might stabilize for larger ligament gap values.

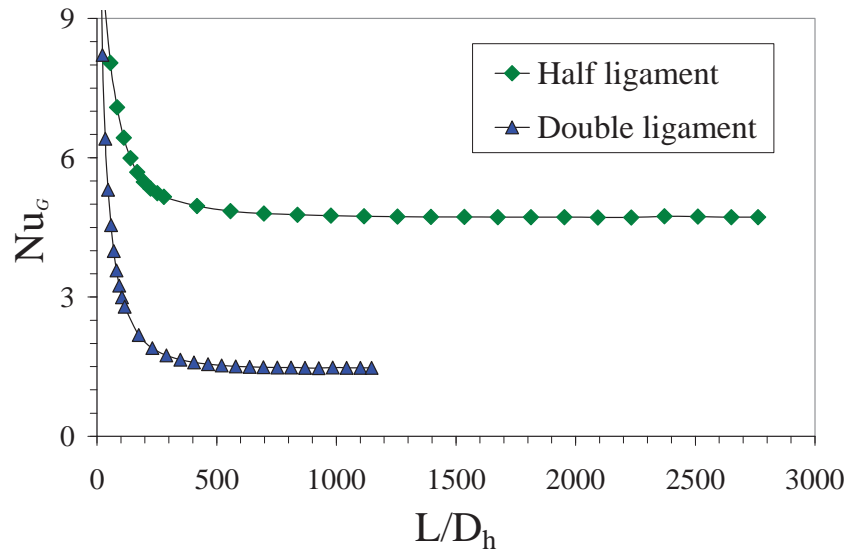


Fig. 4.13 Global Nusselt number in 7-pin bundle: Effect of ligament gap

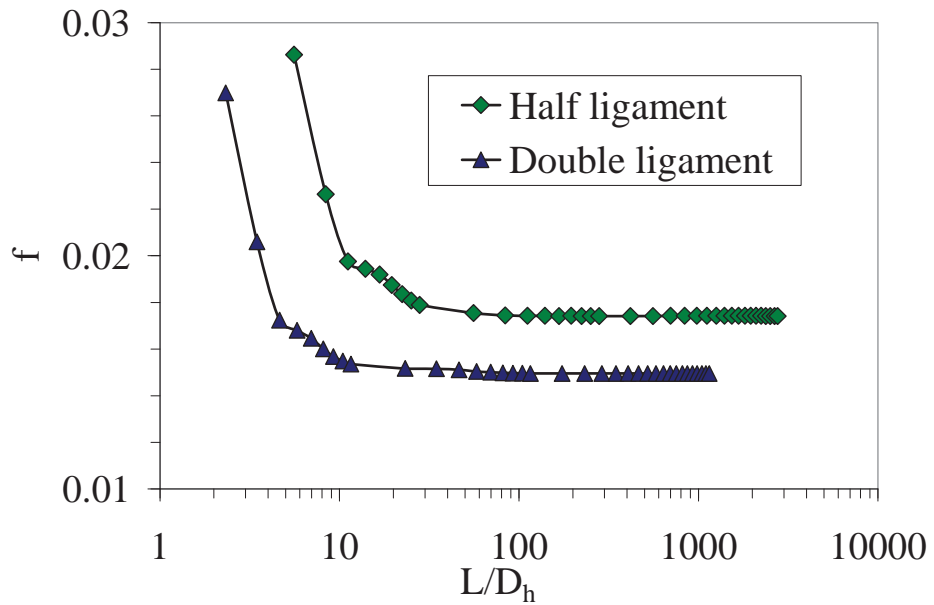


Fig. 4.14a Flow development in 7-pin bundle : Effect of ligament gap

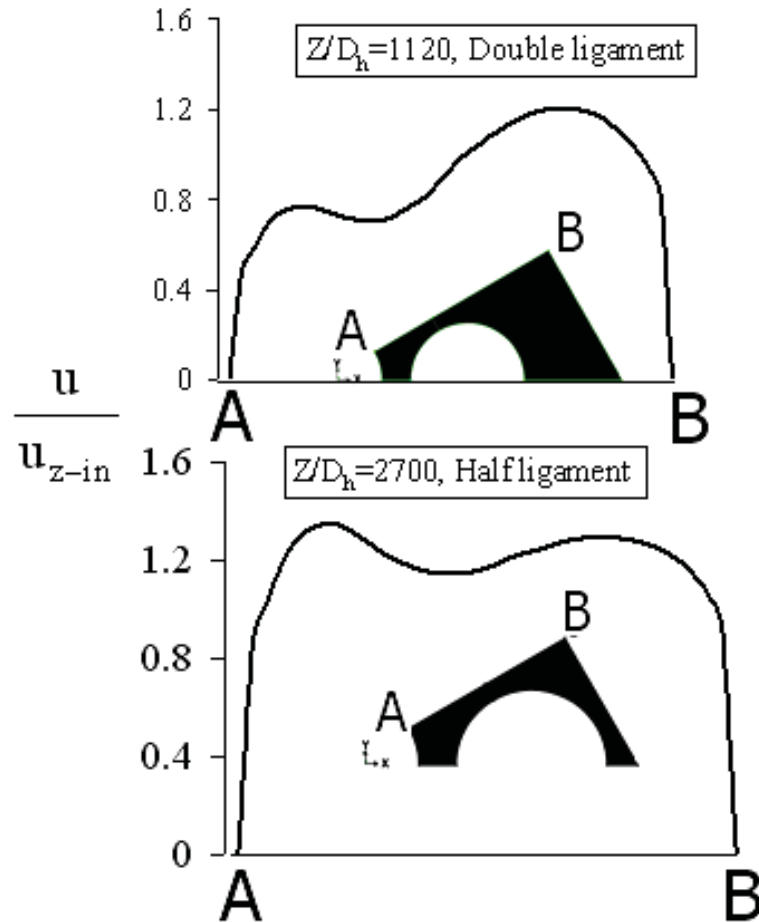


Fig. 4.14b Dimensionless velocity distribution in 7-pin bundle for different ligament gaps at fully developed region

The development of friction factor for different ligament gaps in 7-pin bundle configuration is depicted in Fig. 4.14a. It is clear that flow development is nearly complete within $L/D_h \sim 80$ for half ligament bundle and $L/D_h \sim 100$ for double ligament bundle, which is much less than the Nusselt number development length for both the cases. Friction factor in the case of half ligament is 14% higher than that of double ligament, due to reduction in flow area. Thus, the penalty in friction factor is much smaller than the augmentation in Nusselt number. Fully developed non-dimensional axial velocity distribution in 7-pin bundle for half and double ligament cases is depicted in Fig. 4.14b along the symmetry plane A-B. It is evident from the figure that velocity is higher in the peripheral channel compared to that in the central channel, in the case of double ligament. This means that the flow is moving towards

the periphery from the central channel in the larger ligament case. The lower flow resistance in the peripheral channel causes such flow diversion, as discussed earlier. The reverse is true in the low ligament case.

4.2.2.2 217-Pin Bundle

The values of D_h for the three ligament cases studied in 217-pin bundle are 4.60, 5.02 and 5.88 mm and the corresponding Re values are 0.98×10^5 , 1.07×10^5 , and 1.25×10^5 respectively. The global Nu number development for all the three ligament gaps is depicted in Fig. 4.15a. Contrary to that observed in 7-pin bundle, temperature is under-developed for all the cases studied. However, smaller the ligament, higher is the Nusselt number due to smaller by-pass. The pin-wise variation of average pin Nusselt number (Nu_{C-SC}) is depicted in Fig. 4.15b.

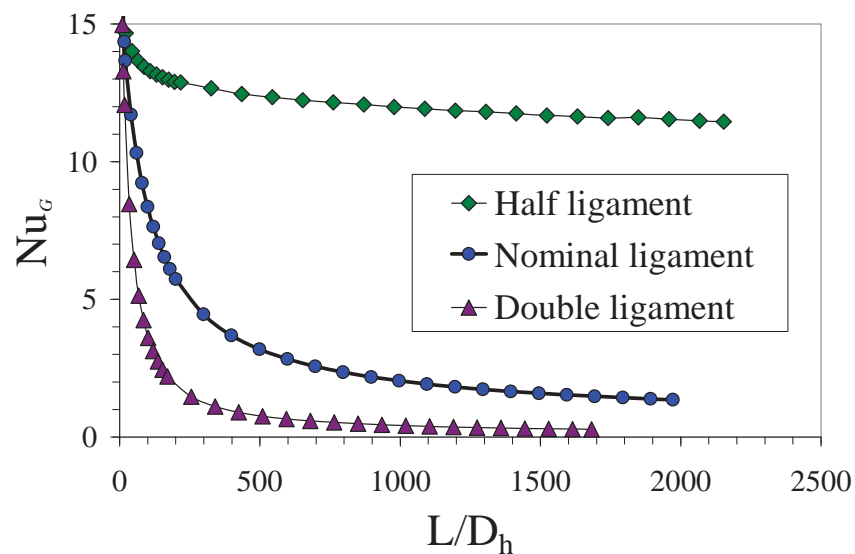


Fig. 4.15a Global Nusselt number in 217-pin bundle : Effect of ligament gap

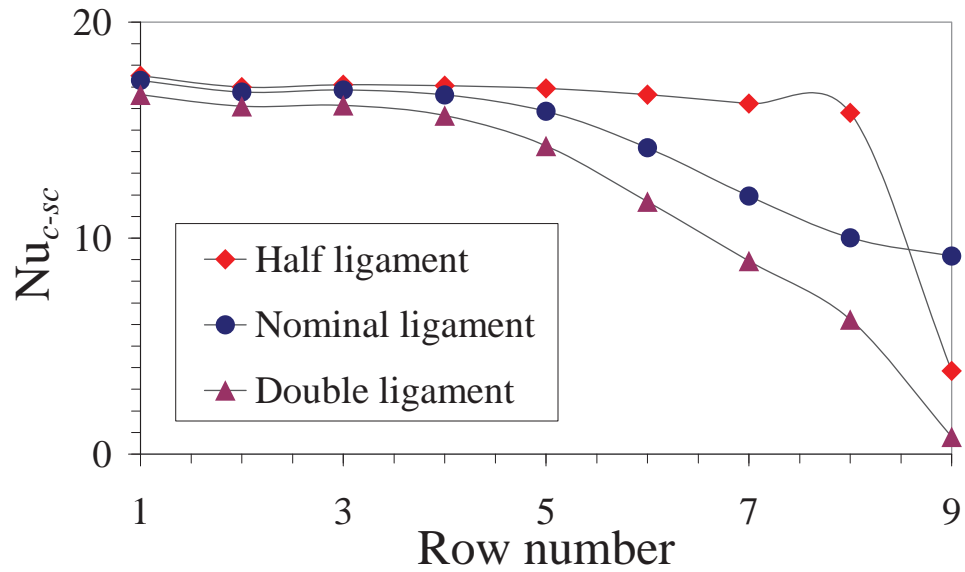


Fig. 4.15b Average pin Nusselt number in 217-pin bundle ($L/D_h = 1972$)

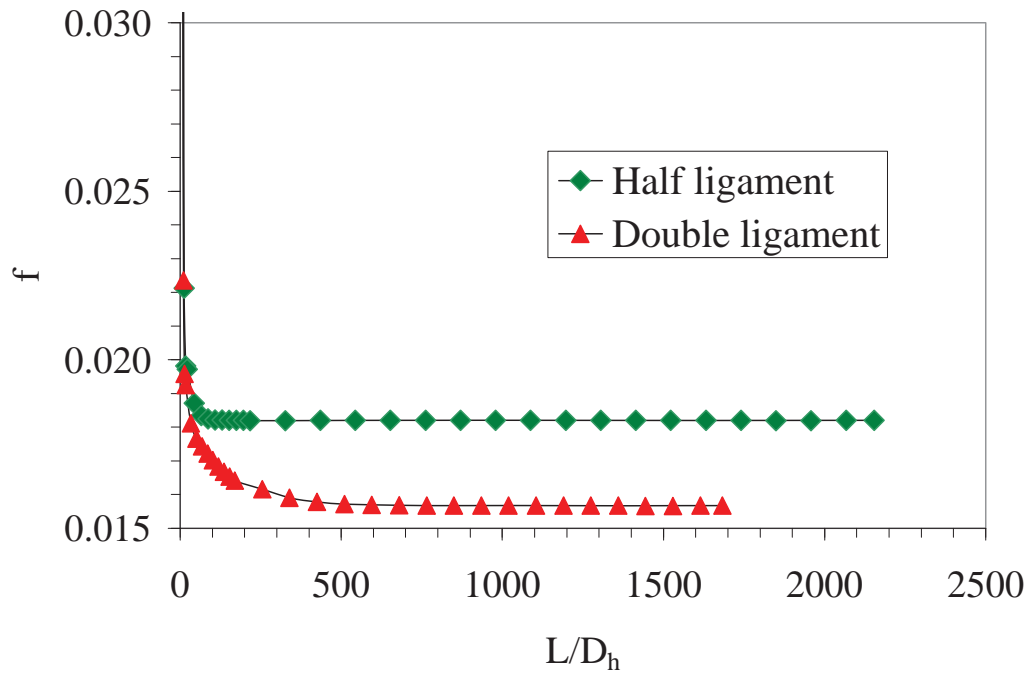


Fig. 4.15c Development of friction factor in 217-pin bundle : Effect of ligament gap

It is clear that if the ligament is wider, the variation in heat transfer coefficient is larger. In other words, the effect of ligament gap on heat transfer coefficient percolates deeper inside the bundle from periphery. But in narrow ligaments, the heat transfer coefficient is nearly uniform for all the interior pins. It is low only for the peripheral pins. This brings out

the strong effect of ligament gap on heat transfer coefficient. The friction factor development in 217 pin bundle (Fig. 4.15c) indicates that ligament gap pronounced effect even in large bundles.

4.2.3 Effect of Pin Diameter

4.2.3.1 7-Pin Bundle

It is shown that inter-channel cross flow resistance depends strongly on the ratio of the pitch to diameter. The larger the 'pitch to diameter' value, the lower is the cross flow resistance. In order to understand the behavior of the flow and temperature developments, three pin diameters have been considered, maintaining the pitch at 8.28 mm. The pin diameters are 3.3, 4.45 and 6.6 mm and the corresponding hydraulic diameters are 12.1, 9.4 and 5.21 mm respectively. The Reynolds number is maintained constant 0.842×10^5 . The corresponding velocities are 2.22 m/s, 2.86 m/s and 5.159 m/s respectively for diameters of 3.3, 4.45 and 6.6 mm. The development of global Nu number for different pin diameters is depicted in Fig. 4.16. The development lengths for both 3.3 mm and 4.45 mm diameter pin bundle are $165 \times D_h$. For 6.6 mm diameter pin bundle it is $575 \times D_h$. It is seen that the development is quicker with smaller pin diameters due to low inter sub-channel cross flow resistance as already explained. Also, the fully developed Nu_G is larger if the diameter is smaller. The development of friction factor for various pin diameters in 7-pin bundle configuration is depicted in Fig. 4.17a. It is seen that flow development is nearly complete within $L/D_h = 125$ for all the diameters. The hydraulic development length is less if pin diameter is more.

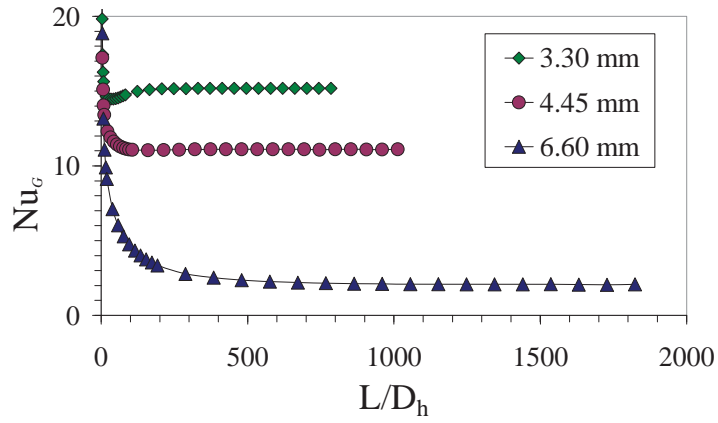


Fig. 4.16 Global Nusselt number in 7-pin bundle : Effect of pin diameter

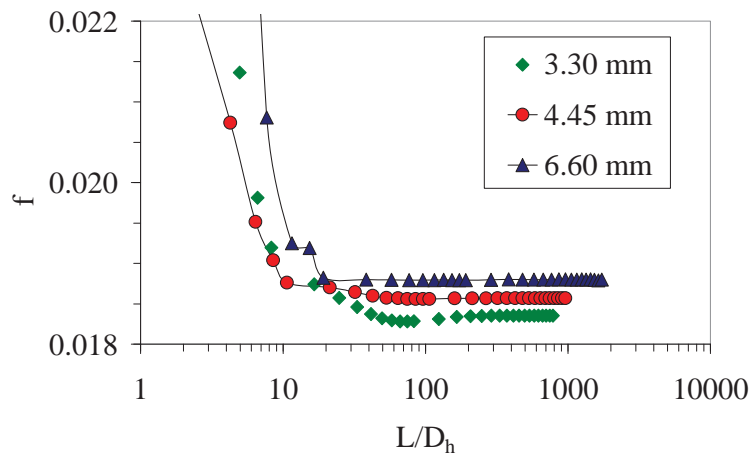


Fig. 4.17a Flow development in 7-pin bundle : Effect of pin diameter

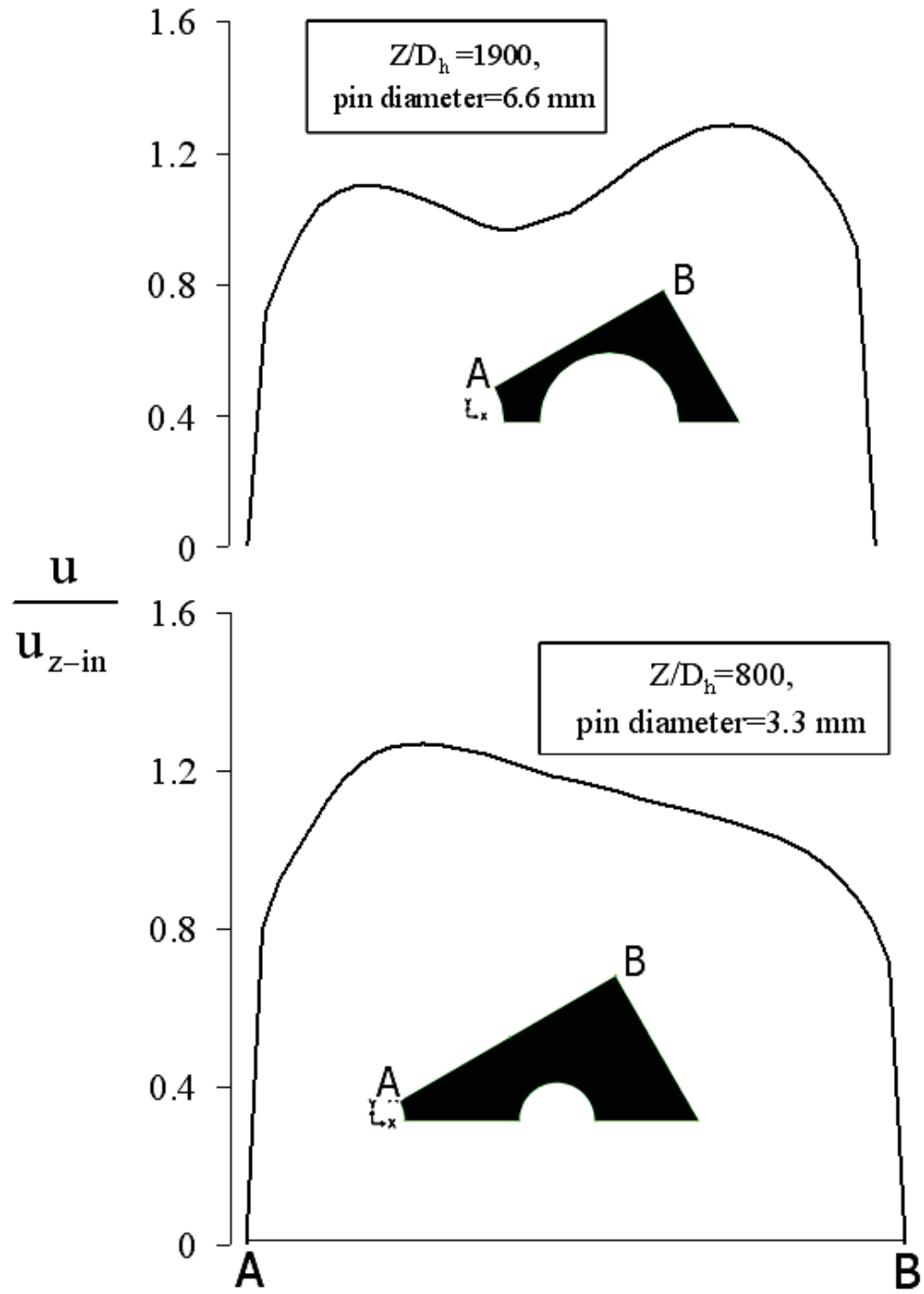


Fig. 4.17b Dimensionless velocity distribution in 7-pin bundle for different diameters at fully developed region

Fully developed non-dimensional axial velocity distribution in 7-pin bundle for 3.3 and 6.6 mm pin diameter configurations is depicted in Fig. 4.17b. It is observed that for 6.6

mm pin diameter configuration, the velocity is higher in the peripheral channel as compared to that in central channel indicating that the flow is moving towards the periphery from the central channel. This indicates that the flow by-pass effect is dominant in large pin diameter configuration. There is a fall in the velocity at a junction between two channels due to narrow gap between the pins. In the case of 3.3 mm the velocity in the central channel is higher compared to peripheral channel.

4.2.3.2 217-Pin Bundle

In order to understand the behavior of the flow and temperature development in 217-pin bundle, two pin diameters have been considered, maintaining the pitch at 8.28 mm. The pin diameters are 3.3 and 6.6 mm, leading to the hydraulic diameters of 19.03 and 5.02 mm respectively. The corresponding Reynolds numbers are 4.05×10^5 and 1.06×10^5 respectively. The global Nusselt number development for the two diameters is depicted in Fig. 4.18a. While the Nu_G attains full development with in $L/D_h \approx 50$ for 3.3 mm pin diameter, it is under-developed for 6.6 mm pin diameter even after $L/D_h = 1000$. But in the case of 7-pin configuration, complete development is realized for all pin diameters. Further, the variation in the fully developed Nu_G for 3.3 to 6.6 mm pin diameters is 20 to 2.8. The corresponding variation in the case of 217-pin bundle is 33 to 1.8. In the smaller pin diameter case, the Nusselt number is higher due to the larger value of Re number, as already explained. The development of friction factor for various ligaments in 217-pin bundle configuration is depicted in Fig. 4.18b. The flow development is achieved within about $120 \times D_h$.

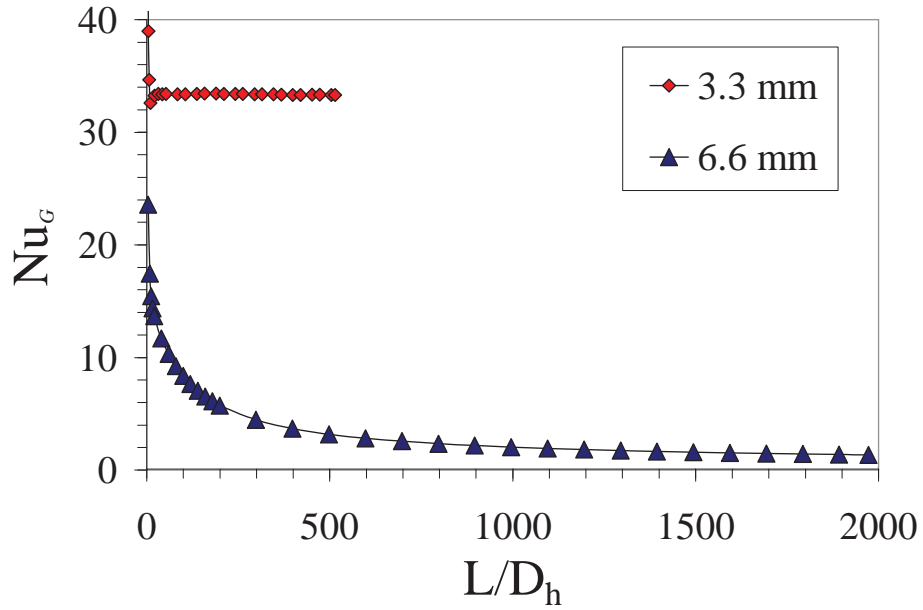


Fig. 4.18a Global Nusselt number in 217-pin bundle : Effect of pin diameter

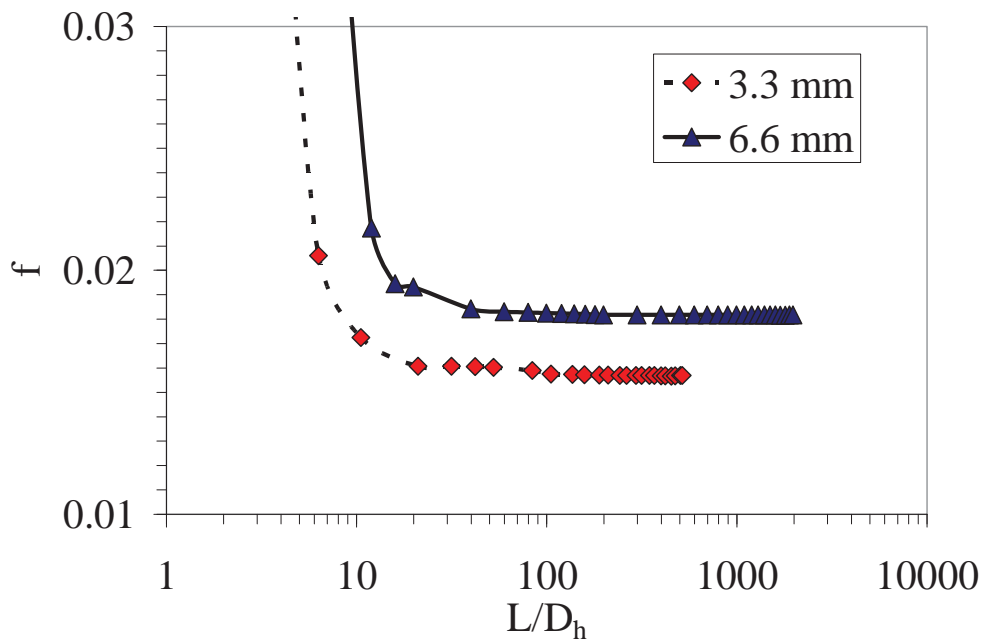


Fig. 4.18b Flow development in 217-pin bundle : Effect of pin diameter

4.2.4 Effect of Reynolds Number

In order to understand the effect of Reynolds number on flow and temperature development lengths in pin bundles, the 7-pin bundle configuration depicted in the Fig. 4.6b is considered.

For the present study four different Reynolds number are chosen, viz., $Re = 0.40 \times 10^5$.

0.84×10^5 , 1.10×10^5 and 1.4×10^5 . The development of friction factor is depicted in Fig. 4.19a and it is clear that the flow development length is short if Reynolds number is large. However, in all these cases the friction factor develops fully within $\sim 30 \times D_h$ and the fully developed friction factor decreases with increase in Reynolds number, as expected. The corresponding Nusselt number development is presented in Fig. 4.19b.

For all the Reynolds numbers studied, Nu_G develops fully within $\sim 1500 \times D_h$. Further, the thermal development length is long if Reynolds number is large, which is in agreement with that observed in the case of pipe flow (Cengel, 2007). Also, the fully developed Nusselt number value is high if Reynolds number is high. It appears that all the reported experimental results are for fully developed region only. Hence, the present results for entrance region could not be compared with any experiments.

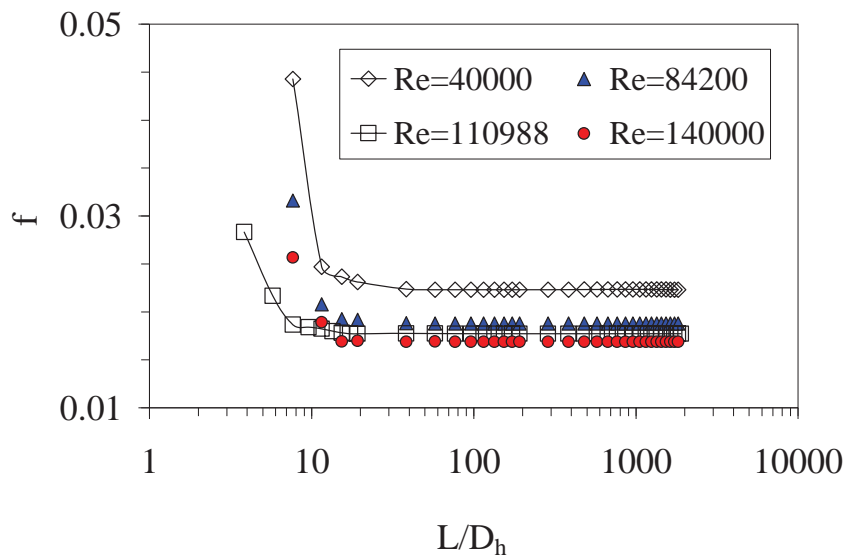


Fig. 4.19a Flow development in 7-pin bundle : Effect of Reynolds number

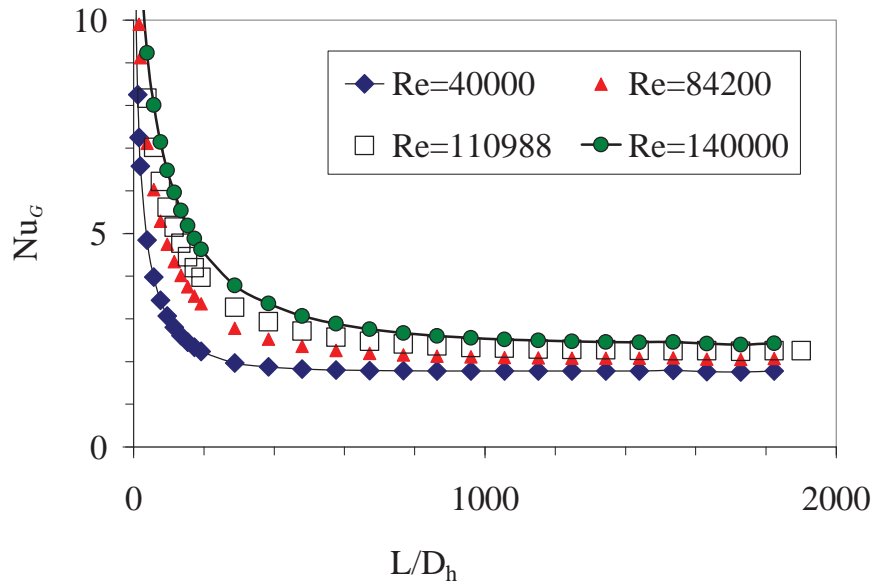


Fig. 4.19b Nusselt number development in 7-pin bundle : Effect of Reynolds number

Table 4.3 Summary of development lengths for various cases studied

Number of pins	Ligament gap	Pin diameter	Flow development length	Thermal development length
1	Actual	6.6	$\approx 30 \times D_h$	$50 \times D_h$
7	Actual	6.6	$\approx 30 \times D_h$	$750 \times D_h$
7	Half	6.6	$\approx 80 \times D_h$	$800 \times D_h$
7	Double	6.6	$\approx 100 \times D_h$	$690 \times D_h$
7	Actual	3.3	$\approx 30 \times D_h$	$165 \times D_h$
7	Actual	4.45	$< 125 \times D_h$	$213 \times D_h$
19	Actual	6.6	$\approx 30 \times D_h$	$> 2000 \times D_h$
61	Actual	6.6	$\approx 30 \times D_h$	$> 2000 \times D_h$
217	Actual	6.6	$\approx 30 \times D_h$	$> 2000 \times D_h$
217	Half	6.6	$\approx 65 \times D_h$	$> 2000 \times D_h$
217	Double	6.6	$\approx 255 \times D_h$	$> 2000 \times D_h$
217	Actual	3.3	$\approx 105 \times D_h$	$\approx 50 \times D_h$

4.3 CLOSURE

Sodium flow and temperature developments in the entrance region of heat generating pin bundles have been studied. The parameters investigated include pin diameter, number of pins, ligament gap and Reynolds number. The flow development is achieved within an axial length of ~ 125 hydraulic diameters. For large pin diameters with more pins, temperature development could not be achieved even after a length of 1000 hydraulic diameters. The clad temperature in the peripheral pins is lower than the cross section bulk fluid temperature. The pin Nusselt number decreases from centre to periphery. For narrow ligament gap, the Nusselt number is large and uniform.

CHAPTER - 5

LAMINAR FLOW AND THERMAL DEVELOPMENT IN HELICAL WIRE-WRAPPED PIN BUNDLES

5.0 INTRODUCTION

As already explained in Chapter-2, most of the earlier studies reported for pin bundles are either for fully developed flows or for only one helical wire pitch. The entrance region behaviour in a pin bundle with helical wires is not reported. In the present chapter pin bundle with multiple helical pitch length is considered and flow in the entrance region is examined critically. Further, detailed parametric studies are carried out for various values of helical pitch, pitch to diameter ratio and Reynolds number.

5.1 SOLUTION METHODOLOGY

5.1.1 Grid Sensitivity Study

Structured grid generation for pin bundles wrapped with helical wires is a challenging task. While generation of unstructured mesh employing tetrahedral cells is relatively easy, the number of cells required is very high. It was found that about 1.32 to 3.28 million grids are required to simulate one helical pitch length of 7-pin bundle (Sreenivasulu and Prasad, 2011). This leads to a large demand on computer memory and also limits the pin bundle lengths that can be simulated. So, the usage of unstructured tetrahedral mesh is not a suitable option for the pin bundle with multiple helical pitches. To overcome this problem, a customised grid generator, GridZ (CFDExpert, 2009) is utilized for generation of structured mesh. At first, a pin bundle with 7-pins is considered for finalising the grid. The diameter of fuel pin, spacer wire and triangular pitch are taken as 6.6 mm, 1.65 mm and 8.28 mm respectively. The length of helical pitch is 200 mm. The Reynolds number and hydraulic diameter are 840 and 3.952 mm respectively. The axial velocity at bundle entry for $Re = 840$ is 0.068 m/s.

Grid independency test is carried out in two ways: (i) by varying the number of grids in radial direction, and (ii) by varying the axial grid. Two different cross-stream mesh densities, viz., 1.181 and 4.233 millions are considered for the same axial grid size by changing the number of divisions around fuel pin and the wire. The number of divisions around the circumference of fuel pin is 36 and 72 respectively as depicted in Fig. 5.1a and Fig. 5.1b. Mesh division in axial direction of fuel pin and wire is shown in Fig. 5.1c.

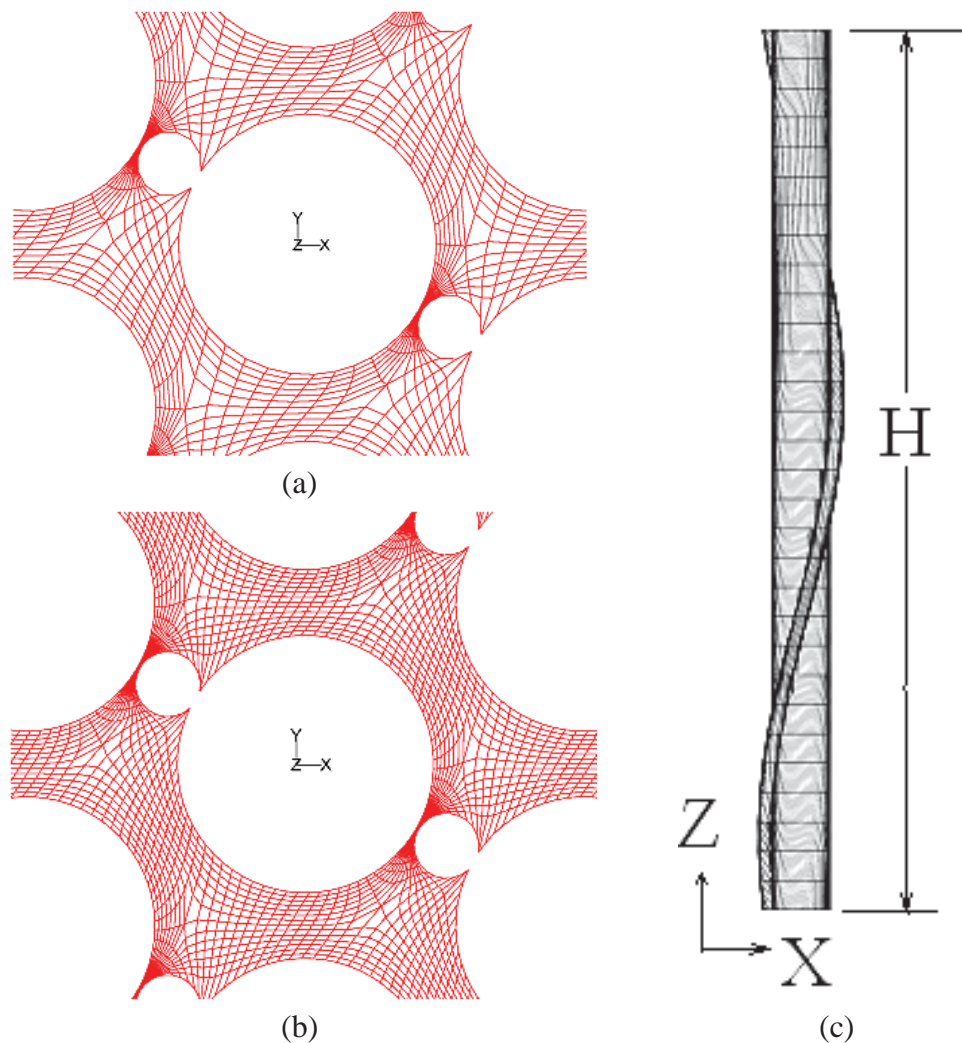


Fig. 5.1 Cross-stream grid distribution (a) 36 divisions around fuel pin (b) 72 divisions around fuel pin (c) Mesh division on fuel pin surface and helical wire surface

The values of global Nusselt number and friction factor at various L/D_h locations in two grid patterns are compared in Table-5.1. The maximum deviation found in Nusselt number is within -3.4% and that in friction factor is within +1.8% between two successive

grid results. Hence, further refinement was considered not essential. Also, due to limitations in computational capability, additional refinement could not be attempted.

Table 5.1 Comparison of global Nusselt number and friction factor for two different radial grids

L/D _h	<i>Nu_G</i>			<i>f</i>		
	72-grids	36-grids	% deviation	72-grids	36-grids	% deviation
7.6	1.523	1.575	-3.4	0.1259	0.1240	1.5
75.9	1.009	1.020	-1.1	0.1133	0.1130	0.3
227.7	1.017	1.023	-0.5	0.1151	0.1130	1.8

After finalizing cross-stream grids, four different axial grids have been considered, with axial grid sizes varying from 6.66 mm to 0.5 mm. The computed global Nusselt number and friction factor values employing various axial grid sizes are presented in Table-5.2a and Table-5.2b respectively. The comparative percentage variation is provided in bracket. It is seen that the grid with 0.5 mm gives an essentially grid independent result.

Table 5.2a Comparison of Nusselt number for four different axial grid sizes

L/D _h	<i>Nu_G</i>			
	6.66mm	4.16mm	2.22mm	0.5mm
10.1	1.410	1.359 (3.8%)	1.350 (0.7%)	1.325 (1.9%)
25.3	1.114	1.092 (2%)	1.073 (1.8%)	1.053 (1.8%)
75.9	1.043	1.027 (1.8%)	1.009 (1.8%)	0.991(1.8%)

Table 5.2b Comparison of friction factor for four different axial grid sizes

L/D _h	<i>f</i>			
	6.66mm	4.16mm	2.22mm	0.5mm
10.1	0.076	0.093 (18%)	0.101 (7%)	0.114 (10%)
25.3	0.084	0.100 (16%)	0.104 (4%)	0.114 (8%)
75.9	0.114	0.115 (0.9%)	0.115 (0%)	0.116 (1%)

Based on various radial and axial grid simulations, the mesh with 72 radial grids around fuel pins and .0.5 mm axial grid size is chosen for further studies. Various seven pin bundle configurations considered (different pin diameters) are presented in the Fig. 5.2.

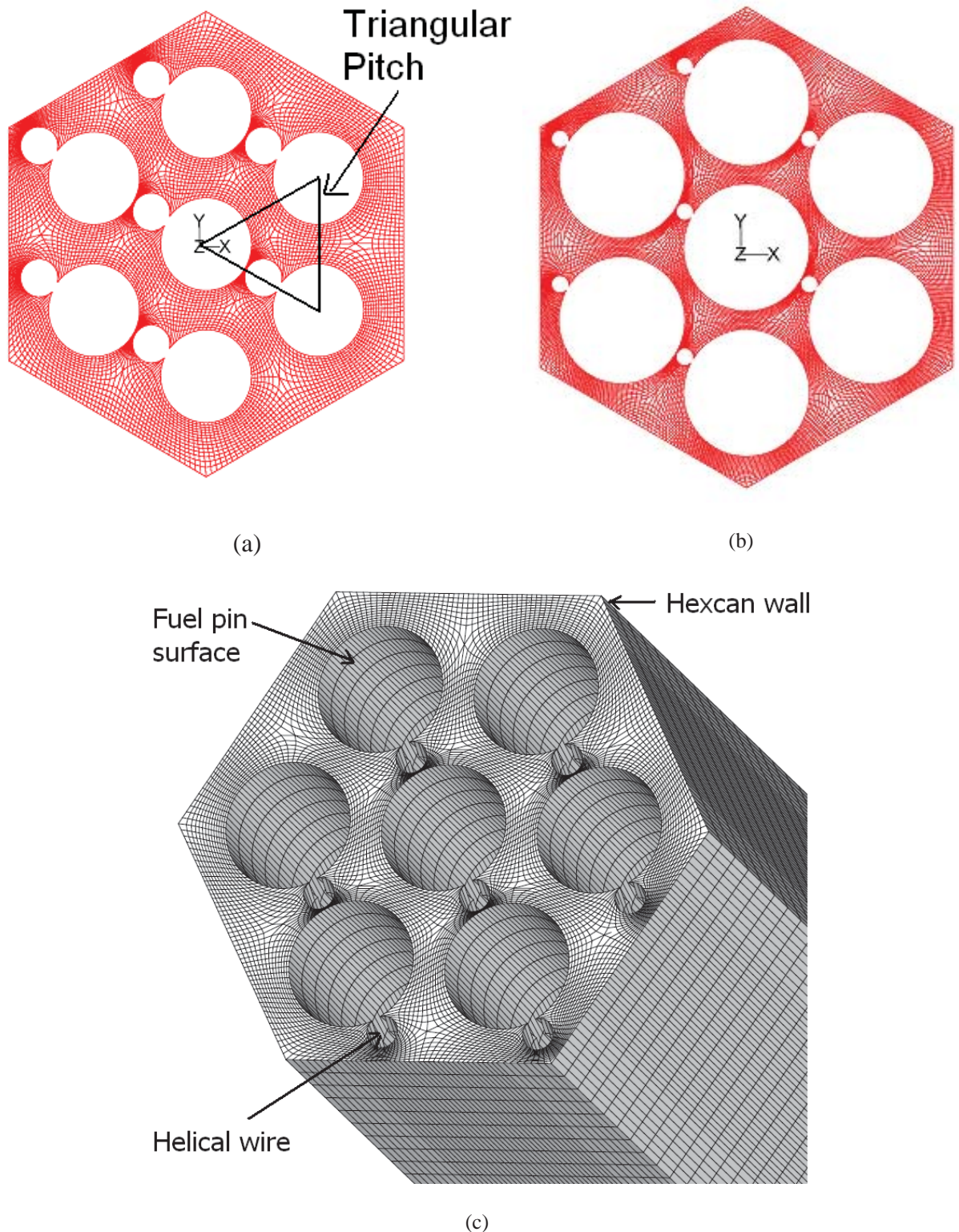


Fig. 5.2 Cross-stream grids considered for 7-pin bundle configurations considered in the present study with (a) $P_t/D_r = 1.42$, (b) $P_t/D_r = 1.14$ and (c) Isometric view of grid generated for the 7-pin bundle with $P_t/D_r = 1.25$

5.1.2 Validation of Sodium Flow through Straight and Helical Pipes

Before analyzing the pin bundle configuration a validation study with circular pipe flow has been undertaken. Liquid sodium is chosen as the fluid. The hydraulic diameter and boundary conditions considered are similar to those of fuel pin bundle, i.e., the diameter of pipe is 3.952 mm, Reynolds number is 840 and length of the pipe is 400 mm. Boundary layer mesh is adopted to capture near wall effects. The inlet temperature is taken to be 693 K and the heat flux applied on the pipe wall is 16 kW/m². The cross-stream mesh adopted is depicted in Fig. 5.3a.

The flow and temperature are allowed to develop simultaneously. The evolution of cross-section averaged cross-stream velocity calculated from Eq. (3.17) is depicted in Fig. 5.3b. From a zero value at the entrance, it increases to a peak value due to the growth of boundary layer and ejection of mass out of boundary layer. Following this, it decreases along the flow direction to attain a zero value in the fully developed region at $\sim 90 \times D_h$. The fully developed friction factor (f) is found to be 0.0767 and it matches well with the friction factor correlation ($f = 64 / Re$) within -0.7%. An exploded view of developing velocity field over a small axial length and the developing temperature field in the entire tube length are depicted in Figs. 5.3c and 5.3d respectively. The retardation of velocity around the pipe wall and increase velocity around the centre-line are well predicted by the code.

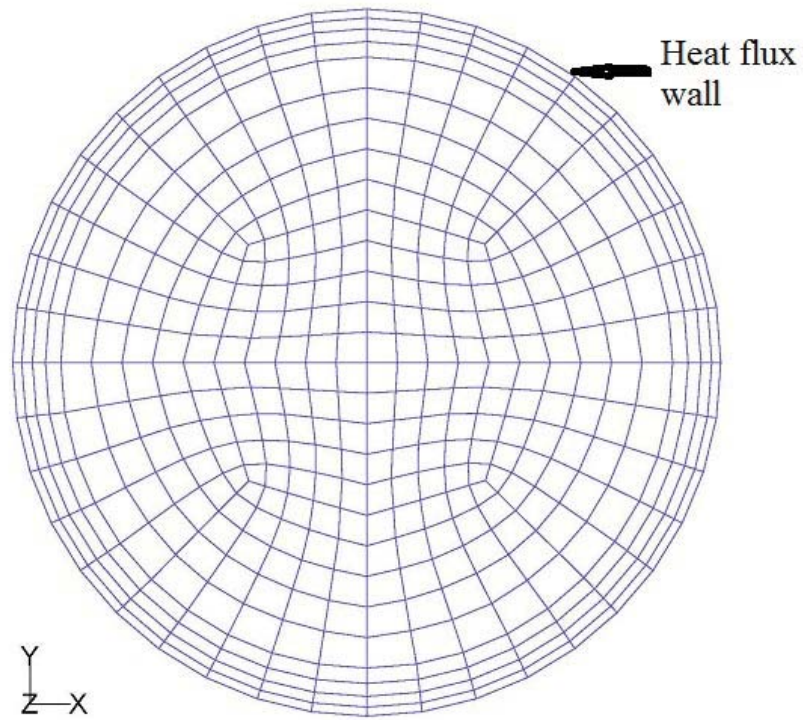


Fig. 5.3a Grid used for sodium flow through pipes ($Re = 840$)

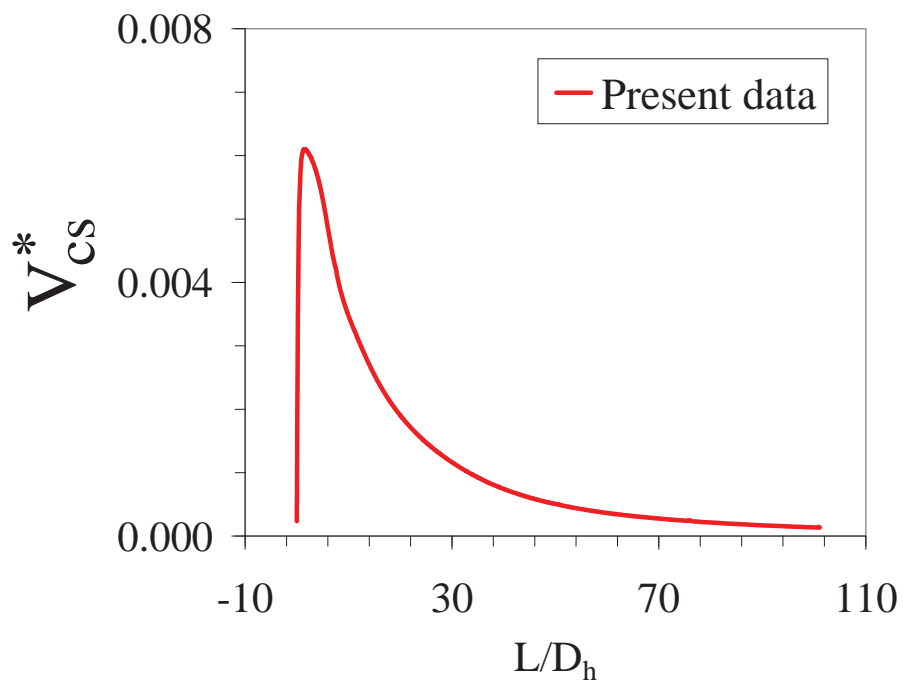


Fig. 5.3b Development of cross-stream velocity for sodium flow through pipes ($Re = 840$)

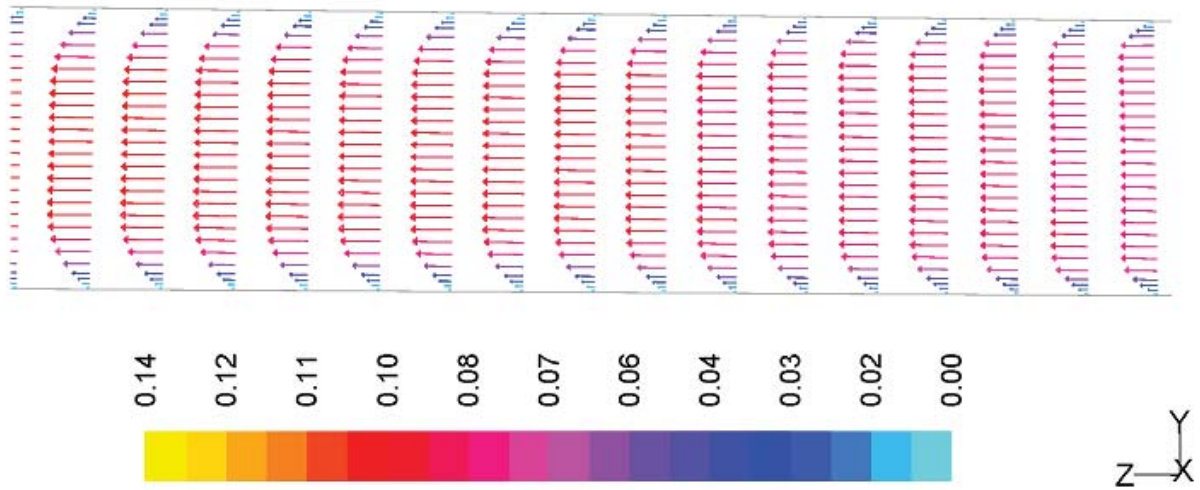


Fig. 5.3c Development of axial velocity vectors for sodium flow through pipes ($Re = 840$)

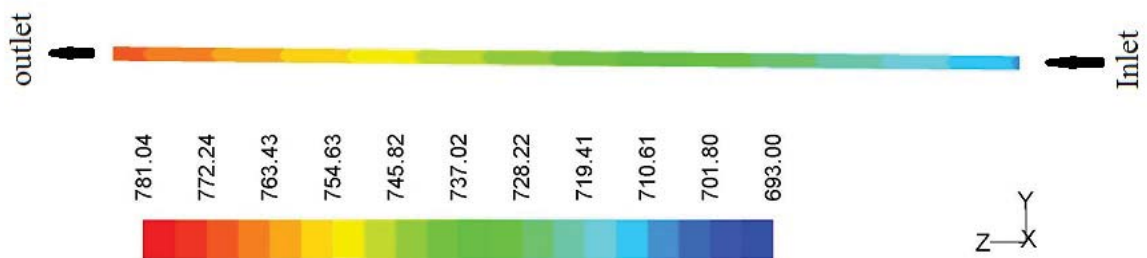


Fig. 5.3d Developing temperature field for sodium flow through pipes ($Re = 840$)

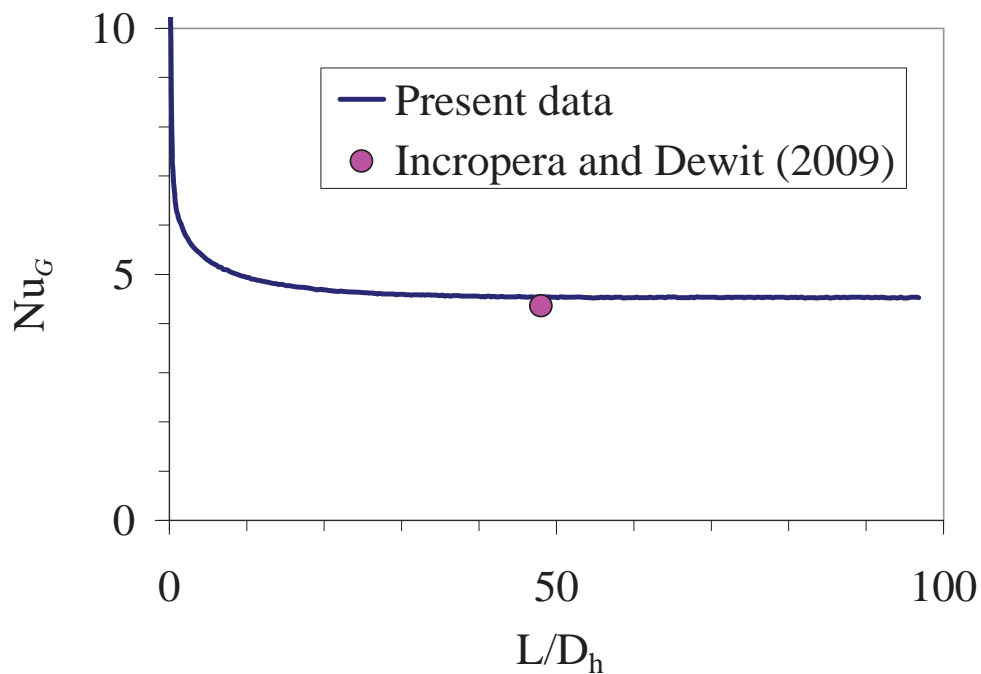


Fig. 5.3e Development of Nusselt number for sodium flow through pipes ($Re = 840$)

The Nusselt number development is portrayed in Fig. 5.3e. Also shown in the same figure is the theoretical data of Incropera and Dewitt (2009) for fully developed case. It is

seen that both the data match within -4%. Hence, the present model is validated for laminar liquid metal flow through ducts.

In addition to the pipe flow validation, flow through helical tube is considered wherein secondary flow is generated in the entrance region as in a fuel pin-bundle. For this study, the fluid medium considered is water and the Reynolds number is 250 as in the work of Lin et al. (1997). The non-dimensional helical pitch, ($\lambda = H / 2\pi R_c$) is 0.6 and the curvature ratio, ($\delta = a / R_c$) is 0.05. The radius of pipe (a) is assumed as 10mm. From this, coil radius ($R_c = 200$ mm) and the helical pitch ($H = 754$ mm) are calculated.

The CFD model of helical tube is depicted in Fig. 5.3f. To facilitate a grid independent solution, three different (cross-stream \times axial) grids have been considered. They are 303×555 , 503×528 and 842×416 . Boundary layer mesh is utilized to capture the effect of wall and the minimum distance between first fluid node and wall is maintained in the range of 0.1 to 0.6 mm. The present results of Nusselt number are portrayed in the Fig. 5.3g. The grids 503×528 and 842×416 provide a nearly grid independent solution. Also given in the figure is the result of Lin et al. (1997). The present results match reasonably well with that of Lin et al. (1997) for the entire entrance length. It shall be highlighted that the results of Lin et al. (1997) are from a numerical study of forced convection through helical tube. The predicted values of fully developed friction factor and Nusselt number have been compared with various experimental data. Hence, comparison of the present data with that of Lin et al. is justified.

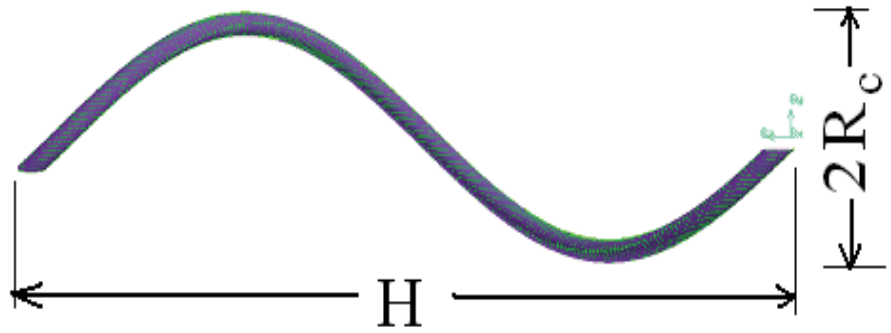


Fig. 5.3f CFD model of helical tube

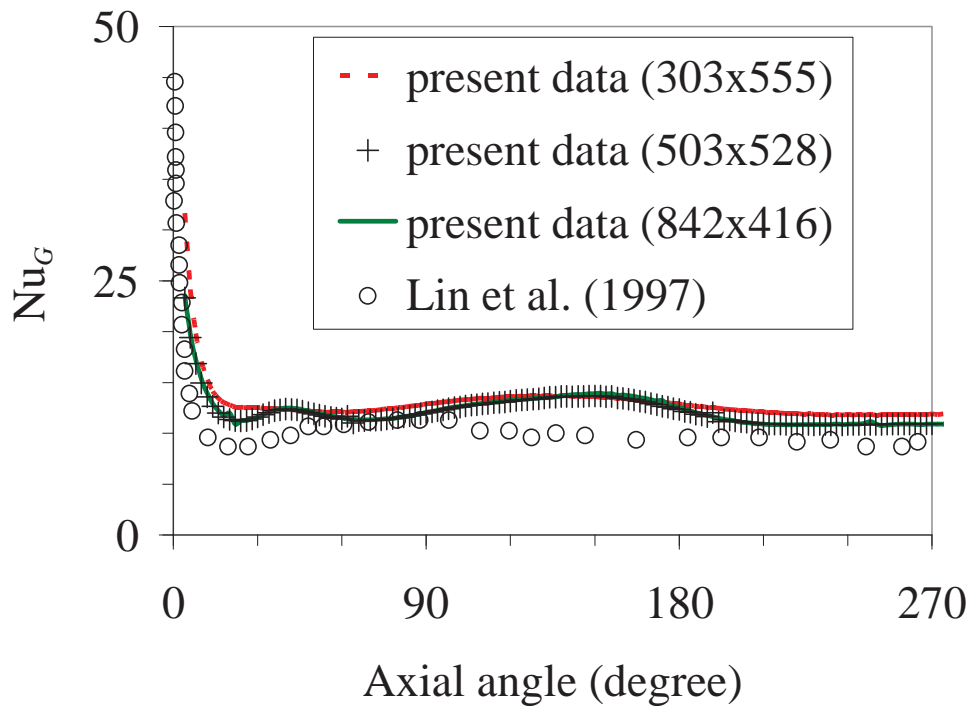


Fig. 5.3g Development of Nusselt number during water flow through helical pipe for $Re = 250$, $\lambda = 0.6$ and $\delta = 0.05$

5.2 RESULTS AND DISCUSSION

After successful validation of the model for liquid metal flow and flow through helical coils, sodium flow through fuel pin bundles with helical spacer wire is simulated. In the present study three different Reynolds numbers, pitch to diameter ratios and helical pitches are considered. The range of parameters studied is presented in Table-5.3. It is reiterated that only 7-pin bundle with 7-axial pitch values has been considered. The developments of cross-

stream velocity, friction factor, and Nusselt number in the entrance region are given special attention.

Table 5.3 Range of parameters analyzed

Parameters	Range
Re	200 - 1600
P_t/D_r	1.14 - 1.42
H	100 – 400 mm

5.2.1 Effect of Reynolds Number

A 7-pin bundle with 100 mm helical pitch is chosen for the current study. The pin diameter and spacer wire diameter are 6.6 mm and 1.65 mm. The hydraulic diameter of the bundle is 3.952 mm. The inlet temperature and the pin surface heat flux are 693 K and 16 kW/m². Four different Reynolds numbers (i.e. 200, 400, 840 and 1600) are considered. The evolution of cross-section average cross-stream velocity in all the four cases calculated using Eq. (3.17) is plotted in Fig. 5.4a. The velocity increases from zero at the inlet to a non-zero value in the fully developed region. The non-dimensional cross-stream velocity is high if Reynolds number is high. Flow may be considered to be fully developed once the cross-stream velocity attains stable spatial oscillation. From this criterion it is seen that higher the Reynolds number, longer is the flow development length. Spatial oscillation prevails even in the fully developed region and the amplitude of oscillation in all the four cases is within ~2.5% of the corresponding mean value.

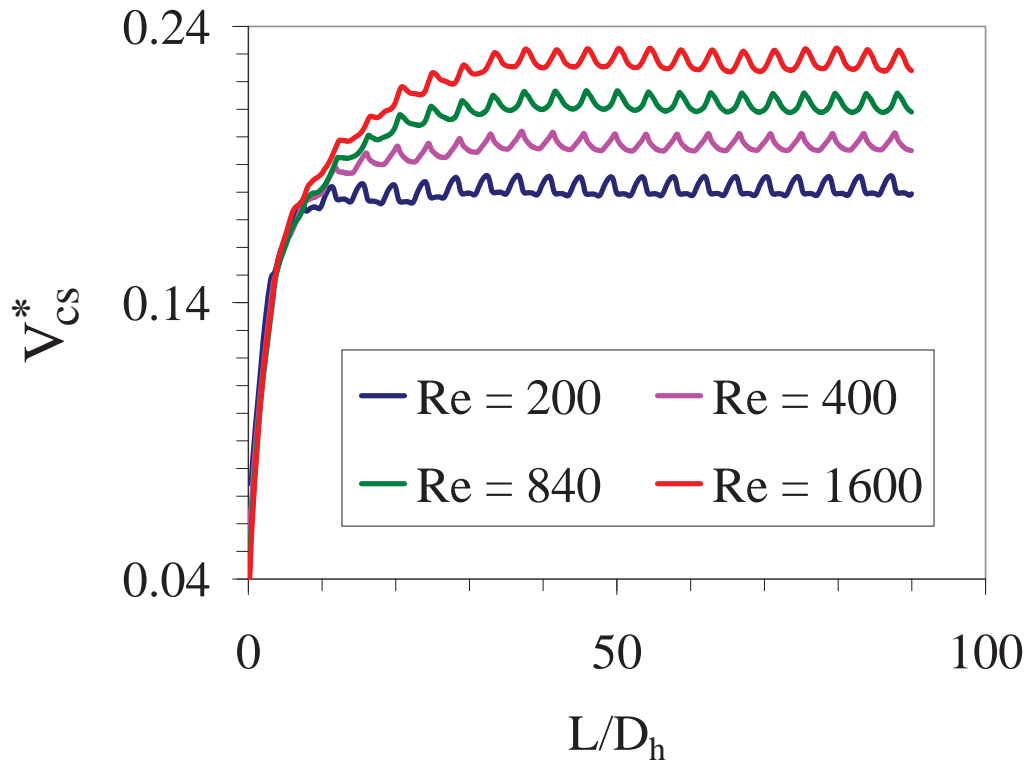


Fig. 5.4a Development of cross-stream velocity in 7-pin bundle for $H = 100$ mm

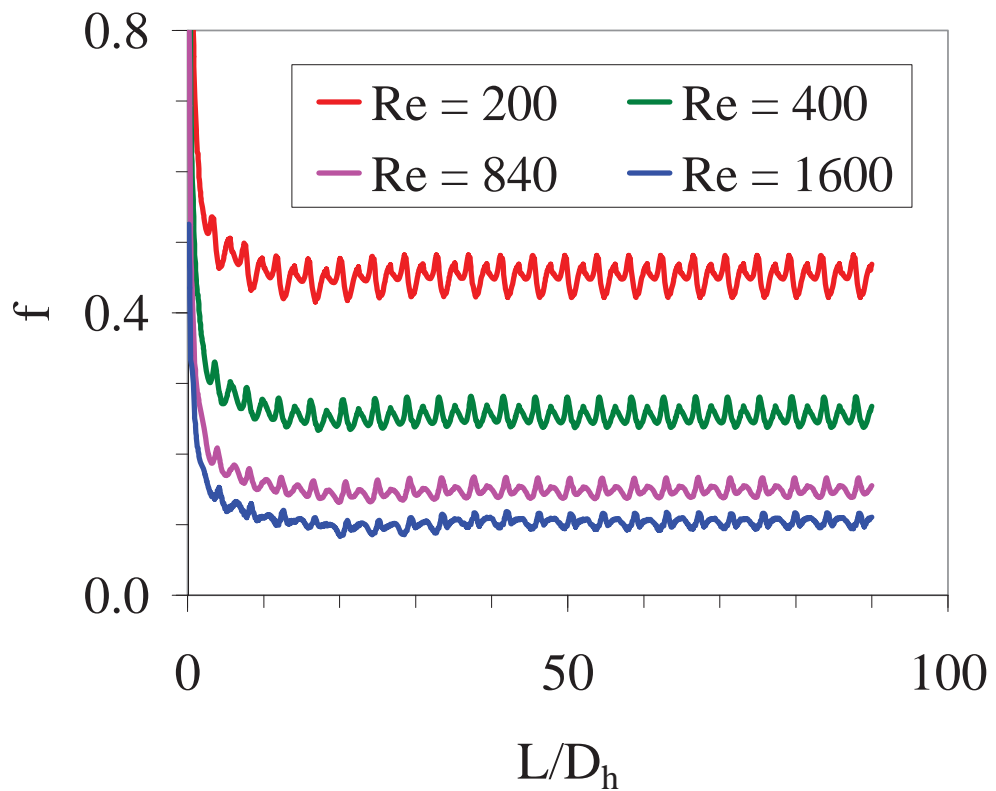


Fig. 5.4b Development of friction factor in 7-pin bundle for $H = 100$ mm

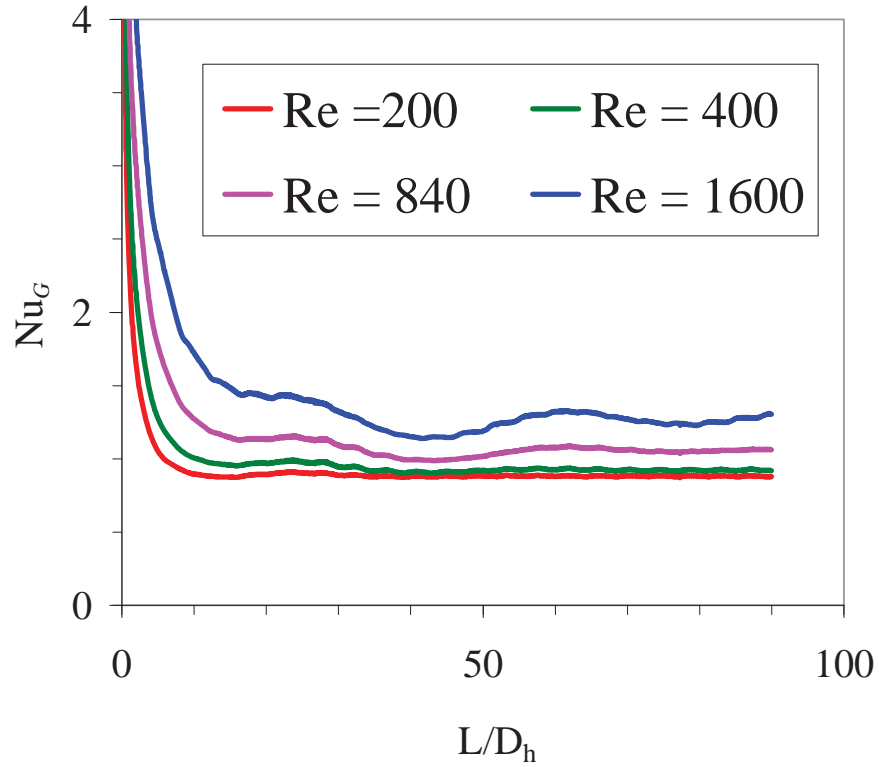


Fig. 5.4c Development of Nusselt number in 7-pin bundle for $H = 100$ mm

The corresponding friction factor development calculated using Eq. (3.18) is depicted in Fig. 5.4b. It is seen that the friction factor reduces very sharply within an axial distance of $10 \times D_h$ from the entry. Afterwards, only a slow change in slope is observed. Flow is fully developed within $\sim 35 \times D_h$ in all the cases. Friction factor is high if the Reynolds number is low as expected. Further, it is seen that the local oscillation prevails for the entire length. The amplitude of oscillation in friction factor is $\sim 10\%$ of the nominal fully developed value. Also, the mean value of fully developed friction factor is more compared to that for flow through straight pipes. For example the mean friction factor for pin bundle is 0.45 at $Re = 200$. The corresponding value for circular pipe is 0.32.

The development of global Nusselt number calculated using Eq. (3.24) is depicted in Fig. 5.4c. The fully developed value of Nusselt number is found to be less than the value in pipe flow (Fig. 5.3b) due to the fact that the hydraulic diameter is small because of the hexcan wall. The value of Nusselt number in pipe flow is found to be 4.3 times higher than

the value in pin bundle for $Re = 840$. Further, Nusselt number is fully developed within $\sim 30 \times D_h$ for $Re < 400$. Periodic spatial oscillation in Nusselt number appears for $Re > 400$ and the amplitude of this oscillation increases with Reynolds number. The Nusselt number in the developing region even goes below the fully developed value and from a heat transfer perspective, the hexagonal pin bundle behaves similar to helical pipes (Acharya et al., 1993). To investigate the effect of pin diameter, it is varied as a parameter and the results are discussed in the next section.

5.2.2 Effect of Pitch to Diameter Ratio

The same configuration used in the previous section ($P_t/D_r = 1.25$ and pin diameter = 6.6 mm) is considered for the results presented in this section also. Additionally, two other configurations ($P_t/D_r = 1.14$ and 1.42 with the corresponding pin diameters, 12 mm and 4 mm) are considered. The helical pitch is 100 mm and Reynolds number is 840. The hydraulic diameters are 4.806 mm, 3.952 mm and 3.416 mm respectively for $P_t/D_r = 1.14$, 1.25 and 1.42. It may be noted that smaller the value of P_t/D_r , tighter is the bundle.

The evolution of cross-stream velocity is portrayed in Fig. 5.5a. It is seen that tighter the pin bundle, the larger is the cross-stream velocity. This is because, when P_t/D_r decreases the sub-channel flow rate increases with the associated increase in cross-stream flow rate. But, the area for cross flow, that is proportional to wire diameter, remains the same. Hence, the cross-stream velocity increases. Also, the hydrodynamic entry length is longer in tighter bundles. Further, the amplitude of spatial oscillations increases as the bundles become tight. Evolution of friction factor is depicted in Fig. 5.5b. In line with the observations made in cross-stream velocity, the friction factor is large in tight pin bundles. Also, large scale periodic spatial oscillations are seen in the fully developed friction factor. The corresponding Nusselt number development is portrayed in Fig. 5.5c. It is seen that the Nusselt number

increases as P_t/D_r ratio increases. To gain further understanding on laminar thermal development, the helical pitch of the wire is varied and the results are discussed in section 5.2.3.

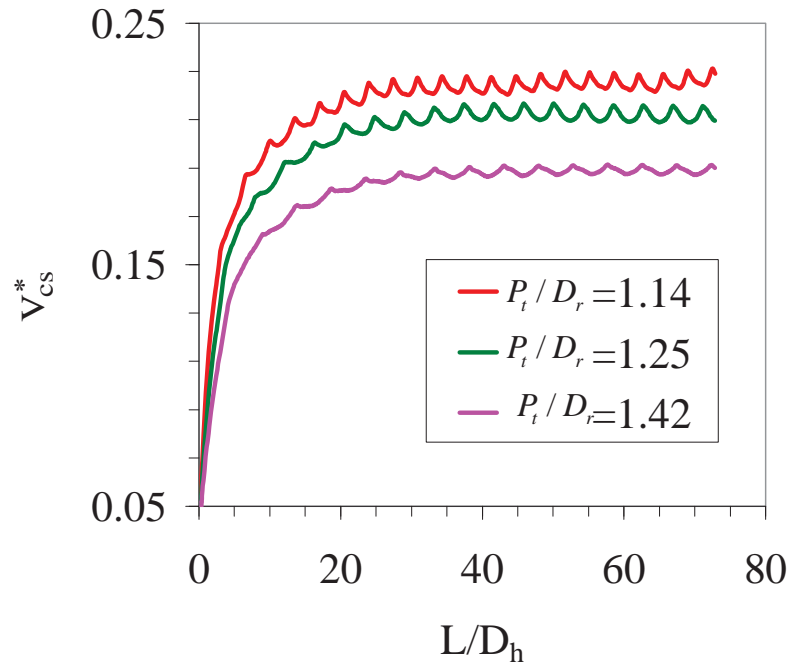


Fig. 5.5a Development of cross-stream velocity in 7-pin bundle for $Re = 840$

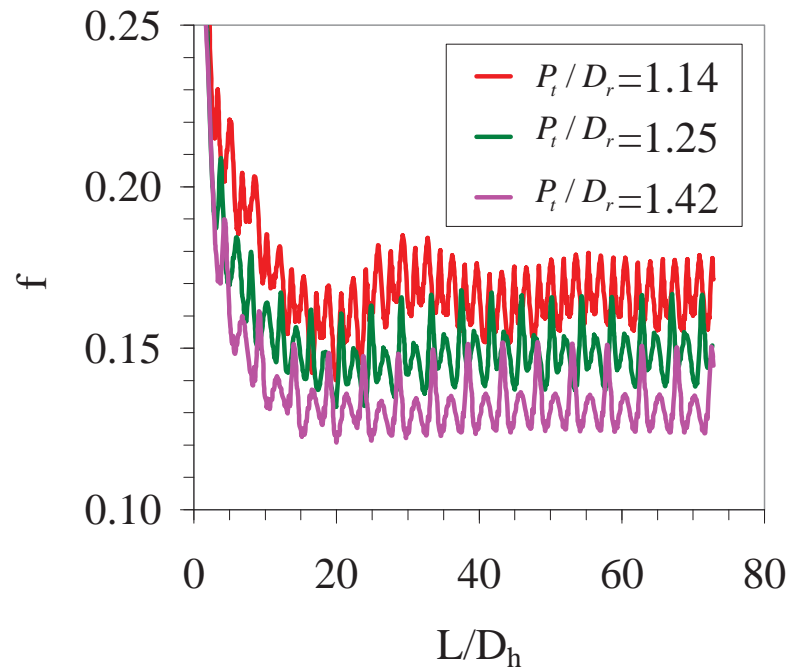


Fig. 5.5b Development of friction factor in 7-pin bundle for $Re = 840$

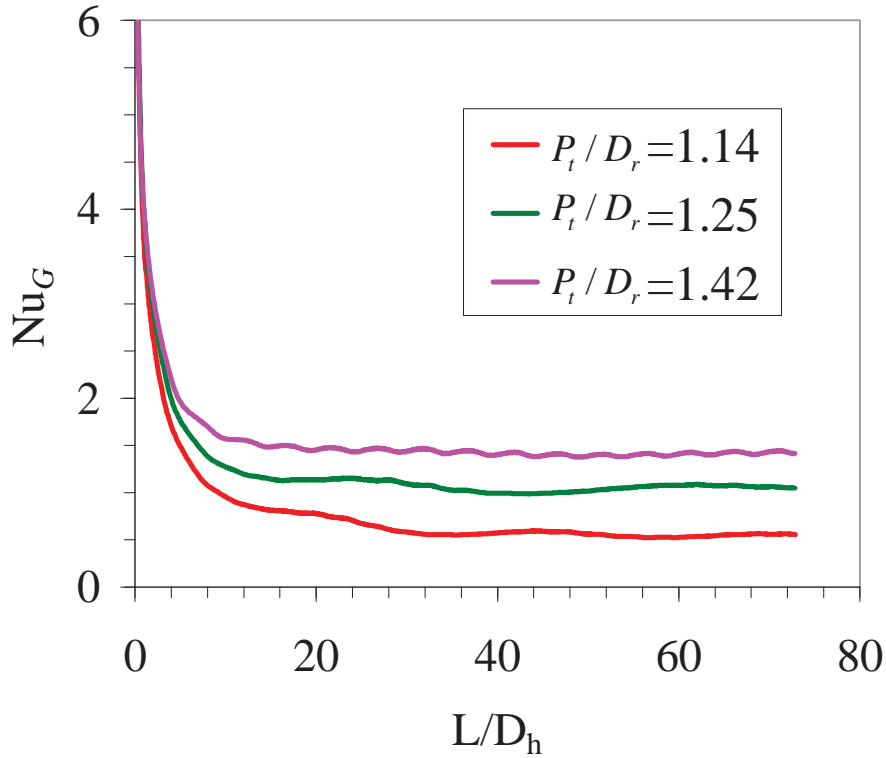


Fig. 5.5c Development of Nusselt number in 7-pin bundle for $Re = 840$

5.2.3 Effect of Helical Pitch

The helical pitch is varied as a parameter in this section. The variations of cross-stream velocity, friction factor and Nusselt number as functions of helical pitch are depicted in Fig. 5.6. The magnitude of secondary flow and hence the cross-stream velocity is high if the helical pitch is small, as expected. Further, the predicted non-dimensional cross stream velocity calculated from Eq. 3.17 for $H = 100$ mm is 0.21. It matches well with the geometrical parameter of the pin bundle, viz., $\pi \times D_r / H$, which is also 0.21. Similar observations were made for all the helical pitches studied. This may probably be used to estimate the magnitude of V_{cs} in pin bundles.

It is seen that the friction factor attains full development in all the cases within a length of $\sim 40 \times D_h$. The fully developed friction factor increases as the helical pitch reduces and it exhibits a strong dependence on helical pitch. On the other hand, the Nusselt number does not exhibit such a strong dependence on helical pitch. An expanded view of friction

factor in the fully developed region for 100mm helical pitch is depicted in Fig. 5.6d along with the position of spacer wire with respect to hexcan wall. It can be observed that within one axial pitch length of 100 mm, there are six crests and an equal number of troughs. The crest appears when the gap between the spacer wire and hexcan wall is minimum near a hexcan face. On the other hand, the trough appears when the wire is approaching the corner between two hexcan walls. This crest-trough pattern repeats six-times within one pitch when the spacer wire position changes along the flow direction. Similar patterns were observed for all the values of helical pitch analyzed herein.

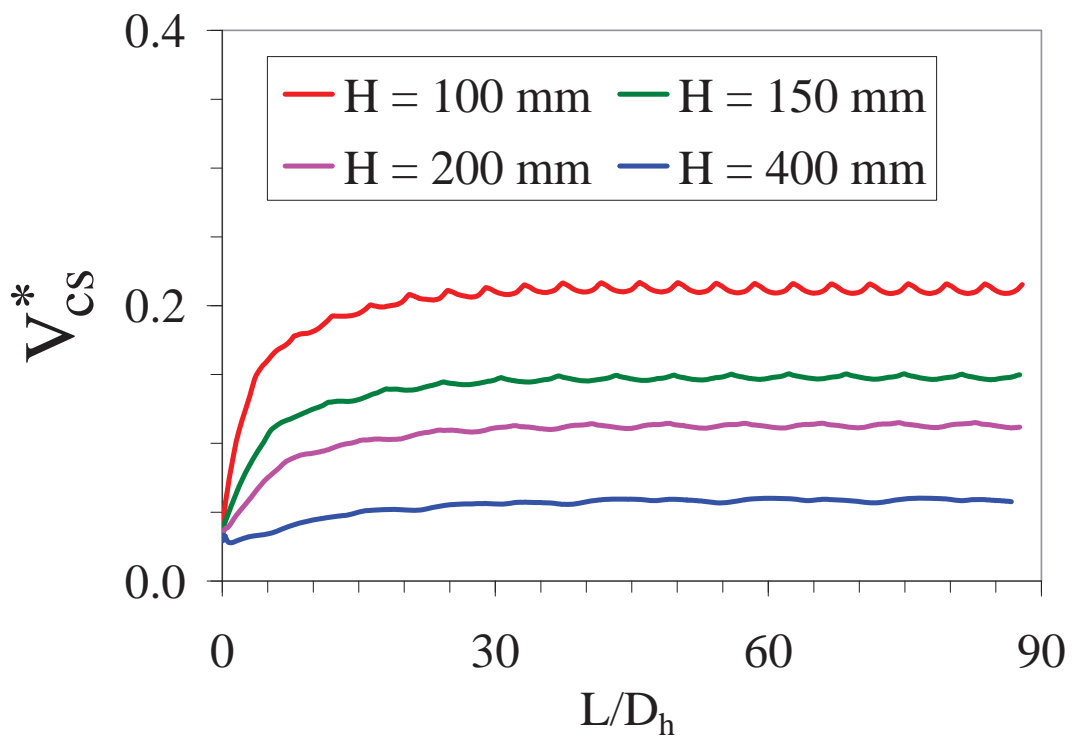


Fig. 5.6a Development of cross-stream velocity in 7-pin bundle for $Re = 840$

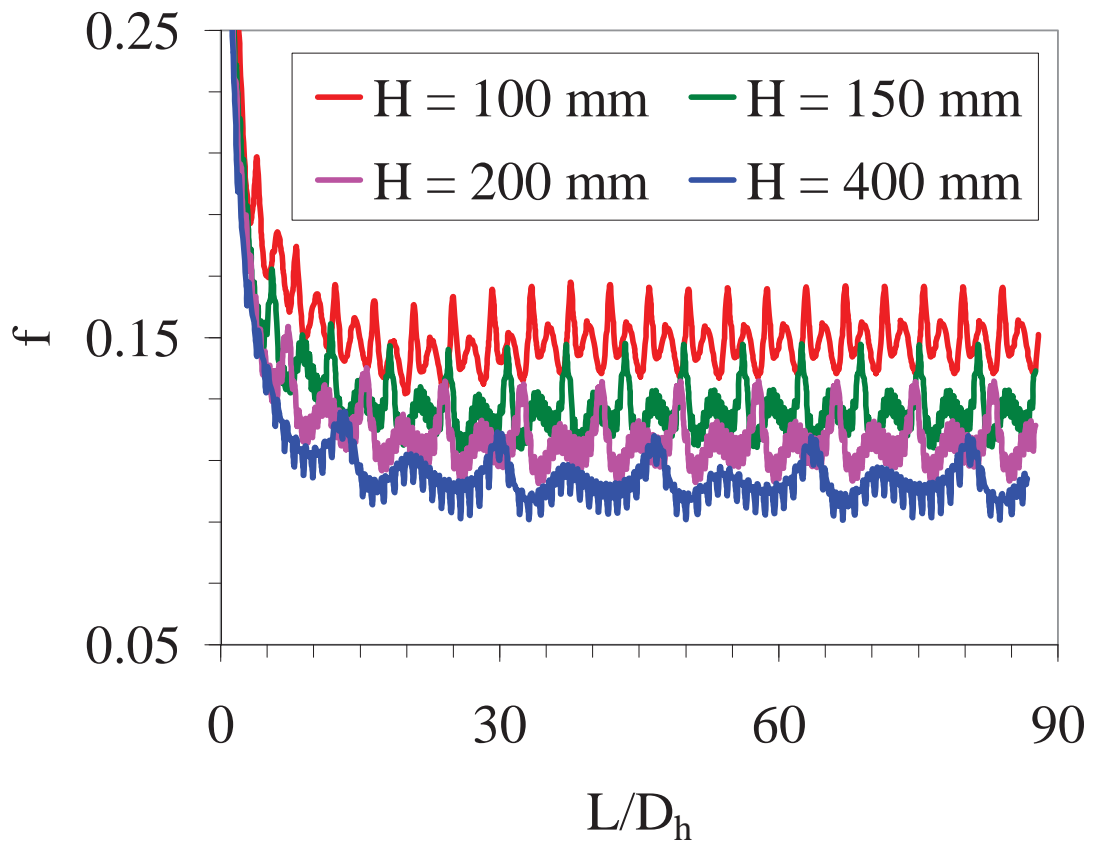


Fig. 5.6b Development of friction factor in 7-pin bundle for $Re = 840$

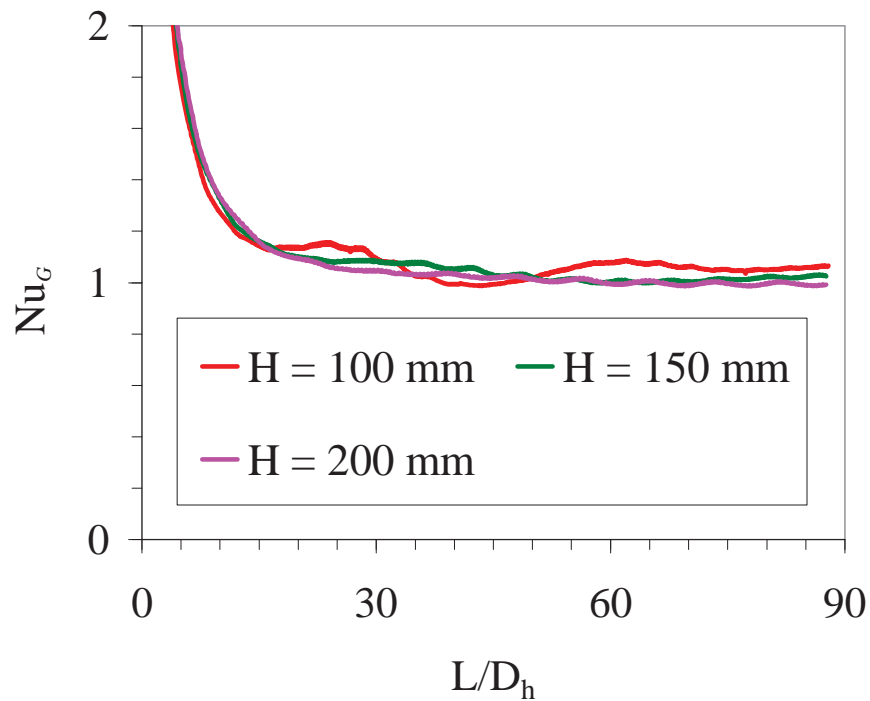


Fig. 5.6c Development of Nusselt number in 7-pin bundle for $Re = 840$

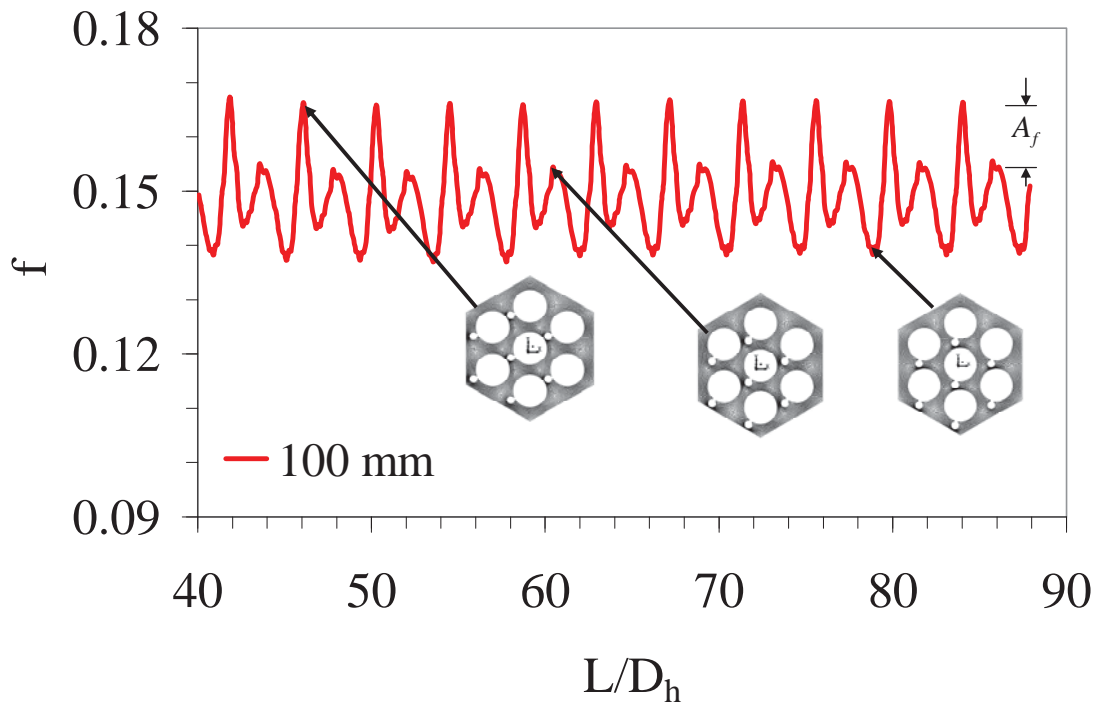


Fig. 5.6d Expanded view of friction factor in the fully developed region for $Re = 840$

Table 5.4 Non-dimensional amplitudes of friction factor and cross-stream velocity in the fully developed region

	$[A_f / \bar{f}] \times 100$	
Re ($P_t/D_r = 1.25$ & $H = 100$ mm)	200	6.1
	400	7.2
	1600	8.9
P_t/D_r ($Re = 840$ & $H = 100$ mm)	1.14	6.5
	1.25	8.7
	1.42	9.6
H in mm ($Re = 840$ & $P_t/D_r = 1.25$)	100	8.9
	150	12.7
	200	13.4

Further, the percentage of the ratio of amplitude to the mean value of friction factor $[A_f / \bar{f} \times 100]$ is calculated in the fully developed region and it is presented in Table-5.4. It can be seen that the percentage monotonically increases with Reynolds number, P_t/D_r ratio and helical pitch length. This is due to the fact that the reduction in mean friction factor is

more than the corresponding reduction in amplitude, for increasing Reynolds number. But, with P_t / D_r ratio and helical pitch length, the amplitude increases while the mean friction factor decreases for a particular Reynolds number. This leads to a large change in the normalized amplitude.

5.3 CLOSURE

Simultaneous development of flow and temperature fields in the entrance region of fuel wire-wrapped pin bundle during liquid metal flow has been investigated. The friction factor and Nusselt number exhibit prominent spatial oscillations. These oscillations are found to be related to the position of spacer wire between pins and hexcan surfaces. The amplitude of fluctuation in friction factor normalized with respect to the mean value is in the range of 6 – 13 %. For identical Reynolds number, the friction factor exhibits a strong dependence on helical pitch of wire wrap. On the contrary, the Nusselt number does not exhibit such a strong dependence on helical pitch. The friction factor and cross-stream velocity are relatively high in tight pin bundles with low P_t/D_r values.

CHAPTER - 6

TURBULENT FLOW AND THERMAL DEVELOPMENT IN WIRE-WRAPPED PIN BUNDLES

6.0 INTRODUCTION

The height of the active fuel zone in a fuel subassembly is typically about one meter, whereas the hydraulic diameter of the sub-channel is ~3.5mm. Hence, it is generally believed that flow and temperature can be taken to be fully developed for a major portion of fuel pin length. Hence, it is essential to understand flow and temperature developments in the entrance regions of fuel subassemblies with helical spacer wires. Dependence of entrance length on helical pitch, formation of local hotspot in the under developed region and influence of the number of pins on entrance parameters are to be understood for proper design of helical wire-wrap subassemblies.

6.1 SOLUTION METHODOLOGY

6.1.1 Grid Sensitivity Study

The customized mesh generator, GridZ (CFDExpert, 2009) has been employed for the generation of a structured mesh. For the purpose of finalising the mesh, a 7-pin fuel bundle with helical spacer wire is chosen. The diameter of fuel pin is 6.6 mm, and that of spacer wire is 1.65 mm. The length of helical pitch is 200 mm and an axial length of 7 pitches has been considered.

Grid independency test is performed in two ways: (i) by varying the grids in cross-stream direction, and (ii) by varying the axial grid. Two different cross-stream mesh densities, viz., 1.181 and 4.233 millions are studied for the same axial grid size by changing the number of divisions around fuel pin and the wire. The number of divisions around the circumference of fuel pin is 36 and 72 respectively as depicted in Fig. 5.1a and Fig. 5.1b and the number of divisions on fuel pin surface and wire surface is depicted in Fig. 5.1c.

Fully developed values of global Nusselt number and friction factor in the two mesh patterns are compared in Table-6.1. Predicted fully developed values of friction factor and Nusselt number are almost the same for both the meshes. But y^+ value is >100 in the case of 1.181 million grids, whereas the recommended value of $y^+ < 100$. Hence, the grid with 72 divisions around the pin is adopted. Hence, further refinement was considered not essential. Also, due to limitations in computational capability, additional refinement could not be attempted.

Four different axial grids have been studied, with total number of control volumes varying from 0.847 to 4.233 millions. It is seen that the grid with 4.233 million structured control volumes gives a grid independent result, as is evident from Table-6.2.

Table 6.1 Comparison of fully developed friction factor and Nusselt number with two different cross-stream grids

Number of control volumes (millions)	Number of divisions around pin	y^+	Friction factor	% variation in friction factor	Nusselt number	% variation in Nusselt number
1.181	36	77-106	0.0220	-	8.979	-
4.233	72	66-90	0.0220	nil	9.250	0.8

Table 6.2 Comparison of fully developed friction factor and Nusselt number with different axial grids

Number of control volumes (millions)	Number of cells around pins	y^+	Friction factor	% variation in friction factor	Nusselt number	% variation in Nusselt number
0.847	72	67-116	0.0214	-	9.761	-
2.016	72	66-90	0.0219	2.4	9.506	-2.6
2.258	72	66-90	0.0221	0.7	9.298	-2.2
4.233	72	66-90	0.0220	-0.4	9.250	-0.5

These simulations needed a minimum RAM of 4 GB. For convergence, present cases required ~ 48 hours of CPU time in an eight core parallel machine. The 19-pin geometry with 10 pitches and 37 pin geometry with five helical pitches required ~ 96 hours of CPU time to converge. Based on y^+ values and predicted friction factor and Nusselt number values, the

grid pattern with 4.233 million grids is taken for all the 7-pin bundle simulations. The corresponding axial grid size and number of divisions around fuel pins are used for 19-pin bundle and 37-pin bundle simulations. The isometric view of grid generated for 7-pin bundle is given in chapter-5 (Fig. 5.2c) and cross-stream grid for 37-pin bundle is depicted in Fig. 6.1.

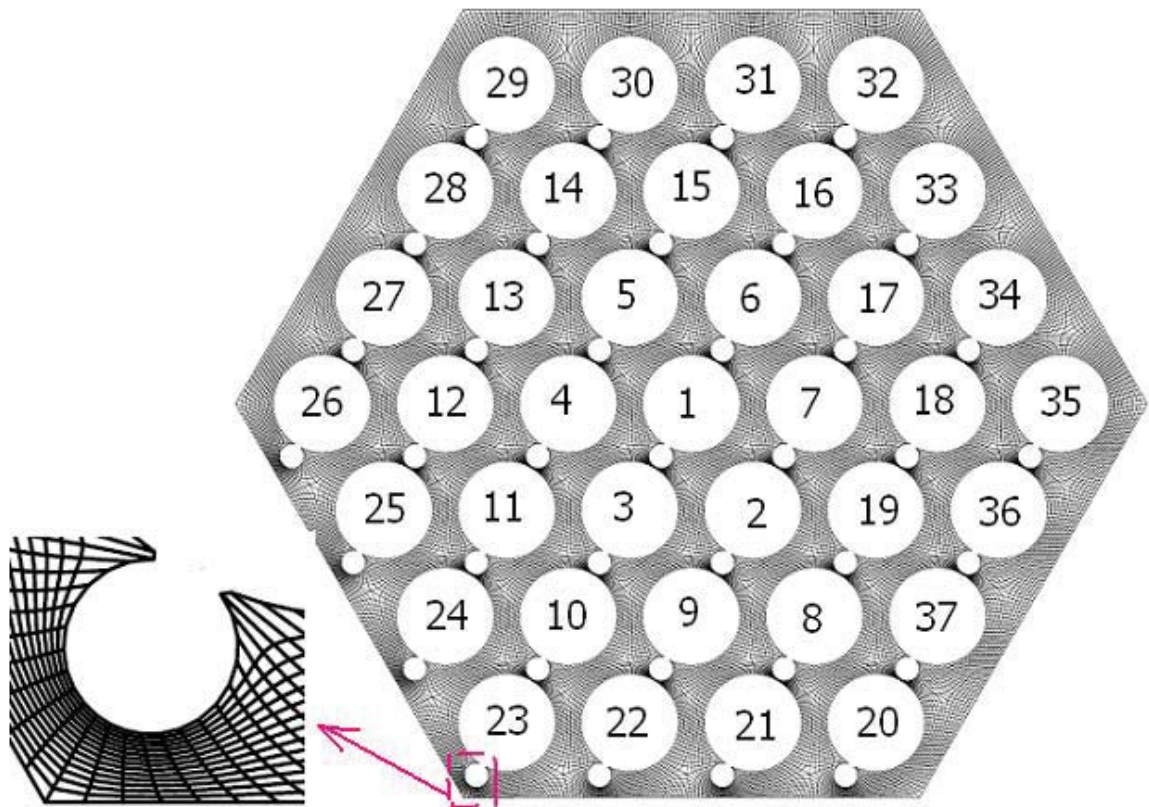


Fig. 6.1 Computational grids considered for 37-pin bundle

6.1.2 Selection of Turbulence Model

Three different turbulence models have been tested before finalising one model. The models considered are (i) *RNG $k-\varepsilon$* model, (ii) *SST $k-\omega$* model, and (iii) Reynolds Stress Model (RSM). Based on the investigations for a 7-pin bundle with helical spacer wire, it is found that the predictions of friction factor by *RNG $k-\varepsilon$* model are not significantly different from the predictions by other models as depicted in Fig. 6.2a. The corresponding Nusselt number prediction is presented in the Fig. 6.2b. Even though, the Nusselt numbers predicted by *RNG*

$k-\varepsilon$ and $SST\ k-\omega$ are different, the former is adopted for all the simulations because of its unique feature of adopting position dependent turbulent Prandtl number (see, Section 3.2.2 for further details)

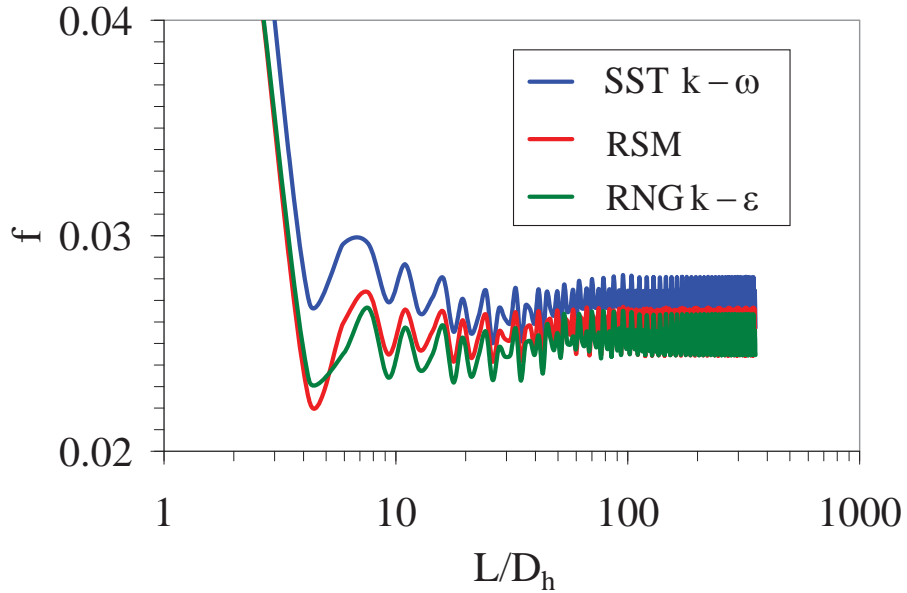


Fig. 6.2a Prediction of friction factor development in 7-pin bundle by various turbulence models ($Re = 0.842 \times 10^5$)

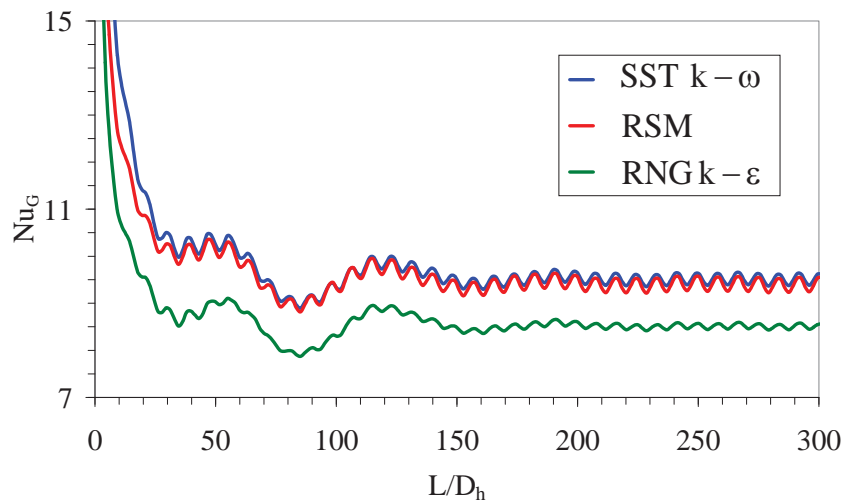


Fig. 6.2b Prediction of Nusselt number development in 7-pin bundle by various turbulence models ($Re = 0.842 \times 10^5$)

6.1.3 Validation

Experimental data reported in the open literature for rod bundle heat transfer during sodium flow in the entrance region is limited. Therefore to validate the present model for liquid

metal flow, experimental study carried out by Rensen (1981) in a cylindrical annulus is chosen. Inner diameter of the annulus is 17.2 mm and its outer diameter is 31.8 mm. Total length of the annulus is 1100 mm. The initial 600 mm length of the entrance region is unheated for the velocity to stabilize. The remaining 500 mm length in the downstream is heated. Among many cases reported, the case chosen for the present study corresponds to an inlet temperature of 350°C with Reynolds number of 0.2×10^5 . The inlet velocity and Prandtl number are 0.484 m/s and 0.0054 respectively. A constant heat flux of 30 kW/m² is applied to the inner wall and the outer wall is adiabatic.

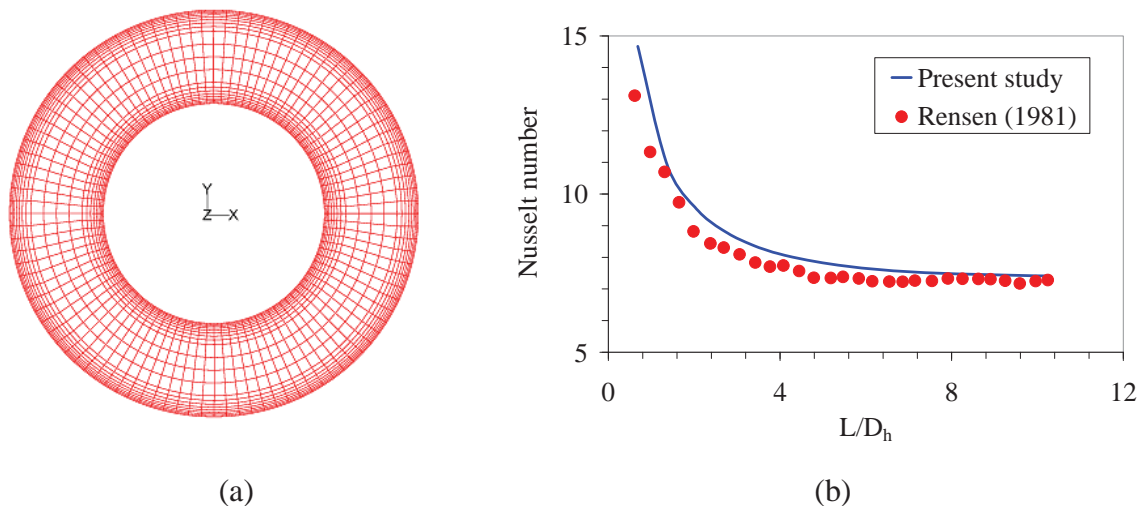


Fig. 6.3 (a) Computational grid considered for the experimental geometry (b) Comparison of predicted Nusselt number development with experimental data

The grid considered for the annular region is depicted in Fig. 6.3a. In the radial direction a fine mesh is employed near walls and a coarse mesh in the annulus centre in order to achieve appropriate y^+ values dictated by wall function requirement and to provide adequate axial mesh points in the flow direction to achieve acceptable mesh aspect ratio. Simulation has been carried out using three-dimensional cylindrical polar coordinate system, despite the fact that two-dimensional axi-symmetric model is adequate for this validation problem. The predicted Nusselt number on the inner wall of the heated section is plotted in

Fig. 6.3b. Also shown in the same figure is the experimental data reported by Rensen (1981). It is seen that the present simulation compares very well with the experimental data right through the length of the flow domain in heated section. The maximum deviation is +5.5 % in the entry region and +1.5% in the fully developed region. Thus, the model is validated for liquid metal application in the entrance region.

In addition to the above validation, it is decided to compare the present model predictions for a fuel pin bundle with spacer wire using liquid sodium coolant, against the correlations reported in open literature. Many correlations have been reported for friction factor in the literature over the years. The results of Baxi and Dalle-Donne (1981), Engel et al. (1979) and Rehme (1973) are chosen for the present comparison among reported correlations. These correlations have been proposed by Bubelis and Schikorr (2008) as suitable for liquid sodium applications. For numerical simulations, a fuel bundle with 7-pins with helical spacer wire is considered. The values of helical pitch (H), wire diameter (D_w) and pin diameter (D_p) are respectively 200 mm, 1.65 mm and 6.6 mm. The hydraulic diameter of the 7-pin bundle assembly is 3.952 mm. The geometry is selected based on the dimensions of medium size fast breeder reactors. The fully developed value of friction factor is compared with experimental correlations in two ways: (i) by varying the Reynolds number and (ii) by varying the helical wire-wrap pitch. Predicted fully developed friction factor values are presented in Fig. 6.4a and Fig. 6.4b. In the case of Reynolds number variation (Fig. 6.4a), friction factor agrees within -14.5% with the Baxi and Dalle-Donne correlation (1981), -8.7% with Engel et al. correlation (1979) and +25% with Rehme correlation (1973). With respect to helical pitch variation (Fig. 6.4b), the present data agrees within -24% with Baxi and Dalle-Donne correlation (1981) and within +21% with Rehme correlation (1973). The deviation is high for short helical pitch values and it reduces as the pitch increases. Similar deviations have been observed by Sreenivasulu and Prasad (2011) also. It may be indicated that the

numerical results of Sreenivasulu and Prasad (2011) are for water. Hence, no attempt is made to compare the present results for sodium with the water results.

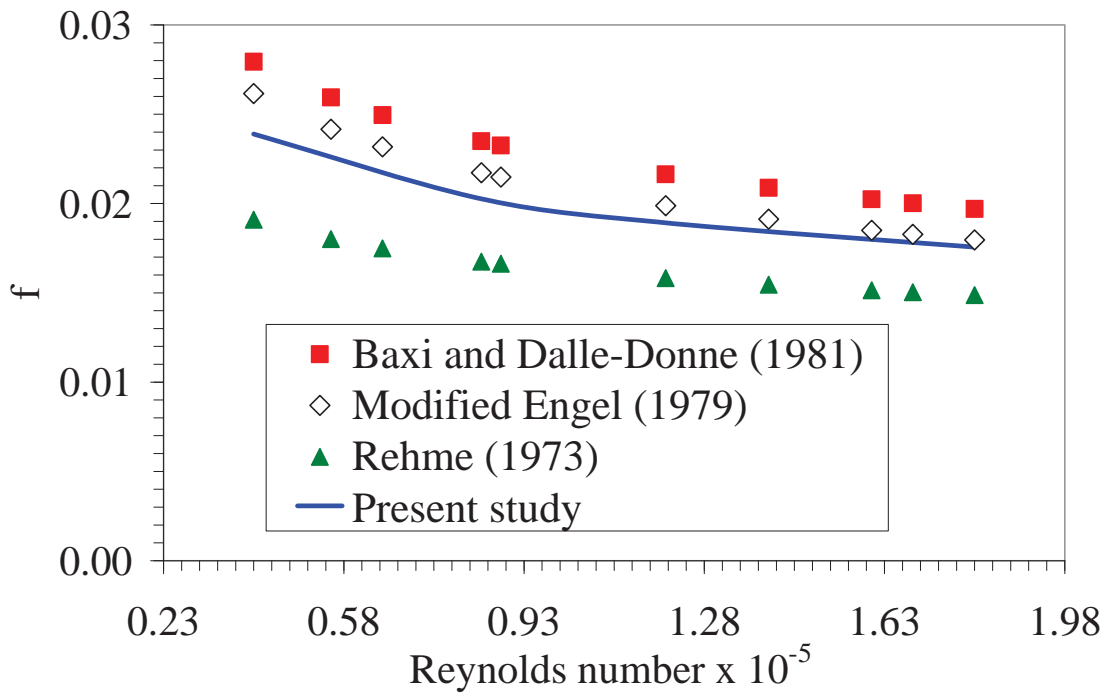


Fig. 6.4a Comparison of fully developed friction factor with experimental correlation for $H / (D_w + D_r) = 24.4$

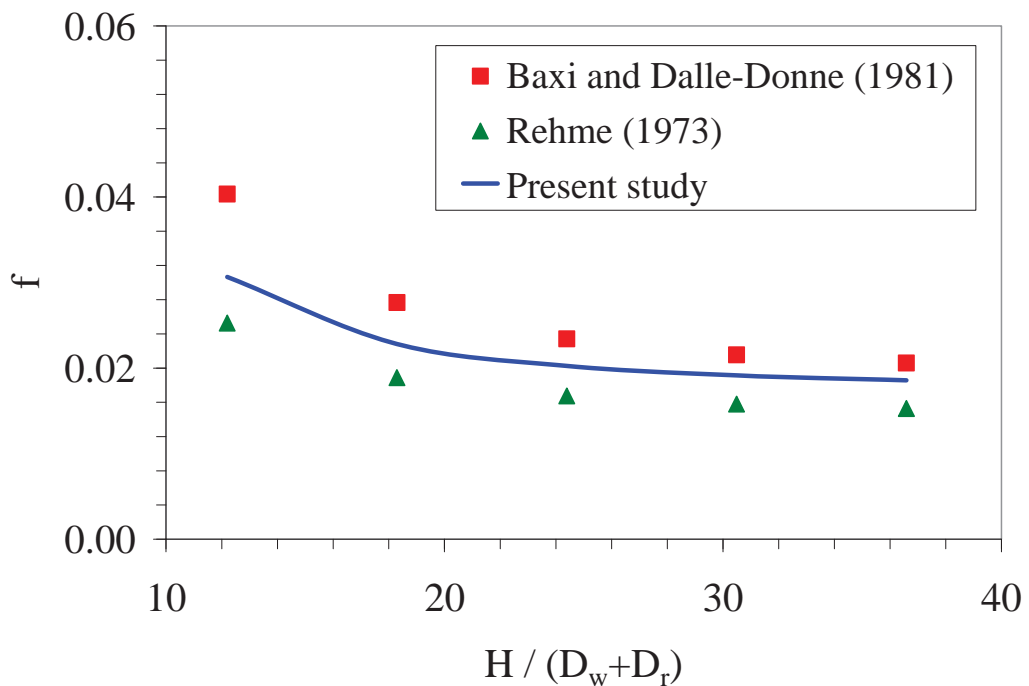


Fig. 6.4b Comparison of fully developed friction factor with experimental correlation for $Re = 0.842 \times 10^5$

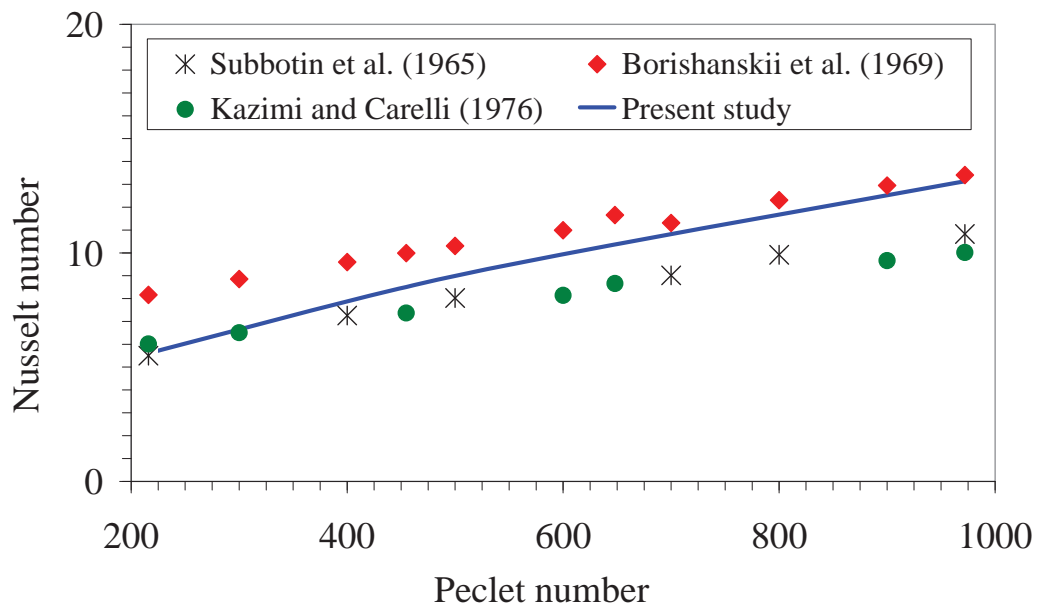


Fig. 6.5 Comparison of fully developed Nusselt number with experimental correlations

The fully developed Nusselt number predicted from the present study for 7-pin fuel bundle is presented in Fig. 6.5, as a function of Peclet number. Also presented in the same figure are data obtained from the experimental correlations reported by many authors. Present data agrees well with the data of both Subbotin et al. (1965) and Kazimi and Carelli (1976) in the lower Peclet number region and with Borishanskii et al. (1969) in the higher Peclet number region. Considering the large variations among correlations reported in the open literature, present validation is judged to be acceptable.

6.2 RESULTS AND DISCUSSION

Reynolds number, helical pitch (H) and the number of pins in fuel bundle (N) are considered as parameters in the present study and the range of each parameter is presented in Table 6.3. The developments of friction factor, Nusselt number, hot-spot factor and cross-stream velocity in the entrance region are investigated in detail.

Table 6.3 Range of parameters studied

Parameters		
Re	H (mm)	N
400- 1.8×10^5	100-300	7-37

6.2.1 Effect of Reynolds Number

It is known that the experimental correlations reported by various researchers are valid for different ranges. Hence, simulations have been carried out for four different Reynolds numbers, viz., 0.4×10^5 , 0.842×10^5 , 1.2×10^5 and 1.8×10^5 . The corresponding inlet velocity values are 3.23, 6.8, 9.69 and 14.53 m/s respectively. For the present study a 7-pin bundle with pin diameter of 6.6 mm, helical wire diameter of 1.65 mm, helical pitch of 200 mm and triangular pitch of 8.28 mm are considered for an axial length of seven times helical pitch. The hydraulic diameter (D_h) of pin bundle is 3.952 mm. The inlet temperature of sodium is 420°C.

The flow enters the bundle without any cross-stream velocity component. But on entering the bundle, cross-stream flow is generated due to two effects, viz., (i) boundary layer development and (ii) induction by helical wire. Boundary layers develop on the pin surfaces and on hexcan wall. Growth of these boundary layers diverts sodium away from the solid surfaces and towards the centre of sub-channels. This hydrodynamic boundary layer growth leads to development of secondary fluid motion. Helical wires also induce cross-stream velocity and guide the flow around the circumference of the pins. The contribution due to boundary layer growth ceases once the boundary layer is completely grown. But the contribution due to helical wire continues to prevail. The cross-stream velocity due to boundary layer growth is generally normal to the surface while that due to helical wire is always around the circumference. Thus there is a complex interaction between these two effects towards the establishment of cross-stream velocity.

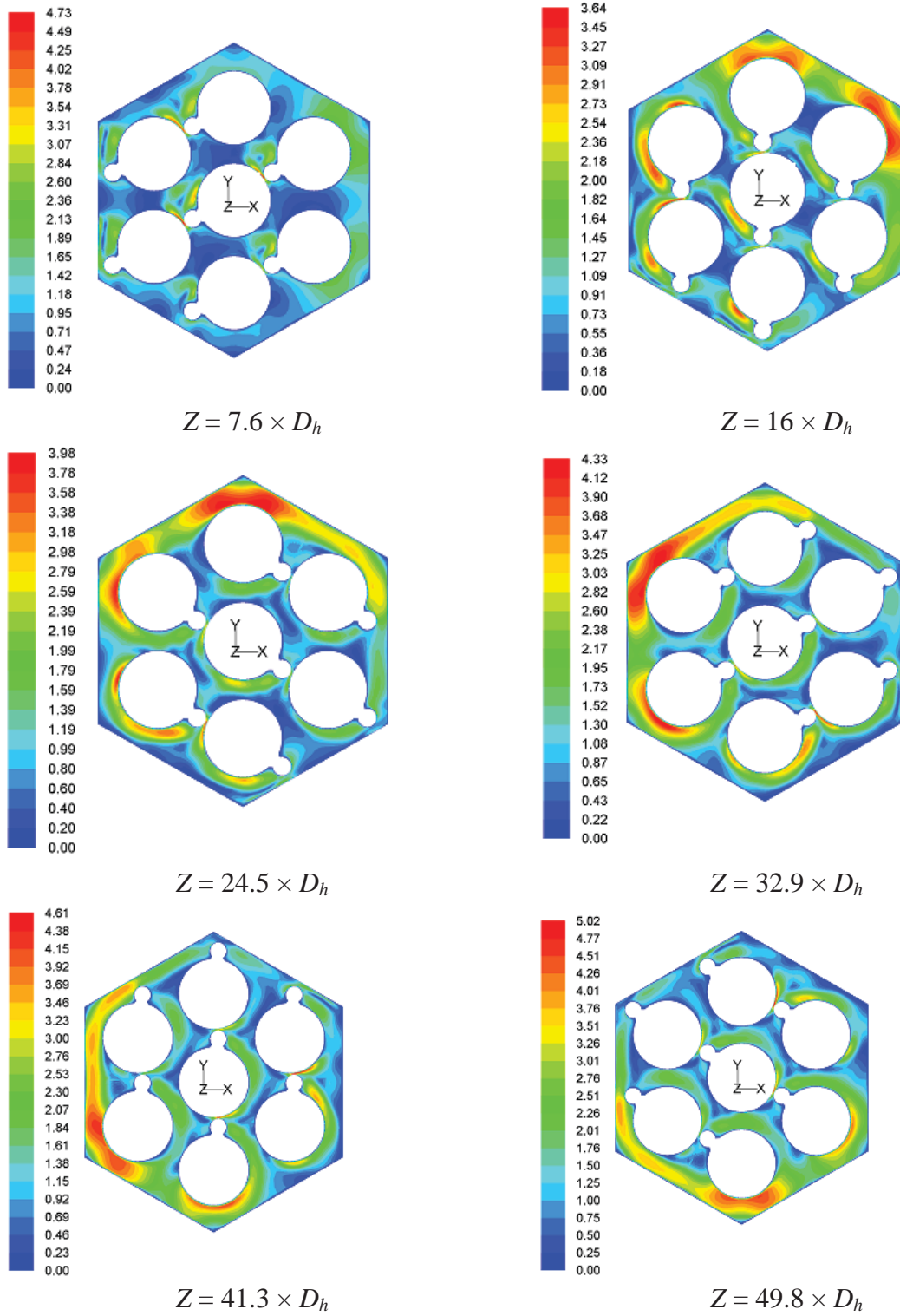


Fig. 6.6a Cross-stream velocity in the 1st helical wire pitch ($Re = 1.8 \times 10^5$)

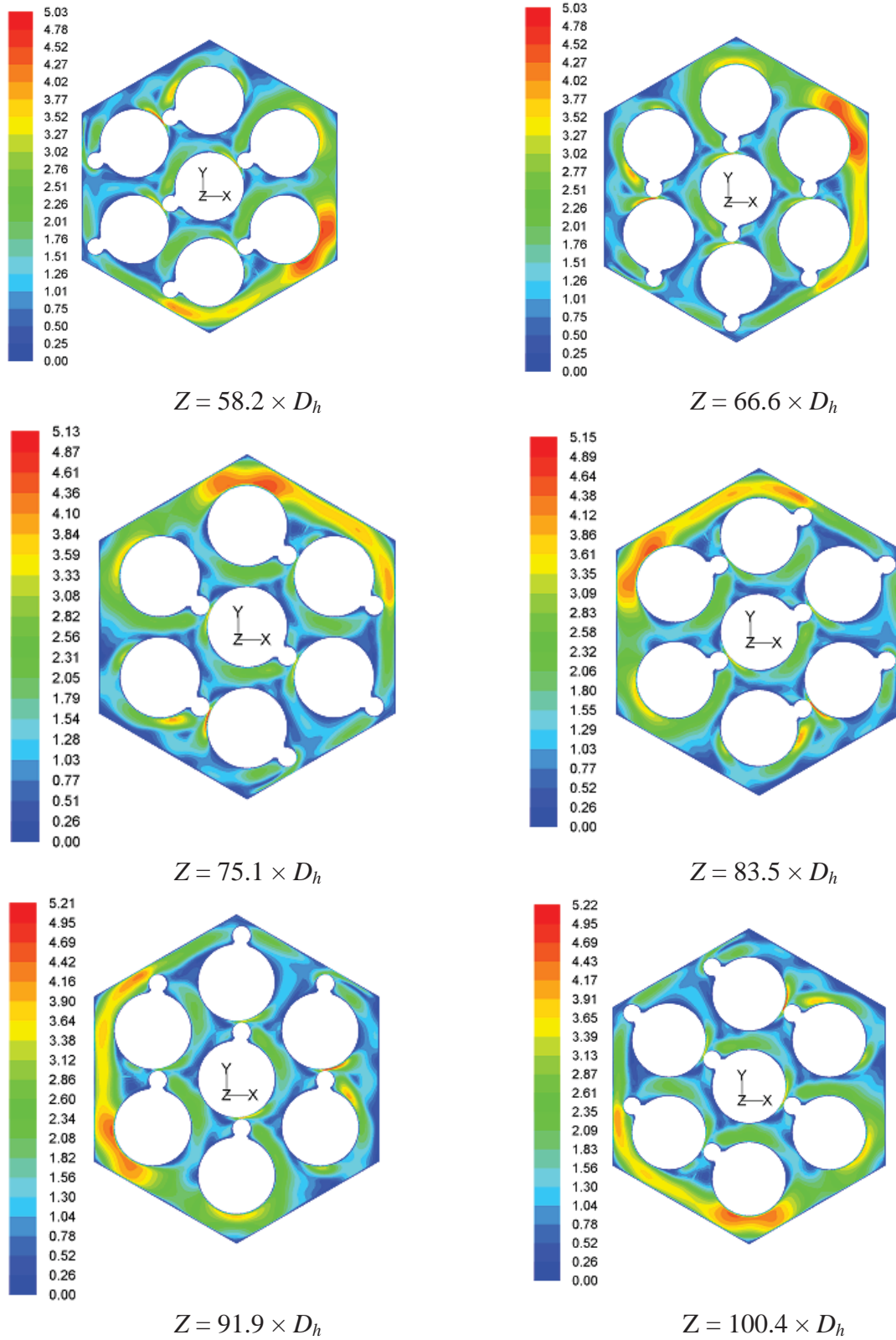


Fig. 6.6b Cross-stream velocity in the 2nd helical wire pitch ($Re=1.8 \times 10^5$)

The development of cross-stream velocity at six axial locations (i.e., for every $1/6^{\text{th}}$ pitch) in the first helical pitch, is depicted in Fig. 6.6a, and the same in the second helical pitch for every $1/6^{\text{th}}$ pitch, is depicted in Fig. 6.6b for $Re = 1.8 \times 10^5$. In the first helical pitch the peak velocity varies between 3.64 m/s and 5.02 m/s. It can be seen that at $Z = 7.6 \times D_h$, the peak velocity is behind the wires. As flow progresses, the peak velocity slowly shifts towards the periphery. In Fig. 6.6, the direction of helical wire is anti-clockwise when viewed along the flow direction. The peak velocity occurs around 3-pins in the periphery while the pins which are in the opposite side face low velocity.

The development of area weighted mean cross-stream velocity in the entrance region is presented in Fig. 6.7a for $Re = 1.8 \times 10^5$. There is a steep increase in cross-stream velocity at the entrance region and the cross-stream velocity attains full development nearly at a length of $65 \times D_h$. This is equal to 1.3 times the length of helical pitch. In the fully developed region, the cross-stream velocity is seen to oscillate periodically with respect to distance about a mean value with small but finite amplitude. The mean value is nearly 27 % of the mean axial velocity. However, the cross-stream velocity around central pin is found to be nearly 13 % of the mean axial flow velocity. This indicates that there is large-scale circumferential flow in the peripheral sub-channels. This flow is responsible for promoting good mixing and hence a nearly uniform temperature along any cross-section. The cross-stream temperature contours presented in Fig. 6.7b supports this statement.

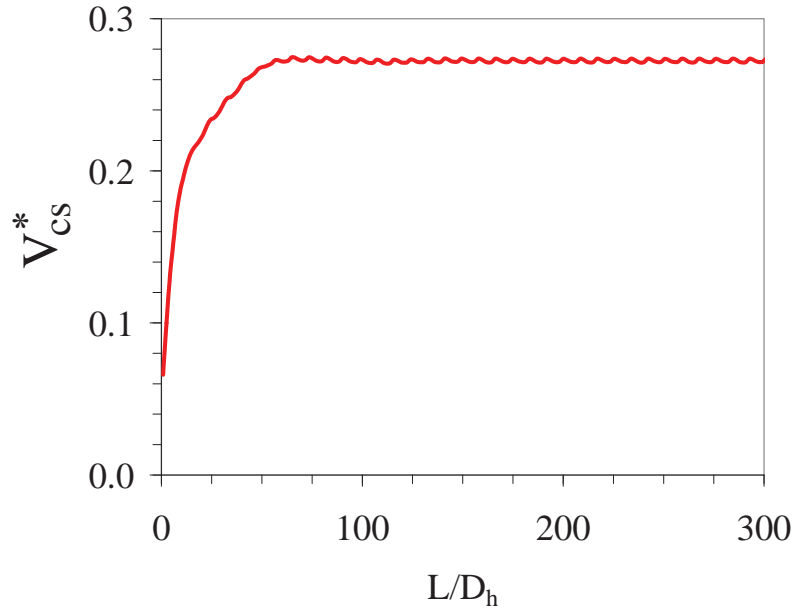


Fig. 6.7a Non-dimensional cross-stream velocity in 7-pin bundle for $Re = 1.8 \times 10^5$

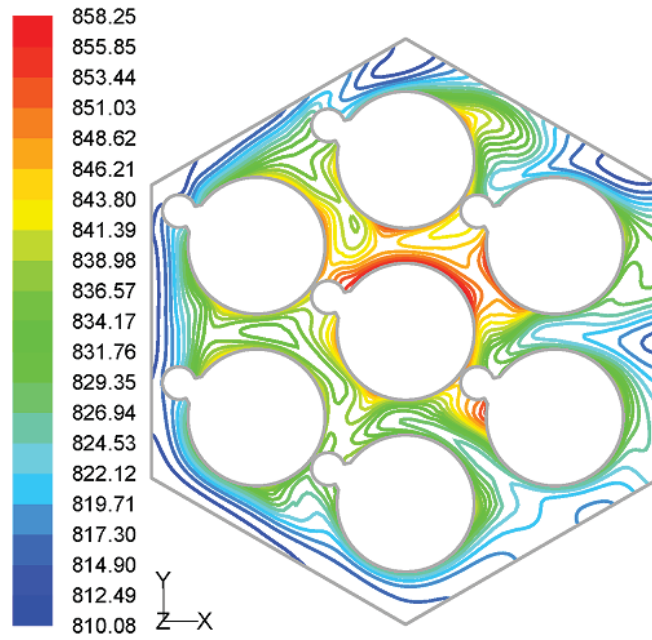


Fig. 6.7b Cross-stream temperature field (K) at $Z = 1.203$ m in 7-pin bundle for $Re = 1.8 \times 10^5$

Evolution of friction factor in the entrance region using Eq. (3.18) is depicted in Fig. 6.8 for various values of Reynolds number at a particular helical pitch. The variation of friction factor in the entrance region of a wire-wrap bundle differs in two ways from that for pipe flow. In the case of pipe or duct flow, the friction factor monotonically decreases in the entrance region and attains a constant value in the fully developed region. But, in the case of

a wire-wrap rod bundle, the friction factor is not constant and it fluctuates periodically over a mean value. The variation/fluctuation over a particular helical pitch corresponds to the position of helical wire with respect to the hexcan wall.

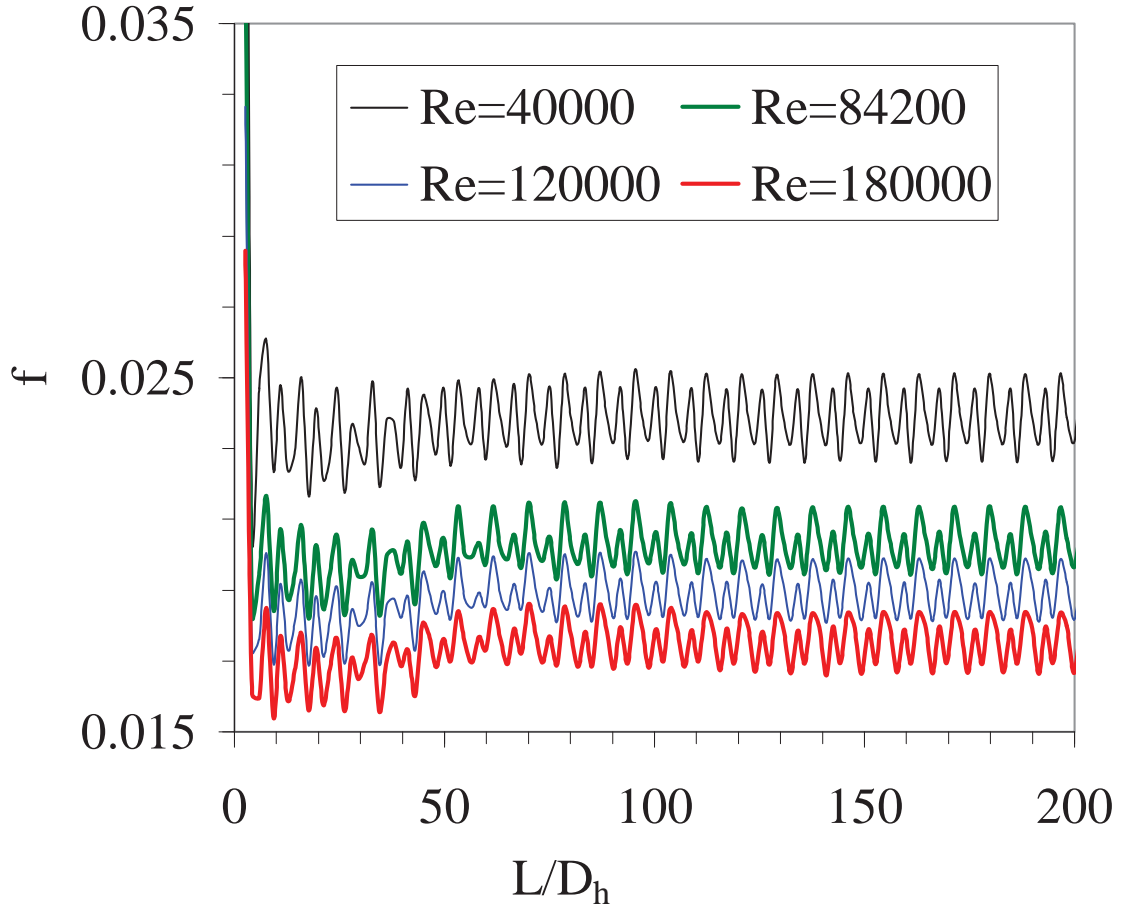


Fig. 6.8 Friction factor development for various values of Reynolds number [$H/(D_w+D_r) = 24.4$]

The fluctuation about the mean value is $\pm 5\%$ for the Reynolds number of 0.4×10^5 . Moreover, the mean value of friction factor in the entrance region reduces below the mean value in the fully developed region. It reduces upto 10% when compared to the fully developed value, for the Reynolds number of 1.8×10^5 . It appears that such results have not been reported in open literature so far.

Evolution of global Nusselt number determined from Eq. (3.24) is depicted in Fig. 6.9 for various values of Reynolds number. The variation of Nusselt number in the entrance

region is also completely different from that in pipes. The Nusselt number passes through three minima before attaining fully developed periodic fluctuations. The Nusselt number attains full development within $L = 200 \times D_h$ in all the cases and this is about 4 times the helical pitch. The lowest heat transfer coefficient is at the second minimum and it is about 8% less than the fully developed mean value in the case of $Re = 1.8 \times 10^5$. In the fully developed region, periodic fluctuation which repeats itself for every helical pitch is observed. This fluctuation is found to be in phase with that observed in friction factor. The amplitude of fully developed fluctuation is $\sim 2\%$ for $Re = 0.4 \times 10^5$, whereas it is much less for higher Reynolds numbers.

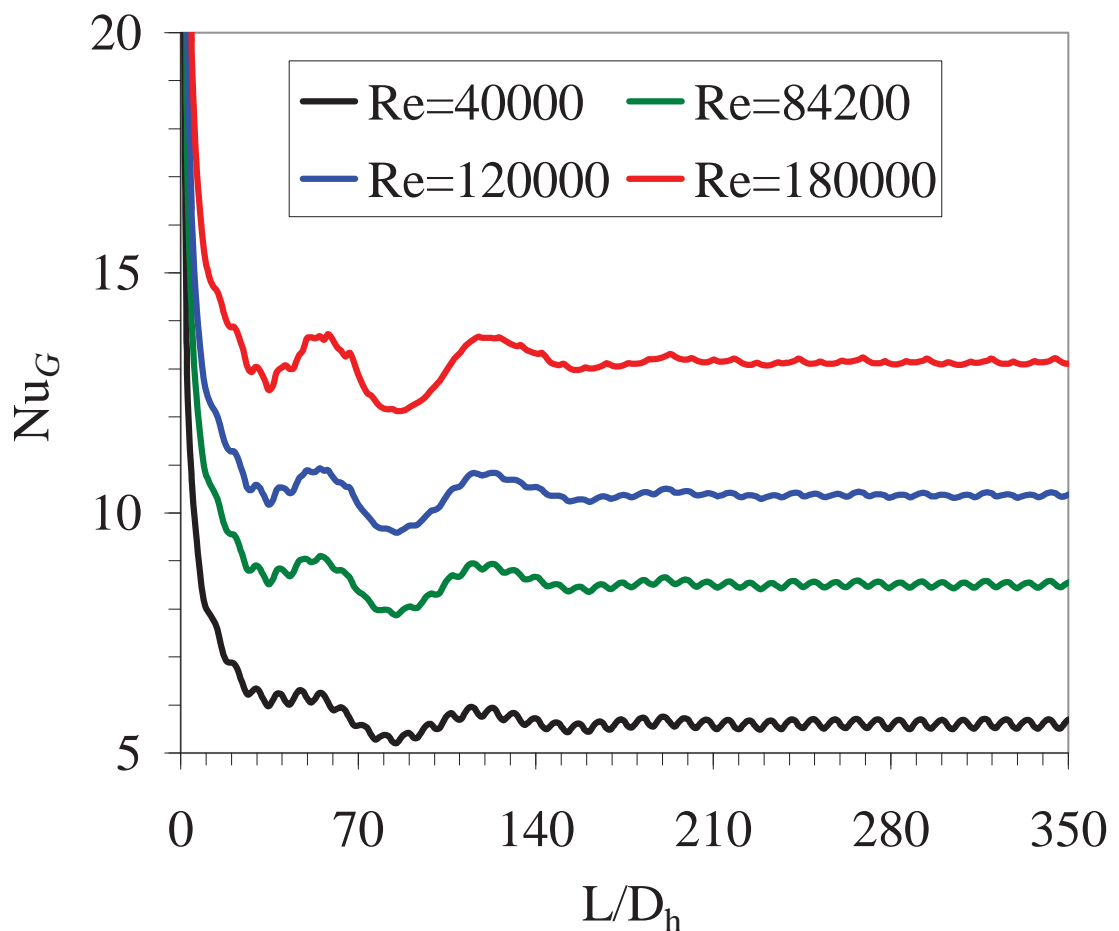


Fig. 6.9 Nusselt number development for various values of Reynolds number [$H/(D_w + D_r) = 24.4$]

Reynolds analogy is known to relate turbulent momentum and heat transfers. The following correlation given by (Bejan, 2004) is reported for liquid metal pipe flow.

$$\frac{S_t}{\left(\frac{f}{2}\right)^{1/2}} \cong (0.11 * \text{Re}^{-0.05}) \text{Pr}^{-0.07} \quad (6.1)$$

where, Stanton number (S_t) = $\frac{h}{\rho C_p w}$

Fully developed values of f , Nu_G and S_t as well as the ratio of Left Hand Side (*LHS*) / Right Hand Side (*RHS*) of Eq. (6.1) are presented in Table-6.4 for various values of Reynolds numbers. It is seen that the ratio of *LHS* / *RHS* is of the order of unity demonstrating the existence of analogy between turbulent momentum and heat transfer, validating the present calculations.

Table 6.4 Analogy between turbulent heat and momentum transfer in sodium flow

Re	Nu_G	f	S_t	LHS / RHS
40000	5.61	0.024	0.028	2.77
84207	8.51	0.020	0.020	2.25
120000	10.37	0.019	0.017	2.02
180000	13.13	0.018	0.015	1.81

It is very interesting to note that there is a periodic variation in the properties even at the fully developed region. The amplitude of fluctuation as a percentage of mean value is presented in the Fig. 6.10 for both friction factor and the global Nusselt number. Traditionally the correlations reported for fully developed flow are considered for core design, assuming that flow development effects are insignificant. But, the present study highlights that entrance region effects and the oscillations in the fully developed region have to be properly accounted during FBR core design. Based on the trend of results for 7, 19 and 37 pin bundles studied, it is clear that similar oscillations in friction factor and Nusselt number are expected in the entrance region of 271-pin bundle. Also the amplitude of oscillations increases with the number of rows of pins.

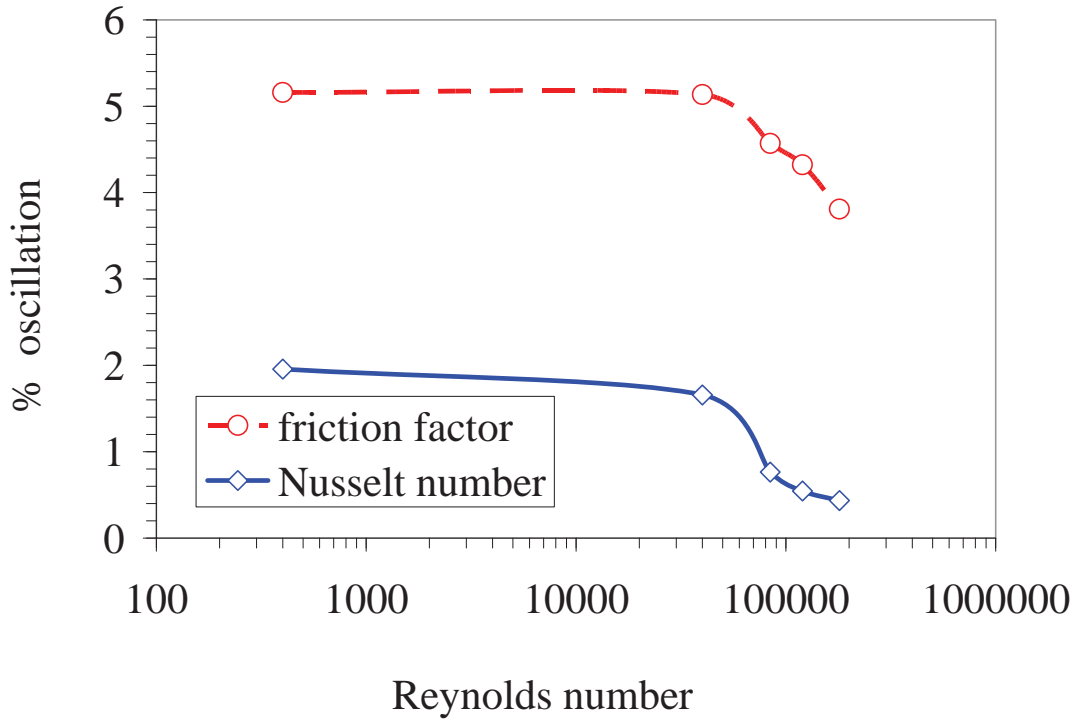


Fig. 6.10 Amplitudes of periodic variation of Nusselt number and friction factor about mean values

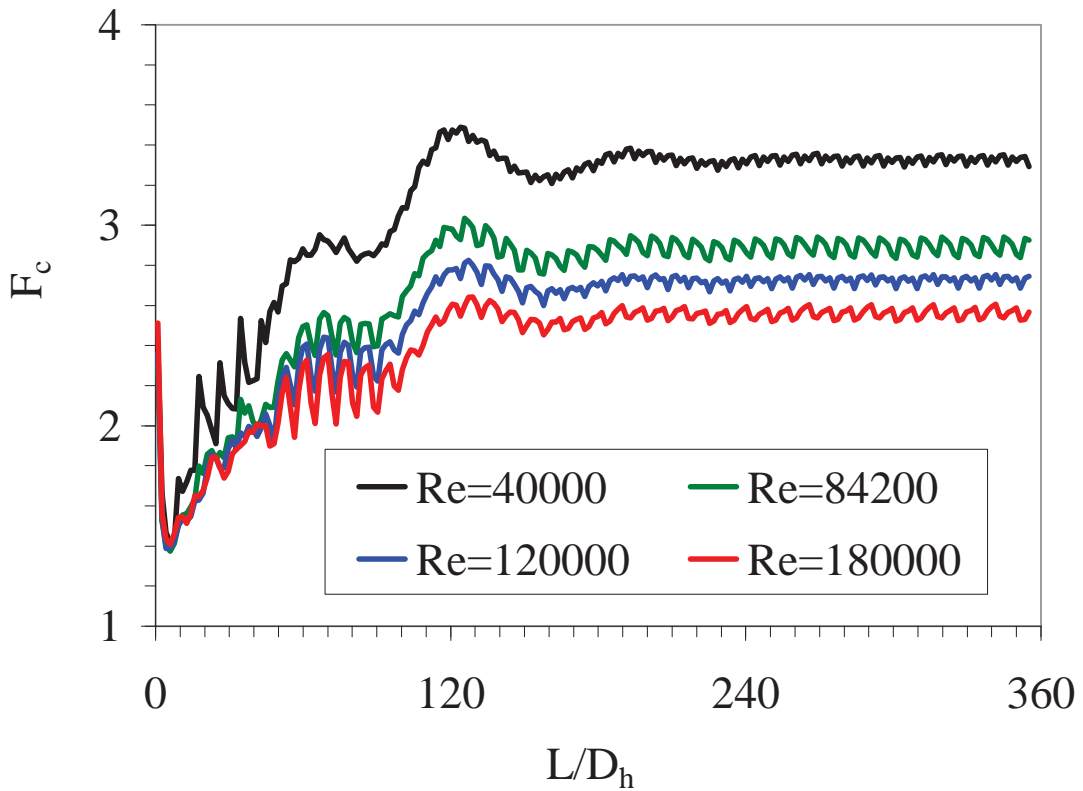


Fig. 6.11a Evolution of hot spot factor for central pin in 7-pin bundle subassembly with $H/(D_w+D_r) = 24.4$

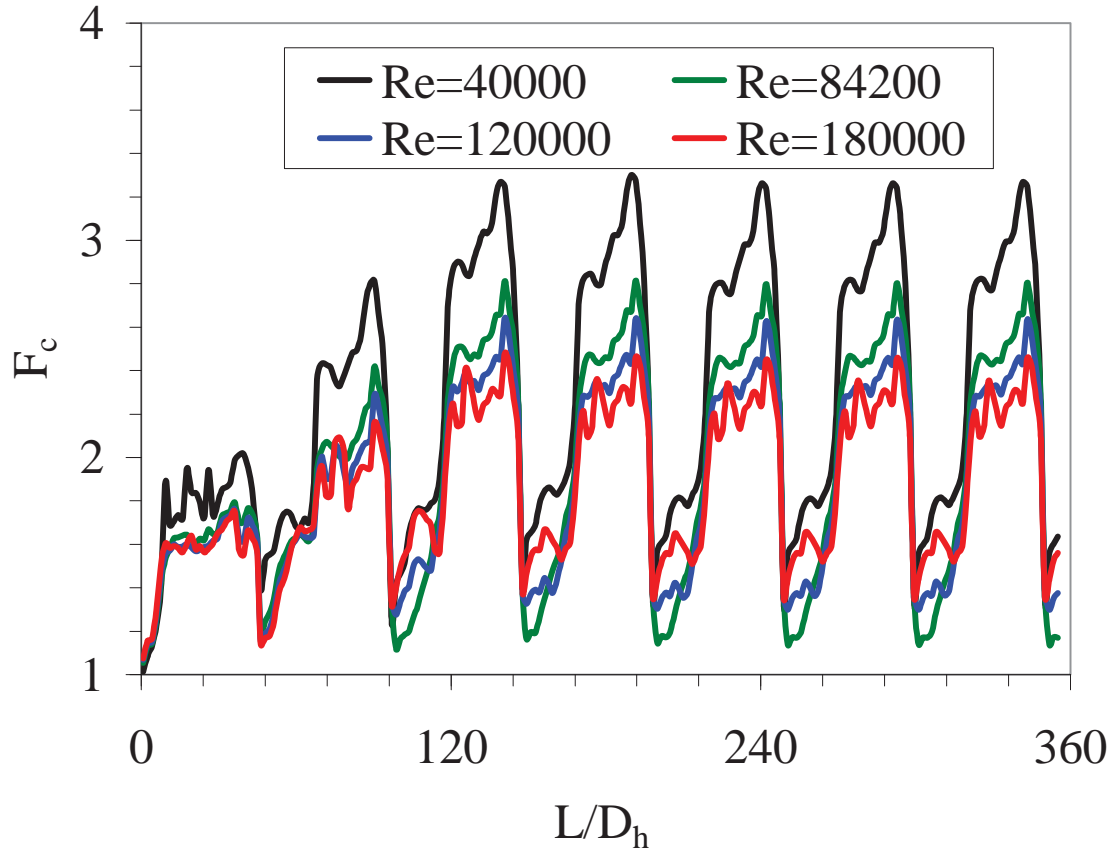


Fig. 6.11b Evolution of hot spot factor for peripheral pin in 7-pin bundle subassembly with $H/(D_w+D_r)=24.4$

The hotspot factor is also a critical parameter in FBR core design. The evolution of hotspot factor for the total length of central pin in the 7-pin fuel bundle configuration determined from Eq. (3.25) is depicted in Fig. 6.11a for various Reynolds numbers. The corresponding value for the peripheral pin is depicted in Fig. 6.11b. It increases from the inlet up to a length of ≈ 2.4 times helical pitch in all the cases. After this maximum, the hot spot factor reduces to attain the fully developed value at $\sim 4 \times H$. The hot spot factor is found to be a function of Reynolds number, with higher value at low Reynolds number. In all the cases studied, the hot spot factor is found to be as high as 3.5. These findings may be useful in the design of the reactor core and in life prediction of fuel pin.

The evolutionary behaviour of hot spot factor in the peripheral clad is different from that of the central clad. In this case, the hot spot factor changes periodically along with

magnitude. One period is equal to one helical pitch. The increase in hot spot factor is large from the first pitch to the second helical pitch. Subsequent variations in magnitude of hot spot factor are small. The peak hot spot factor value is attained at ≈ 2.4 times the helical pitch, after which the range of variation is approximately same. Further, the factor is seen to be a strong function of Reynolds number at low Reynolds number regime. But at high Reynolds number, it exhibits a weak dependence on Reynolds number.

6.2.2 Effect of Helical Spacer Wire Pitch

Based on the previous results, it is decided to carry out a detailed study to understand the effect of helical pitch on flow development. For this purpose, the 7-pin fuel bundle with pitch varying from 100 mm to 300 mm is considered. The hydraulic diameter is same for all these cases, i.e., 3.952 mm and the Reynolds number is 0.842×10^5 . This Reynolds number is chosen based on the conditions prevailing in a typical medium size fast reactor.

The cross-stream velocity for various helical pitches in the fully developed region (end of 7th pitch) is depicted in Fig. 6.12. The local peak cross-stream velocity is the highest for the fuel bundle with 100 mm pitch. The magnitude of cross-stream velocity is seen to be inversely proportional to the helical pitch length. Also, there is a strong correlation between the locations of spacer wire and the peak velocity. Evolution of average cross-stream velocity in the entrance region is depicted in Fig. 6.13 for fuel bundles with various helical pitch values. It is clear from the figure that the flow is fully developed at $L \approx 70 \times D_h$ in all the cases.

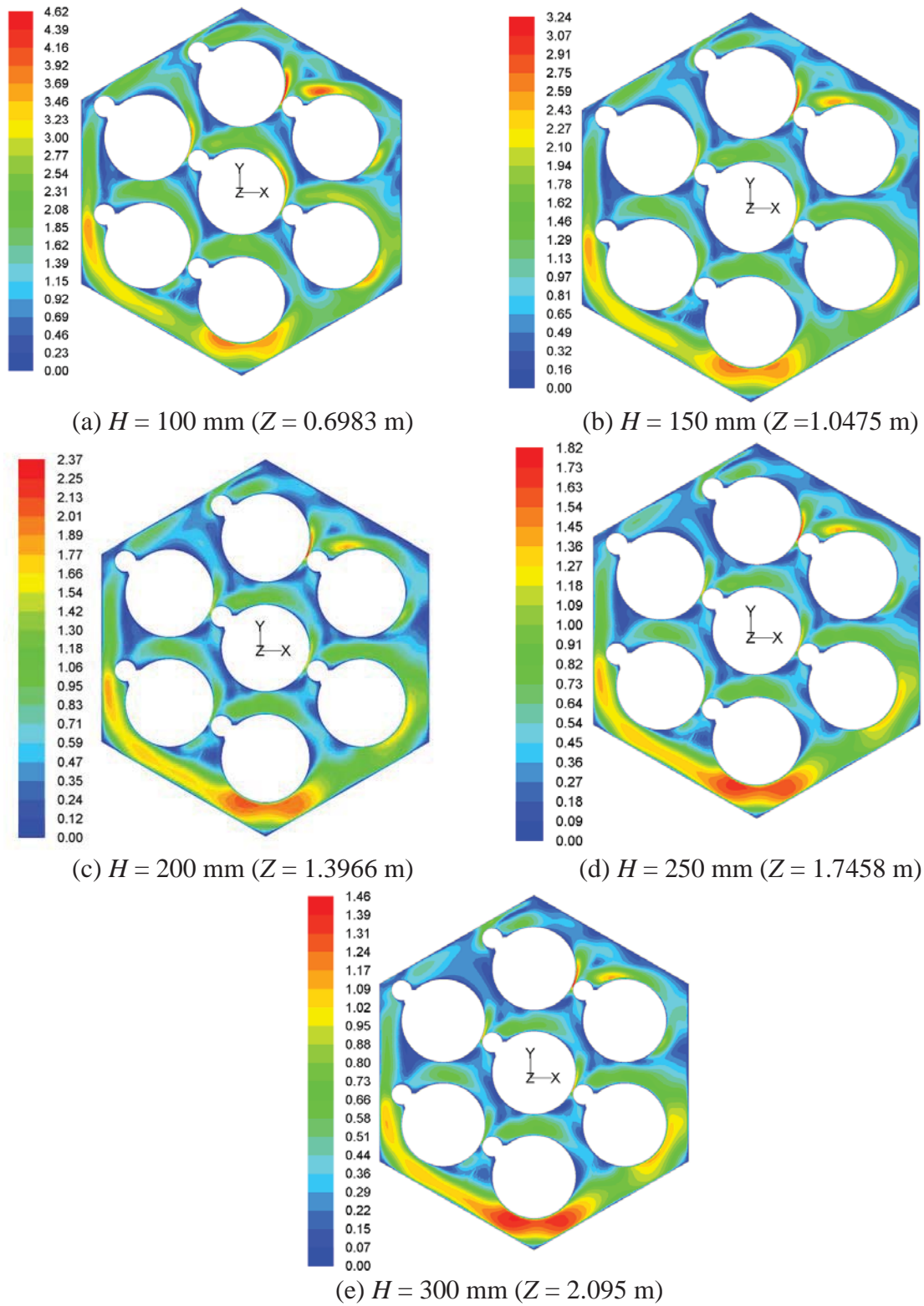


Fig. 6.12 Cross-stream velocity at the end of 7th pitch for 7-pin bundle with helical pitch
 (a) 100 mm (b) 150 mm (c) 200 mm (d) 250 mm and (e) 300 mm for
 $Re = 0.842 \times 10^5$

Cross-stream flow attains full development at lengths of 2.76, 1.84, 1.38, 1.1 and 0.92 times the corresponding helical pitch in the case of 100 mm, 150 mm, 200 mm, 250 mm and 300 mm pitch respectively. The corresponding values of physical lengths are 276, 274, 275, 275, and 276. This suggests that the physical value of flow development length is not significantly affected by the helical pitch. So, this is the minimum length required to be modeled for any type of flow studies. The average cross-stream velocity in the fully developed region for 100 mm helical pitch is $\approx 26\%$ of the axial velocity. As the pitch length increases, the cross-stream velocity decreases drastically.

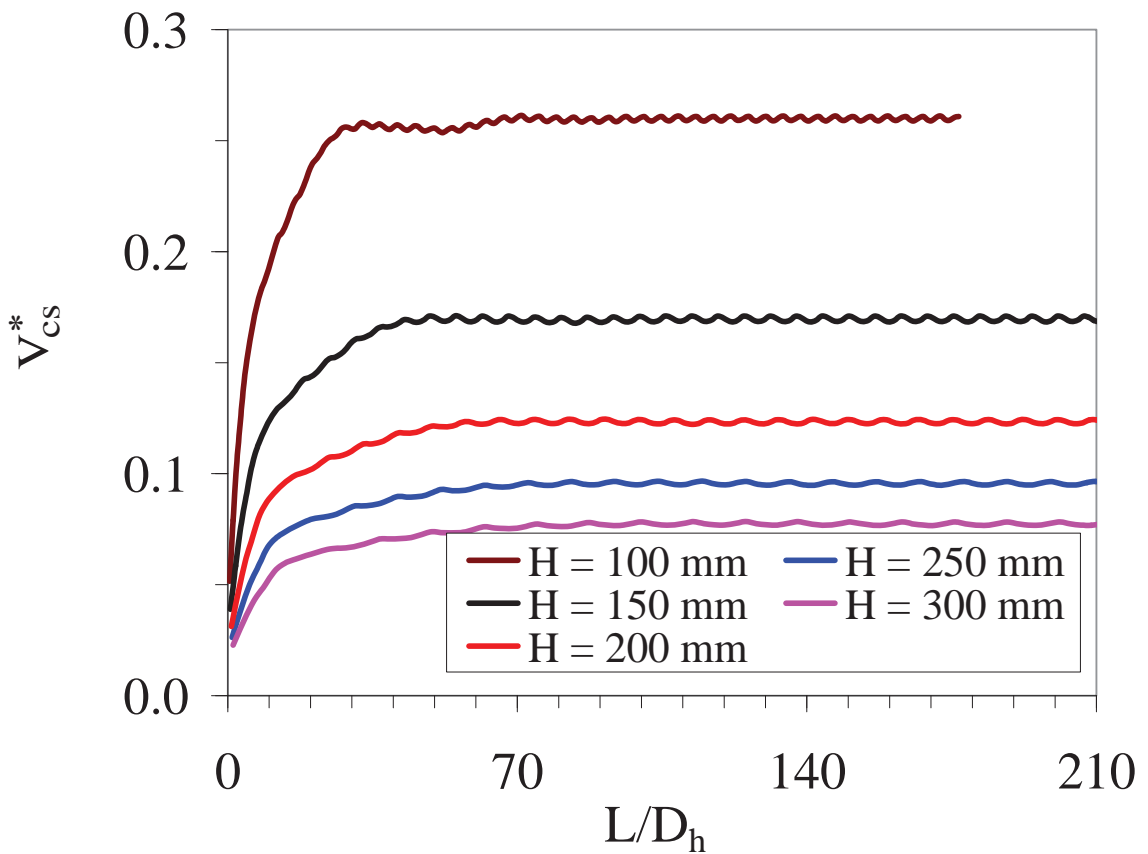


Fig. 6.13 Non-dimensional cross-stream velocity for $Re = 0.842 \times 10^5$

Evolution of friction factor determined from Eq. (3.18) is depicted in Fig. 6.14 for fuel pin bundles with five different helical pitches. It is clear that shorter the helical pitch, larger is the friction factor due to enhanced cross-stream velocity (Fig. 6.13). In the fully

developed region, the average pressure drop in the 100 mm helical pitch is 26% higher than that of the 150 mm helical pitch. Further, the amplitude of periodic oscillation about mean value in the developed region is 11% for 100 mm pitch and it reduces to 4% in 300 mm pitch. The mean value in the entrance region falls steeply for 100 mm helical pitch than for the larger pitches.

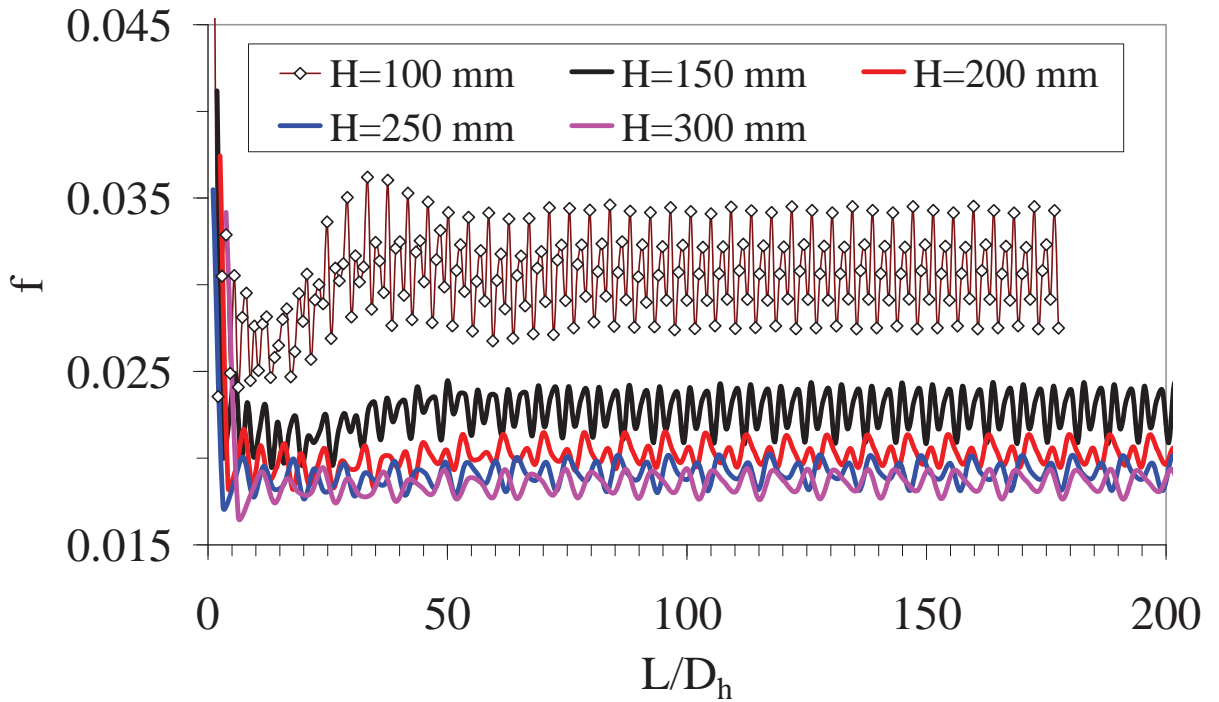


Fig. 6.14 Friction factor development with different helical pitch for $Re = 0.842 \times 10^5$

Evolution of global Nusselt number determined from Eq. (3.24) is depicted in Fig. 6.15 for various helical pitch values. Periodic oscillation is present in the Nusselt number of fully developed region but the magnitude is smaller than that observed in friction factor. Present results indicate that the helical spacer pitch has a pronounced influence on the heat transfer coefficient. The predicted fully developed global Nusselt number decreases from 13.3 to 6.6 when the helical pitch increases from 100 mm to 300 mm. It can be seen from the figure that there are three minima in the entrance region before Nu_G attains the fully developed value in all these cases.

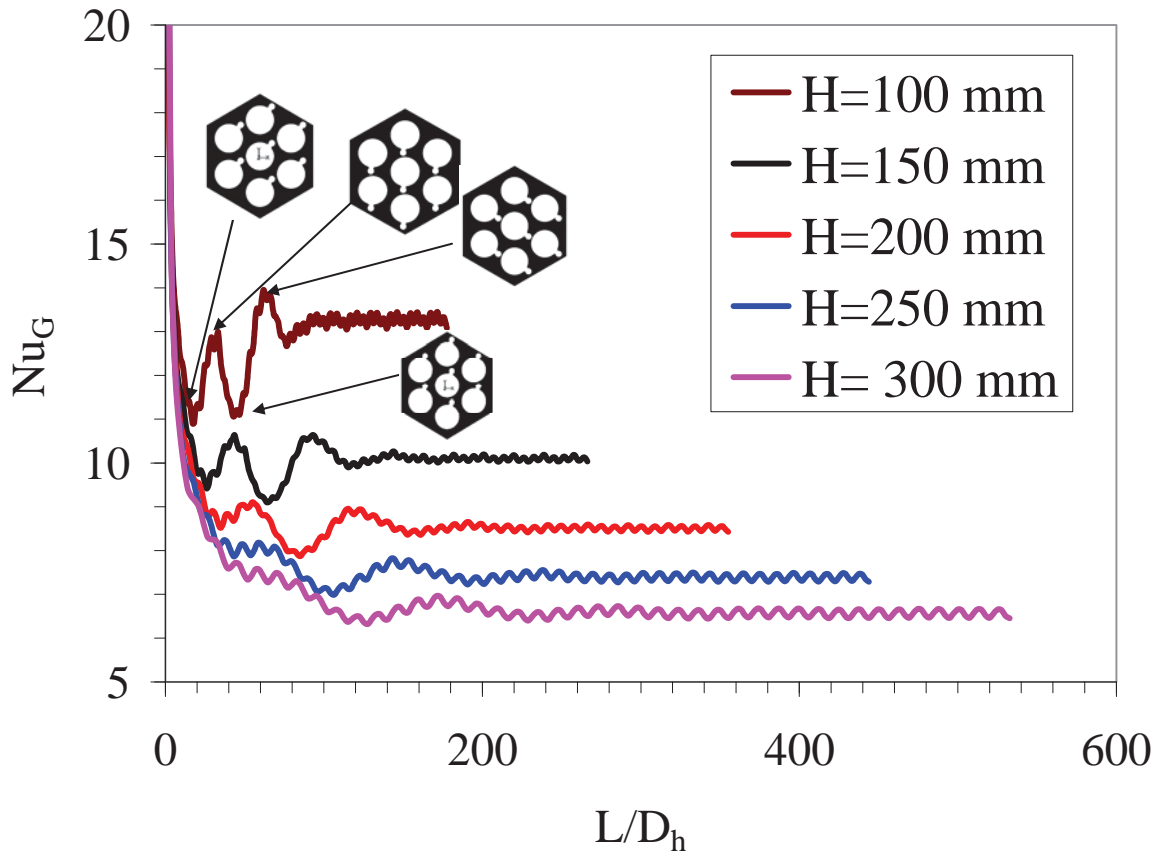


Fig. 6.15 Nusselt number development with different helical pitch for $Re = 0.842 \times 10^5$

The lowest minimum is ~18% less than the fully developed value for 100 mm pitch. The corresponding value for 300 mm pitch is only 4%. This highlights an important point that the core design based on fully developed Nusselt number correlations is not conservative. The variation of fully developed global Nusselt number, as a function of helical pitch is depicted in Fig. 6.16a. Also shown in the same figure is the fully developed friction factor. On moving from 300 mm to 200 mm, it is seen that the increase in Nusselt number is more than the increase in pressure drop. On reducing the helical wire pitch to 150 mm from 200 mm, the friction factor increases by 7% and the corresponding increase in Nusselt number is only 4%. Among all the configurations 250 mm helical pitch gives an optimum performance.

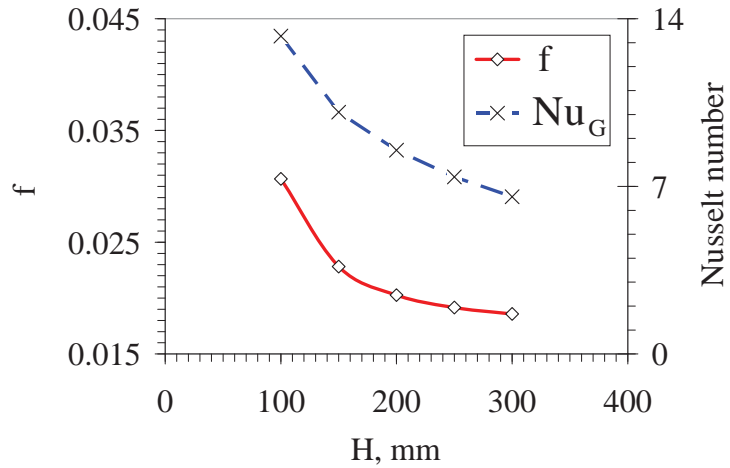


Fig. 6.16a Comparison of fully developed mean friction factor and mean Nusselt number variations with helical pitch for $Re = 0.842 \times 10^5$

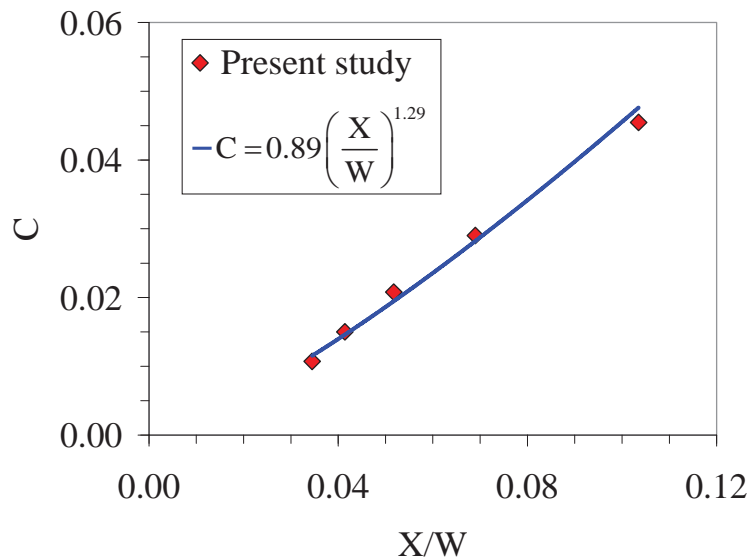


Fig. 6.16b Dependence of coefficient 'C' on triangular pitch and helical pitch

It is decided to propose a correlation for Nusselt number which will exemplify a clear dependency on helical pitch variation. For this, the correlation form proposed by Kazimi and Carelli (1976) is considered. By using the present data of Nusselt number and Peclet number, the coefficient (C) determined from Eq. (6.2) is depicted in Fig. 6.16b. Also shown in the figure is the power law fit for the present data which matches well with an RMS (Root mean square) value of 0.989 for the correlation coefficient 'R'.

All the helical pitches (in the range $H = 100$ mm to 300 mm) are considered except 200 mm which has already been used. The Reynolds numbers considered are 0.40×10^5 and 1.8×10^5 . For fuel pin bundle heat transfer, Kazimi and Carelli (1976) proposed a Nusselt number correlation of the form.

$$Nu = 4.497 + C (Pe)^{0.86} \quad (6.2)$$

In the present work, following Kazimi and Carelli (1976) a correlation in the form of Eq. (6.3) is proposed for fuel pin bundles with helical spacer wire with fully developed flow conditions,

$$Nu = 4.497 + 0.89 \left(\frac{P_t / D_r}{H / (D_r + D_w)} \right)^{1.29} (Pe)^{0.86} \quad (6.3)$$

The above correlation fits the CFD predictions for Nusselt number within $\pm 4\%$. The applicable range for this correlation is, $1.1 \leq (P_t / D_r) \leq 1.4$, $12 \leq (H / (D_r + D_w)) \leq 36$ and $198 \leq Pe \leq 890$. The proposed correlation is compared with the existing correlations as depicted in Fig. 2.1b. The correlation developed in the present study is found to compare very well with that of Kazimi and Carelli (1976), Subbotin et al. (1965) and Borishanskii et al. (1969). The local Nusselt number (Nu_θ) in the fully developed region (at the start of 7th pitch) for the central pin determined from Eq. (3.22) is depicted in Fig. 6.17a for various helical pitch configurations. The position of the spacer wire with respect to axis and the direction of ‘ θ ’ are indicated in Fig. 6.17b along with the central (C) and peripheral (P) pins. The wire-wrap falls between $\theta = 141^\circ$ and 171° . It is clear that Nu_θ is inversely proportional to the helical pitch, i.e., it is highest for 100 mm pitch and lowest for 300 mm pitch. The peak Nu_θ occurs between $\theta = 240^\circ$ and 300° for all these cases where the cross-stream velocity is high.

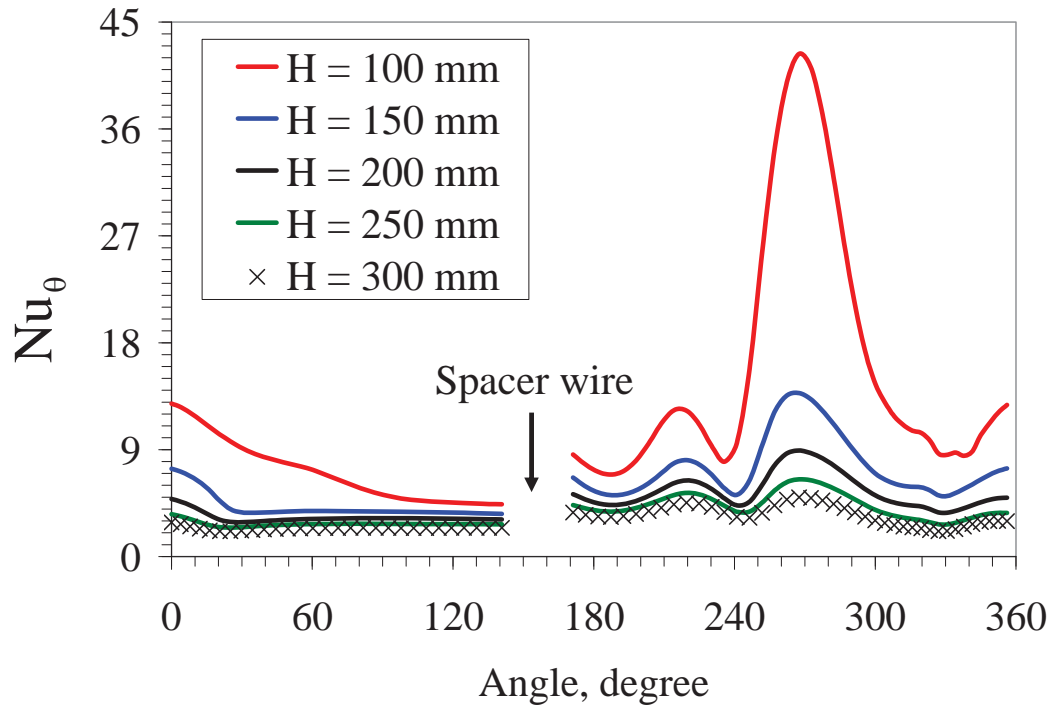


Fig. 6.17a Circumferential variation of local Nusselt number at the start of 7th pitch for central clad with $Re = 0.842 \times 10^5$

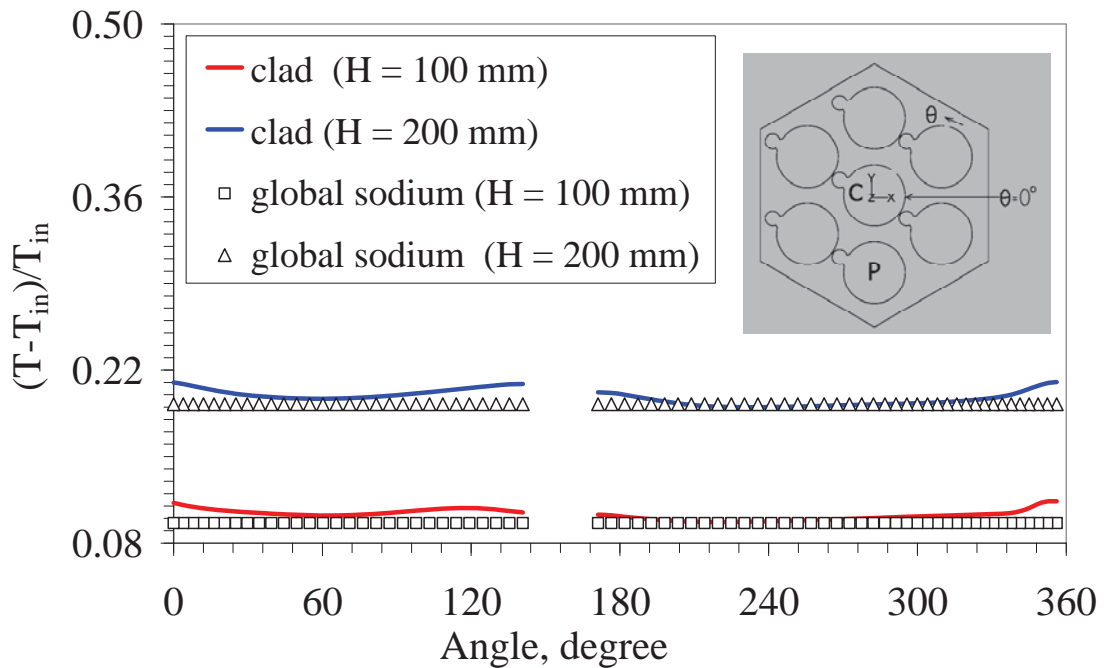


Fig. 6.17b Non-dimensional temperature at the start of 7th pitch for peripheral clad (C - central pin and P - peripheral pin)

The corresponding peripheral pin temperature is depicted in Fig. 6.17b for two helical pitch configurations. Also given in the figure is the global bulk sodium temperature, T_{G-Na} .

Unlike the central pin, the local Nusselt number in peripheral pin turns out to be negative at some circumferential places. So, it is decided to plot the temperature of pins as well as bulk sodium temperature. It is evident from the figure that the sodium temperature is less for short helical pitch values. The local clad temperature is either close to the global sodium temperature or even less than the global sodium temperature. However, the local clad is always hotter than the local sodium temperature.

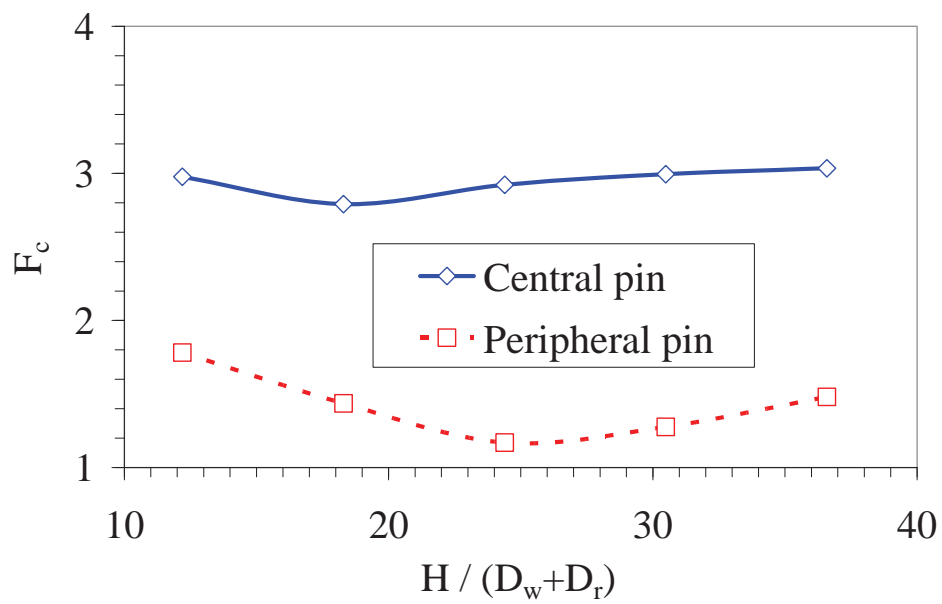


Fig. 6.18 Hotspot factor variation with helical pitch for $Re = 0.842 \times 10^5$

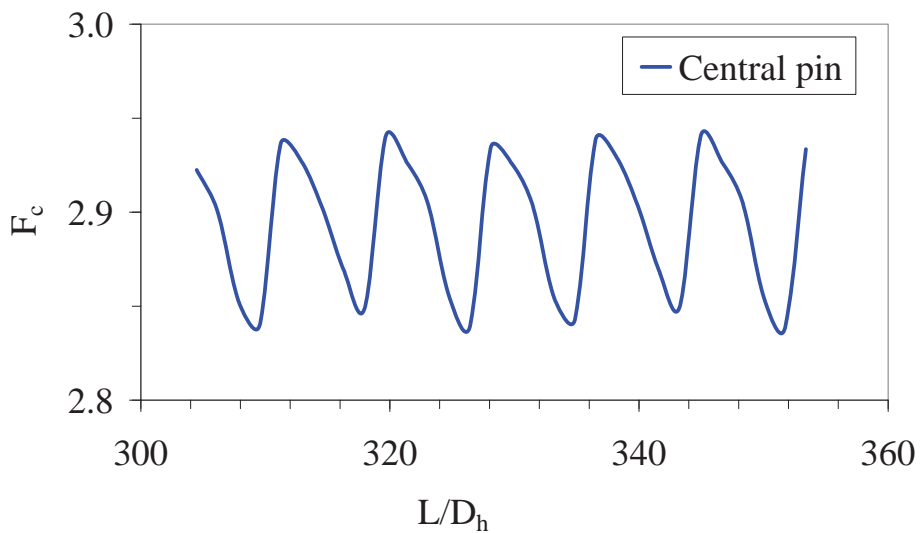


Fig. 6.19 Hotspot factor at 7th pitch for 200 mm helical pitch configuration and $Re = 842 \times 10^5$

The local hot spot factor (F_c) in the fully developed region (at the start of 7th pitch) for the central pin as determined from Eq. (3.25) is depicted in Fig. 6.18 for various helical pitch configurations. Unlike the Nusselt number, the hot spot factor is almost the same in all these cases except for $H = 150$ mm. The mean value of the factor is 6% less than in the other cases. Also shown in the figure is the hot spot factor for the peripheral pin. Hot spot factor for peripheral pin decreases for change in helical pitch value 100 mm to 250 mm and it increases when helical pitch changes from 250 mm to 300 mm. At 200 mm pitch it is predicted to be the lowest i.e., it is 34% less than in the case of 100 mm and its 26% less than in the case of 300 mm pitch.

Further, the local hot spot factor along the 7th pitch for the central pin is presented in Fig. 6.19. Small oscillations can be seen about its mean value. There is one cycle for every 33.33 mm axial length which is equal to 1/6th of helical wire-wrap pitch of 200 mm. This occurs because of the wire rotation along with the cross-stream flow.

In addition to the dependency of flow and thermal parameters on helical pitch the turbulent parameters are evaluated. For this purpose, two parameters viz., turbulent kinetic energy (k) and turbulent dissipation rate (ε) are considered. The average turbulent kinetic energy along the flow direction is depicted in Fig. 6.20a. It does not vary much with the swirl. Because, the maximum difference is only ~6% between 100 mm and 150 mm helical pitches. Further increase in helical pitch does not alter the turbulent kinetic energy. In the entrance region, the turbulent kinetic energy also reduces below that of fully developed value. The average turbulent dissipation rate along the flow direction is depicted in Fig. 6.20b. Contrary to the turbulent kinetic energy, dissipation rate changes when helical pitch changes. However the highest value is in 100 mm helical pitch, where the swirling (secondary flow) is large.

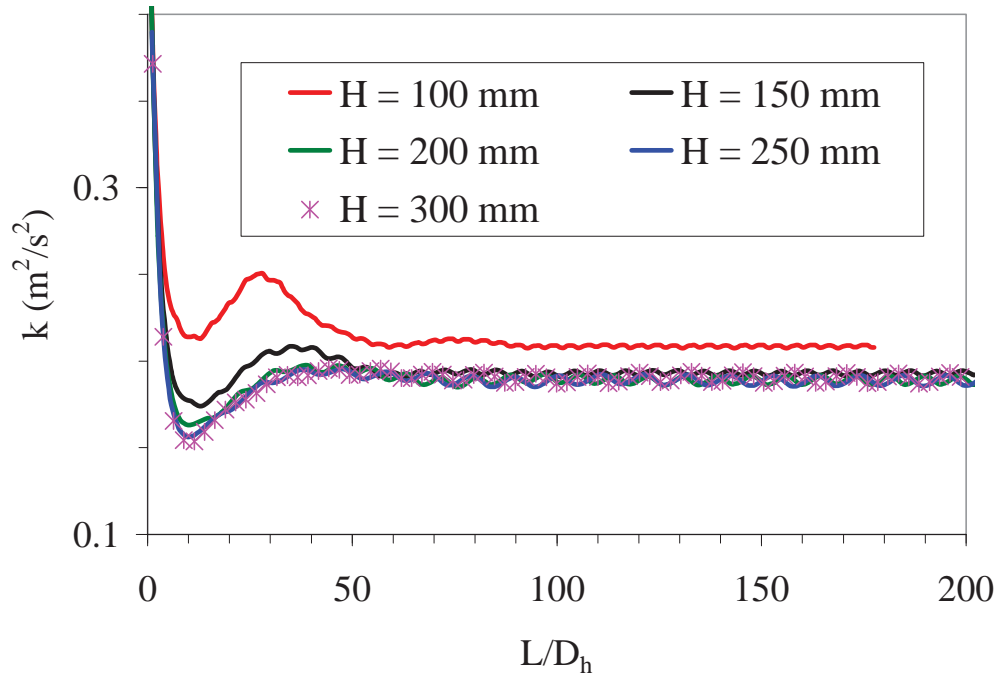


Fig. 6.20a Average turbulent kinetic energy variation with different helical pitch for $Re = 0.842 \times 10^5$

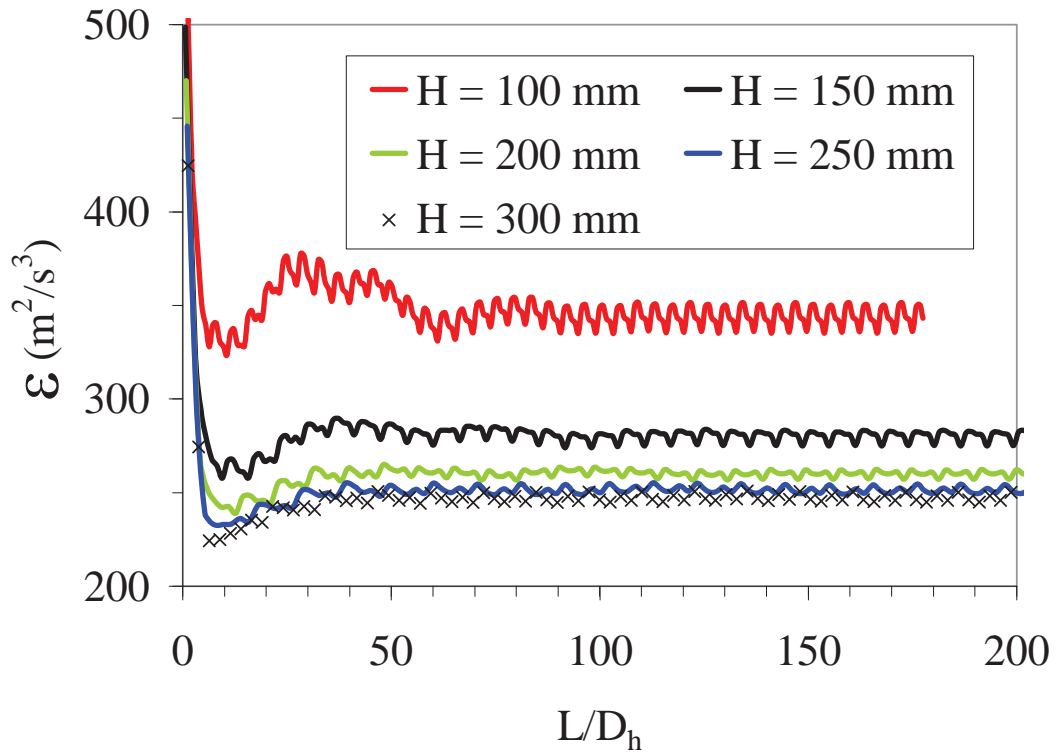


Fig. 6.20b Average turbulent dissipation rate variation with different helical pitch for $Re = 0.842 \times 10^5$

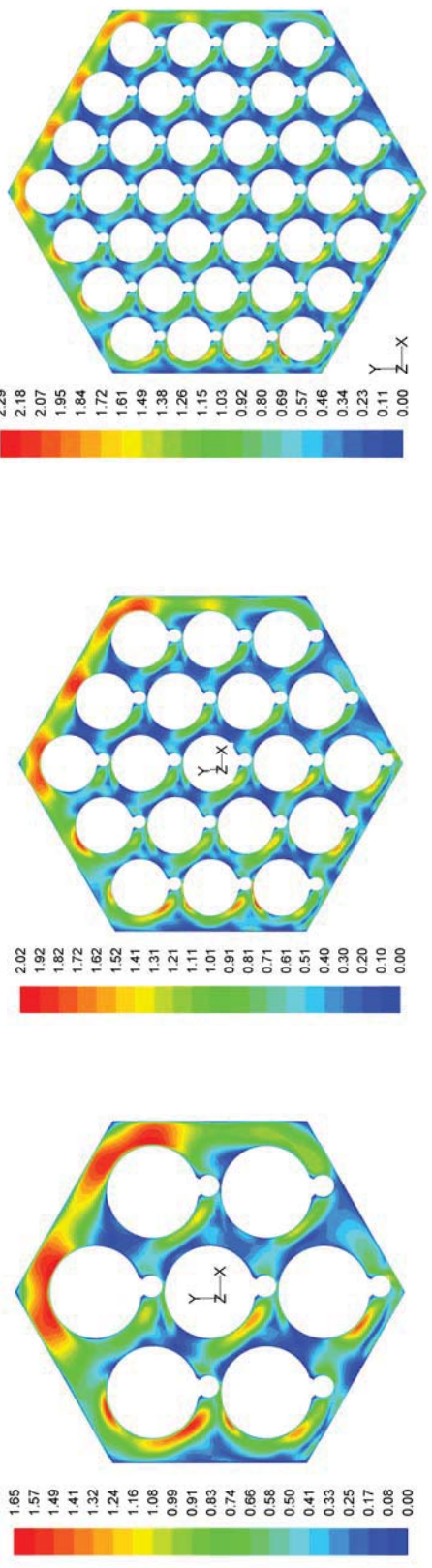
6.2.3 Effect of Number of Fuel Pins

In order to understand the effect of the number of fuel pins on entrance flow characteristics, the number of pins is varied from 7 to 37. The value of helical pitch is maintained as 200 mm in all the cases. The computer memory limits the number of pins that could be considered. The hydraulic diameter for 7, 19 and 37 pins is 3.952, 3.905 and 3.846 mm respectively and the corresponding Reynolds number is 0.842×10^5 , 0.832×10^5 and 0.819×10^5 respectively. The inlet velocity is kept constant for all these cases at 6.8 m/s.

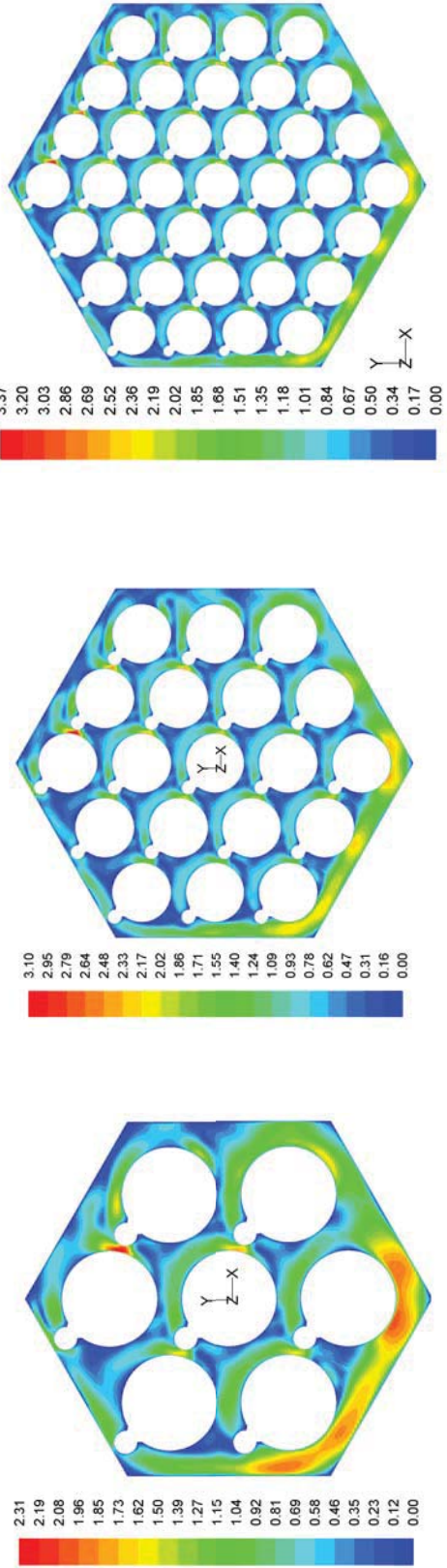
The cross-stream velocity values in bundles with various number of pins at two different axial positions, viz., one at entrance region ($L = 17.9 \times D_h$) and the other at fully developed region ($151 \times D_h$) are depicted in the Fig. 6.21a. It is seen from the figures that the peak cross-stream velocity increases when the number of pins increases for identical inlet velocity. This is due to the fact that (i) the cross-stream velocity is produced by helical spacer wire and (ii) it is proportional to the number of wires in the bundle.

The circumferential velocity prevails predominantly in the peripheral sub-channels adjoining a face of the hexcan. The mean non-dimensional cross-stream velocity magnitude evolution in the entrance region is depicted in Fig. 6.21b for all the three fuel pin bundles up to $L = 210 \times D_h$. From this figure it is understood that the flow attains full development within $70 \times D_h$, $90 \times D_h$ and $L = 110 \times D_h$ in 7, 19 and 37 pin bundles respectively. Though the flow requires different lengths for full development, the final average cross-stream velocity is the same for all the bundle configurations. At the same time the local peak velocity is more if number of pins is more. It is 34% higher in the bundle with 19-pins than in 7-pin bundle, in the fully developed region ($L = 15 \times D_h$). Similarly, it is 46 % higher in the bundle with 37-pins compared to the bundle with 7-pins. This indicates that the velocity non-uniformity is large in bundles with large number of pins. This will manifest into large temperature non-uniformity. Further, the mean cross-stream velocity in the entrance region exceeds the fully

developed value in large pin bundles. Within one axial pitch length, six peaks and six troughs are seen in the velocity exhibiting cyclic symmetry for every 1/6th pitch.



at $L/D_h = 17.9$



at $L/D_h = 151$

Fig. 6.21a Cross-stream velocity contours in 7, 19 and 37 pin fuel bundles

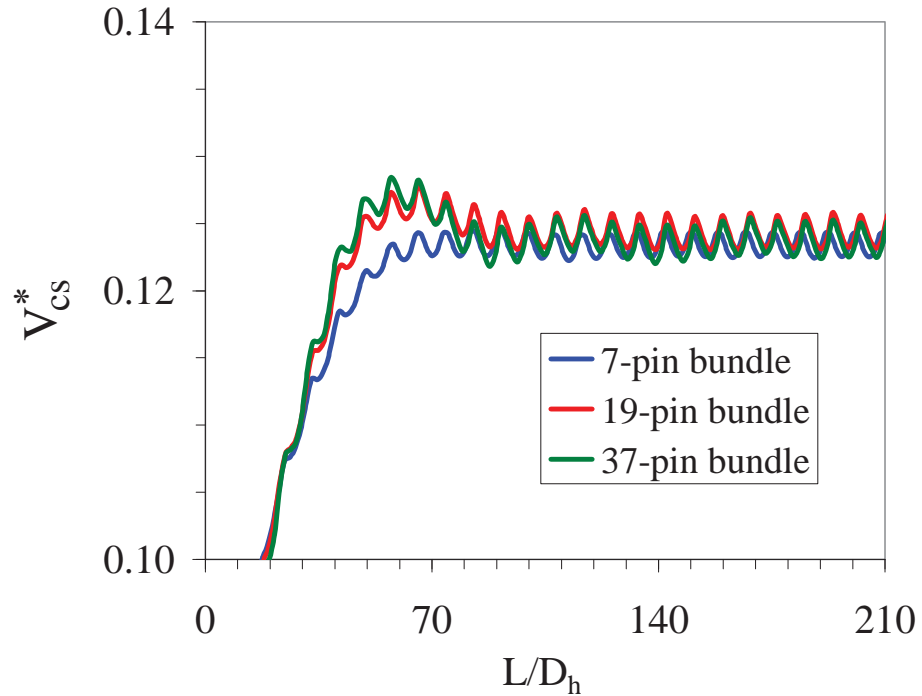


Fig. 6.21b Cross-stream velocity in various fuel pin bundles

Evolution of friction factor determined from Eq. (3.18) is depicted in Fig. 6.22a for 7, 19 and 37 fuel pin bundles. Also, an expanded view of friction factor in the entrance region is depicted in Fig. 6.22b. It is seen that in the case of 19 and 37 pin bundles, the average friction factor in the entrance region falls below the fully developed value before recovery. In the fully developed region, the friction factor exhibits a periodic oscillation along the length. There are six pronounced peaks and troughs in one axial pitch length. But, unlike the cross-stream velocity whose fluctuations were observed to be nearly sinusoidal with single frequency value, the friction factor fluctuations appear to have multiple frequency values. The amplitude of periodic oscillation is larger when the number of pins is more. The amplitudes of oscillation in 7, 19 and 37 pin bundles are respectively $\approx 5\%$, 6% and 10% of the corresponding mean values.

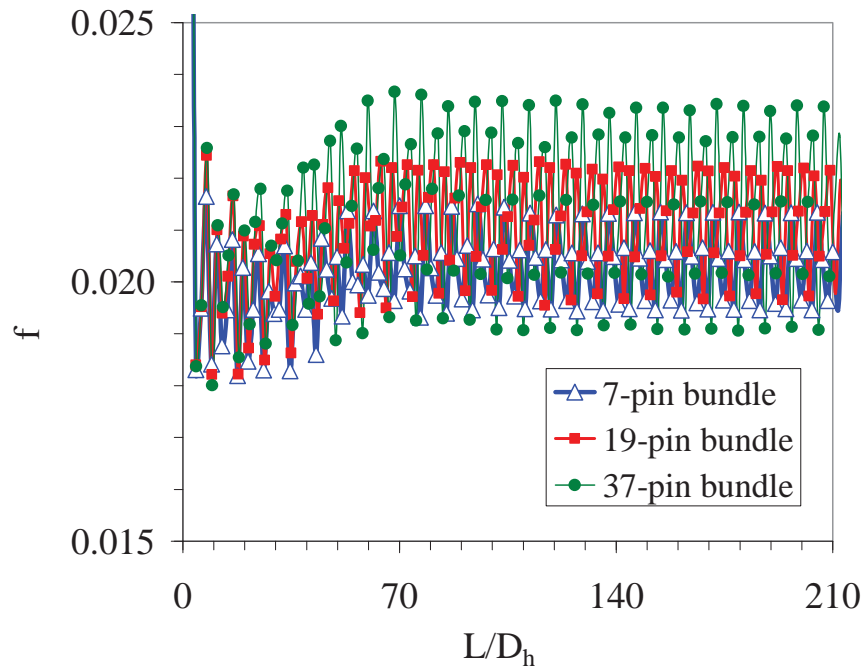


Fig. 6.22a Friction factor development in fuel pin bundles

The circumferential velocity is mainly induced by the presence of wire-wrap. It is further augmented by the fluid ejection from the boundary layers developing near the internal pins. The fluid diverted towards the gap between the peripheral pins and hexcan is more if the number of pins is large. But, the area for circumferential flow in the gap between peripheral pins and hexcan is the same for all the pin bundles. This perhaps is the reason for the increasing amplitude with increase in number of pins. Further, though the amplitudes of oscillation are different for various pin bundles, the average friction factor value in the fully developed region is almost the same.

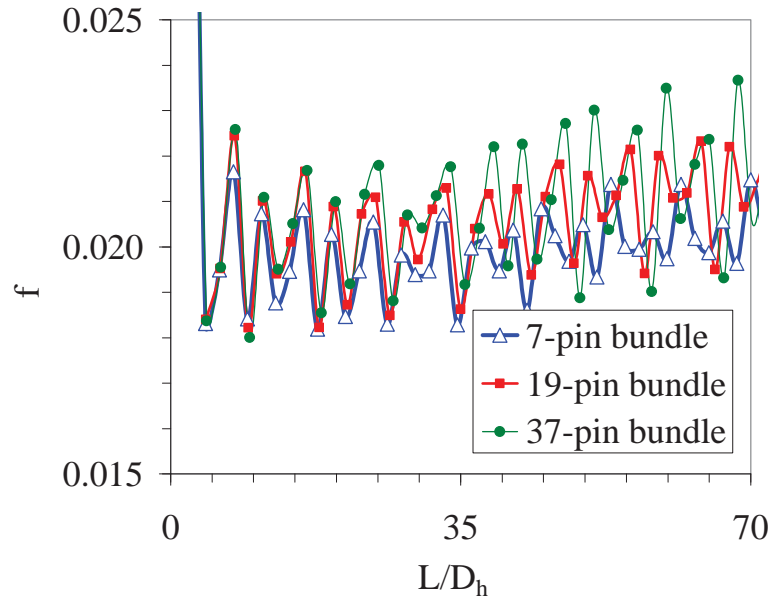


Fig. 6.22b Expanded view of friction factor development in fuel pin bundles

The corresponding global Nusselt number determined from Eq. (3.24) is depicted in Fig. 6.23 for 7, 19 and 37 pin bundles. In the initial part of the entrance region ($L/D_h \leq 100$), the Nusselt number is higher if the number of pins is larger. But, in the later part of the entrance region, the converse is true. This is because the cross-flow enhances the heat transfer rate significantly. Cross-flow resistance is proportional to the number of pins in the bundle and this also restricts the flow communication among sub-channels in the entrance region. Also there is an effect of combination of boundary layer growth and cross-flow development. In the later part, both the velocity boundary layer and the cross-flow are fully developed. The Nusselt number attains full development within an axial length $200 \times D_h$, i.e., for 7-pin bundle. But, for 19-pin bundle it takes over $50 \times D_h$, which is equal to 10 times the helical wire pitch. Nusselt number in 37-pin bundle is not fully developed upto $250 \times D_h$.

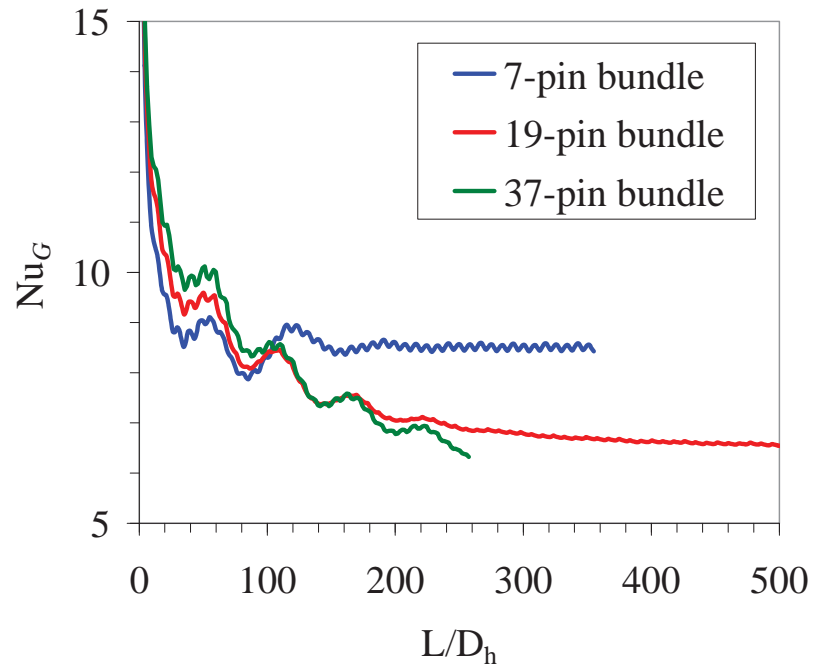


Fig. 6.23 Global Nusselt number development in fuel pin bundles

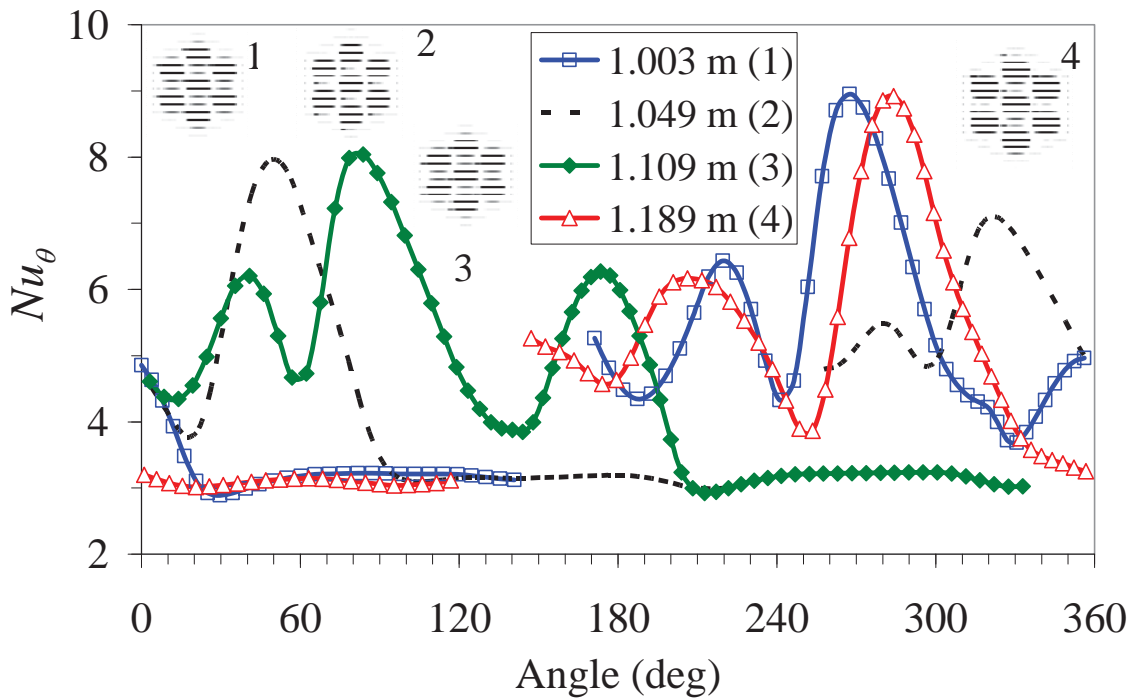


Fig. 6.24a Circumferential Nusselt number for central pin in 7-pin bundle at the 6th helical Pitch

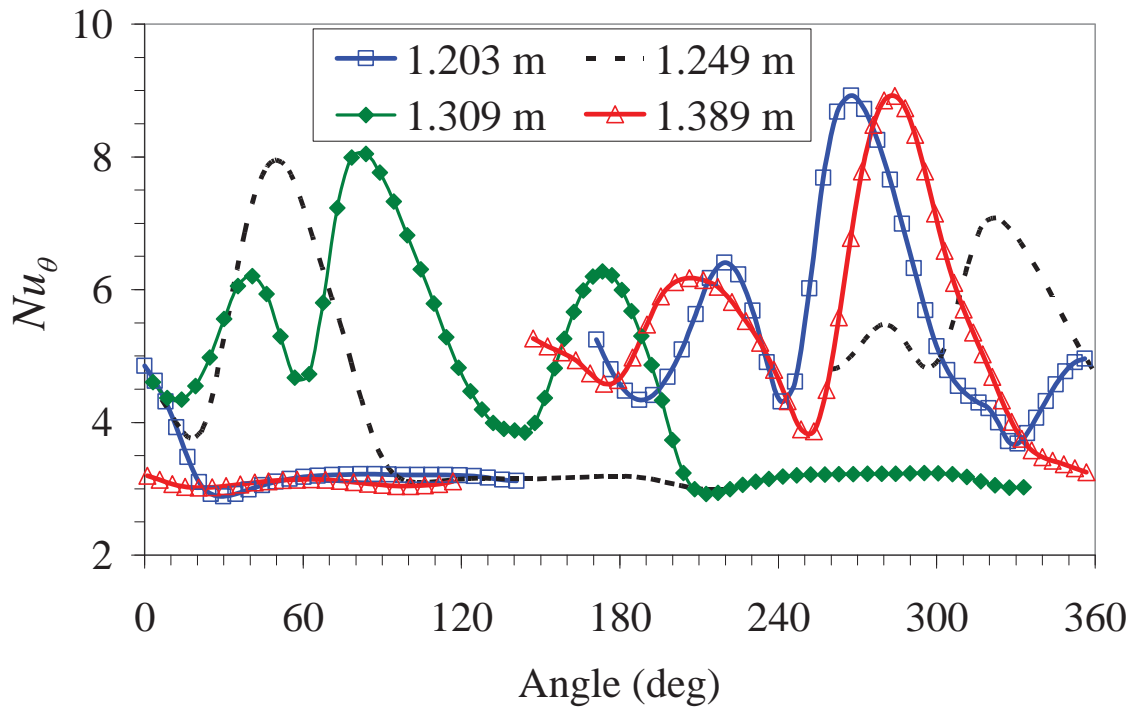


Fig. 6.24b Circumferential Nusselt number for central pin in 7-pin bundle at the 7th helical pitch

The 7-pin bundle configuration is chosen for detailed investigation of local Nusselt number. The local circumferential Nusselt number determined from Eq. (3.19) is depicted in Fig. 6.24a for central pin at four axial positions (at 1.003 m, 1.049 m, 1.109 m and 1.189 m) in the 6th pitch. Also shown in the figure are the wire-wrap positions with respect to axis and they are numbered as 1, 2, 3 and 4 in the sequence of axial position. The direction of ' θ ' is indicated in Fig. 6.17b along with the central (C) and peripheral (P) pins. There are three prominent peaks in the Nusselt number in each case. The peaks occur in the direction of wire rotation and in front of the wire. Considering 1.109 m (case no-3) length case, first rise starts within 10° in front of the wire position and ends around 60° from the helical wire position. The second rise starts immediately and ends at $\approx 144^\circ$. The third rise also starts immediately and it comes down within 212°. Behind the wire-wrap there is a small variation in Nusselt number for at least 116°.

The reason for this higher Nusselt number for positions in front of the wire is the high cross-stream velocity at these positions. The local circumferential Nusselt number for the central pin at four positions (at 1.203 m, 1.249 m, 1.309 m and 1.389 m) in the 7th pitch is presented in Fig. 6.24b. These positions are exactly 200 mm downstream from the previous positions discussed for 6th pitch. The predicted local Nusselt number at four different positions at 7th pitch is exactly same as that observed at the 6th pitch indicating the validity of temperature development. The reason for this higher Nusselt number for positions in front of the wire is the high cross-stream velocity at these positions. The cross-stream velocity at the cross-sections of 6th and 7th helical pitch is presented in Fig. 6.24c.

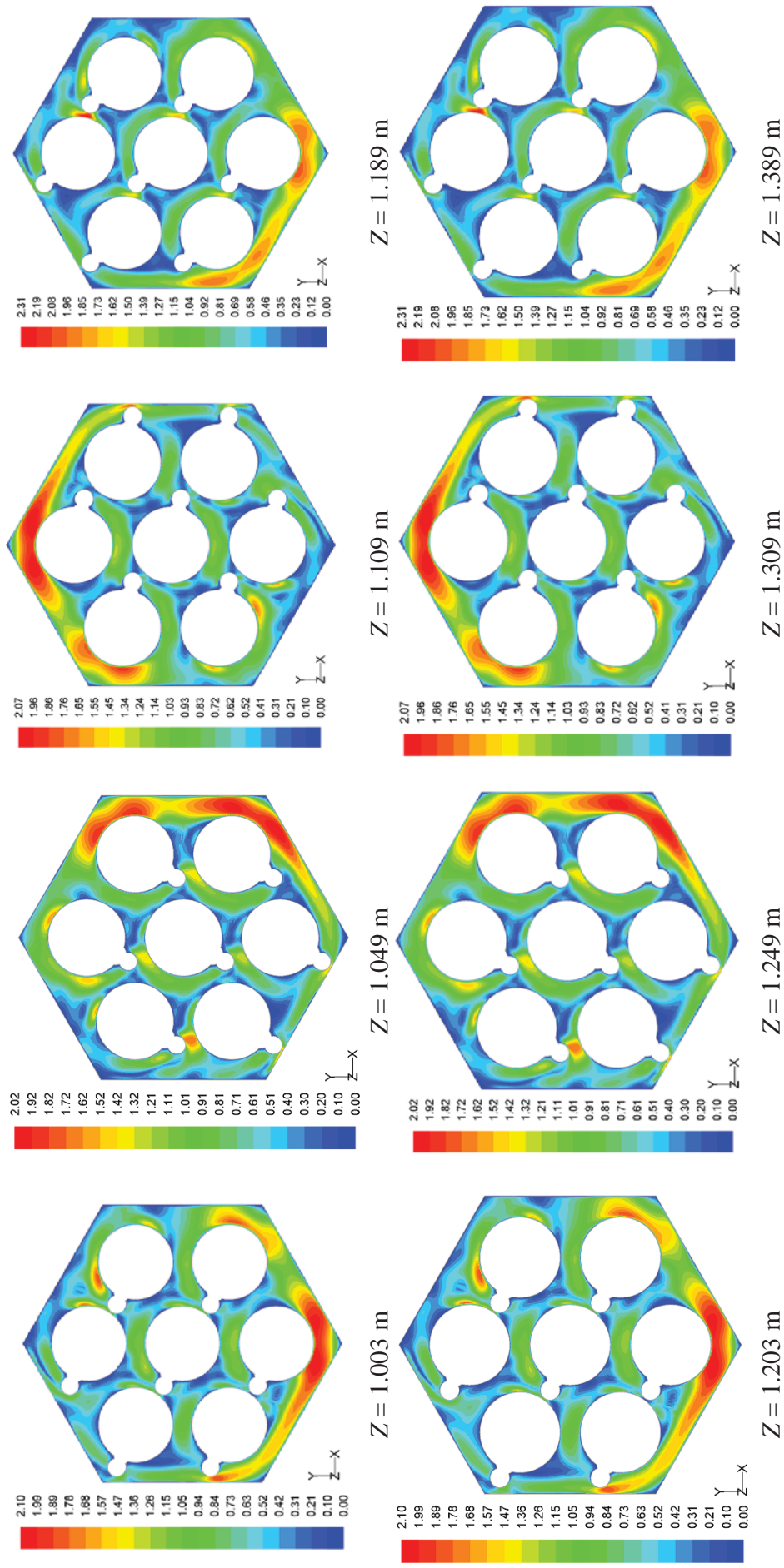


Fig. 6.24c Cross-stream velocity in 7-pin bundle at the 6th and 7th helical pitch

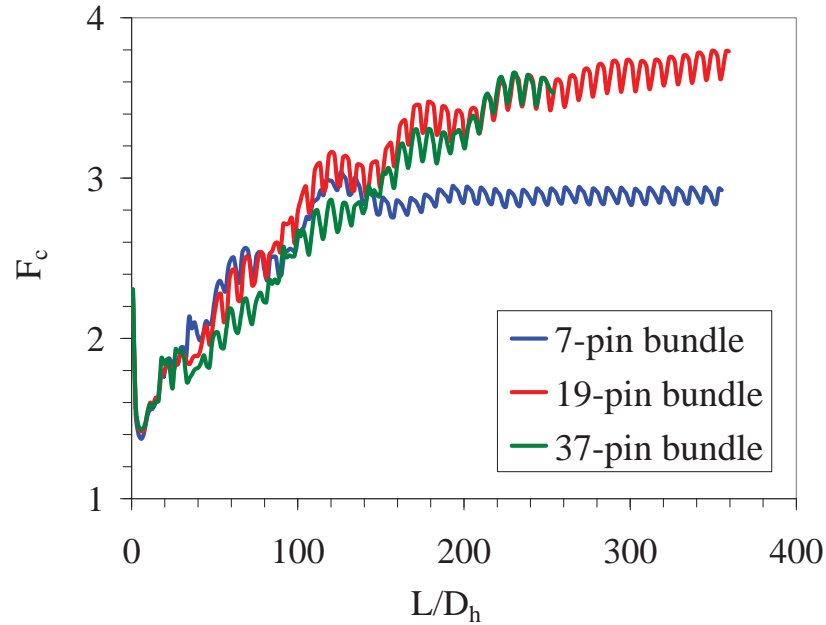


Fig. 6.25 Hotspot factor in the 7,19 and 37-pin fuel bundles

The predicted value of hot spot factor determined from Eq. (3.25) is depicted in Fig. 6.25 for various pin bundles for the full domain. The hot spot factor increases from the entrance region up to some length in all the cases. In a 7-pin bundle it increases up to $\approx 120 \times D_h$ and for 19-pin bundle it increases up to $500 \times D_h$ and after that it remains constant. The peak hot spot factor in 7-pin bundle and 19-pin bundle are 3 and 3.9 respectively. But for 37-pin bundle it is increasing till $250 \times D_h$ and in this case, higher axial lengths could not be considered due to limitations on the computer memory.

Further, the ratio of amplitude (a) to the mean value of friction factor (\bar{f}) (where, $A_f = (f_{\max} - f_{\min})/2$ and $\bar{f} = (f_{\max} + f_{\min})/2$) is calculated in the fully developed region and it is presented in Table-6.5. It can be seen that the percentage monotonically increases with Reynolds number, number of pins and decreases with helical pitch. This is due to the fact that the reduction in mean friction factor is more than the corresponding reduction in amplitude, for

increasing Reynolds number. But, with P_f/D_r ratio and helical pitch length, the amplitude increases while the mean friction factor decreases for a particular Reynolds number. This leads to a large change in the normalized amplitude.

Table 6.5 Non-dimensional amplitudes of friction factor in the fully developed region of turbulent flow

		$[A_f / \bar{f}] \times 100$
Re ($P_f/D_r = 1.25$ & $H = 200$ mm)	0.842×10^5	4.4
	1.20×10^5	4.7
	1.80×10^5	4.9
N ($Re = 84000$ & $H = 200$ mm)	7	4.4
	19	6.0
	37	10.1
H in mm ($Re = 84000$ & $P_f/D_r = 1.25$)	100	11.3
	150	7.6
	250	5.2
	300	4.9

6.3 CLOSURE

Simultaneous development of flow and temperature fields in the entrance region of FBR fuel pin bundles with helical spacer wires has been investigated. The Reynolds number, pitch of helical spacer wire and the number of pins in the bundle are varied as parameters. Flow is fully developed at $L \approx 70 \times D_h$ in all the cases investigated. In the wire-wrap rod bundle, the friction factor is not constant and it fluctuates periodically over a mean value. The mean value of the friction factor in the entrance region reduces below the mean value in the fully developed region. The mean fully developed friction factor is inversely proportional to the helical pitch. But, it is independent of the number of pins in the bundle. The development of Nusselt number is slower as compared to flow development. It attains full development within $L = 200 \times D_h$ in all the pin bundles with 7-pins. But, for the 19-pin bundle, the development over $500 \times D_h$, which is equal to 10 times the helical wire pitch. Nusselt number variation exhibits a strong dependence on helical

pitch, similar to that of friction factor. The following correlation for Nusselt number for fully developed flow is proposed:

$$Nu = 4.497 + 0.89 \left(\frac{P_t / D_r}{H / (D_r + D_w)} \right)^{1.29} (Pe)^{0.86}$$

for $1.1 \leq (P_t / D_r) \leq 1.4$, $12 \leq [H / (D_r + D_w)] \leq 36$ and $198 \leq Pe \leq 890$.

The hot spot factor is more either if Reynolds number is less or the number of pins in the bundle is more. This factor varies from 3 to 4. Elaborate CFD simulation of 217 pin bundle requires huge memory and parallel computation, which is not addressed in this thesis. However, the trends of the results as a function of number of pins suggest the following:

- The average friction factor in the fully developed region is independent of the number of pins. Hence, the present results of friction factor can be used for 217 pin bundle.
- The amplitude of fluctuation in friction factor is seen to increase with number of pins at the rate of about 4% per row of pins. Hence, for a 217 pin bundle with 8 rows, the fluctuation is expected to be about 32%, by straight extrapolation. However, this requires further confirmation.
- The cross velocity is independent of the number of pins and hence its magnitude for 217 pins can easily be inferred.
- The Nusselt number is found to be a decreasing function of number of pins. Also, the developmental length is found to be increasing with number of pins. Hence, detailed simulation of 217 pins is essential to estimate the Nusselt number in the case of full-size fuel subassembly.

CHAPTER-7

THERMAL HYDRAULIC EFFECTS OF POROUS BLOCKAGE IN HELICAL WIRE-WRAPPED BUNDLES

7.0 INTRODUCTION

Particles of local blockages may be active or passive. In the case of particles of active blockages (fragments of failed fuel) which are carried by the coolant flow, the blockage can be detected by delayed neutron detection signal (Natesan et al., 2007). But, detection of passive blockages (foreign particles transported with coolant) is difficult (Roychowdhury et al., 2002). In order to understand the effect of local blockages, a detailed parametric study has been carried out. The size, shape, cross-stream position, and porosity of the blockage have been systematically varied as parameters. A 19-pin bundle has been considered for all the simulations. It is chosen because it is the smallest bundle with all the three types of sub-channels, viz., interior, edge and corner sub-channels, as in large pin bundles. The position of the blockage was fixed at the mid height of the bundle. A fixed value of helical pitch (200 mm) has been taken and seven helical pitch lengths have been modelled in all the cases. The diameter of pin, diameter of wire and triangular pitch are 6.6 mm, 1.65 mm and 8.28 mm respectively.

7.1 SOLUTION METHODOLOGY

7.1.1 Grid Sensitivity Study

Detailed grid independence test, has been carried out as explained in Chapter-6. Based on this test, a grid pattern with 6.773 million grids is found to give a grid independent result for the 19-pin bundle simulations. The cross-stream mesh adopted for the computations in the 19-pin bundle is depicted in Fig. 7.1.

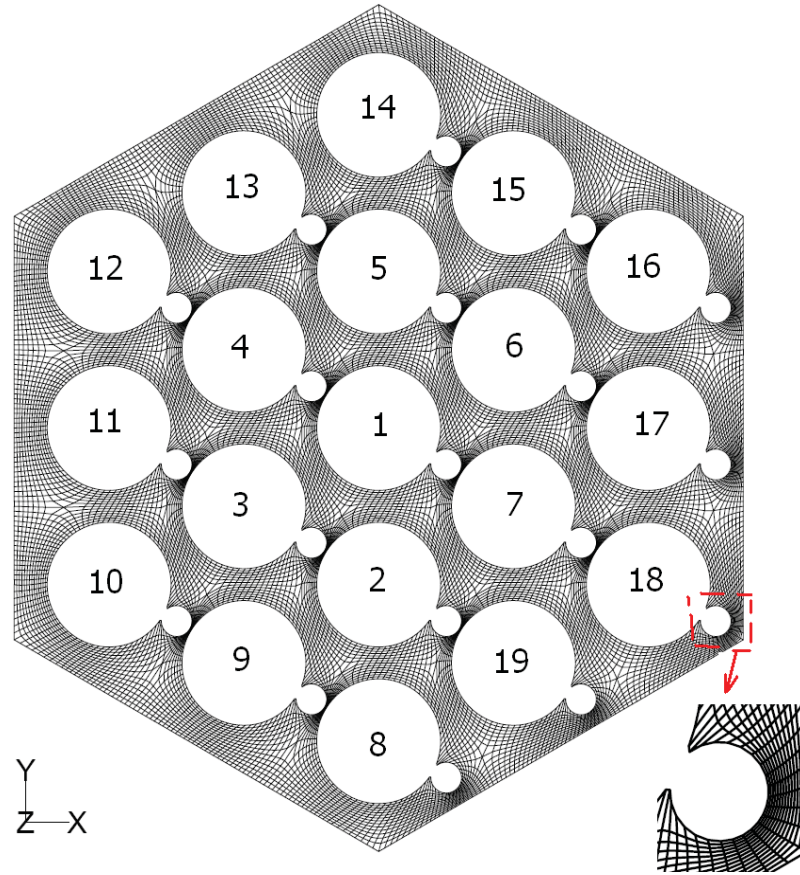


Fig. 7.1 Optimized cross-stream mesh used in 19 pin-bundle CFD studies

7.1.2 Validation Studies

Before analyzing the fluid in pin bundles with blockages, it is important to validate the CFD model against suitable benchmark results. For this purpose, the experimental study of SCARLET-II (Olive and Jolas, 1990) is considered. SCARLET-II experiment was conducted with 19-pin wire-wrap bundles including a central blockage comprising six sub-channels of 60 mm long along the flow direction, as shown in Fig. 7.2a. The cross-sectional view of the present CFD model geometry considered is also highlighted in the same figure. In the pin bundle, the central blockage is located over the axial distance between 585 mm and 645 mm from the beginning of heated length. Pin diameter is 8.5 mm and the pins are arranged in triangular pitch of 9.79 mm with an electrical heating of 45 kW/pin. The spacer wire diameter

is 1.25 mm with a lead of 180 mm and sodium inlet velocity is 6.415 m/s at 245.8°C. Porosity of the blockage is 0.32.

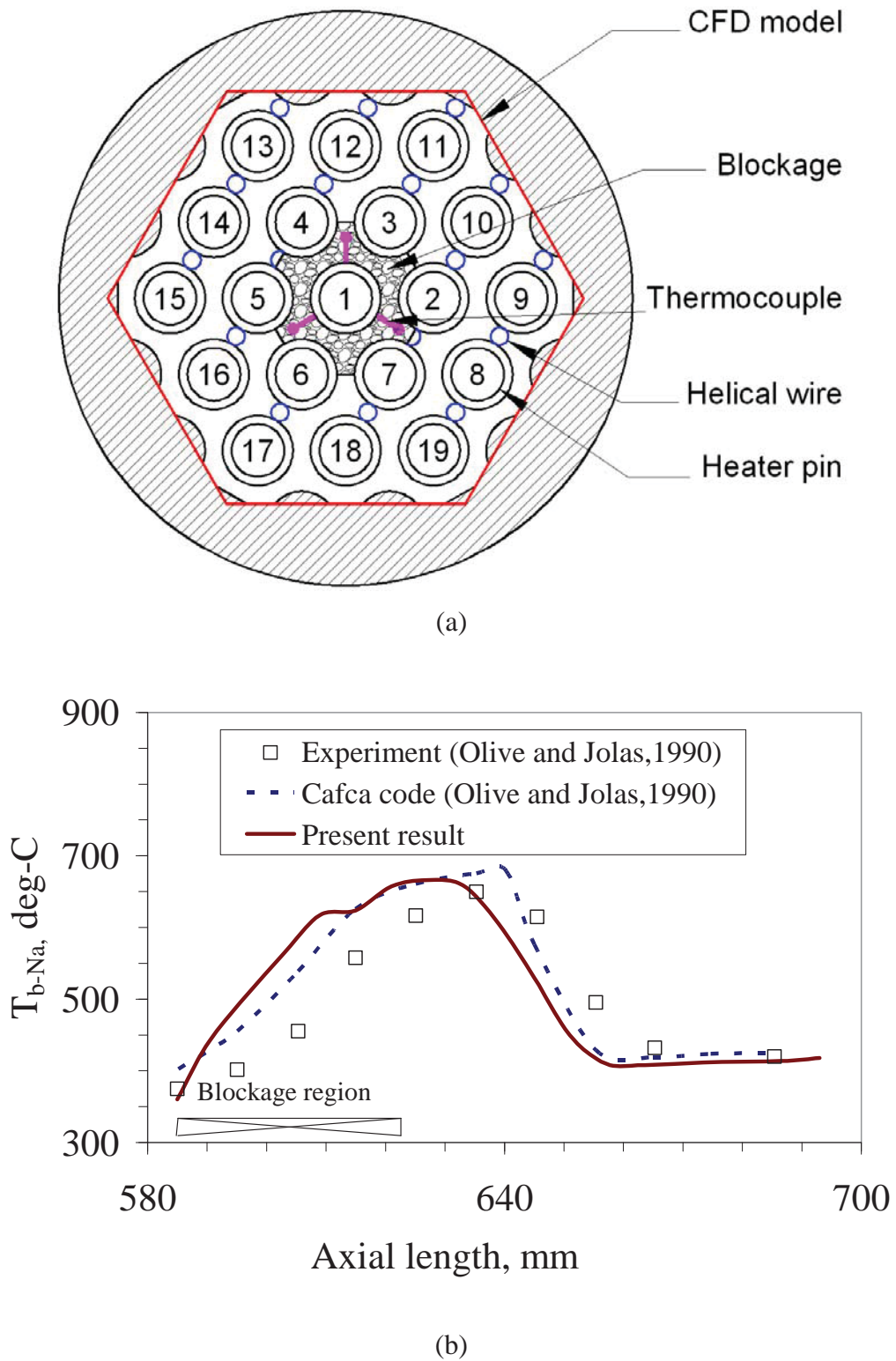


Fig. 7.2 Validation of present calculation with SCARLET-II experiment (Olive and Jolas, 1990) (a) SCARLET-II test section (b) Comparison of temperature in the blocked region

The temperature indicated in Fig. 7.2b is the average sodium temperature, $\left(T_{b-na} = \frac{\int_A u_z T dA}{\int_A u_z dA}\right)$ in the blockage region, where A is the cross-section of the blockage normal to mean flow direction. Sodium temperature in the blocked region increases steeply till $3/4^{\text{th}}$ of the blockage length and it reduces subsequently. Also shown in Fig. 7.2b is the temperature variation predicted by the Cafca code (Olive and Jolas, 1990). It is seen that the maximum temperature predicted by the present model is in good agreement with the reported data. But, the present model marginally over predicts the axial temperature gradient and compares favorably with the prediction of Cafca code (Olive and Jolas, 1990). However, the peak temperature in the blocked region which is an important safety parameter predicted by the present code (665°C) compares very well with measured data, viz., 650°C . Thus, the present CFD model can be considered to be validated for simulating pin bundles with porous blockage.

In addition to the thermal validation for the pin bundle, a hydraulic validation study has been carried out. For this, the 91-pin wire-wrapped bundle experimental study reported by Lorenz and Ginsberg (1977) is considered. The present sub-channel non-dimensional axial velocity distribution in the 19-pin bundle at fully developed region is compared with the experimental data. The experimental and computational velocity distributions are depicted in Figs. 7.2c and 7.2d respectively. Also, the comparison of maximum velocities in central, intermediate and peripheral sub-channels is presented in Table-7.1. This comparison shows that the present results satisfactorily match with the experimental data (within $\sim 3\%$).

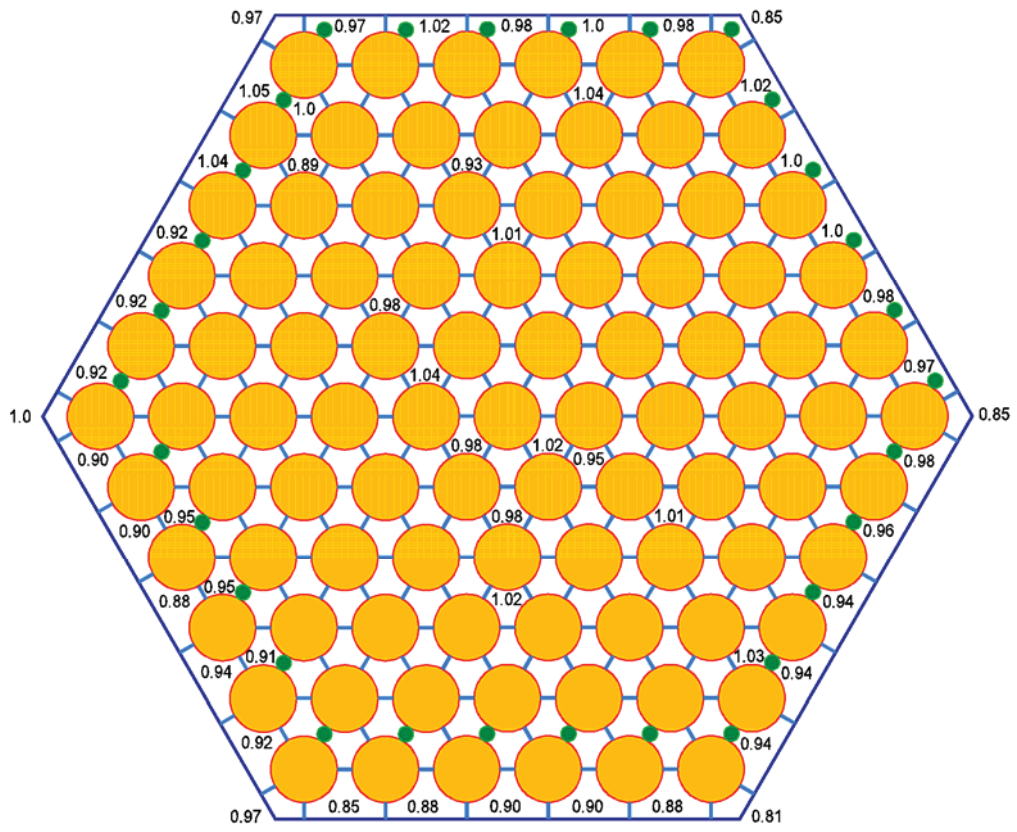
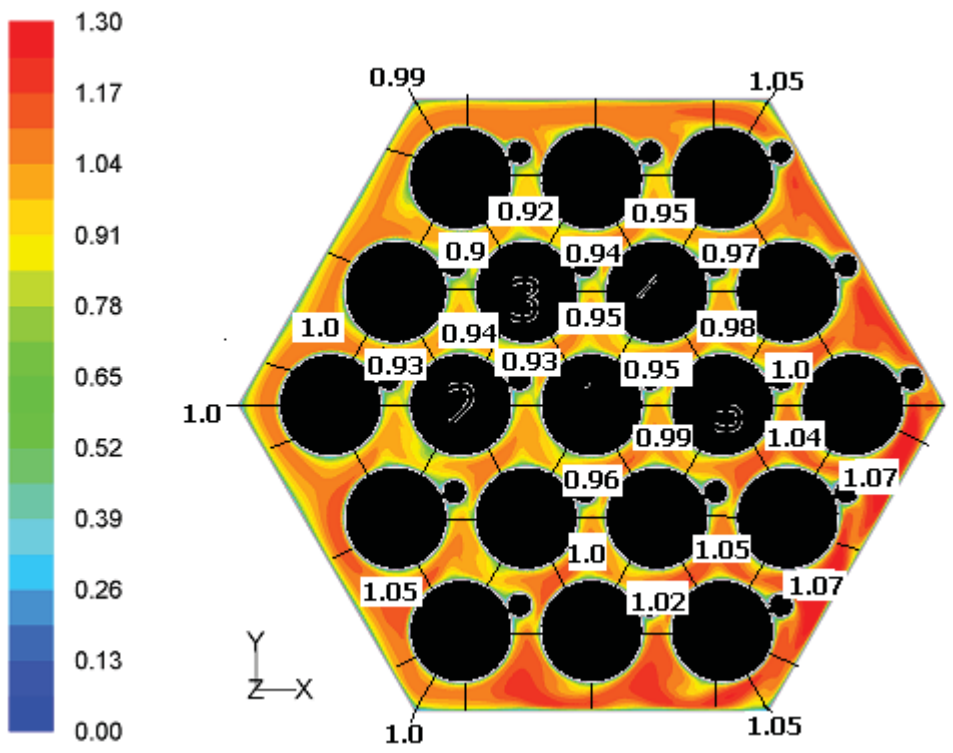


Fig. 7.2c Experimental non-dimensional axial velocity (V_s/V_i) distribution



(b)

Fig. 7.2d Present non-dimensional axial velocity (V_s/V_i) at $Z = 780$ mm

Table 7.1 Comparison of non-dimensional axial velocity (V_s / V_i) with water model experiments

Type of study	No. of pins in the bundle	Maximum non-dimensional velocity in the sub-channels		
		Central sub-channel	Intermediate sub-channel	Peripheral sub-channel
Experiment	91	1.02	1.04	1.05
Present	19	0.99	1.05	1.07

7.2 RESULTS AND DISCUSSION

Axial and circumferential temperatures, cross-stream velocity and cross-stream temperature distributions are investigated in detail. Five different types of blockages are modelled in the present study. Figures for all the shapes of blockages are included in Table 7.2. Based on the literature survey it understood that the axial growth of the blockage is highly possible. Various shapes of the blockages have been studied for academic interest. A schematic of the pin bundle with blockage is depicted in Fig. 7.3a and the cross sections of different types of blockages studied are depicted in Figs. 7.3b - 7.3d. The details of blockages considered are presented in Table-7.2.

As already discussed, blockages can be of different shapes and sizes in the pin bundle. In the present study, two different shapes viz., cylindrical and conical shapes are considered. Also, the blockage size can be different for each case. The position of blockage can be either in the central region or near the corner of the sub-channels. In all these cases, the starting point of blockage is considered to occur at the middle of the pin bundle, i.e., 700 mm from the entry. The length of the blockage is considered to be 200 mm for most of the cases except one. Heat flux applied on the clad surface is 1600 kW/m^2 . The coolant flow Reynolds number is maintained as 97900 and the inlet temperature is 670 K (397°C) for all the cases. The reference value of blockage porosity is taken as 40%.

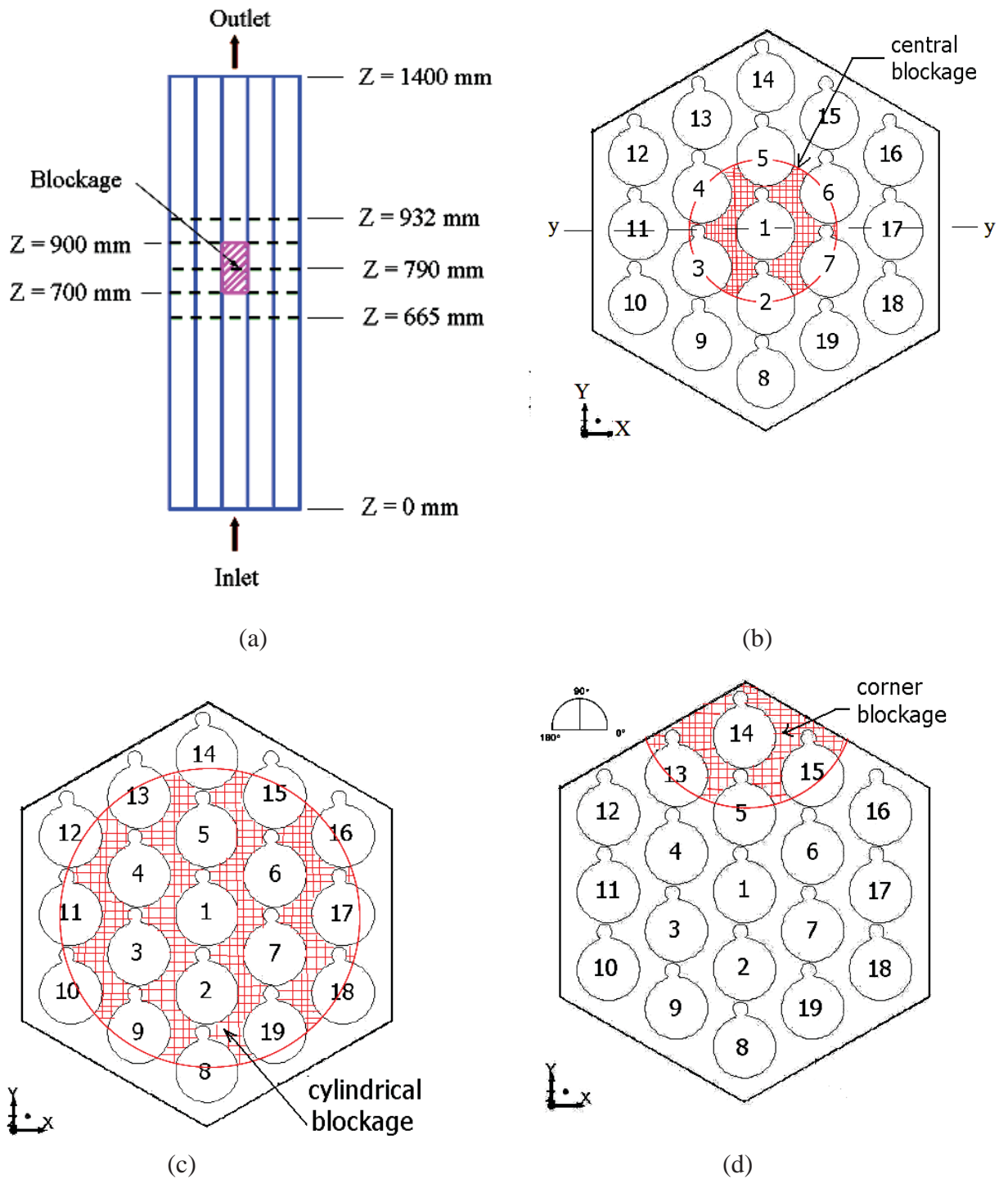


Fig. 7.3 (a) Schematic of pin bundle with blockage, (b) 19-pin bundle with cylindrical and conical blockages ($B1, B2$ & $B3$) at the centre of subassembly located within 700-900 mm axial position (c) 19-pin bundle with cylindrical central blockage ($B4$) at the centre of subassembly located within 700-900 mm axial position and (d) 19-pin bundle with cylindrical blockage ($B5$) at a corner of subassembly located within 700-900 mm axial position

Table 7.2 Details of blockages considered in the 19-pin bundle configuration

Global shape of blockage formed	Length (mm)	Radius (mm)	Blockage region/ Number of sub-channels blocked	Blockage tag	Shape of blockage (Not to scale)
Cylindrical	200	8.28	central / 6	blockage -1 (<i>B1</i>)	
Conical	200	8.28	central / 6	blockage -2 (<i>B2</i>)	
Cylindrical	100	8.28	central / 6	blockage -3 (<i>B3</i>)	
Cylindrical	200	16.56	central / 24	blockage -4 (<i>B4</i>)	
Cylindrical	200	8.28	corner / 5	blockage-5 (<i>B5</i>)	

7.2.1 Effect of Blockage in Pin Bundle

To start with, the results for a pin bundle with central blockage *B1* (six central sub-channels blocked as shown in Fig. 7.3b) are compared, with that of a pin bundle without blockage. In order to understand the thermal hydraulic characteristics, the cross-stream velocity vectors, isotherms and circumferential clad temperature distributions are plotted at three cross-sections viz., $Z = 665, 790,$ and 932 mm (see, Fig. 7.3a for the position of these cross-sections).

The cross-stream velocity vectors and the isotherms for the corresponding cross-sections are depicted in Figs. 7.4a and 7.4b. Among these, the first and last cross-sections are outside the blockage region and the middle one is within the blockage region. It is clear from Fig. 7.4a that the secondary flow and velocity magnitudes are larger in the near wall channels. The near wall sodium flows in the anti clockwise direction (in the direction of wire wrap) with a high velocity zone $\sim 60^\circ$ ahead of wire wrap.

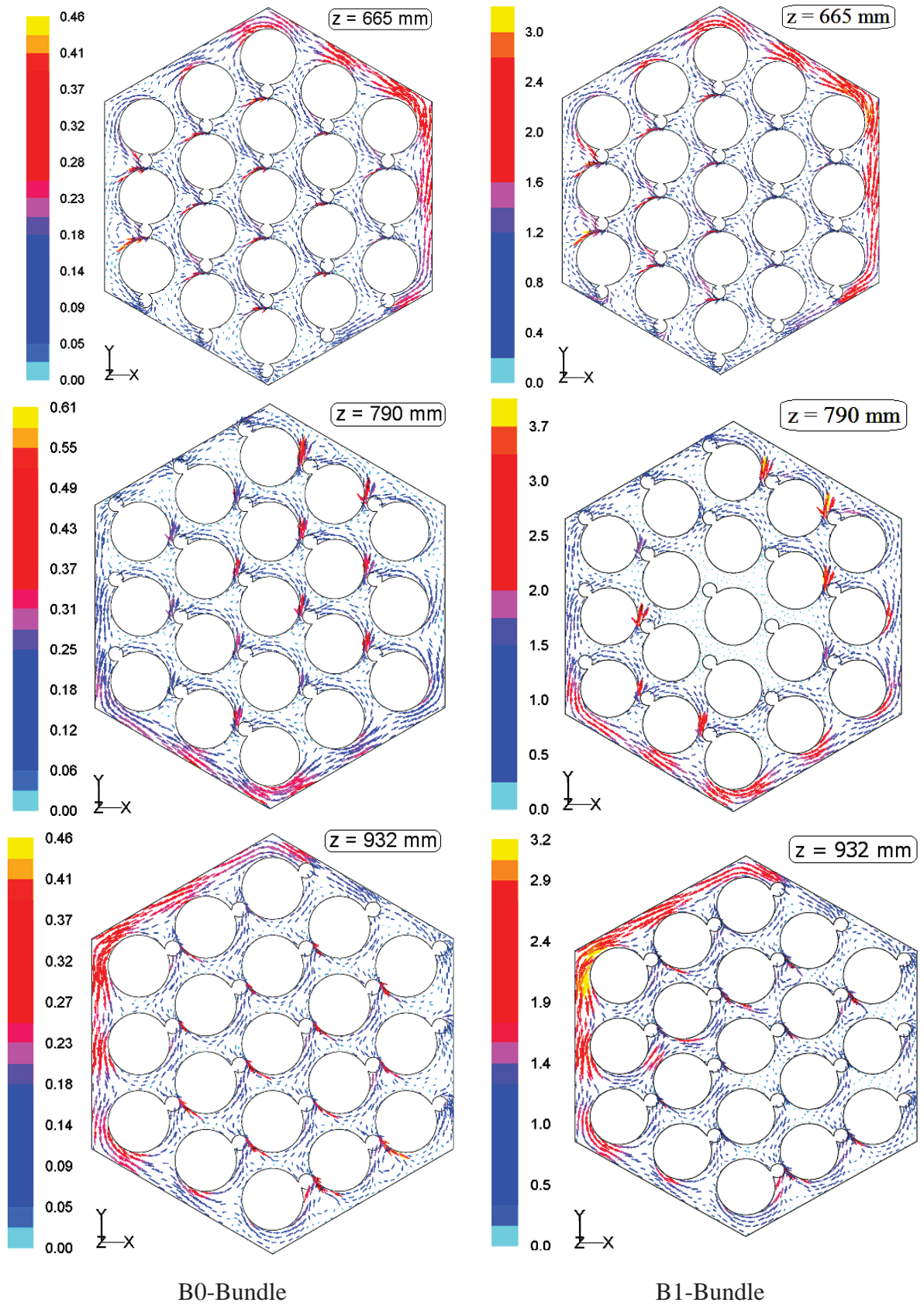


Fig. 7.4a Comparison of cross-stream velocity (m/s) vectors of *B1* bundle with normal bundle (*B0*-Bundle)

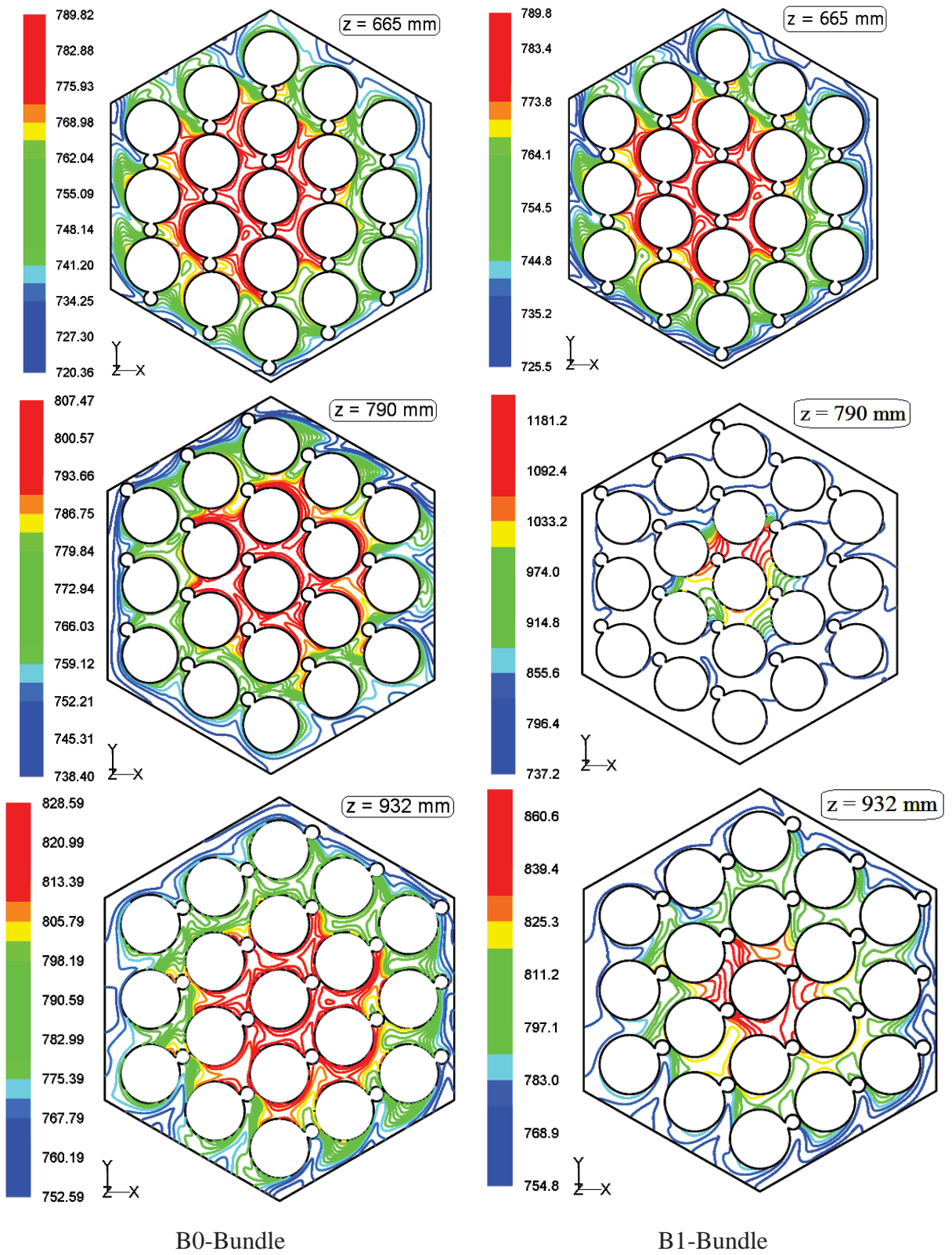


Fig. 7.4b Comparison of isotherms (K) of *B1* bundle with normal bundle

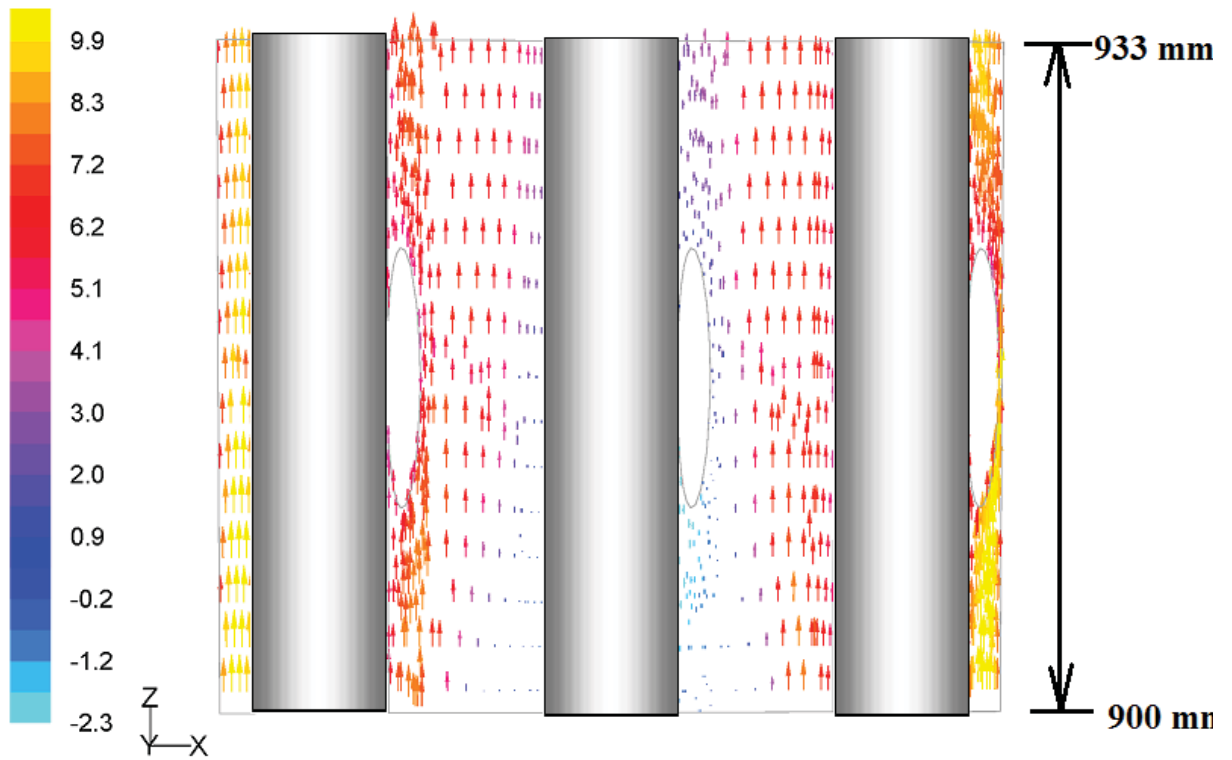


Fig. 7.4c Axial velocity in *BI* bundle behind the blockage

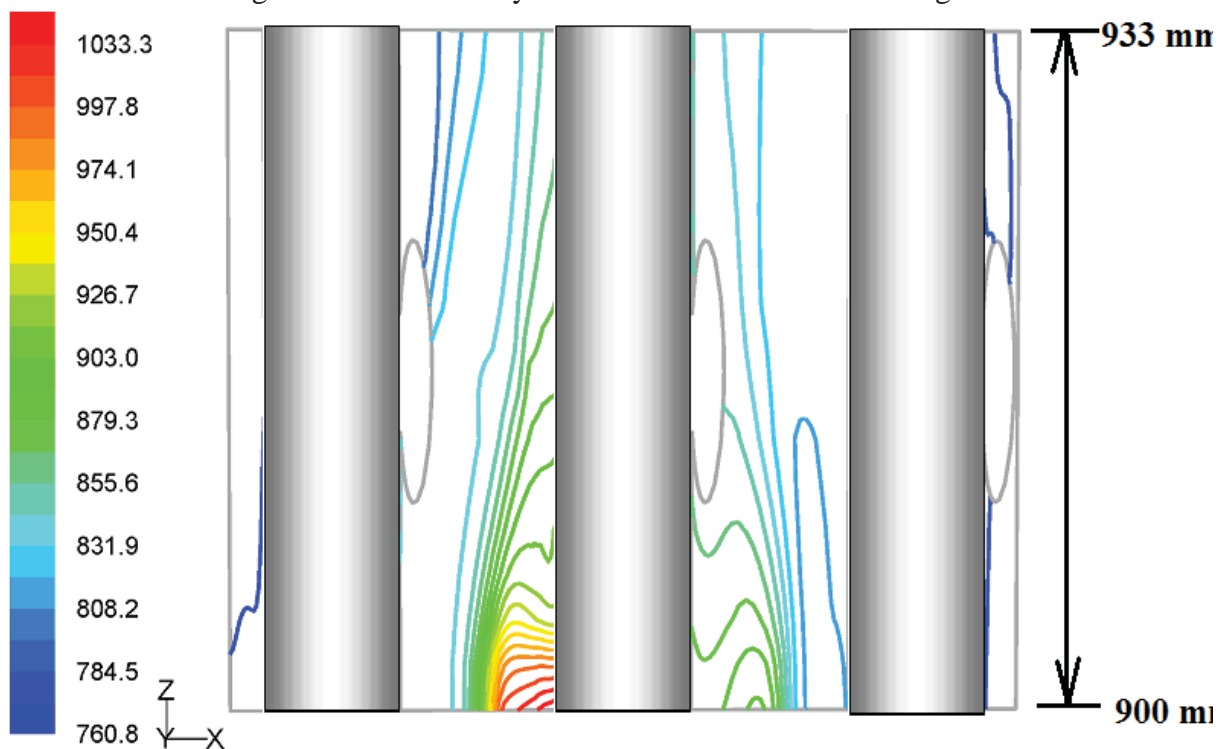


Fig. 7.4d Isotherms (K) of *BI* bundle behind the blockage

The isotherms (Fig. 7.4b) at the cross sections of $z = 665$ mm and 932 mm depict significant radial variation of sodium temperature in the bundle with high temperature prevailing at the inner sub-channels and low temperature prevailing at outer sub-channels.

But, this non-uniformity increases to a large extent at $Z = 790$ mm due to the presence of blockage and diversion of flow from centre towards the outer sub-channels.

Axial velocity (U_z) behind the *BI* blockage for the axial length of 33 mm (from 900 mm to 933 mm) is depicted in Fig. 7.4c. It is understood that from this figure there is no wake formation behind the blockage. But low velocity is observed in the inner sub-channels compared to outer channels. Sodium temperature for the corresponding section is depicted in Fig. 7.4d. Because of low velocity the fluid temperature is high in the inner sub-channels.

The evolution of average clad surface temperature of fuel pins with axial position is calculated using Eq. 3.26 and it is depicted in Fig. 7.5a. It is seen that the axial variation of average clad temperature in the pin bundle with blockage is only $\sim 5\%$ more than that in the normal bundle (without blockage also referred as B0). This suggests that local increase in central clad temperature is nearly compensated by reduction in peripheral pin temperatures. The axial variation of maximum clad temperature in the bundle is also compared in the Fig. 7.5a. Unlike the average clad temperature, the difference between the two cases is very large. The peak clad temperature increases very sharply within the blockage zone. But at the end of blockage the peak temperature decreases sharply and then gradually increases. This is due to the fact that the swirling flow generated by wire promotes good mixing of various sub-channel streams behind the blockage. Further, the bulk temperature of sodium just downstream of blockage is same for all the cases from heat balance considerations, where heat flux and mass flow rate are identical. Also, the clad temperature exhibits strong fluctuations due to the interaction of helical spacer wire with the coolant flow.

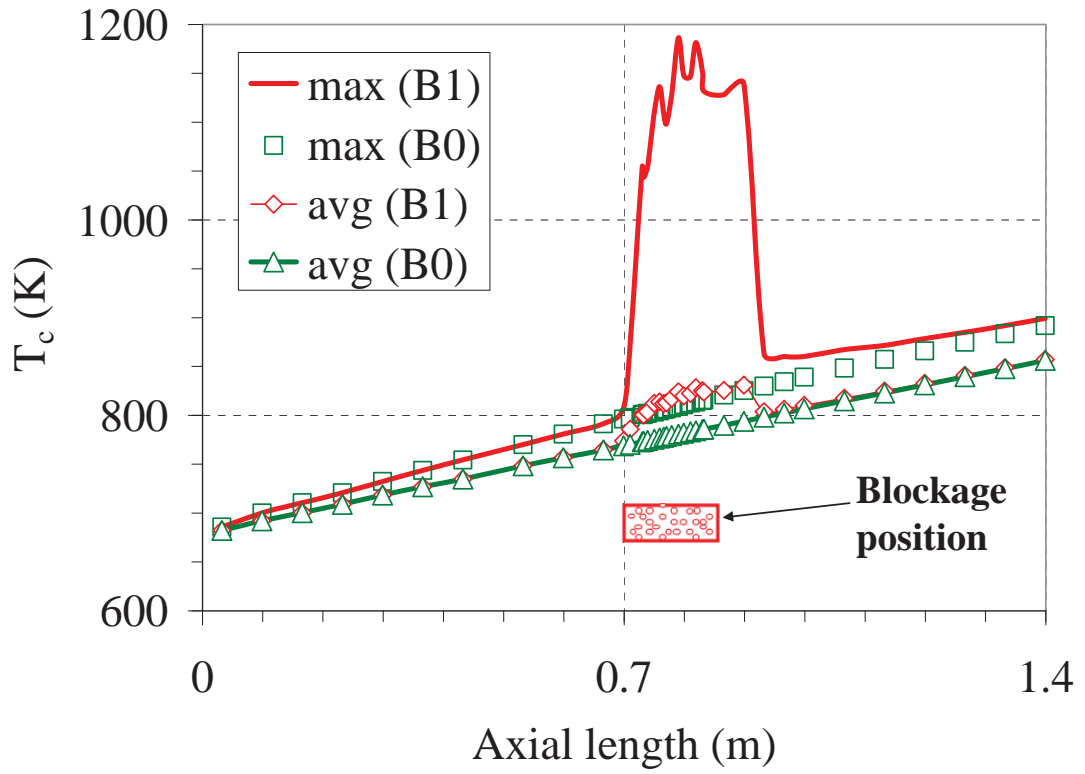


Fig. 7.5a Comparison of peak and average clad temperature in pin bundle with *B1* blockage against that without blockage (*B0*)

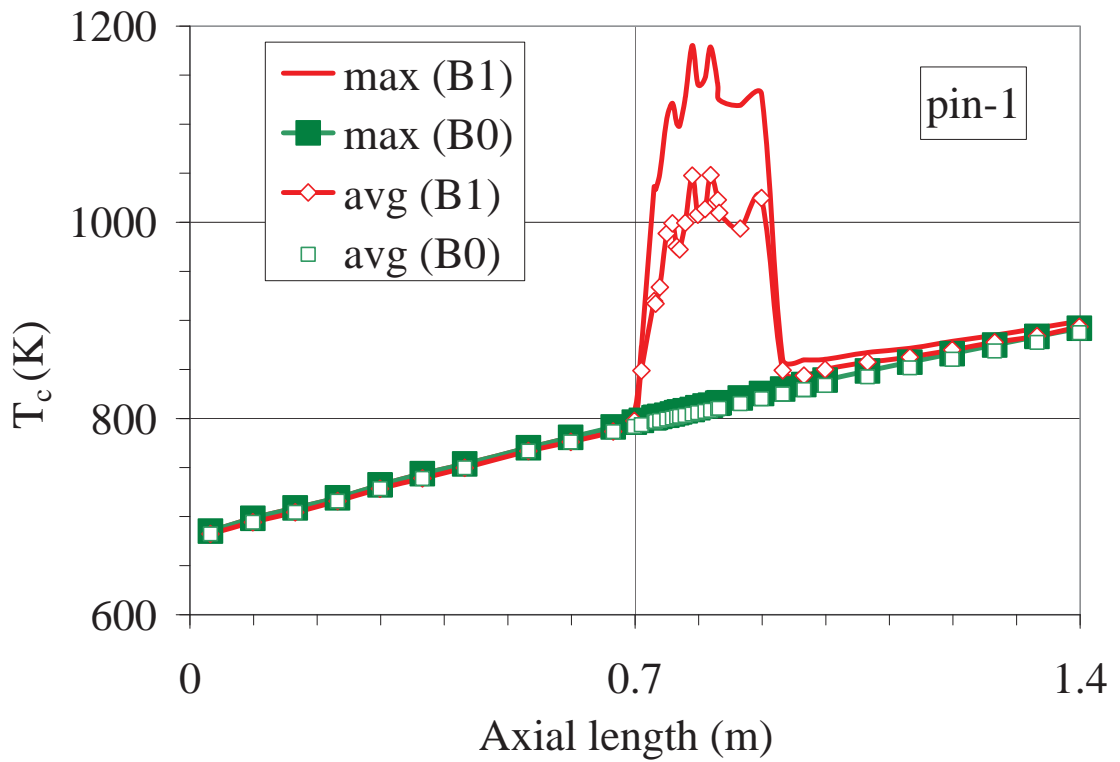


Fig. 7.5b Comparison of peak and mean clad temperatures in pin-1

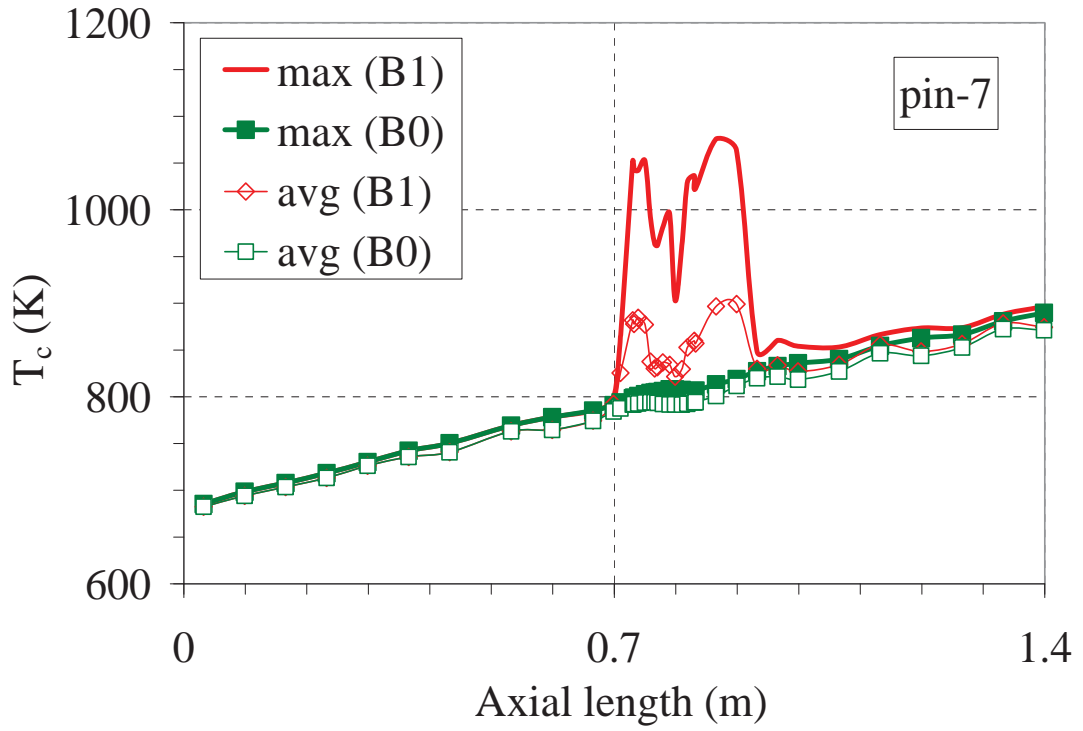


Fig. 7.5c Comparison of peak and mean clad temperatures in pin-7

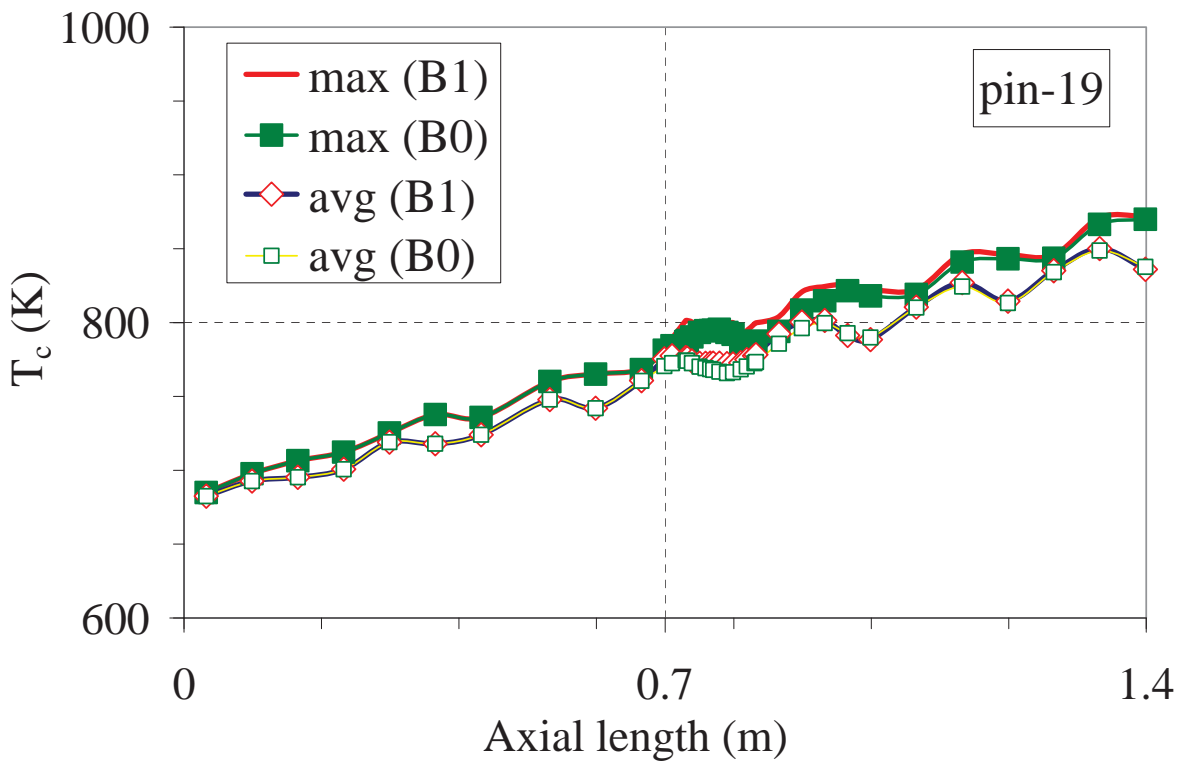


Fig. 7.5d Comparison of peak and mean clad temperatures in pin-19

The incipient boiling wall superheat for the present boundary conditions is determined to be very small, based on the experimental predictions reported by Uotani and Haga (1984). So, nucleate boiling of sodium is expected once clad temperature just exceeds the sodium boiling point. The maximum clad temperature in the present case is 1186 K. The peak clad temperature crosses the boiling point of sodium, viz., 1155 K. Hence, boiling of sodium is imminent within the blockage of central sub-channels. Since boiling is not modelled in the present study, the results are not strictly valid if clad temperature exceeds ~ 1155 K.

Further, to understand the effect of blockage on individual clad, three pins viz., pin-1, pin-7 and pin-19 as indicated in Figs. 7.5b, 7.5c, 7.5d, are chosen. Figure 7.5b depicts local and mean clad temperatures of pin-1. In a normal bundle, the clad temperature increases almost linearly in line with the uniform heat flux supplied to the pins. Also, there is not much difference between the peak and average clad temperatures suggesting the circumferential variation in the clad temperature of pin-1 is very small.

But in the case of blocked pin bundle, there is significant difference between the mean and peak clad temperatures at any axial position for pin-1 which is completely engulfed by the porous blockage. This suggests that the circumferential variation in pin-1 exceeds 125 K, which can induce significant circumferential stresses in the pin. Further, comparison of normal and blockage bundle results suggests that the effect of blockage is highly localized without significant wake effects downstream of the blockage.

The corresponding temperature distributions for pin-7 which is partly exposed to porous blockage are depicted in Fig. 7.5c. It is clear that the absolute value of temperature in pin-7 (which is placed in the middle row) is lower than that for pin-1. However, the circumferential variation in clad temperature (~ 175 K) is much higher than that of pin-1. This is expected, as one part of this pin is exposed to the porous blockage while the other part is in the free zone. Temperature distribution in pin-19 which is far away from the blockage is

depicted in Fig. 7.5d. It is clear that clad temperature in pin-19 is nearly unaffected by the central blockage. The circumferential temperature variation is relatively high in the non-porous zones than in pin-1 due to flow by pass effects in the peripheral sub-channels. Further, the clad temperature exhibits a non-monotonic variation with respect to axial length. This variation is repetitive and could be correlated to the specific position of spacer wire in the peripheral sub-channels.

Circumferential clad temperature distribution in pin-1 and pin-19 for blocked and normal bundles are depicted in Fig. 7.6 for various axial positions. The maximum difference in the circumferential temperature variation $[(\Delta T_{\theta})_{max}]$ for the cases with cylindrical blockage (B1) and normal bundle is presented in Table-7.3. It is evident that in the bundle with blockage, $(\Delta T_{\theta})_{max}$ occurs in pin-7 at $Z = 865$ and 730 mm. As mentioned before, this is because pin-7 experiences high temperature on one side and low temperature on the other side, as seen in Fig. 7.4b. The circumferential clad temperature distribution inside the blockage zone (Fig. 7.6a) indicates that the clad attains the peak value where the helical wire contacts the clad. This is due to the fact that the sodium flow within the blockage around clad-wire interface is nearly stagnant.

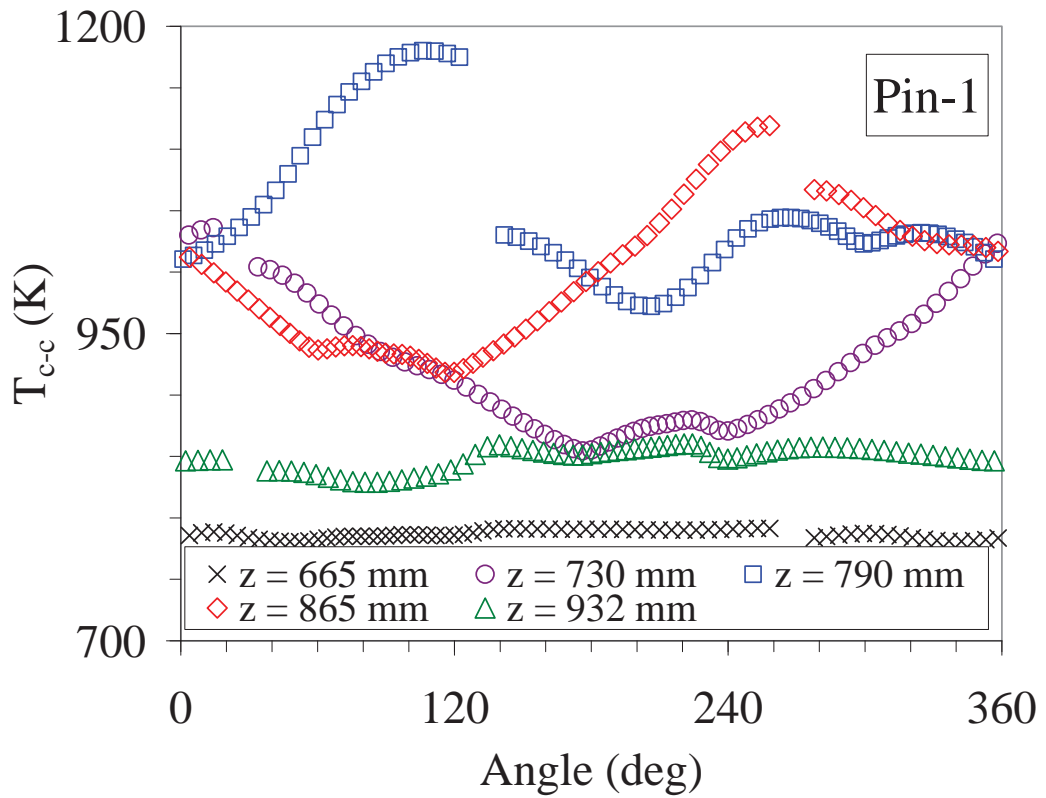


Fig. 7.6a Circumferential clad temperature distribution in pin bundle with *B1* type blockage: (a) pin-1

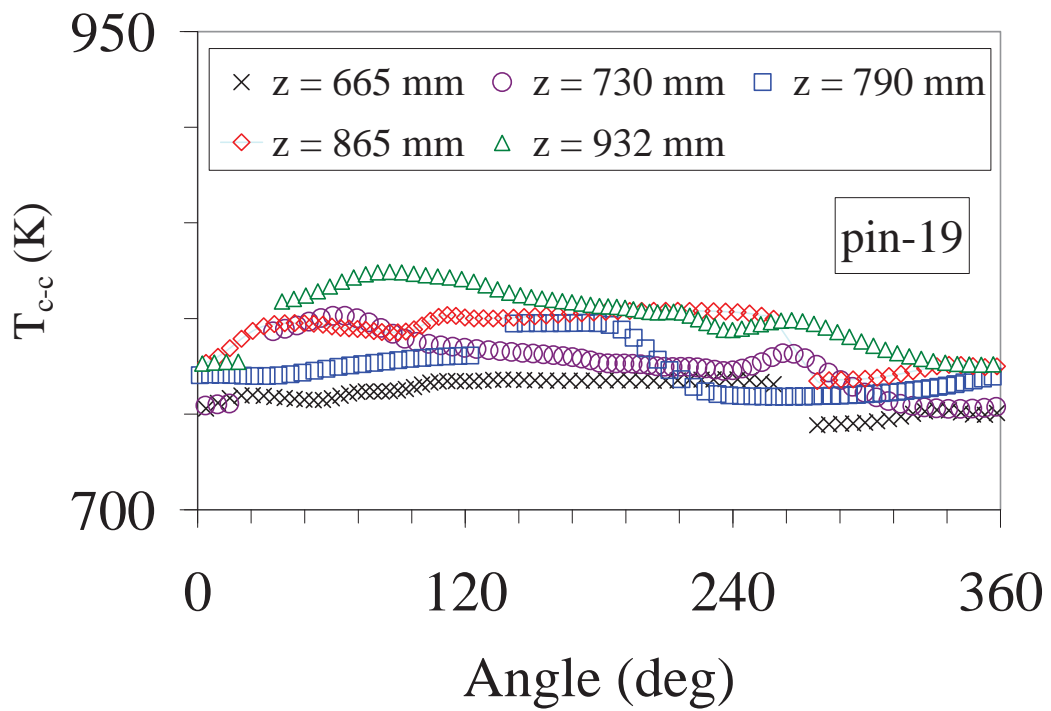


Fig. 7.6b Circumferential clad temperature distribution in pin bundle with *B1* type blockage: pin-19

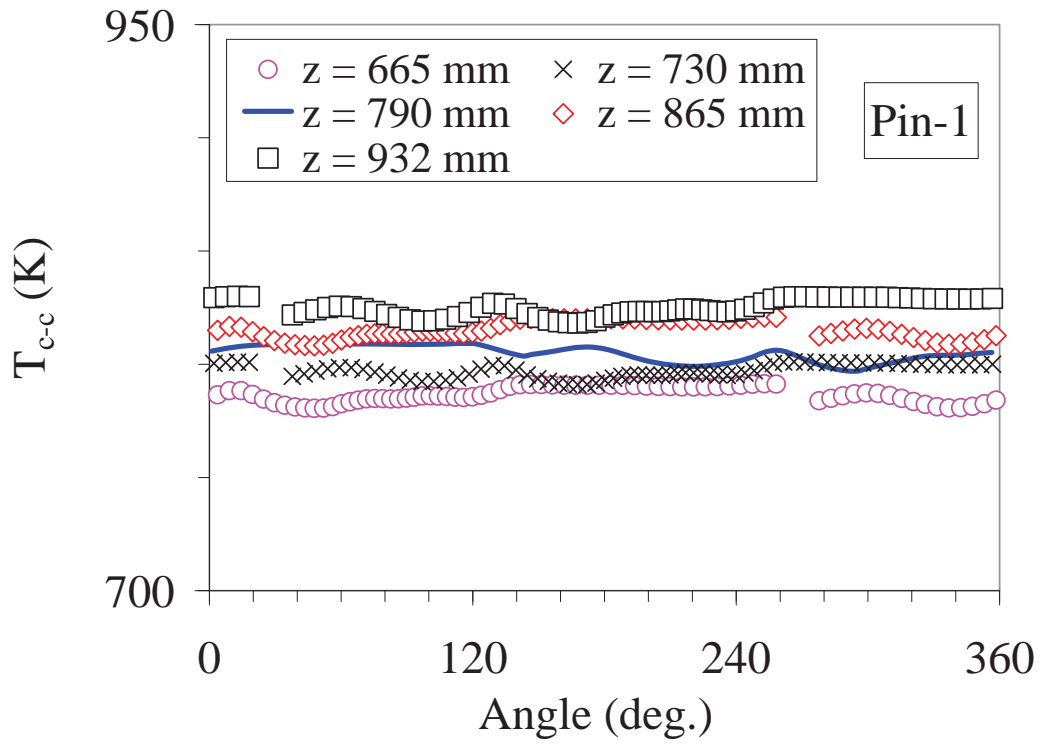


Fig. 7.6c Circumferential clad temperature distribution in normal pin bundle: pin-1

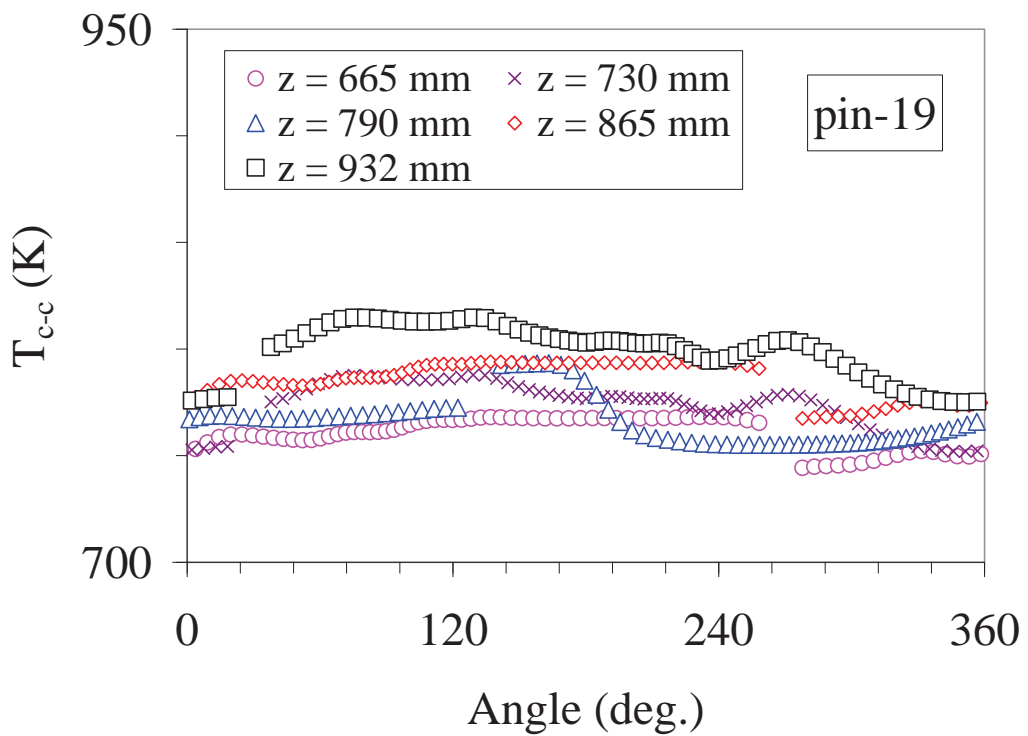


Fig. 7.6d Circumferential clad temperature distribution in normal pin bundle: pin-19

Table 7.3 Maximum difference in circumferential clad temperature $[(\Delta T_{\theta})_{max}]$ (K)

Z, m	B1-blockage bundle			Bundle with no blockage		
	Pin-1	Pin-7	Pin-19	Pin-1	Pin-7	Pin-19
0.665	10.8	23.0	24.1	6.6	5.9	6.8
0.730	181.7	257.5	48.6	10.2	19.5	35.9
0.790	207.9	211.7	38.6	12.2	34.3	38.3
0.865	200.8	278.5	36.7	12.7	25.4	26.6
0.932	31.4	31.9	48.5	11.8	21.8	39.7

7.2.2 Effect of Blockage Geometry

Blockage formation in the fuel subassemblies can be from different sources, such as debris of failed fuel pins, spacer wire, foreign materials left during construction and corrosion products or impurity deposition in the flow channels. Hence, the shape and size of the blockages can be different from one another. Hence, detailed investigation on the effects of various shapes of blockages is essential which explained in succeeding sections.

7.2.2.1 Effect of Blockage Shape

In this section two different shapes of the blockage are considered, i.e., cylindrical (*B1*) and conical (*B2*) shape. Both blockages are taken for an axial length of 200 mm and they are positioned at the centre of the subassembly. Except for the shape of the blockage, all other conditions are same as given in Section 7.2.1.

The cross-stream velocity vectors and isotherms were discussed in detail in section 7.2.1 for *B1*-blockage. The cross-stream velocity and sodium temperature for the pin bundle with conical (*B2*) blockage are depicted in Figs. 7.7a and 7.7b respectively.

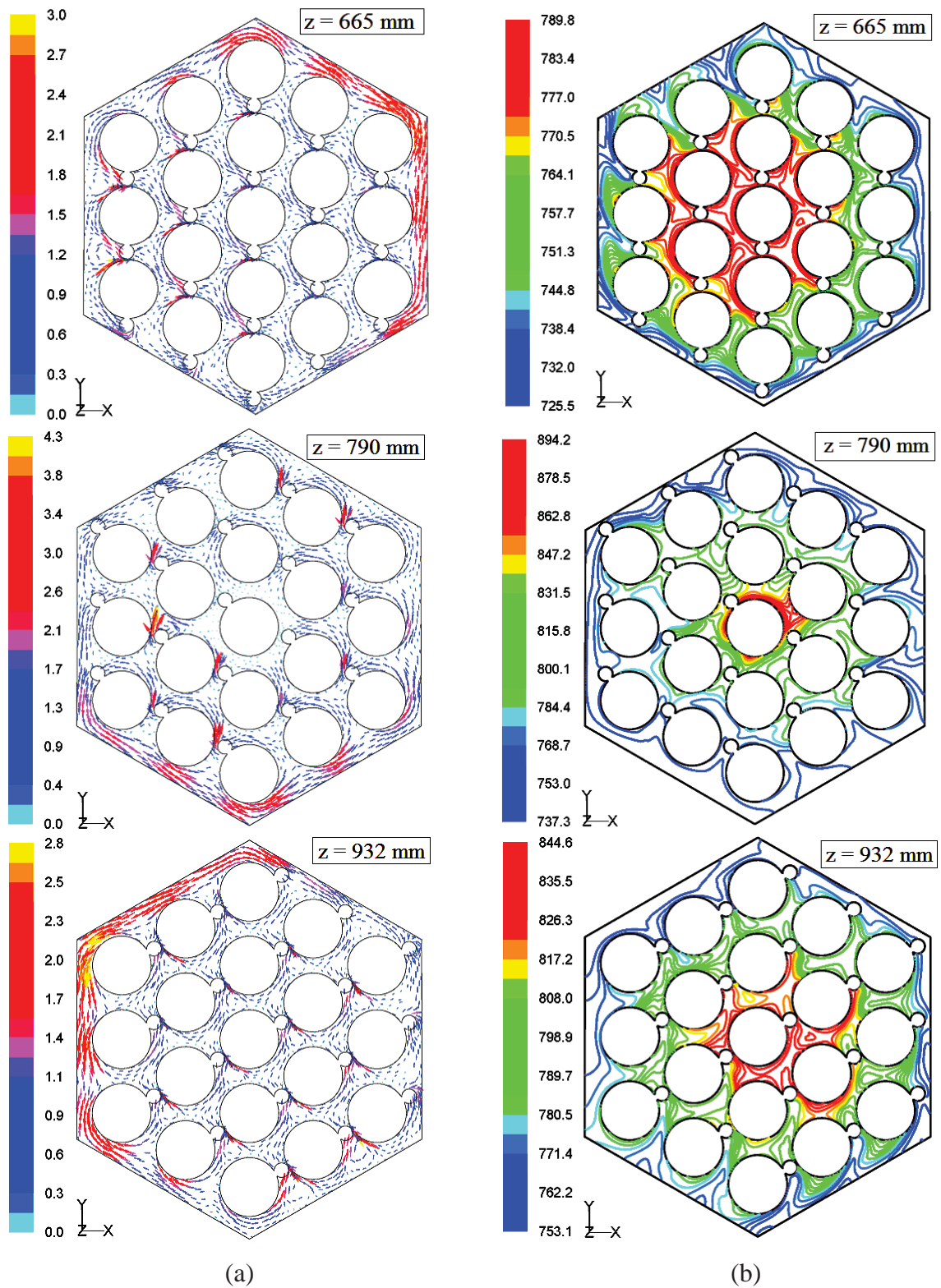


Fig. 7.7 (a) Cross-stream velocity (m/s) vectors for *B2* type blockage and (b) Isotherms (K) for *B2* type blockage

The maximum cross-stream velocity is observed to occur at the cross-section of $Z = 790 \text{ mm}$. The peak velocity is observed near the hexcan walls as well as in the space between

the wire wrap and fuel pins. From the isothermal maps, it is clear that the effect of *B2*-blockage persists only upto an axial length of $Z = 790$ mm. At this cross-section, the peak temperature is significantly less than that of pin bundle with *B1*-type blockage. This suggests that the effect of porous blockage is primarily limited to the porous zone and the peak clad temperature is proportional to the volume of the porous zone.

The evolution of maximum clad temperature in the pin bundle with conical blockage (*B2*) is compared with that of cylindrical blockage (*B1*) in Fig. 7.8a. The peak temperature in conical blockage is significantly less than that in the cylindrical blockage. Further, the peak temperature occurs at $Z = 790$ mm for *B1*-blockage and at $Z = 738$ mm for *B2*-blockage suggesting that the peak temperature in the conical block occurs closer to the cone base. Also given in Fig. 7.8a is the global average clad temperature. The average clad temperatures for both the shapes are comparable.

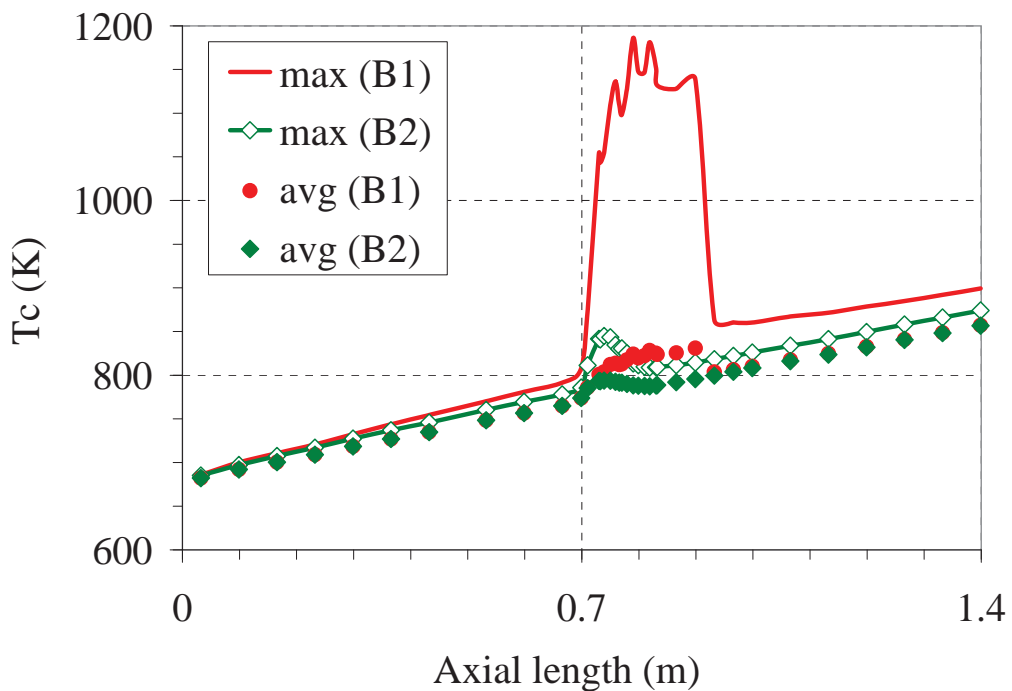


Fig. 7.8a Comparison of peak and average clad temperature in *B1*-blockage bundle with *B2*-blockage

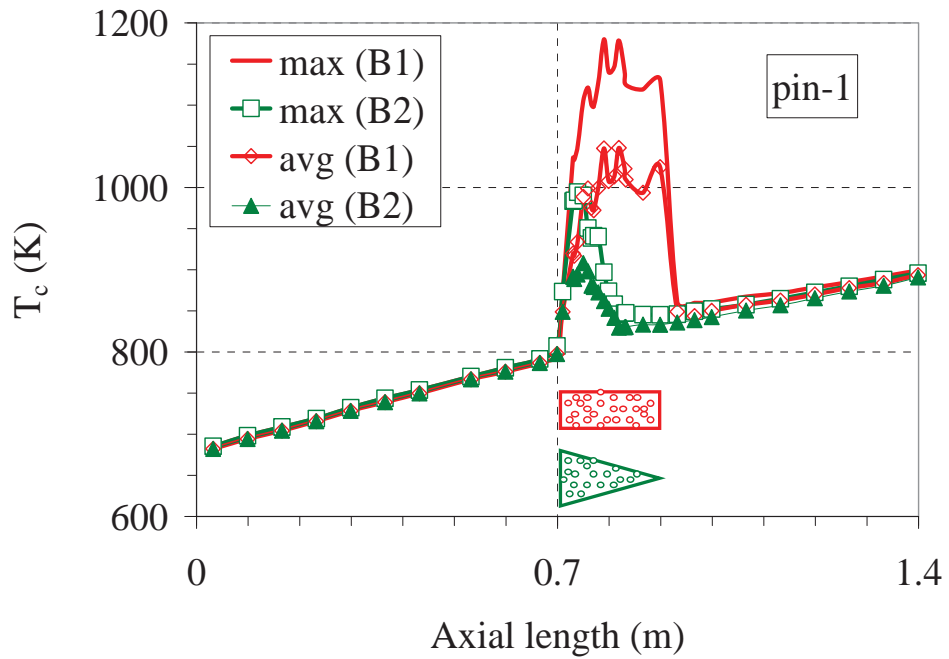


Fig. 7.8b Comparison of peak and mean clad temperatures in pin-1 (*B1* and *B2*-blockages)

Clad temperature distributions of individual pins were also compared for different blockage shapes. The peak and mean clad temperatures of pin-1 are compared in Fig. 7.8b. Clad temperatures for conical blockage are much less than those for cylindrical blockage within the porous zone. However, on the upstream and downstream regions of the porous zone, clad temperatures are nearly identical for both the shapes. This further, suggests that wake regions are almost absent in a rod bundle with spacer wire. The clad temperatures for pin-19 are nearly identical for both the blockages, demonstrating the local influence of central blockages.

Circumferential temperature difference $[\Delta T_{\theta \max}]$ for conical blockage at various axial positions is presented in Table-7.4 for various pins. The value of $(\Delta T_{\theta})_{\max}$ is the highest just above the cone base and it decreases monotonically along the flow direction as the cone tapers down. Comparing with the corresponding values for cylindrical blockage given in Table-7.3, it is clear that $(\Delta T_{\theta})_{\max}$ is much less for the conical blockage than that for

cylindrical blockage. This suggests lower level of thermal stress in the fuel pins for conical blockage, in general. These values for peripheral pins are however, comparable.

Table 7.4 Maximum difference in circumferential clad temperature $[(\Delta T\theta)_{max}]$ in K] for B2-bundle

Z, m	Pin-1	Pin-7	pin-19
0.665	10.8	23.0	24.1
0.730	143.4	196.6	46.9
0.790	66.2	36.2	36.5
0.865	25.1	46.3	30.4
0.932	24.8	30.5	48.5

7.2.2.2 Effect of Blockage Size

In addition to the different shapes of blockages, there is a probability for blockages of different sizes to be formed in the fuel subassembly. Three different sizes of blockage have been considered here, corresponding to the cases of (i) Axial length = 200 mm and six sub-channels blocked (*B1*), (ii) Axial length = 100 mm and six sub-channels blocked (*B3*) and (iii) Axial length = 200 mm and twenty four sub-channels blocked (*B4*), as shown in Fig. 7.3c. It is to be remembered that the blockage begins at an axial length of $Z = 700$ mm from the entry in all the cases.

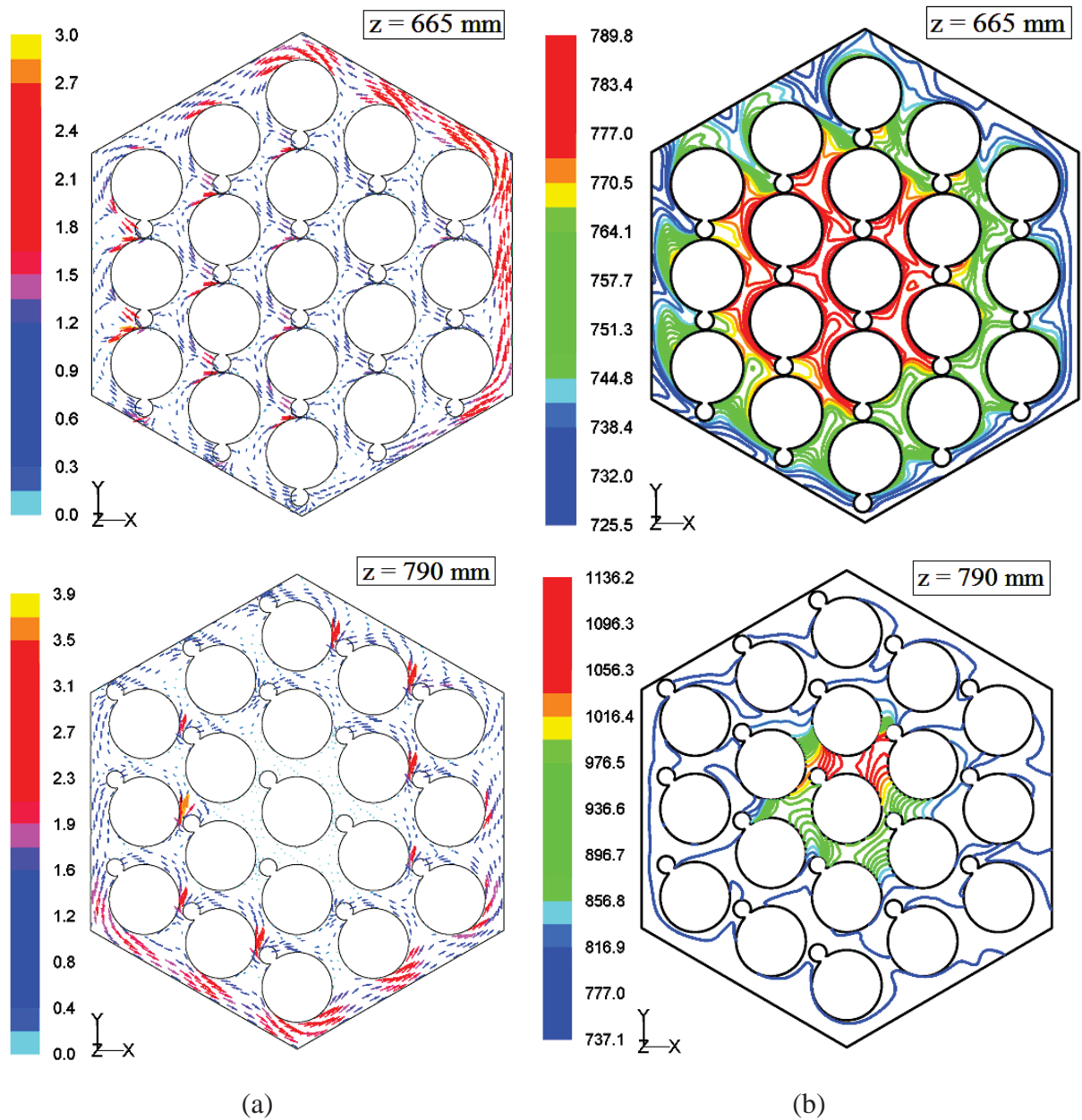


Fig. 7.9 (a) Cross-stream velocity (m/s) vectors for $B3$ type blockage and (b) Isotherms (K) for $B3$ type blockage

The cross-stream velocity vector plot at different cross-sections and the corresponding isotherms are depicted in Figs. 7.9a and 7.9b for a pin bundle with $B3$ -blockage. The corresponding plots for a bundle with $B4$ -blockage are depicted in Figs. 7.10a and 7.10b.

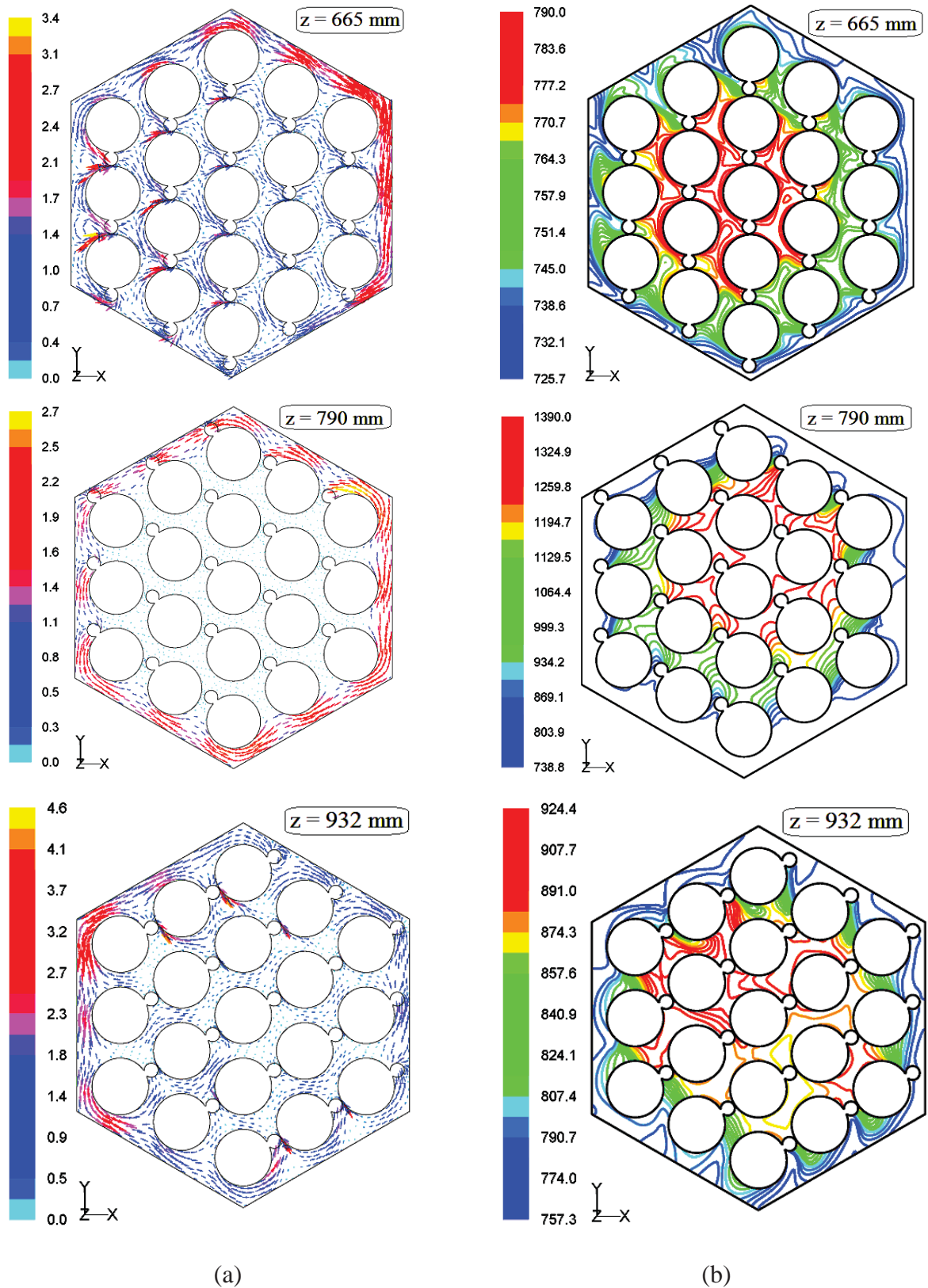


Fig. 7.10 (a) Cross-stream velocity (m/s) vectors for *B4* type blockage and (b) Isotherms (K) for *B4* type blockage

The peak cross-stream velocity occurs within the blockage region for *B1* and *B3*-blockages and it is outside the blockage region in the case of *B4*. The cross-stream velocity is identical in a bundle with *B1* or *B3*-blockage up to the end of blockage. This indicates the parabolic nature of flow and heat transfer at such high Reynolds and Peclet numbers. The temperature values for the bundle with *B3* are almost the same as in a bundle with *B1*-blockage. But in *B4*, the isotherm map is completely different. This is because the maximum cross stream flow is in the region of wall sub-channels. The maximum clad temperature difference in the cross-section $[(\Delta T_{c-s})_{max}]$ is 909 K at $Z= 865$ mm in the bundle with *B4*-blockage.

The peak temperature values calculated in the bundle with *B1*, *B3* and *B4*-blockages along the flow length are depicted in Fig. 7.11a. It is clear that the peak temperature in the blockage zone is a very weak function of blockage axial length. However, it is strongly influenced by the radial extent of blockage. The peak temperature is higher if the radial extent is larger. It is clear that there is a risk of sodium boiling in *B4*-blockage also. Since boiling is not modelled in the present study, the results are not strictly valid if clad temperature exceeds ~ 1155 K. The peak and mean clad temperatures of pin-19 for various blockages are compared in Fig. 7.11b. It is clear that while the axial blockage extent does not influence the pin temperature, the radial extent of blockage exhibits prominent influence. When the radial width of the blockage is more, the circumferential temperature variation is also larger as expected even for the peripheral pins.

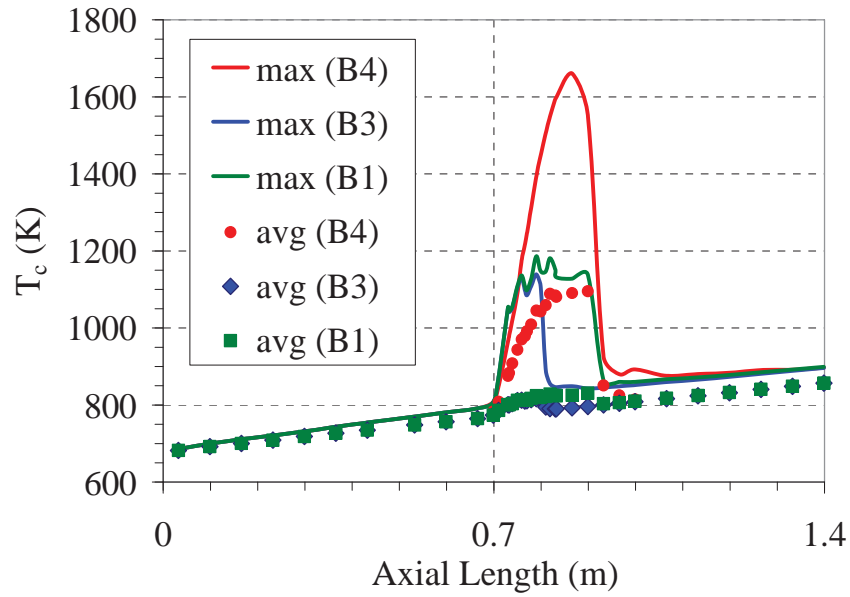


Fig. 7.11a Comparison of peak and average clad temperature in *B1*-blockage bundle against *B3* and *B4* blockage

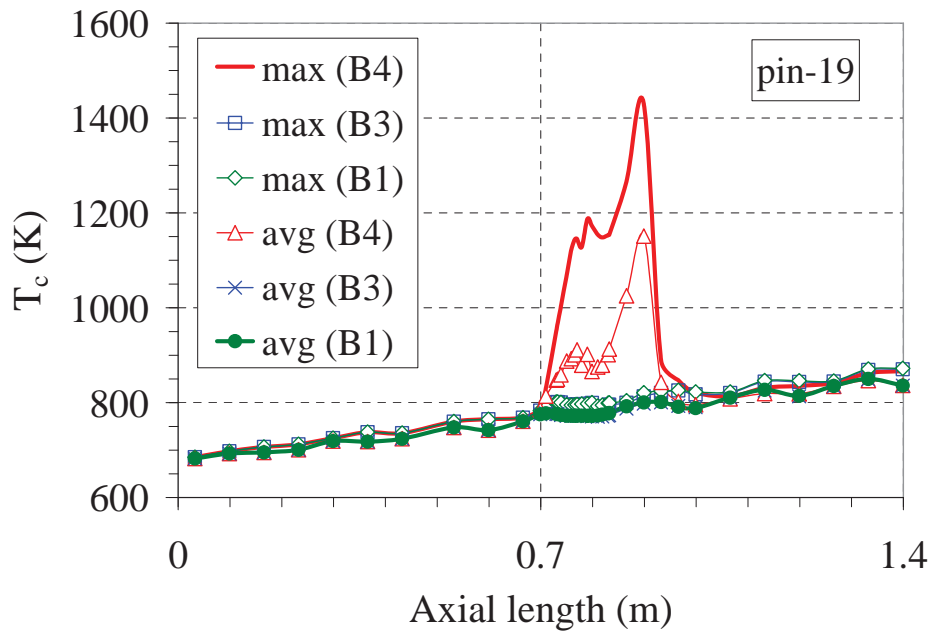


Fig. 7.11b Comparison of peak and mean clad temperature in pin-19 (*B1*, *B3* and *B4*-blockage)

7.2.3 Effect of Radial Position of Blockage

As already discussed blockages can form either in the centre sub-channels or around the corner sub-channels near hexcan wall. Also the SCARLET experiments (Olive and Jolas, 1990) were carried out with both central and wall sub-channel blockages in the wire wrapped

pin bundles. Schultheiss (1987) observed that the blockages have the potential to grow predominantly in the axial direction. Based on the above discussion, it is decided to model the wall sub-channel blockage with 200 mm axial length. The blockage cross-section is 120° sector of a cylinder. It fully includes pin-14 and partially includes pin-13, pin-5 and pin-15 as shown in Fig. 7.3d.

The cross-stream velocity vectors at different cross-sections are depicted in Fig. 7.12a. The peak cross-stream vectors before the blockage in the present case are the same as in the other cases. Here, the high velocity mass flow pattern along the wall sub-channels is uninterrupted due to the presence of blockage. Flow in the peripheral sub-channels reverses its direction after hitting the blockage as seen from the figure. This leads to a change in the secondary flow pattern. The corresponding isotherms are depicted in Fig. 7.12b. The peak temperatures and central pin temperatures are relatively less than those in a bundle with central blockage. This is because most of the flow from the peripheral sub-channels is redirected towards central sub-channels.

Evolution of global average clad temperature for a bundle with *B5*-blockage is depicted in Fig. 7.13a. Also given in the figure is the average temperature in the bundle with *B1*-blockage. The average temperature in *B5*-bundle is marginally less than that in *B1*-bundle, suggesting that a corner blockage is somewhat less critical than the central blockage. However, the clad temperatures are nearly identical in the upstream and downstream of both *B1* and *B5* blockages. Also shown in the same figure is the distribution of maximum clad temperature in *B1* and *B5* bundles. The peak clad temperature in *B5*-bundle is less than that of *B1*-bundle.

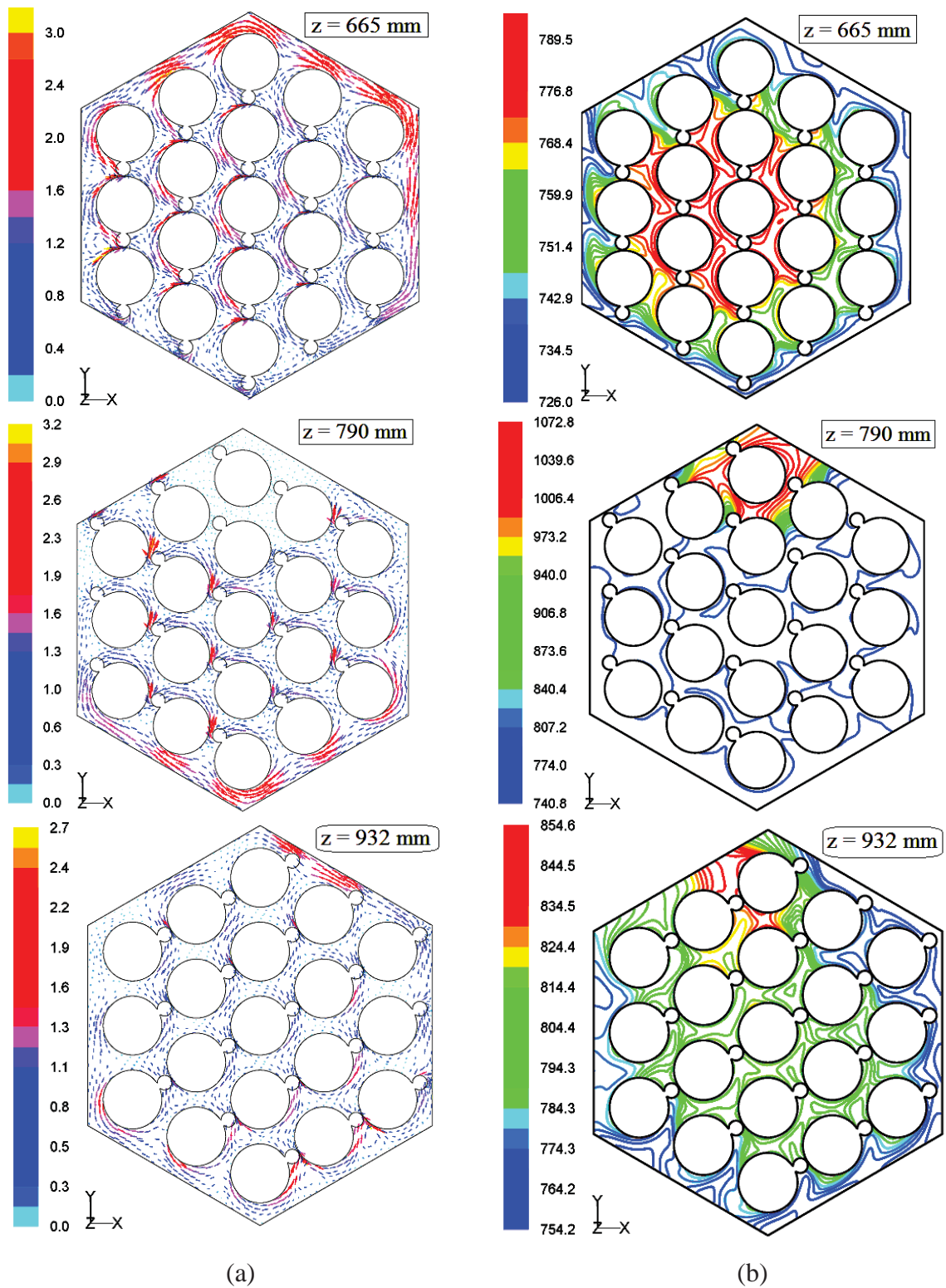


Fig. 7.12 (a) Cross-stream velocity (m/s) vectors for $B5$ type blockage and (b) isotherms (K) for $B5$ type blockage

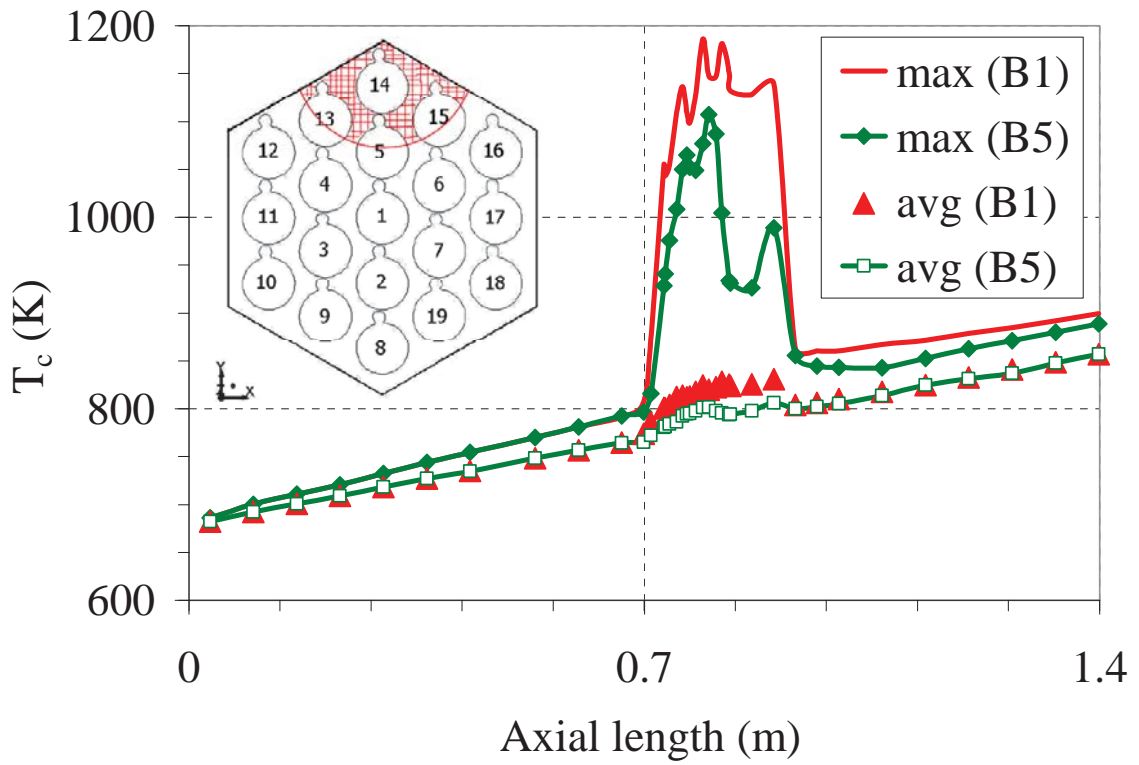


Fig. 7.13a Comparison of peak and average clad temperature in *B1* bundle against *B5* bundle

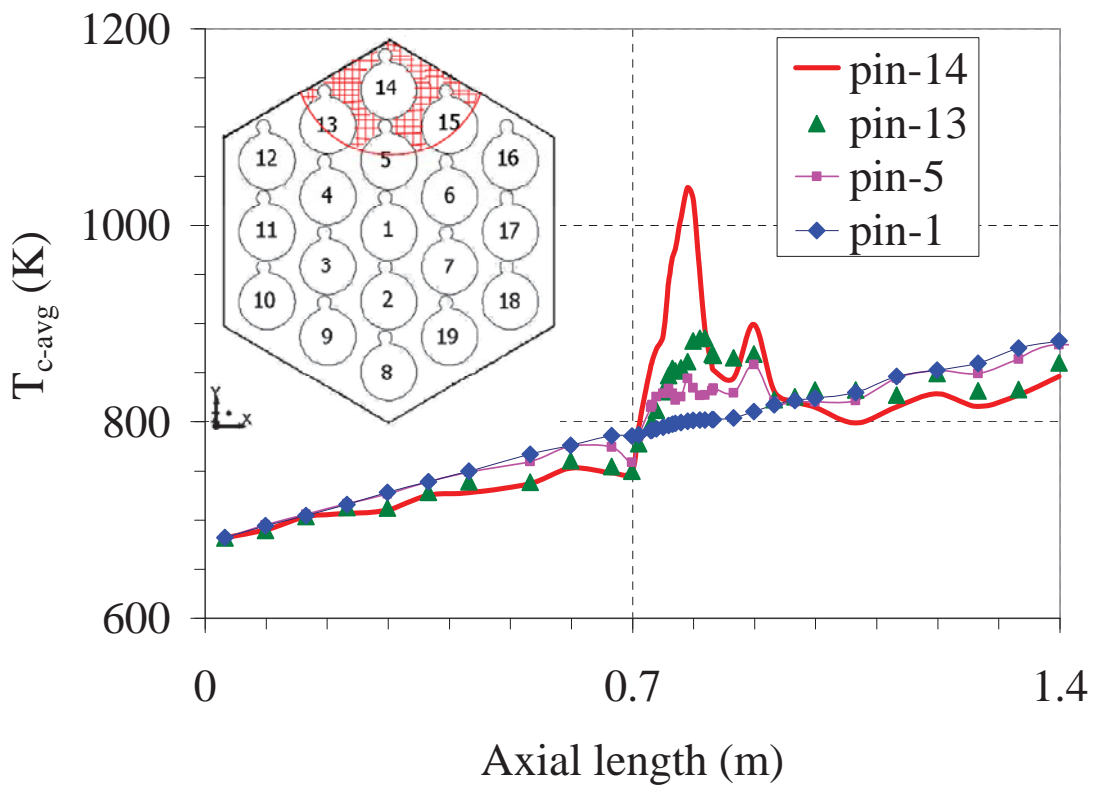


Fig. 7.13b Comparison of mean clad temperatures in pin-1, pin-5, pin-13 and pin-14 in *B5* bundle

The evolution of average clad temperature for pins 1, 5, 13 and 14 in *B5*-bundle is depicted in Fig. 7.13b. Clad temperatures at both downstream and upstream regions of the blockage in the outer row of pins are lower than those of pin-1 as expected, because of the higher cross-stream velocity.

Table 7.5 Maximum in circumferential clad temperature difference $[(\Delta T_{\theta})_{max}$ in K] for a *B5*-bundle

Z, m	Pin-14	Pin-13	Pin-1
0.665	32.6	45.6	12.2
0.730	150.4	161.7	21.3
0.790	75.12	256.0	7.6
0.865	122.7	122.51	13.22
0.932	56.3	41.1	13.5

Maximum circumferential clad temperature differences at different cross-sections for pins 1, 13 and 14 are computed and presented in Table-7.5. Unlike in *BI*-bundle, the pin-1 has the lowest $(\Delta T_{\theta})_{max}$. It is clear from Fig. 7.3d that pin -13 is exposed to blockage on one side and high velocity flow on the other side. Comparing the $(\Delta T_{\theta})_{max}$ values of pin-13 with pin-7 in *BI*-bundle (which is also partially exposed to blockage), it is clear that $(\Delta T_{\theta})_{max}$ is high for a corner blockage. But comparing $(\Delta T_{\theta})_{max}$ for pin-14 in *B5*-bundle with pin-1 in *BI* bundle, it is clear that for pins that are completely shrouded by porous blockage. The $(\Delta T_{\theta})_{max}$ is relatively low for corner blockage.

7.2.4 Effect of Blockage Porosity

Porosity is a measure of the fractional sodium volume within the blockage. It is essential to understand the role of porosity on clad temperature distribution within the pin bundle. This parameter is varied from 20% to 60 %. It shall be remembered that larger the porosity lower will be the flow resistance through the blockage.

The cross-stream velocity vectors and isotherms for the *BI*-bundle with 20% and 60% porosity values at $Z = 790$ mm are depicted in Figs. 7.14a-7.14d. The cross-stream velocity

vectors for 40% porosity were depicted in Fig. 7.4a. The peak cross-stream velocity value is essentially the same for all blockage porosity values. Unlike the cross-stream velocity, the peak clad temperature changes with the porosity. Clad temperature is higher if the porosity value is lower.

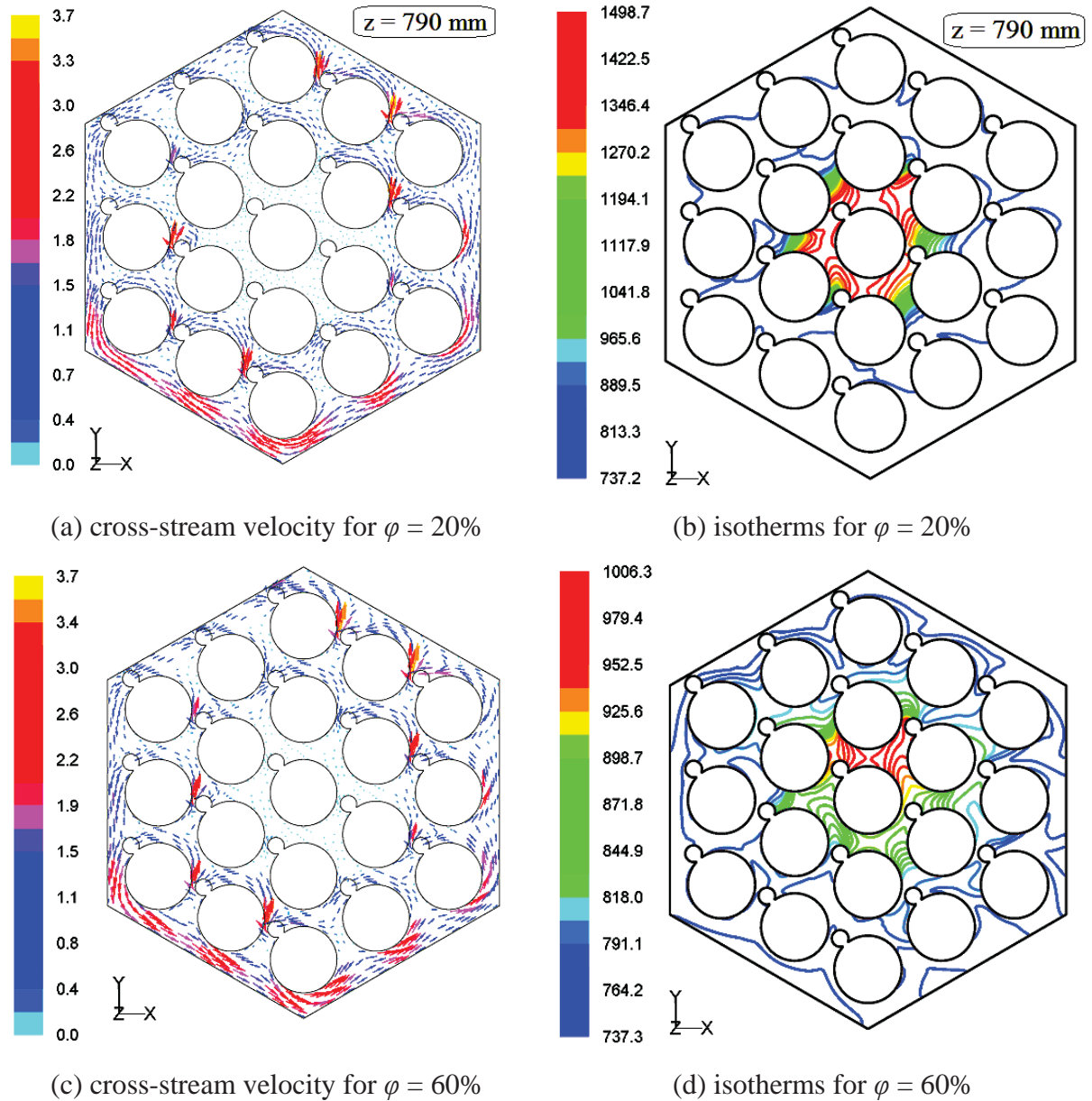
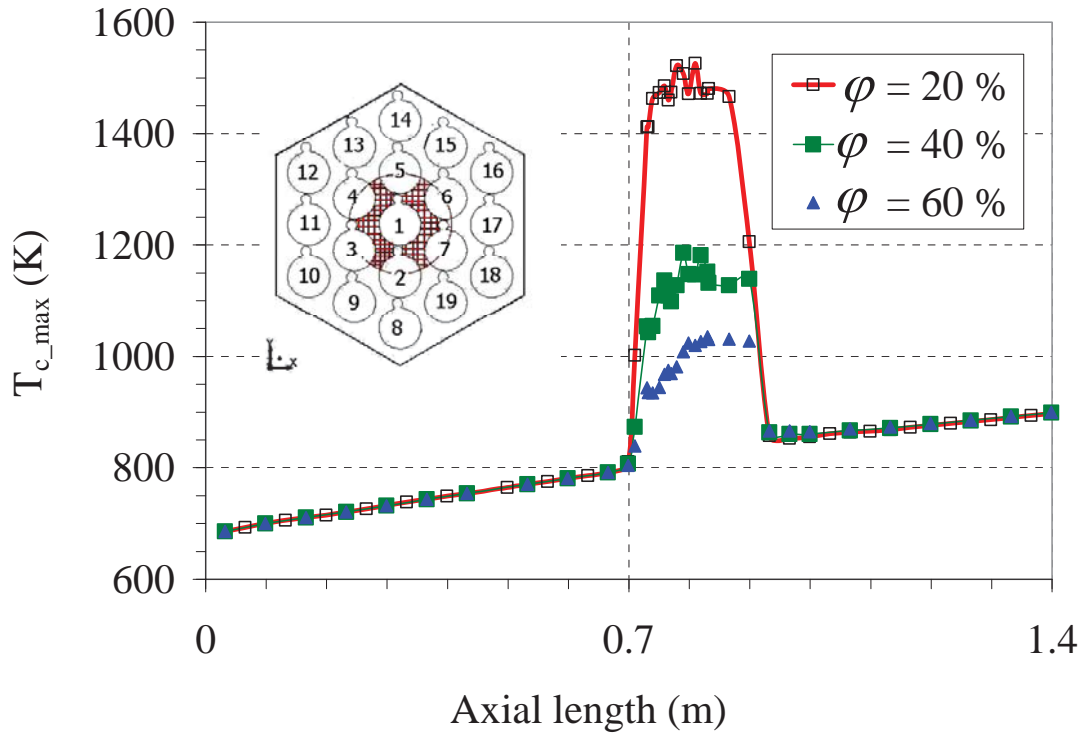


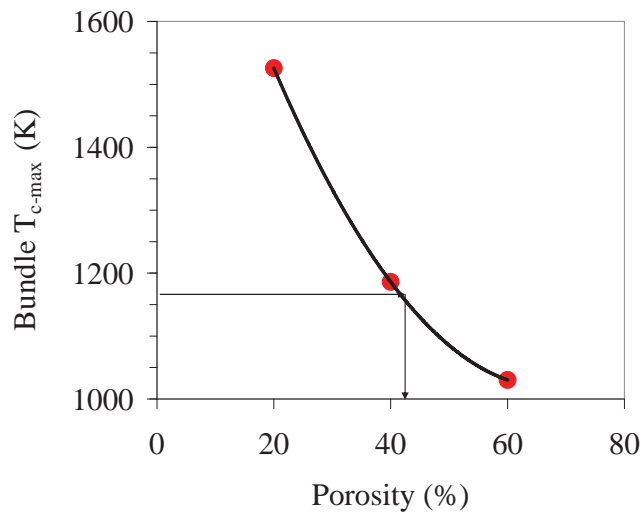
Fig. 7.14 Cross-stream velocity (m/s) vectors and isotherms (K) for *BI* type blockage with different porosity values

Evolution of the maximum clad temperature (T_{c-max}) in *BI*-bundle with 20%, 40% and 60% porosity values is depicted in Fig. 7.15a. The clad temperature is identical in the

downstream and upstream regions of the blockage. Within the blockage region, the clad temperature crosses the sodium boiling point in the cases of 20% and 40% porosity values, but in the 60% porosity case it does not. Hence, a pin bundle with six central sub-channels blocked having a porosity $\leq 45\%$ has the risk of sodium boiling.



(a)



(b)

Fig. 7.15 (a) Comparison of peak clad temperature with 40% porosity *BI*-blockage against 20% and 60% and (b) Bundle peak clad temperature variation with porosity

The peak clad temperature variation within the blockage region as a function of porosity is depicted in Fig. 7.15b. It is clear that the clad temperature reduces when the porosity increases. The rate of rise of clad temperature becomes steep as the porosity value decreases. The values of $(\Delta T_{\theta})_{max}$ in the bundle with B1-blockage is presented in Table-7.6 for different porosity values viz., 20% and 60%. The $(\Delta T_{\theta})_{max}$ in the individual clads decreases as the porosity value of blockage increases. Due to large $(\Delta T_{\theta})_{max}$ thermal stresses will be more in the pins partially exposed to blockage and partially exposed to the coolant.

In the present study, the starting position of the blockage is middle of the bundle. Results are presented for peak as well as mean clad temperatures. It is possible that the blockage can occur in hot upper zone of the bundle. It is known that the temperature difference between mean and peak clad temperatures would remain the same independent of the blockage position. Hence, knowing the mean clad temperature, the peak clad temperature can be calculated.

Table 7.6 Maximum difference in circumferential temperature $[(\Delta T_{\theta})_{max}$ in K] in a bundle with B1-blockage and 20% and 60% porosity values

Z, m	Porosity 20%			Porosity 60%		
	Pin-1	Pin-7	Pin-19	Pin-1	Pin-7	Pin-19
0.665	10.8	23.0	24.1	10.8	23.0	24.1
0.730	339.1	614.1	47.2	101.3	140.9	52.9
0.790	213.7	511.8	39.5	150.5	112.8	37.9
0.865	357.2	667.4	40.5	139.3	149.5	36.5
0.932	28.2	23.7	47.2	36.4	39.7	48.8

7.2.5 Detection of Blockage by Core Temperature Monitoring System

As already indicated in the previous sections, flow simulations have been carried out for an axial length of 7 helical pitches with the pitch length being 200 mm. The nominal inlet velocity is 7.3 m/s, sodium flow rate is 3.866 kg/s and the corresponding Reynolds number is

87,500. For these parameters, the pressure drop across the fuel bundle of the 19 pin reference assembly for various blockage types is presented in Table-7.7.

Table 7.7 Actual flow and the corresponding outlet temperature from blocked subassemblies

Blockage type	ΔP for 3.866 kg/s flow rate (bar)	Q_{act} , (kg/s)	ΔT_{out} (K)	$\Delta T_{BX}-\Delta T_{B0}$ (K)	T_{c-max} (K)
B0	1.8092	3.866	178.3	-	848.3
B1	1.9480	3.726	184.9	6.6	1186.2
B2	1.8780	3.795	181.6	3.3	848.3
B3	1.9022	3.770	182.8	4.5	1139.2
B4	3.7127	2.699	255.4	77.1	1660.9
B5	1.9680	3.707	185.9	7.6	1107.2

The pressure drop for the normal bundle (i.e., bundle without blockage, $B0$) is 1.809 bars and the sodium temperature increase across the normal subassembly (ΔT_{out-B0}) is 178.3 K. In order to have the same pressure drop in the blocked bundle, the flow rate would reduce to Q_{act} . This is because in pool type fast reactors, a large number of subassemblies are fed by a common high pressure inlet plenum, known as Grid plate (Fig. 1.2). The calculated values of Q_{act} for different blockage types are also presented in Table-7.7. As a consequence of flow reduction due to blockage, the values of ΔT_{out-BX} from blocked subassembly increases as indicated in Table-7.7. The sodium outlet temperature increase as sensed by the core temperature monitoring thermocouples (Fig. 1.2) located just above the subassembly exit, ($\Delta T_{out-BX}-\Delta T_{out-B0}$) is presented in Table-7.7 along with the peak clad temperature (T_{c-max}). It can be seen that the temperature increase in thermocouple reading is less than 10 K for all the bundles except for $B4$ bundle. The threshold value of temperature increase for reactor trip by core temperature monitoring system is typically 10 K (see, Maity et al., 2011). Thus, it is clear that local sodium boiling around the clad surrounded by blockage is possible even when the bulk temperature of sodium exiting the subassembly is much less than the reactor trip

threshold. The ratio of blockage cross section to total flow cross section of the subassembly in B4 bundle is ~51%. The corresponding values for all the other bundles are less than 13%. In power reactors, the number of fuel pins per subassembly is generally large (in the range of 217 – 271). Hence, the ratio of blockage cross section in the full size subassemblies is expected to be significantly less than 13%. Consequently, the flow reduction and sodium outlet temperature rise are expected to be much less than 10 K. This leads to the conclusion that it is difficult to detect small size internal blockages by core monitoring thermocouples before sodium boiling occurs.

7.2.6 Effect of Thermal Conductivity

In the present simulations, effective thermal conductivity (K_{eff}) is calculated using the arithmetic mean (Eq. 3.14) and the blockage particles are taken to be made of stainless steel. For the nominal porosity of 40%, the K_{eff} turns out to be 39.3 W/m-K. When harmonic mean (Eq. 3.15) is taken, then the value of K_{eff} turns out to be 25.4 W/m-K. When this lower value of K_{eff} is considered, the peak value clad temperature in porous zone increases by ~80 K as can be seen in Fig. 7.16. However, it is sometimes customary to use geometric mean (Eq. 3.16) to calculate K_{eff} in porous zone (Nield and Bejan, 2013). The value of K_{eff} by geometric mean turns out to be 31.2 W/m-K.

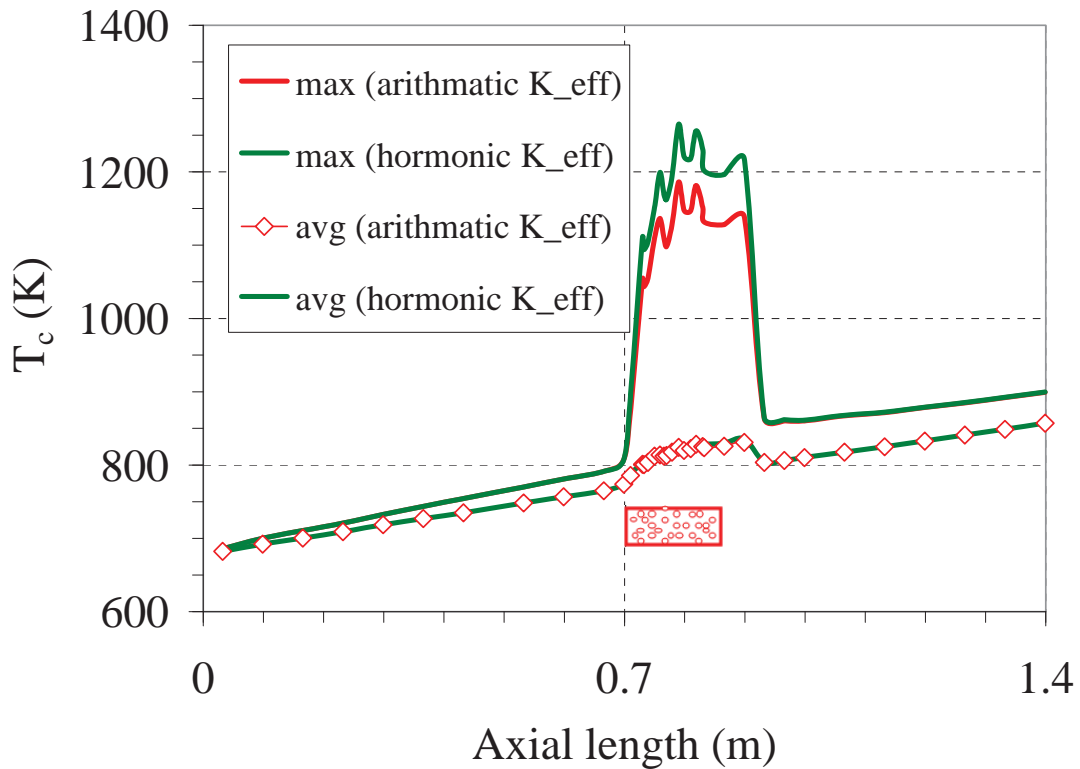


Fig. 7.16. Comparison of predicted clad temperature adopting different expressions for effective thermal conductivity

7.3 CLOSURE

Detailed three-dimensional blockage study has been carried out for wire-wrapped 19-pin fuel bundles. The parametric study consists of the effects of blockage geometry (shape and size), its radial position, and blockage porosity. The clad temperature within the blockage region is seen to exhibit strong spatial fluctuations due to the interaction of helical spacer wire with the porous blockage. The maximum difference in the circumferential temperature of clad, which is a critical parameter for fuel pin mechanical design, is large in pins that are partially exposed to the blockage. Also, the peak clad temperature exhibits a non-linear relationship with porosity of the blockage. It is seen that the effect of blockage is highly localized without significant wake effects downstream of the blockage. This suggests that the wake regions are almost absent in a rod bundle with spacer wire due to the cross-stream velocity induced by the spacer wire. The peak clad temperature is found to be proportional to

the volume of the porous zone. Maximum circumferential difference in the clad temperature is low for a corner blockage as compared to that of a central blockage. Sodium boiling is imminent in the fuel pin bundle with six sub-channel central blockage when porosity value reduces below 45%. Based on the detailed parametric studies, it is apparent that detection of small size internal blockages by core monitoring thermocouples is difficult in reactors with subassemblies having large number of pins (for example 217 or 271).

CHAPTER-8

CONCLUSIONS

8.0 INTRODUCTION

In the preceding chapters, two types of studies have been carried out with the help three-dimensional CFD Simulations, viz., (1) flow and thermal development in fuel pin bundles and (2) flow and temperature fields in a bundle with porous blockage. The focus of the studies have been to understand (i) development of friction factor, Nusselt number and cross flow in the entrance region, (ii) thermal and hydraulic entry lengths, (iii) hotspot factors, (iv) circumferential variation in clad temperature and (v) peak and mean clad temperatures in normal and blocked fuel pin bundles. Liquid sodium is the fluid considered for all the studies.

Detailed parametric studies have been carried out by varying the number of pins, pin / wire diameters, helical pitch, ligament gap, Reynolds number, size, position and porosity of the blockage. The computational results have been compared with appropriate experimental / numerical results published in open literature. Reasonable comparison has been observed for fully developed flows and flows with internal blockage. Major conclusions of these studies are highlighted in the following sections.

8.1 FLOW AND THERMAL DEVELOPMENT IN BARE FUEL PIN BUNDLES

- ❖ While the flow development is achieved within an axial distance of about 125 hydraulic diameters, the thermal development is attained at similar axial distances only if the pin diameter is small or the number of pins is less.
- ❖ For large pin diameters with more pins, temperature development could not be achieved even after a length of 1000 hydraulic diameters. This is due to the weak communication among sub-channels in tightly packed bundles. Further, the clad temperature in the peripheral pins is lower than the cross section bulk fluid

temperature, which is a consequence of the large cross sectional variation in fluid temperature.

- ❖ Helical spacer wires shorten thermal development length and enhance global Nusselt number. But their influence on flow development length is marginal.

8.2 LAMINAR FLOW AND THERMAL DEVELOPMENT IN HELICAL WIRE-WRAPPED PIN BUNDLES

- ❖ The friction factor and Nusselt number exhibit prominent spatial oscillations in the entrance region, contrary to that seen in the case of straight channels.
- ❖ While the friction factor exhibits a strong dependence on helical pitch the Nusselt number does not exhibit such a strong dependence on helical pitch.
- ❖ A strong non-zero cross-stream velocity prevails in the fully developed region of pin bundle, unlike in straight channels. The mean value of non-dimensional cross-stream velocity is found to scale as $\pi d/H$.

8.3 TURBULENT FLOW AND THERMAL DEVELOPMENT IN HELICAL WIRE-WRAPPED PIN BUNDLES

- ❖ The magnitude of mean cross-stream velocity is inversely proportional to the helical pitch and is nearly independent of the number of pins.
- ❖ Flow development length is $\approx 70 \times D_h$ and is nearly independent of the helical pitch.
- ❖ The Nusselt number passes through multiple minima before attaining fully developed periodic fluctuations. Larger the number of pins, longer is thermal development length.
- ❖ The following correlation for fully developed Nusselt number is proposed:

$$Nu = 4.497 + 0.89 \left(\frac{P_t / D_r}{H / (D_r + D_w)} \right)^{1.29} (Pe)^{0.86}$$

for $1.1 \leq (P_t / D_r) \leq 1.4$, $12 \leq [H / (D_r + D_w)] \leq 36$ and $198 \leq Pe \leq 890$.

- ❖ The average friction factor in the fully developed region is independent of the number of pins and hence, the present results of friction factor can be used for 217 pin bundle.
- ❖ The amplitude of fluctuation in friction factor is seen to increase with number of pins at the rate of about 4% per row of pins. Hence, for a 217 pin bundle with 8 rows, the fluctuation is expected to be about 32%, by straight extrapolation.

8.4 THERMAL HYDRAULIC EFFECTS OF POROUS BLOCKAGE IN WIRE-WRAPPED BUNDLES

- ❖ Effect of blockage is highly localized without significant wake effects downstream of the blockage.
- ❖ Effect of porous blockage is primarily limited to the porous zone and the peak clad temperature is proportional to the volume of the porous zone.
- ❖ The peak temperature in the blockage is strongly influenced by the radial extent of the blockage
- ❖ Sodium boiling is imminent in pin bundle with six sub-channel central blockage when porosity value reduces below 45%.
- ❖ Detection of small size internal blockages by core monitoring thermocouples is difficult in reactors with subassemblies having large number of pins (for example 217 and 271).

8.5 PROPOSED FUTURE WORK

- ❖ Flow over porous block inside the pin bundle may exhibit unsteady behavior with complex flow structures. Hence, unsteady simulations can be carried out to understand their effect on fluctuating clad temperatures that can lead to thermal fatigue of the clad.
- ❖ The Nusselt number is found to be a decreasing function of the number of pins. Also, the developmental length is found to increase with the number of pins. Hence,

detailed CFD simulation of 217 pin bundle is essential to determine the thermal characteristics of full-size fuel subassembly.

- ❖ There is lack of experimental results, especially for the entrance flow in pin bundles with wire wrap. These experimental results are essential for validation of the CFD results. Further, it is seen that the results of pin bundle are highly sensitive to ligament gap, number of pins, procedure of averaging the clad / coolant temperatures etc. Hence, all the geometrical and flow / thermal parameters need to be properly documented while reporting the experimental results.

APPENDIX-1

THERMO PHYSICAL PROPERTIES OF SODIUM AS FUNCTION OF TEMPERATURE

Where,

C_p = specific heat (kJ/kg-K)

k = Thermal conductivity (W/m-K)

μ = Dynamic viscosity (N-s/m²)

ρ = Density (kg/m³)

H = Enthalpy (J/Kg)

P_v = Vapour pressure (Pa)

β = Volumetric expansion in (K⁻¹)

Pr = Prandtl number

Temperature (°C)	$C_p \cdot 10^3$ (kJ/kg-K)	k (W/m-K)	$\mu \cdot 10^3$ (N-s/m ²)	ρ (kg/m ³)	Pr -
250	1320.5	78.5	0.385	892.2	0.0065
300	1304.2	76.0	0.340	880.5	0.0058
350	1290.2	73.6	0.307	868.8	0.0054
400	1278.5	71.2	0.281	857.0	0.0050
450	1269.1	68.8	0.260	845.1	0.0048
500	1262.1	66.3	0.243	833.1	0.0046
550	1257.3	63.9	0.228	821.1	0.0045
600	1254.9	61.5	0.216	808.9	0.0044
650	1254.7	59.1	0.206	796.7	0.0044
700	1256.9	56.6	0.197	784.3	0.0044
750	1261.4	54.2	0.189	771.9	0.0044
800	1268.2	51.8	0.182	759.4	0.0045

REFERENCES

- [1] Acharya, N., Sen, M., Chang, H.C., 1993, Thermal entrance length and Nusselt numbers in coiled tubes, *International Journal of Heat and Mass Transfer*, **37**, 336-340.
- [2] Baxi, Dalle-Donne, 1981, Heat Transfer and Fluid Flow in Nuclear Systems. In: Pergamon Press, ISBN 0-08-027181-2.
- [3] Bejan, A., 2004, *Convection Heat Transfer*, 3rd edition, Wiley-India, Delhi.
- [4] Bieder, U., Barthel, V., Ducros, F., Quéméré, P., Vandroux, S., 2008, CFD calculations of wire-wrapped fuel bundles: modeling and validation strategies, *CEA-Grenoble, DEN/DER/SSTH/LDAL, 15 rue des Martyrs, F-38054 Grenoble*.
- [5] Borishanskii, V.M., Gotovski, M.A, Firsova, E.V., 1969, Heat transfer to liquid metals in longitudinally wetted bundles of rods, *Atomnaya Energiya*, **27(6)**, 549 - 552.
- [6] Bubelis, E., Schikorr, M., 2008, Review and proposal for best fit of wire-wrapped fuel bundle friction factor and pressure drop predictions using various existing correlations, *Nuclear Engineering and Design*, **238**, 3299-3320.
- [7] Cengel, Y.A., 2007, Heat and Mass Transfer, third edition, *Tata McGraw-Hill Education Private limited*, New Delhi, pp. 457.
- [8] CFDExpert, 2009, *Zeus Numerix Pvt. Ltd.*, Mumbai.
- [9] Chandra, L., Roelofs, F., Houkema, M., Jonker, B., 2009, A stepwise development and validation of a RANS based CFD modeling approach for the hydraulic and thermal-hydraulic analysis of liquid metal flow in a fuel assembly, *Nuclear Engineering and Design* **239(10)**, 1988 - 2003.
- [10] Chandra, L., Roelofs, F., 2011, CFD analyses of liquid metal flow in sub-channels for gen IV reactors, *Nuclear Engineering and Design*, **241**, 4391-4403.
- [11] Chang, W.P., Ha, K.S., Suk, S.D., Jeong, H.Y., 2011, A comparative study of the MATRA-LMR-FB calculation with the SABRE result for the flow blockage accident in the sodium cooled fast reactor, *Nuclear Engineering and Design*, **241**, 5225 - 5237.
- [12] Chauhan, A.K., Prasad, B.V.S.S.S., Patnaik, B.S.V., 2013, Thermal hydraulics of rod bundles: The effect of eccentricity, *Nuclear Engineering and Design*, **263**, 218-240.
- [13] Cheng, B.C., Todreas, N.E., 1986a. Prediction of coolant temperature field in a Breeder reactor including interassembly heat transfer, COO-2245-20 TR, Review-1.
- [14] Cheng, S.K., Todreas, N.E., 1986b, Hydrodynamic models and correlations for bare and wire-wrapped hexagonal rod bundles - bundle friction factors, sub-channel friction factors and mixing parameters, *Nuclear Engineering and Design*, **92**, 227-251.

- [15] Chetal, S.C., Balasubramaniun, V., Chellapandi, P., mohanakrishnan, P., Pudhiyavinayagam, P., Pillai, C.P., Raghupathi, S., Shanmugham, T.K., Sivathanu Pillai, C., 2006, the design of the Prototype Fast Breeder Reactor, **236**, 852-860.
- [16] Chun, M.H., Seo, K.W., 2001, An Experimental study and assessment of existing friction factor correlations for wire-wrapped fuel assemblies, *Annals of Nuclear Energy*, **28**, 1683 - 1695.
- [17] Dwyer, O.E., Tu, P.S., 1960, Analytical study of heat transfer rates for parallel flow of liquid metals through tube bundles, Part 1. *Chemical Engineering Progress Symposium Series*, **56 (30)**, 183 –193.
- [18] Ergun, S., 1952, Fluid Flow through Packed Columns, *Journal of Chemical Engineering Progress*, **48(2)**, 89 - 94.
- [19] Engel, F.C., Markley, R.A., Bishop, A.A., 1979, Laminar, transition and turbulent parallel flow pressure drop across wire-wrap-spaced rod bundles, *Nuclear Science and Engineering*, **69**, 290–296.
- [20] Feldman, E.E., Hornbeck R.W., Osterle, J.F., 1982, A numerical solution of laminar developing flow in eccentric annular ducts, *International Journal of Heat and Mass Transfer*, **25**, 231-241.
- [21] Fischer, P., Lottes, J., Siegel, A., 2007, Large eddy simulation of wire-wrapped fuel pins I: Hydrodynamics in a Periodic Array, *Joint International Topical Meeting on Mathematics & Computation and Supercomputing in Nuclear Applications (M&C + SNA)* Monterey, California.
- [22] FLUENT, 2007, *FLUENT 6.3 user's guide*, FLUENT Inc., USA.
- [23] Fontana, M.H., Macpherson, R.E., Gnadt, P.A., Parsly, L.F., Kress, T.S., Wantland, J.L., 1973, Effect of partial blockages in simulated LMFBR fuel assemblies, Contract No.W-7405-eng-26, *Oak Ridge National Laboratory*, Oak Ridge, Tennessee - 37830.
- [24] Friedland, A.J., Bonilla, C.F., 1961, Analytical study of heat transfer rates for parallel flow of liquid metals through tube bundles, *American Institute of Chemical Engineers Journal*, **7 (1)**, 107 – 112.
- [25] Gajapathy, R., Velusamy, K., Selvaraj, P., Chellapandi, P., Chetal, S.C., 2007, CFD investigation of helical wire-wrapped 7-pin fuel bundle and the challenges in modelling full scale 217 bundle, *Nuclear Engineering and Design*, **237(24)**, 2332 - 2342.
- [26] Gajapathy, R., Velusamy, K., Selvaraj, P., Chellapandi, P., Chetal, S.C., 2009, A Comparative CFD investigation of helical wire-wrapped 7, 19 and 37 fuel pin bundles and its extendibility to 217 pin bundle, *Nuclear Engineering and Design*, **239**, 2279 - 2292.
- [27] George, M.A., Dobson, G.P., 1990, Fast reactor subassembly blockage studies-calculations of temperatures within a blockage, in the wake of a blockage and at thermocouple detector locations, 4 (Session-3), *International Fast Reactor Safety*

Meeting, Snowbird, Utah.

- [28] Graber, V.H., Rieger, M., 1972, Experimentelle Untersuchung des Wärmeübergangs an Flüssigmetalle (NaK) in parallel durchströmten Rohrbündeln bei konstanter und exponentieller Wärmeflussdichteverteilung, *ATKE Bd*, **19**, 23 - 40.
- [29] Han, J. T., 1979, Heat transfer in a partially- blocked sodium cooled rod bundle, Contract No.W-7405-eng-26, *Oak Ridge National Laboratory*, Oak Ridge, Tennessee - 37830.
- [30] Holtz, R.E., Fauske, H.K., 1971, The prediction of incipient boiling superheats in liquid metal cooled reactor systems, *Nuclear Engineering and Design*, **16**, 253-265.
- [31] Incropera, F.P., Dewitt, D.P., 2009, *Fundamentals of Heat and Mass Transfer*, 5th edition, John Wiley & Sons (Asia), pp. 485 – 487.
- [32] Kawamura, H., Ohsaka, K., Abe, H., Yamamoto, K., 1998, DNS of turbulent heat transfer in channel flow with low to medium-high Prandtl number fluid, *International Journal of Heat and Fluid Flow*, **19**, 482-491.
- [33] Kazimi, M.S., Carelli, M.D., 1976. Heat transfer correlation for Analysis of CRBRP Assemblies, *Westinghouse Report*, CRBRP-ARD-0034.
- [34] Knudsen, J.G., Katz, D.L., 1958, *Fluid Dynamics and Heat Transfer*, McGraw-Hill, New York.
- [35] Launder, B.E., Spalding, D.B., 1974, The numerical computation of turbulent flows. *Computer Methods in Applied. Mechanics and Engineering*, **3**, 269 - 289.
- [36] Lin, C.X., Zhang, P., Ebadian, M.A., 1997, Laminar forced convection in the entrance region of helical pipes, *International Journal of Heat and Mass Transfer*, **40**, 3293-304.
- [37] Maity, R.K., Velusamy, K., Selvaraj, P., Chellapandi, P., 2011, Computational fluid dynamic investigations of partial blockage detection by core-temperature monitoring system of a sodium cooled fast reactor, *Nuclear Engineering and Design*, **241**, 4994 - 5008.
- [38] Manglik, R. M., Bergles, A.E., 1988, Laminar flow heat transfer in a semi-circular tube with uniform wall temperature, *International Journal of Heat and Mass Transfer*, **31**, 625-636.
- [39] Manglik, R.M., Bergles, A.E., 1996, Thermally developing laminar flows in circular-segment ducts with uniform wall temperature, *Proc. 9th International Symposium on Transport Phenomena in Thermal-Fluids Engineering*, **2**, 831-836.
- [40] Mareska, M.V., Dwyer, O.E., 1964, Heat transfer in a mercury flow along bundles of cylindrical rods, *ASME Journal of Heat Transfer*, **86**, 180 - 186.
- [41] Mikityuk, K., 2009, Heat transfer to liquid metal: review of data and correlations for tube bundles, *Nuclear Engineering and Design*, **239(4)**, 680-687.

- [42] Massoud, M., 2005, *Engineering Thermofluids: Thermodynamics, Fluid Mechanics, and Heat Transfer*, Springer, Berlin Heidelberg, New York.
- [43] Natesan, K., Velusamy, K., Selvaraj, P., Chellapandi, P., Chetal, S.C., 2007, Thermal hydraulic study on detection of random failure of fuel by delayed neutron detection system, *Nuclear Engineering and Design*, **237**, 2219-2231.
- [44] Natesan, K., Sundararajan, T., Narasimhan, A., Velusamy, K., 2010, Turbulent flow simulation in a wire-wrap rod bundle of an LMFBR, *Nuclear Engineering and Design*, **240(5)**, 1063-1072.
- [45] Nield, D.A., Bejan, A., 2013, *Convection in porous media*, 4th edition, Springer publication, New York.
- [46] Novendstern, E.H., 1972, Turbulent flow pressure drop model for fuel rod assemblies utilizing a helical wire-wrap spacer system, *Nuclear Engineering and Design*, **22**, 19 - 27.
- [47] Olive, J., Jolas, P., 1990, Internal blockage in a fissile super-phenix type of subassembly: the SCARLET experiment's and their interpretation by the CAFCA-NA3 code, *Nuclear Energy*, **29**, 287 - 293.
- [48] Patankar, S.V., 1980, *Numerical Heat Transfer and Fluid Flow*, McGraw-Hill, New York,.
- [49] Péniguel, C., Rupp, I., Rolfo, S., Guillaud, M., 2010, Thermal-hydraulics and Conjugate Heat Transfer Calculation in a Wire-Wrapped SFR Assembly, *Proceedings of International congress on Advances in National Power Plants (ICAPP)*, Paper No. 10174.
- [50] Ravichandar, S.C., Rajan Babu, V., Puthiyavinayagam, P., Chellapandi, P., 2007, Allowable flow reduction due to blockage in radial blanket subassembly, Report: PFBR-31130-DN-1011, *Indira Gandhi centre for atomic research (IGCAR), kalpakkam*.
- [51] Raza, W., Kim, K.Y., 2008, Comparative Analysis of Flow and Convective Heat Transfer between 7-Pin and 19-Pin Wire-Wrapped Fuel assemblies, *Journal of Nuclear Science and Technology*, **45(7)**, 653 - 661.
- [52] Rehme, K., 1973, Pressure drop correlations for fuel element spacers, *Nuclear Technology*, **17**, 15–23.
- [53] Rensen, Q., 1981, Experimental investigation of turbulent heat transfer to liquid sodium in the thermal entrance region of an annulus, *Nuclear Engineering and Design*, **68**, 397 - 404.
- [54] Roelofs, F., Gopala, V.R., Chandra, L., Viellieber, M., Class, A., 2012, Simulating fuel assemblies with low resolution CFD approaches, *Nuclear Engineering and Design*, **250**, 548-559.

- [55] Rolfoa, S., Péniguelb, C., Guillaudc, M., Laurencea, D., 2012, Thermal-hydraulic study of a wire spacer fuel assembly, *Nuclear Engineering Design*, **243**, 251-262.
- [56] Roychowdhury, D.G., Govindarajan, S., Chetal, S.C., Bhoje, S.B., 2000, Design approach to local blockages, *Energy technology data exchange world energy base (ETDEWEB)*, 289 - 300.
- [57] Roychowdhury, D.G., Ravichandar, S.C., Govindarajan, S., 2002, Fuel subassembly blockage analysis in prototype fast breeder reactor, *National Conference on Nuclear Reactor Safety, Mumbai*.
- [58] Rowe, D.S., 1973, COBRA-3C: A digital Computer Program for Steady-State and Transient Thermal-Hydraulic Analysis of Rod Bundle Nuclear Fuel Elements, BNWL-1965.
- [59] Schultheiss, G.F., 1987, On local blockage formation in sodium cooled reactors, *Nuclear Engineering and Design*, **100**, 427-433.
- [60] Seong, S.H., Jeon, W.D., Choi, S.K., Kim, S.O., 2006, Establishment of the design requirements for a flow blockage detection system through a LES analysis of the temperature fluctuation in the upper plenum, *Annals of Nuclear Energy*, **33**, 62-70.
- [61] Shang, Z., 2009, CFD investigation of vertical rod bundles of supercritical water-cooled nuclear reactor, *Nuclear Engineering and Design*, **239**, 2562 - 2572.
- [62] Sobolev, V., 2006, Fuel rod and assembly proposal for XT-ADS pre-design. *Coordination meeting of WPI&WP2 of DMI IP EUROTRANS*, Bologna.
- [63] Shah, R.K., London, A.L., 1978, Laminar flow forced convection in ducts, *Advances in Heat Transfer Academic Press, New York*.
- [64] Sreenivasulu, T., Prasad, B.V.S.S.S., 2009, Prasad, Flow and heat transfer characteristics in an annulus wrapped with a helical wire, *International Journal of Thermal Sciences*, **48**, 1377 - 1391.
- [65] Sreenivasulu, T., Prasad, B.V.S.S.S., 2011, Flow and heat transfer characteristics in a seven tube-bundle wrapped with helical wires, *International Journal of Advancements in Technology*, **2(3)**, 350-381.
- [66] Srinivasan, G., Suresh Kumar, K.V., Rajendran, B., Ramalingam, P.V., 2006, The Fast Breeder Test Reactor-Design and operating experiences, **236**, 796-811.
- [67] Steiner, H., Konys, J., 2006, Heat and mass transfer calculations in heavy liquid metal loops under forced convection conditions, *Nuclear Engineering and Design*, **348**, 18-25.
- [68] Subbotin, V.I., Ushakov, P.A., Kirillov, P.L., Ibragimov, M.H., Ivanovski, M.N., Nomofilov, E.M., Ovechkin, D.M., Sorokin, L.N., Sorokin, V.P., 1965, Heat transfer in elements of reactors with a liquid metal coolant. In: *Proceedings of 3rd International Conference on Peaceful uses of Nuclear Energy*, 8, New York, pp. 192-200.

- [69] Tenchine, D., 2010, Some thermal hydraulic challenges in sodium cooled fast reactors, *Nuclear Engineering and Design*, **240**, 1195–1217.
- [70] Todreas, N.E., Kazimi, M.S., 1993, *Nuclear Systems I: Thermal Hydraulic Fundamentals*, 2nd edition, Taylor & Francis, Levittown.
- [71] Uotani, M., Haga, K., 1984, Experimental investigation of sodium boiling in partially blocked fuel subassemblies. *Nuclear Engineering and Design*, **82**, 319-328.
- [72] Ushakov, P.A., Zhukov, A.V., Matyukhin, M.M., 1977, Heat transfer to liquid metals in regular arrays of fuel elements, *High Temperature*, **15**, 868 - 873.
- [73] Velusamy, K., Garg, V.K., 1993, Entrance flow in elliptical ducts, *International Journal of Numerical Methods in Fluids*, **17**, 1079-1096.
- [74] Velusamy, K., Chellapandi, P., Chetal, S.C., Raj, B., 2010, Overview of pool hydraulic design of Indian prototype fast breeder reactor, *Sadhana*, **35(2)**, 97–128.
- [75] Zhimin, Y., 2000, Thermal hydraulic behaviour of subassembly local blockage in China experiment fast reactor, *Energy technology data exchange world energy base (ETDEWEB)*, 281-288.
- [76] Zhukov, A.V., Kuzina, Yu.A., Sorokin, A.P., Leonov, V.N., Smirnov, V.P., Sila-Novitskii, A.G., 2002, An experimental study of heat transfer in the core of a BREST-OD-300 reactor with lead cooling on models, *Thermal Engineering*, **49(3)**, 175 - 184.

NOMENCLATURE

a	Radius of the helical pipe
A	Amplitude
A_f	Cross sectional flow area
$B0$	No blockage
$B1, B2, B3, B4, B5$	Different shapes and sizes of blockage
C	Turbulent model constants (or) coefficient in Nusselt number correlation
C_p	Specific heat at constant pressure
D_h	Hydraulic diameter, [= 4 × flow area / wetted perimeter]
D_r	Fuel pin diameter
D_w	Diameter of helical spacer wire
f	Friction factor
\bar{f}	Average friction factor, [($f_{\max} + f_{\min}$)/2]
F_c	Hotspot factor
$F_{h,j}$	Effective heat flux containing laminar and turbulent contributions
h	Heat transfer coefficient
H	Helical pitch of pipe (or) spacer wire
k	Turbulent kinetic energy
K	Thermal conductivity of coolant
L	Length in the stream-wise direction
N	Total number of pins in the bundle
Nu	Nusselt number
Nu_c	Average pin Nusselt number based on T_{G-Na}
Nu_θ	Local pin Nusselt number based on T_{G-Na}

Nu_{c-sc}	Average pin Nusselt number based on T_{SC-Na}
Nu_G	Global Nusselt number
p	Pressure
P_t	Triangular pitch of fuel pins
Pe	Peclet number, $[w_{in} \times D_h / \alpha]$
Pr	Prandtl number $[\mu \times C_p / K]$
Pr_t	Turbulent Prandtl number
P_w	Wetted perimeter
Q_{act}	Actual mass flow rate
q''	Heat flux
R_c	Radius of the coil
Re	Reynolds number $[\rho \times w_{in} \times D_h / \mu]$
s_{ij}	Strain rate tensor
S_t	Stanton number
T	Temperature
T_{c-avg}	Average clad temperature
T_{c-c}	Circumferential-clad temperature
T_{c-max}	Maximum clad temperature
$T_{C\theta}$	Local clad temperature at any axial section
T_{G-Na}	Global cross-stream average sodium temperature at any Z
T_h	Peak clad temperature at any axial section
T_{in}	Coolant inlet temperature
T_{SC-Na}	Average sodium temperature of all sub-channels surrounding the pin at any Z
T'	Instantaneous fluctuating component of temperature
\bar{T}_c	Circumferential averaged clad temperature at any Z

$u_{i,j,k}$	Velocity components
u'_i, u'_j	Instantaneous fluctuating component of velocity in x, y direction
u^*	Friction velocity
V_{cs}^*	Cross stream velocity
w	Axial velocity of coolant
w_{in}	Coolant inlet velocity in Z-direction
W	Ratio of helical pitch to diameter of pin and wire [$H / (D_w + D_r)$]
$x_{i,j,k}$	Spatial coordinates
X	Ratio of pitch to diameter of pin (P_t / D_r)
y^+	Wall distance
Z	Axial coordinate (stream wise coordinate)

Greek Symbols

α	Thermal diffusivity of coolant
Δp	Overall pin bundle pressure drop
ΔT_{B0}	Overall temperature difference in normal pin bundle
ΔT_{BX}	Overall temperature difference in blockage pin bundle
$(\Delta T_\theta)_{max}$	Maximum difference in circumferential clad temperatures
ΔT_{out}	Overall pin bundle temperature difference
δ	Curvature ratio, [a / R_c]
δ_{ij}	Kronecker delta
ε	Turbulent dissipation rate
λ	Non-dimensional pitch, [$H / 2\pi R_c$]
μ	Laminar viscosity
μ_{mol}	Molecular viscosity

μ_t	Turbulent (or eddy) viscosity
ν	Kinematic viscosity
φ	Porosity of the medium
ρ	Density of coolant
ψ	Diffusivity of heat / Eddy diffusivity of momentum
$\sigma_k, \sigma_\varepsilon$	Turbulent Prandtl numbers of k and ε
θ	Angle around the pin
τ_{ij}	Total stress

Abbreviations

CDS	Central differencing scheme
CFD	Computational fluid dynamics
CPU	Central processing unit
FBR	Fast breeder reactor
FSA	Fuel subassembly
GB	Gigabyte
HDS	Hybrid differencing scheme
LHS	Left hand side
MUSCL	Monotone upstream-centered schemes for conservation laws
RAM	Random access memory
RHS	Right hand side
RNG	Renormalization Group
RSM	Reynolds stress model
SC	Sub-channel
SIMPLE	Semi-implicit pressure linked equations

SST Shear stress transport
UDS Upwind differencing scheme

PUBLICATIONS BASED ON THE THESIS

INTERNATIONAL JOURNAL PAPERS

1. Investigations of flow and temperature field development in bare and wire-wrapped reactor fuel pin bundles cooled by sodium. **Govindha Rasu, N.**, Velusamy, K., Sundararajan, T. Chellapandi, P., Annals of Nuclear Energy, 55, 29-41 (2013).
2. Simultaneous development of flow and temperature fields in wire-wrapped fuel pin bundles of sodium cooled fast reactor. **Govindha Rasu, N.**, Velusamy, K., Sundararajan, T. Chellapandi, P., Nuclear Engineering Design, 267, 44-60 (2014).
3. Thermal hydraulic effect of porous blockage in fuel subassembly of sodium cooled Fast Reactor. **Govindha Rasu, N.**, Velusamy, K., Sundararajan, T. Chellapandi, P., Annals of Nuclear Energy, 70, 64-81 (2014).
4. Flow and thermal development in wire-wrapped fuel pin bundle of sodium cooled Fast Reactor during low flow conditions. **Govindha Rasu, N.**, Velusamy, K., Sundararajan, T. Chellapandi, P., (Communicated to Progress in Nuclear Energy).

CONFERENCE PROCEEDINGS

5. Investigation of thermal development during liquid sodium flow in a heat generating pin bundle and effect of peripheral sub-channels. **Govindha Rasu, N.**, Velusamy, K., Sundararajan, T., 21st National & 10th ISHMT- ASME Heat and Mass Transfer Conference, paper code: ISHMT_IND_12_31, IIT Madras, India (2011).
6. Influence of pin diameter on flow development in heat generating fuel bundles during liquid sodium flow. **Govindha Rasu, N.**, Dakshinamoorthy, V., Velusamy, K., Sundararajan, T., 38th National Conference on Fluid Mechanics and Fluid Power (FMFP), paper code: HT-17, MANIT, Bhopal, India (2011).
7. A CFD study of flow blockage in fuel pin bundles of Fast Breeder Reactor. **Govindha Rasu, N.**, Velusamy, K., Sundararajan, T., Chellapandi, P., 22st National & 11th ISHMT- ASME Heat and Mass Transfer Conference, IIT Kharagpur, paper code: HMTTC1300101, India. (2013).